AMPLIFICATION-FREE DETECTION AND LIVE-CELL IMAGING OF NUCLEIC ACIDS

Eoin Brennan B.Sc.

Thesis Submitted for Award of

Doctor of Philosophy

School of Chemical Sciences

Dublin City University

Research Supervisors:

Prof. Robert J. Forster (DCU)

Prof. Raymond L. Stallings (RCSI)

July 2015

Declaration

I hereby certify that this material, which I now submit for assessment on the programme of study leading to the award doctor of philosophy is entirely my own work, and that I have exercised reasonable care to ensure that the work is original, and does not to the best of my knowledge breach any law of copyright, and has not been taken from the work of others save and to the extent that such work has been cited and acknowledged within the text of my work.

Signed: _____

ID No.: _____

Date: _____

This thesis is dedicated to the memory of my mother, Denise.

ACKNOWLEDGEMENTS

I would like to take this opportunity to express my sincere appreciation to everyone who has helped to motivate and guide me during my research here in DCU.

Firstly, I would like to thank my supervisor Prof. Robert Forster, you helped me find my passion for research and your guidance and support has been invaluable throughout my PhD. I'd like to thank my co-supervisor Prof. Raymond Stallings for his mentorship throughout my research. I would also like to express my gratitude to Prof. Tia Keyes for her advice.

I would like to thank the members of our research group that I have worked with for the past four years. In particular, Dr. Elaine Spain for her help with electrochemistry and SEM imaging and Dr. Roisin Moriarty who assisted me with cell culture and cell imaging.

I would also like to sincerely thank my friends and family who have supported me in my studies. A huge thank you to my mum Bernadette, for her optimism and guidance especially when helping me with my thesis and for sticking by me through thick and thin! To my father Henry, who has been with me every step of the way, I couldn't have done it without you Dad, thank you for everything! Thank you Fiona, the best sister a brother could have. Finally, I thank my girlfriend and closest friend Megan for making the last three years the best of my life, and for keeping me sane through stressful times.

BioAT centre Funded under the Programme for Research in Third-Level Institutions and co-funded under the European Regional Development fund.

This material is based upon works supported by the Science Foundation Ireland under Grant No. 10/IN.1/B3021.

Table of Contents:

CHAPTER 4: Solution Phase Detection of miR-132

CHAPTER 5 Live Cell Imaging of miR-132

List of Figures

Glossary

Acronym	Explanation
6-FAM	6-Carboxyfluorescein
A	Adenine
A.U.	Arbitrary Units
Au	Gold
BHQ	Black Hole Quenchers
BMM	Base Mismatch
BODIPY	Boron-Dipyrromethene
C	Cytosine
C12	Dodecanethiol Monolayer
CNT	Carbon Nanotube
COOH	Carboxylic Acid
CPP	Cell Penetrating Peptide
CV	Cyclic Voltammetry
Cy5	Cyanine-5
Dabcyl	4-((4-(dimethylamino)phenyl)azo)benzoic Acid
DGCR8	DiGeorge Syndrome Critical Region 8 Gene
DMSO	Dimethyl Sulfoxide
DNA	Deoxyribonucleic Acid
DNase	DNA Nuclease
EA	Electrochemical Area
EDC	1-Ethyl-3-(3-dimethylaminopropyl)carbodiimide
EtOH	Ethanol
Fluc	Firefly Luciferase
FRET	Förster Resonance Energy Transfer
G	Guanine
GFP	Green Fluorescent Protein
Gluc	Gaussia Luciferase

H_2O_2	Hydrogen Peroxide
H_2PtCl_6	Hydrogenhexachlorideplatinate (IV) Hydrate
H_2SO_4	Sulphuric Acid
HCl	Hydrochloric Acid
HeNe	Hydrogen Neon
IRF	Instrument Response Function
K_2HPO	Dipotassium Phosphate
LNA	Locked Nucleic Acid
LP	Long Pass
MB	Molecular Beacon
MB1	Molecular Beacon, Version 1
MB2	Molecular Beacon, Version 2
miRNA	Micro RNA
mRNA	Messenger RNA
MS	Microspheres
NA	Nucleic Acid
NaOH	Sodium Hydroxide
NP	Nanoparticle
PAP	Poly(A) Polymerase
PBS	Phosphate Buffered Saline
PCR	Polymerase Chain Reaction
PNA	Peptide Nucleic Acids
Pol II	RNA Polymerase II
pre-miRNA	Precursor MicroRNA
pre-mRNA	Premature Messenger RNA
pri-miRNA	Primary-MicroRNA
Pt	Platinum
PtNP	Platinum Nanoparticle
qRT-PCR	Quantitative Reverse Transcription PCR
RF	Roughness Factor

RFP	Red Fluorescent Protein
RISC	RNA-Induced Silencing Complex
RNA	Ribonucleic Acid
RNase	Ribonuclease
RNase	RNA Nuclease
RT	Reverse Transcriptase
SEM	Scanning Electron Microscopy
SWCNT	Single Walled Carbon Nanotubes
T	Thymine
TCSPC	Time-Correlated Single Photon Counting
U	Uracil
UTR	Un-Translated Region
UV	Ultraviolet–Visible Spectroscopy

Symbols	Explanation	Units
A	Area of working electrode	cm^2
A	Amplitude at time 0 (Lifetime)	counts
A^G	Geometric Area	cm^2
aM	attomolar	-
A_P	Area under curve	cm^2
β_{max}	Maximum Specific Binding	A.U.
C	Capacitance	F
cm	centimetre	-
d	diffusion length	cm
D	Diffusion coefficient	cm^2s^{-1}
E	Potential	V
F	Faradays Constant	C
J	Spectral overlap integral	cm^6
K^2	Orientation factor	-
K_a	Association Constant	-
mL	millilitre	-
mM	millimolar	-
µm	micrometre	-
µM	micromolar	-
MW	Molecular Weight	$gmol^{-1}$
nm	nanometer	-
nM	nanomolar	-
P-Value	Significance Level	-
Q	Total Charge	C
R_0	50% efficient energy transfer	Å
t	time	s
τ	Fluorescent Lifetime	ns
Tm	Melting Temperature	°C
X^2	Chi-Square Value	-

$\Delta G°$	Gibbs free energy	$kJmol^{-1}$
ϕ_D	Fluorescence quantum yield	-

Abstract

A number of approaches which aim to achieve amplification free nucleic acids detection are reported. The first approach uses dual function platinum nanoparticles to detect DNA. These particles physically separate DNA capture and electrocatalytic detection, which allows for significant enhancement for the sensitivity of DNA detection. Platinum nanoparticles were grown in the defect sites of an alkane thiol monolayer. These particles could then be functionalised with a capture DNA strand, and subsequently released from the surface by sonication. Using this method attomolar limits of detection were achieved.

A molecular beacon for the detection and quantification of miR-132 is also reported. The stem-loop structure comprises a sequence complementary to miR-132, modified with a 6-FAM dye and dabcyl quencher on either end. In the absence of the target, self-binding occurs bringing the luminophore and quencher into close proximity significantly decreasing the emission intensity. In the presence of miR-132, the signal is greatly enhanced, with a linear increase in intensity from a molar ratio of 0.25 to 2.00 of target. The structure could also efficiently differentiates between target and mismatched nucleic acid sequences. In the presence of a single base mismatch, the intensity is approximately a factor of 2 lower than a fully complementary target reflecting its lower association constant.

The molecular beacon was then introduced into neuroblastoma cells by electroporation, allowing the miR-132 to be imaged within live cells. miR-132 appears to be localised within the nucleus of the cells where its concentration is of the order of 1μM. Transfection of the cells with an anti-miR-132, resulted in a decrease in the average emission intensity of 18%, however due to high variability in miR-132 between individual cells, confirmation of a statically significant difference was not possible.

A displacement assay for the detection of miR-132, a biomarker of neuroblastoma, was also investigated. In this work, a capture strand of DNA complimentary to miR-132 was bound to a surface. A probe strand of DNA partially complimentary to this capture was attached to a large microsphere functionalised with Cy5 dye for visualisation of the particle. These microspheres where then bound to the surface by hybridization. This caused quenching of the dye excited state by the gold. When the fully complimentary miRNA target was added, it displaced the probe strand, and attached microsphere. This

resulted in a “switching on” of dye emission from the particles. This has the potential for single molecule miRNA detection, with a single binding event can generate a large detectable signal.

CHAPTER 1

Theoretical Framework and Survey of Literature

1.1 Introduction

Micro ribonucleic acid (miRNA) has been shown to have an essential role in a wide variety of biological pathways.[1] As such, cells which have become cancerous tend to have a differential expression of miRNA compared to healthy cells. Analysis of the miRNA expression of a wide number of cancer types has found miRNA deregulation in the majority of cases.[2]

Recently, detection of miRNA expression has been identified as an attractive method of determining disease state for a wide range of cancers.[3] Live-cell imaging has the potential to allow for real-time analysis of this miRNA expression profile that can enable recognition of the molecular subtype of cancer, which can inform the treatment strategy.[4] For example neuroblastoma, the most common extracranial solid tumour found in children, has significantly differential progression, with some patients recovering with no treatment, whereas for others the prognosis is poor, even with aggressive treatment.[5]

Early detection has been linked to improved survival rates for a number of cancers.[6-8] The miRNA biomarkers associated with early stage cancerous cells tend to be present at very low concentrations (fM), which makes detection challenging.[9]

Currently, the state of the art detection method is Polymerase Chain Reaction (PCR) whereby a miRNA of interest is amplified to detectable limits.[8,10] While this method has exceptional sensitivity, with detection of a few as 10 miRNA copies possible,[11] it requires highly purified samples and highly skilled personnel[12]. This is acceptable in the context of centralised laboratories, but has the effect of significant increasing the cost and time for detection. In order for wide-scale screening of miRNA expression to occur, the detection strategy needs to be both inexpensive and simple to perform. This research aims to achieve amplification-free selective and sensitive nucleic acid detection.

1.2 Nucleic Acids

DNA contains all of the information needed to build a cell, to become tissues and form organs. This information is stored as genes, with each gene responsible for a trait of the organism[13]. The DNA must be protected from damage to ensure the integrity of this data.[14] For this reason the DNA is contained in the nucleus of the cell, where transport is tightly controlled.[15] To convey the information contained in the DNA to the rest of the cell, the DNA is transcribed into ribonucleic acid (RNA).[16]

DNA and RNA share a number of structural similarities, with both being linear polymers, made up of individual building blocks called nucleotides or bases.[17] RNAs tend to be shorter than DNA, usually in the range of hundreds to thousands of bases, whereas DNA is longer and can run to millions of nucleotides in length.[18] RNA and DNA are composed of four nucleotides[19]. These nucleotides are bound to a backbone, which is composed of a 5 carbon sugar phosphorylated at carbon 5 and containing a hydroxyl group at carbon 3. This gives DNA and RNA directionality, and by convention DNA is read from the 5' end to the 3' end.[20] A phosphodiester bond links the individual bases together, from the 3' end of one base to the 5' end of another.[21]

The backbone of DNA contains a sugar known as 2-deoxyribose, which is a pentose sugar containing an oxygen bound to two hydroxyl groups. RNA, however, contains the sugar Ribose, which contains a forth hydroxyl group on C3. This additional hydroxyl makes RNA more reactive than DNA, and allows the cell to identify RNA.[22] Another property of this hydroxyl group is that RNA can be cleaved into individual nucleotides in a basic solution.[23]

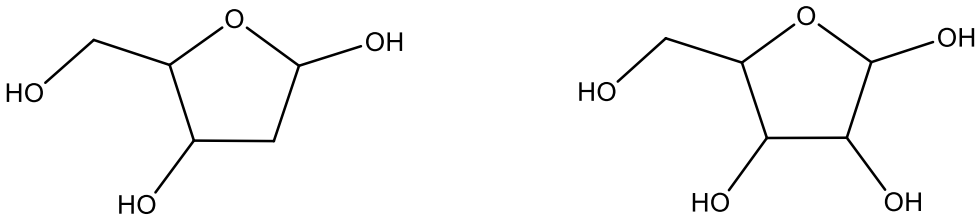

2-deoxyribose Ribose

Figure 1.1: Backbone sugars of nucleic acids, with DNA (left) and RNA (right).

RNA and DNA have a total of 5 nucleotides. These are Guanine (G) and Adenine (A), which contain a six membered ring fused to a five membered ring, and Thymine (T),

Cytosine (C) and Uracil (U) which contain a single 5 membered ring. A, G and C are found in both DNA and RNA, with T being found only in DNA and U only being found in RNA. Thymine is the non-methylated form of Uracil. [24]

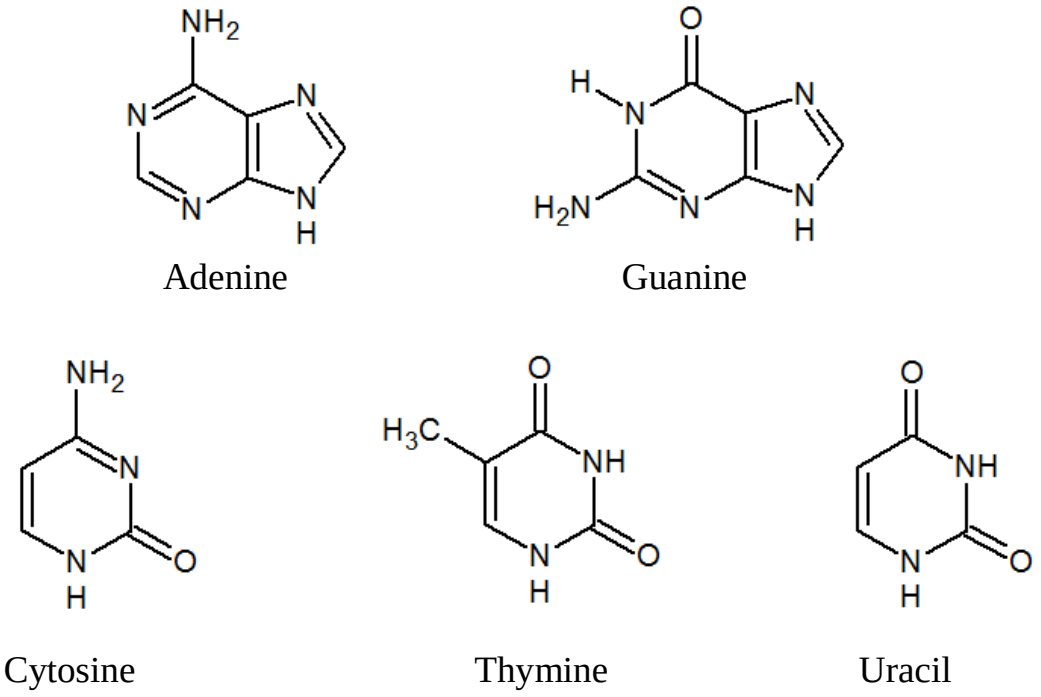

Figure 1.2: Structure of nucleic acid nucleotides.

1.2.1 Base Pairing

In 1953 Watson and Crick discovered that DNA had a double helix structure.[19] This was a major breakthrough for our understanding of the nature of DNA and of the way in which it functions to store genetic information. They found that DNA is composed of two strands of nucleotides which bind together to form a double helix. This means each cell has two complete copies of the information needed to operate that cell. If one of these strands becomes damaged, then this can be identified by its comparison, which allows the damaged cell to enter programed cell death, to prevent these mutations from causing harm to the organism.[25,26]

The two strands are antiparallel, with one strand going from 5' to 3' and the other going from 3' to 5'.[20] Base pairing holds the two strands tightly together. A is paired to T by two hydrogen bonds, and G is bound to C by three hydrogen bonds. [27] The GC pairing is stronger, with a higher binding energy due to interactions with the secondary

structure of double stranded DNA which contributes significantly to the strength of the double helix, with hydrophobic interactions, van der Waals forces, and stacking.[28]

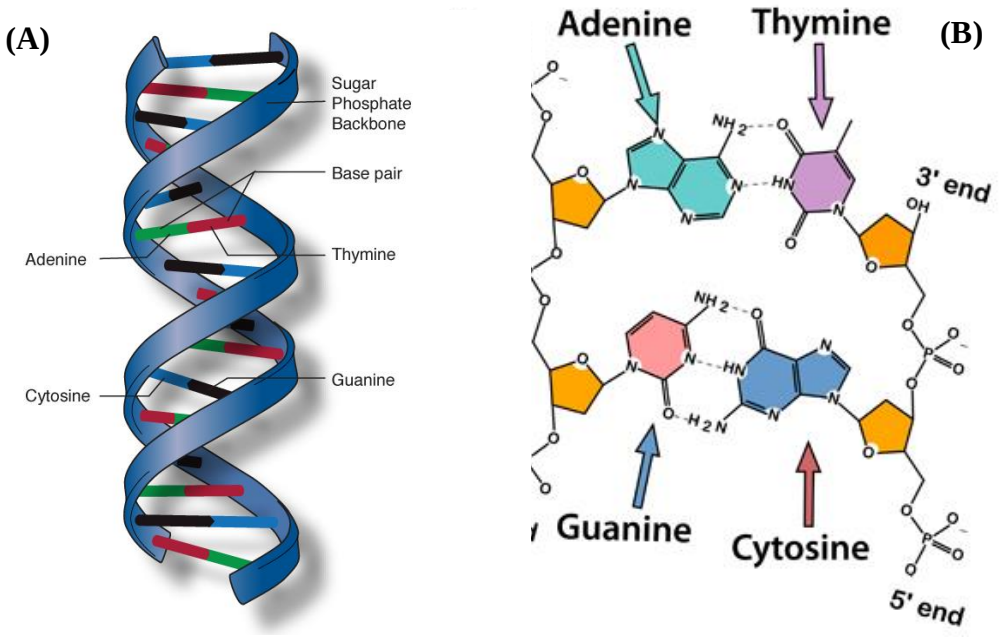

Figure 1.3: The double helix structure of DNA, adapted from: National Human Genome Research Institute "Talking Glossary of Genetic Terms"[29] (B) The base pairing of DNA adapted from "DNA II" Vision learning Vol. BIO-3.[30]

In order for the information stored within the DNA to be accessible, the DNA helix must be capable of unwinding and separating. This process is called denaturation or melting, and can be achieved in the lab by increasing the temperature of a solution containing DNA.[31] As the temperature increases, so does the kinetic energy of the DNA. At a certain point, the kinetic energy of the DNA is sufficient to break the hydrogen bonds holding the strands together. This is known as the melting temperature of the DNA and can be used as a measure of strength of base pairing between two strands.[32]

This melting point is determined by a number of factors. As previously discussed the strength of the GC bond is stronger than the AT bond and so a higher GC content will result in a more stable helix requiring a higher melting temperature.[33] The pH of the solution can also have a major impact on the melting temperature. At a low pH, the bases can become protonated, resulting in a positive charge causing repulsion between the two strands.[34]

1.2.2 Messenger RNA

A number of different types of RNA are transcribed in the nucleus and contribute to the correct functioning of the cell. The types of RNA can be broken down in to two broad categories; protein-coding[35] and non-protein coding[36]. Messenger RNA (mRNA) is the primary coding RNA. Its function is to transfer information from the DNA to the ribosome of the cell.[37] During mRNA synthesis, the part of the DNA that contains the relevant information is copied into RNA by a polymerization reaction mediated by RNA polymerase.[38] The RNA is encoded from 5' to 3', with the 3' hydroxyl group being attacked by the nucleophilic phosphate group. RNA is synthesized at a rate of approximately 1000 nucleotides per minute at normal physiological conditions.[39] Messenger RNA is coded so that three nucleotides carry the information for one amino acid, called a codon.[17]

The RNA produced is known as premature-mRNA (pre-mRNA) and is identical to the template strand of DNA, with the exception of T which is replaced by U.[40] The RNA is then processed in the nucleus to produce mature mRNA, see Figure 1.4. At the 5' end, the cap is modified with a guanine nucleotide which allows the ribosome and transport proteins to recognize the mRNA.[41] The un-translated regions (UTR) are the areas at either end of the coding sequences which do not contribute to protein synthesis. These regions play an important role in the post transcriptional regulation of mRNA, allowing the cell to fine tune the expression of proteins by altering the expression of miRNA.[42] The coding sequence contains the codons for the synthesis of the protein, and is flanked by a start and stop codon which tells the ribosome when to begin and finish translation of the messenger RNA.

The majority of RNA produced and present in a cell does not code for the production of a protein. These RNAs are known as non-coding RNA.[43,44,44]

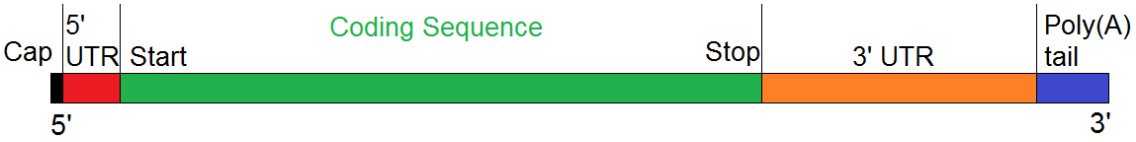

Figure 1.4: Schematic for the structure of a typical messenger RNA

1.3 Micro RNA

Micro RNAs (miRNAs) are a class of small RNA molecules, approximately 16 to 29 nucleotides long, which regulate gene expression at the post-transcriptional level.[45] The primary function of miRNA is to down regulate the synthesis of proteins by protein-coding genes.[46] This is achieved by the degradation or inhibition of mRNA. miRNAs have also been implicated in the activation of targeted mRNA translation. In this way, miRNAs are capable of switching between upregulation and downregulation of proteins, depending on the cell cycle.[47] This makes measurement of miRNA expression an important indicator of cellular function, which allows for the detection of cells with abhorrent expression, for example in cancerous tissue.

miRNAs in circulating blood is an attractive target for disease detection, potentially allowing for non-invasive screening for a range of illnesses including cancer and a number of infections.[9] Detection of miRNA has applications in early disease detection and theranostics, however this requires highly sensitive detection strategies.

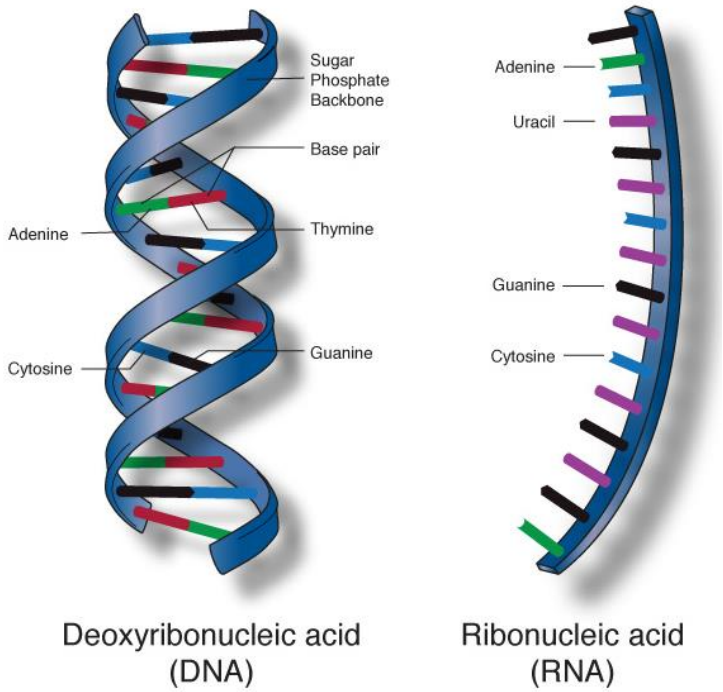

Figure 1.5: Adapted from National Institutes of Health. National Human Genome Research Institute. "Talking Glossary of Genetic Terms" [48]

1.3.1 Biogenesis

Micro RNAs are produced in the nucleus of the cell by transcription from genes. This transcription is performed by RNA polymerase II (Pol II)[49] which can bind to a promoter region on the DNA to transcribe the tail region. The initial RNA strand produced is several hundred bases long, is known as primary-microRNA (pri-miRNA), and can contain the elements for a number of miRNAs.[50] The 5' end is capped with a distinctive nucleotide, and the 3' end contains a number of adenosines, and is known as the "poly(A)" tail.

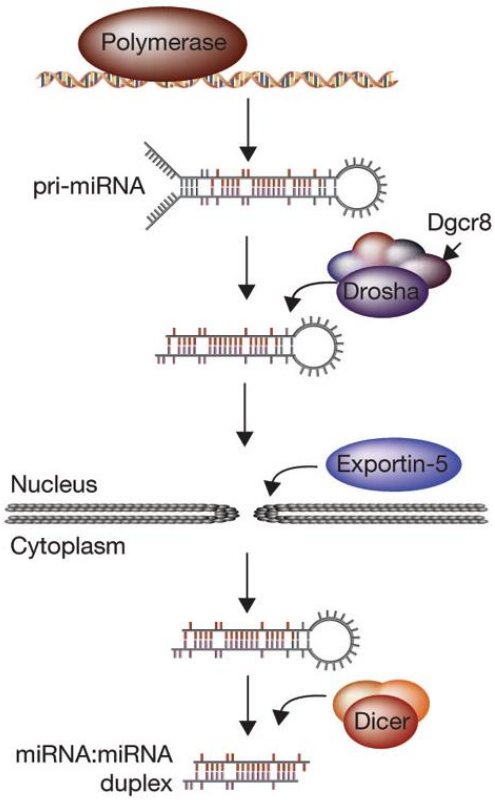

Figure 1.6: Formation of mature miRNA. Adapted from: Small RNAs tell big stories in Whistler, Nature Cell Biology.[51]

Processing of the pri-miRNA is performed by a protein called DiGeorge Syndrome Critical Region 8 Gene (DGCR8) which combines with the enzyme Drosha to form the "microprocessor complex"[52]. Drosha is a protein which can cleave DNA. The pri-mRNA is then cleaved by the microprocessor complex to produce a 60 to 70 base strand with a hairpin structure called precursor microRNA (pre-miRNA). The hairpin formed has a two base overhang at the 3' end.

The pre-miRNAs are transported out of the nucleus by a transport protein called Exportin-5, which identifies the two base overhang.[53] Once in the cytoplasm, the pre-miRNA hairpin is cleaved from the enzyme Dicer to form a miRNA/miRNA duplex approximately 22 bases in length.[54] These two strands of mature miRNA produced are imperfectly hybridized. Generally, only one of these strands is biologically active, while the other is degraded.[55]

Since the pre-miRNA produced in the nucleus contains the same sequence as the mature form, detection strategies which rely on nucleic acid recognition can also detect this species. While this can lead to an increase in the apparent expression of the miRNA detected, the quantity of pre-miRNA present tends to be proportional to the mature miRNA present in the cell.[56]

1.3.2 Mechanism of Action

These mature miRNA are then integrated into a ribonucleoprotein effector complex to form the "RNA-induced silencing complex" (RISC).[57] This complex uses the miRNA strand to identify its target, usually messenger RNA, based on complementarity between the miRNA and mRNA. The messenger RNA is then down regulated by either degradation or by preventing the mRNA from being transcribed. If the miRNA is perfectly complimentary to its target, the mRNA will be cleaved by the enzyme Argonaute2. If the miRNA is imperfectly complimentary, the translation of the mRNA is suppressed.[58]

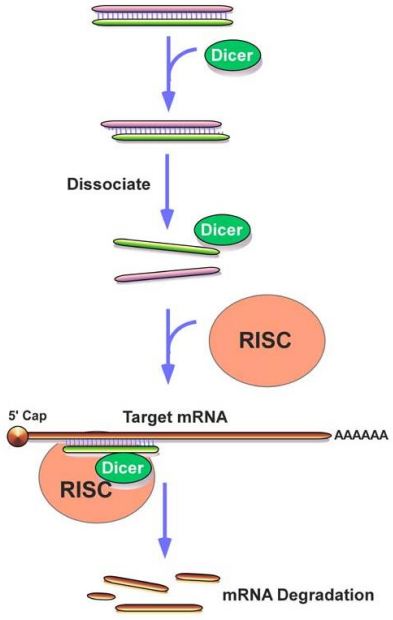

Figure 1.7: Diagram showing the formation of the RNA induced silencing complex, and the subsequent silencing of the mRNA.[59]

1.4 Micro RNA as a Cancer Biomarker

Recently, the role of miRNA as potential biomarkers has been investigated. An ideal biomarker should meet a number of criteria; it should allow identification of a particular disease or condition, provide information on the stage of the illness, be detectable in clinical samples or via non-invasive methods and allow monitoring on clinical response to an intervention.[60] miRNA have the potential to meet each of these requirements.

The essential role of miRNA in a variety of biological pathways is well known.[1] Cancerous cells show a differential expression of miRNA when compared to cells that are healthy. miRNA deregulation has been identified as occurring in the majority of cases examined for miRNA expression covering a wide range of types of cancer.[2] This deregulation occurs for oncomirs, which are miRNAs which suppress the genes responsible for cell differentiation and apoptosis,[61] and tumour suppressor miRNA which are downregulated in cancer.[3] Together, these up and down regulated miRNA form an expression profile which is unique to the cancer subtype. This profile can then be used to diagnosis the illness and to inform treatment.

Expression profiling of ovarian cancer tumours found that compared to normal ovarian cells, miR-100 was downregulated in 76 % of tumours. Significantly, miR-214 and miR-200a were found to be upregulated in high-grade and late-stage tumours. Furthermore, tumours with higher expression of miR-214 were found to be resistant to cisplatin.[62] This expression profile highlights the ability of miRNAs to aid in the identification, staging and to inform the treatment of cancer.

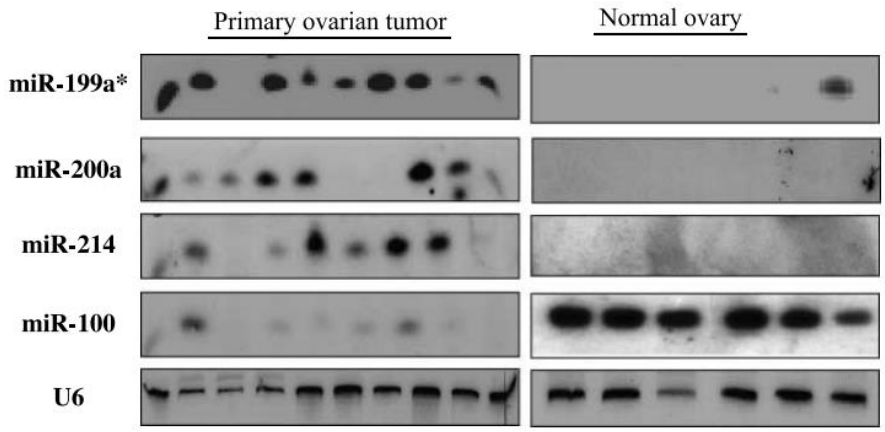

Figure 1.8: Expression of miR-199, miR-200a, miR-214 and miR-100 in primary ovarian tumours (left) compared to normal ovarian tissue (right). [62]

A study by Wu at al. [63]identified a panel of four miRNA biomarkers to determine the risk of metastasis in clear cell renal cell carcinoma (ccRCC). The miRNA identified were miR-10b, miR-139-5p, miR130b and miR-199b-5p. Using a qPCR based assay this miRNA panel proved capable for the determination of metastasis risk and prognosis, with 76 % sensitivity and 100 % selectivity. This is particularly significant since no other means of predicting metastases in ccRCC is currently available.

While these studies focused on clinical tumour samples, research into circulating miRNA as a biomarker is also on-going.[60] Stable miRNAs have been detected in a number of bodily fluids, including blood and saliva.[64] This is attractive for minimally invasive detection of cancer. miRNAs are vulnerable to RNase degradation in the extracellular environment.[65] Blood has been shown to contain RNases[66], so the presence of stable circulating miRNA suggests a protection mechanism for these miRNA. Some studies have shown that encapsulation with proteins or lipid membranes may act to shield miRNAs from degradation.[67,68]

A study by Kerin et al.[69] investigated miRNA biomarkers for the early detection of breast cancer. A panel of 7 miRNA were identified which were differentially expressed in the whole blood of patients with breast cancer compared to a health control. Two miRNA in particular, miR-195 and let-7a were found to be significantly higher on average, with a 19.25 fold increase for miR-195. Detection of an elevated level of miR-195 proved capable of predicting individuals with cancer at a rate of 100 % specificity and 85.5 % sensitivity.

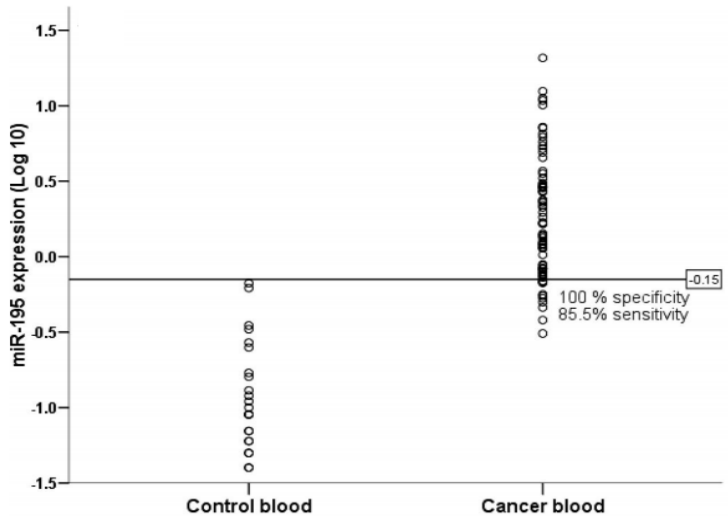

Figure 1.9: Difference in miR-195 expression in blood of breast cancer patients(right) compared to a health control (left), with line showing a concentration which achieves 100% specificity and 85.5% sensitivity.[69]

Tewari et al.[70] studied the expression of miRNAs in human plasma from patients with prostate cancer. A panel of four miRNA which are upregulated were identified, miR-141, miR-16, miR-24 and miR-19b. Significantly, detection of elevated miR-141 could identify an individual with cancer at 60 % sensitivity and 100 % specificity. The concentration which corresponded to detection of cancer in this work was approximately 25 fM.

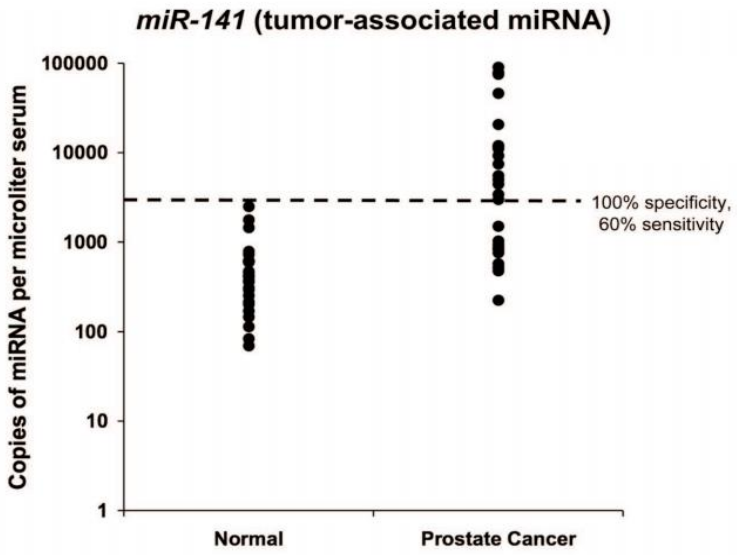

Figure 1.10: Detection of mioR-141 in the serum of 25 healthy controls (left) and 25 patients with metastatic prostate cancer (right) with line showing a concentration which achieves 100% specificity and 60%% sensitivity. [70]

While significant research is on-going to identify miRNA panels for the detection and prognosis of various cancer subtypes[60], the ultra-low concentrations of the miRNA biomarkers involved require highly sensitive methods for effective detection. As illustrated in Figure 1.10, the concentrations of miRNA in blood are extremely low, in the attomolar range. The importance of multiplexed detection strategies is highlighted in these studies. For the early detection of cancer, widespread screening would be required, which can be facilitated by point of care detection. To achieve these goals, the detection strategy must be inexpensive, rapid and simple[71] while it must also be compatible with multiplexed detection of multiple miRNAs, and achieve detection in the attomolar range. In the studies previously discussed, PCR was used for the determination of miRNA expression level. While PCR is highly sensitive and capable of multiplexed detection, the cost and time associated with a measurement make implementation of wide-scale screening difficult to implement.[12]

1.5 miRNA Detection

1.5.1 Northern Blot Analysis

The earliest attempts to quantify miRNAs were by northern blotting. This procedure starts with the extraction of RNA from the sample of interest. The miRNA are then separated on the basis of size using gel electrophoresis, and transferred to a nylon membrane by a capillary blotting system. The RNA can then be covalently attached to the membrane by a variety of methods. Traditionally, this was done by UV light or heat. A labelled nucleic acid probe is then added to the system, which hybridizes specifically to the miRNA of interest. The nylon sheet is then washed to remove the non-specifically bound probe, and the bound probe can be detected by X-ray film.[72]

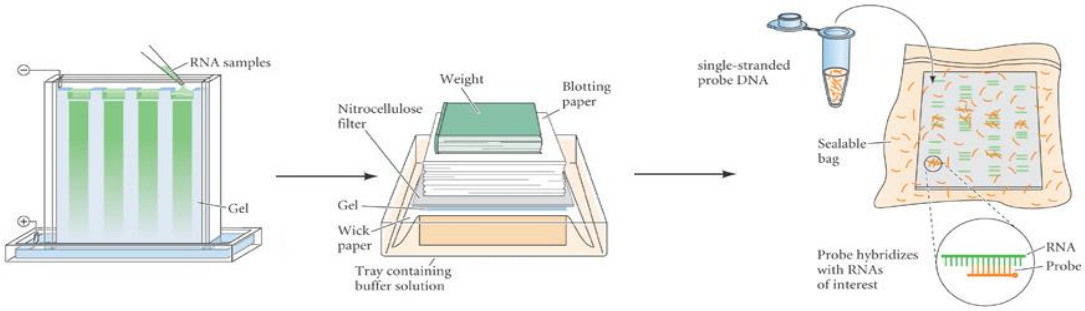

Figure 1.11: Basic procedure for carrying out a northern blot analysis. Adapted from: Developmental Biology, 2014, 10th Edition [73]

This method was originally designed for use in mRNA detection, and so a number of alterations have been made to improve detection sensitivity.[74] Cross linking by UV light or heat can cause damage to miRNA, and is thus generally unsuitable. Recently, 1-ethyl-3-(3-dimethylaminopropyl)carbodiimide (EDC) has been used to crosslink miRNAs to the nylon membrane, and this has improved sensitivity by 25 to 50 fold. The nucleic acid probes traditionally used were DNA based, however for miRNA detection, this results in poor sensitivity and long hybridization times. The use of locked nucleic acids (LNA) results in significant improvement and using these improved methods, miRNA has been detected as low as 0.05 fmol.[75]

Overall, this method benefits from simplicity and ease of use, however it does require significant time to setup, run and detect the miRNA of interest. It also requires a number of steps, from RNA purification to gel electrophoresis, EDC binding and addition of probe.

1.5.2 qRT-PCR

Quantitative reverse transcription polymerase chain reaction (qRT-PCR) is a method of miRNA detection based on the specific amplification of the miRNA of interest.[76] PCR is a process which amplifies DNA in a highly specific manner. The first step in qRT-PCR is to synthesise "copy" DNA (cDNA) from the extracted RNA. This is done using reverse transcriptase (RT)[77]. In a typical experiment, two different reverse transcriptions are carried out. Using random primers all of the RNA in a sample is reverse transcribed to cDNA, and this cDNA is used to amplify an endogenous control (housekeeping gene).[78] The second type utilises microRNA-specific RT which, unlike the first RT, only reverse transcribes a single miRNA. This primer binds to the miRNA of interest and allows the reverse transcriptase enzyme to identify the miRNA and to generate cDNA. This process is destructive, with the miRNA being disassembled as the DNA is assembled (Figure1.11).[79] The resulting cDNA can be used in subsequent PCR reactions.

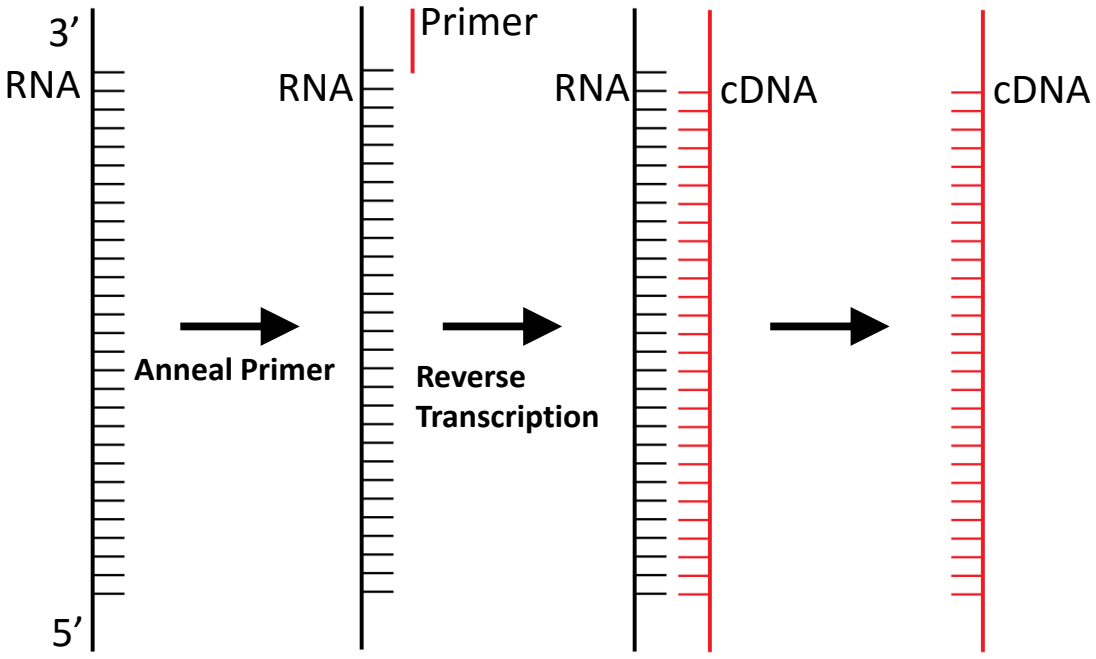

Figure 1.12: Scheme for reverse transcription from RNA to cDNA in PCR.

In real time PCR, results are obtained from an early phase of the PCR run. This early phase of amplification is known as the exponential phase and is very specific.[80] A

nucleotide sequence called a TaqMan probe is used in addition to two primers, deoxynucleotides and a DNA polymerase enzyme.[81] The probe is tagged with a florescent molecule, known as a Reporter, and an excited state acceptor molecule called a Quencher.[82] When the DNA polymerase synthesising the new DNA reaches the annealed probe, it cleaves the probe. This increases the distance between the Quencher and the Reporter, allowing the fluorescent signal from the Reporter to increase. The increase in signal is proportional to the amplification of the target, see Figure 1.12.[83]

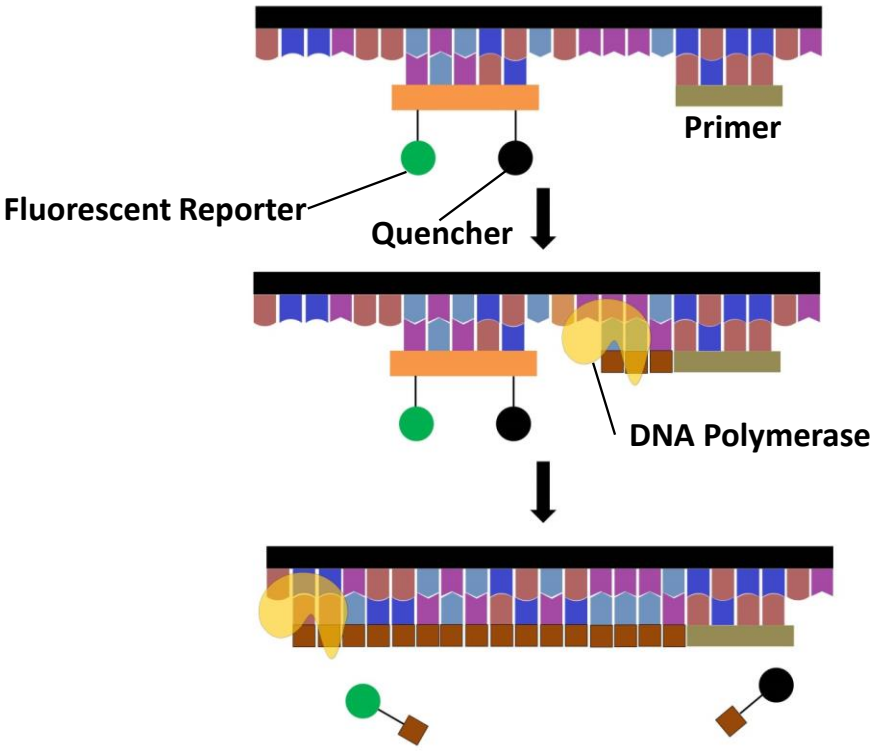

Figure 1.13: Diagram showing generation of fluorescent signal during quantitative PCR.

In each cycle, the amount of target miRNA is doubled. After a certain number of cycles, the florescence will become intense enough to be detected and this cycle number is known as the Ct value.[84] The more miRNA present in the original sample, the more quickly this will happen i.e. the lower the Ct value. Using this Ct value the relative quantification of a target miRNA can be calculated. The endogenous control is used to normalise samples.[85] qRT-PCR is capable of detecting a very low concentration of miRNA, in some cases a copy number of 10 or less.[11] Unfortunately, PCR currently requires highly purified samples. This significantly increased the time for a detection, and requires highly skilled technicians.[12] This makes PCR unsuitable for a point of care setting.

1.5.3 Optical Detection Methods

Optical detection of miRNA has the potential to be considerably faster than northern blotting or PCR, but can have issues with sensitivity.[86] In a simple miRNA microarray, a strand of nucleic acid which is complimentary to the target of interest is covalently bound to a surface, this is commonly referred to as the "capture" strand.[87] The extracted RNA, containing the miRNA target, is then labelled with a fluorescent label and exposed to the surface. The target miRNA binds to the capture strand, and the remaining RNA is rinsed from the surface. The miRNA concentration can then be determined using a fluorescence reader to measure the intensity.[88]

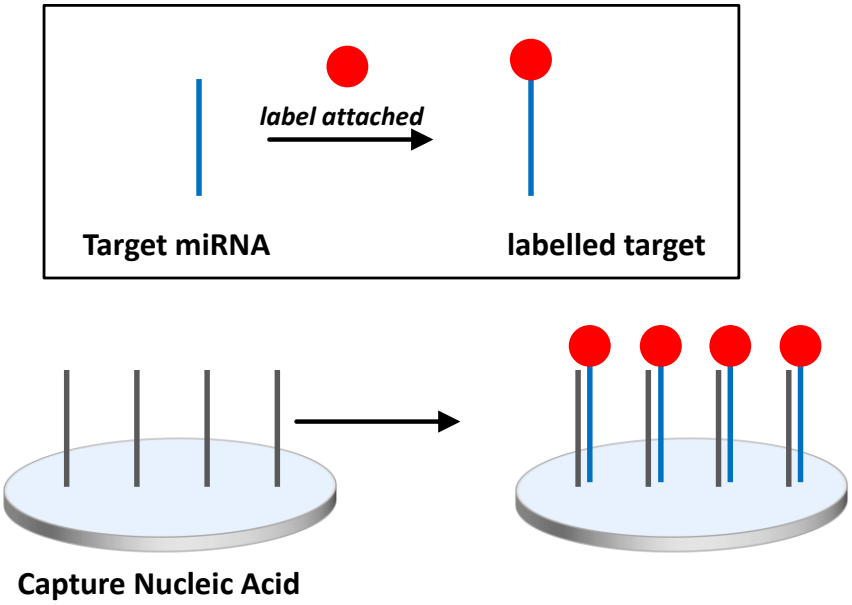

Figure 1.14: Diagram of a nucleic acid microarray with labelled miRNA target.

Biological Labelling

Labelling of the miRNA can be done in a number of different ways. Direct labelling is the modification of the miRNA with a dye and has been widely applied in many settings.[89] One such method is Guanine labelling, whereby the miRNA is modified at the N7 position of guanine moieties with a fluorophore. This has the advantage of allowing the attachment of multiple dyes to a single miRNA, which improves the signal intensity. However, it means that the sensitivity is directly determined by the Guanine content of miRNA, and this can vary greatly between different miRNA.[90]

Another direct labelling method uses T4 RNA ligase which couples to the 3' terminal of miRNA to attach a dye molecule.[91] It was discovered that this method is only suitable for RNA in the 18-25 nucleotide size range. Further investigation showed that this method requires the OH moiety present on the 3' terminal of mature miRNA. This provides significant benefits, as labelling of other RNA in an extracted sample represents a considerable source of background signal. This specificity removes the need to separate the miRNA from other RNA present, improving detection time. One disadvantage of this method is that only a single dye is attached to each miRNA, which severely reduces the limit of detection. The sensitivity of this method has been shown to be superior to northern blotting, but considerably less effective that qRT-PCR.[92]

Another method of direct labelling involves the use of Poly(A) polymerase (PAP) enzyme, which causes the addition of a polynucleotide tail, 20-50 nucleotides long, on the 3' terminal. This poly(A) tail can then be modified using any NHS-ester dye. An advantage of this method is that multiple dye molecules can be attached to each miRNA, which improves sensitivity, and unlike guanine labelling, the sequence of miRNA being examined has been shown to have no impact on this labelling. The limit of detection for this method was determined as 0.14 fmol using miR-124.[93]

Chemical labelling

miRNA labelling using chemical methods allows for much more diversity than biological means. One such method involves the oxidation of the 3' hydroxyl groups using sodium periodate to form a reactive di-aldehyde. This was then reacted with Biotin-X-hydrazide in a condensation reaction to yield biotinylated miRNA, which could then be precipitated using ethanol. A quantum dot was then attached to the biotin specifically using streptavidin. Quantum dots have very high quantum efficiency, and so maximise the detection sensitivity. This method also has the benefit of consistency between different miRNA. While this particular reaction yielded a modest limit of detection of 0.4 fM, this procedure allowed for the attachment of more sophisticated detection moieties.[94]

1.5.3.1 Indirect Labelling

Direct labelling suffers from the need to modify the target miRNA before detection, which presents several challenges, such as different labelling efficiencies for different miRNAs, and increased background signal due to the presence of other miRNA which are labelled due to non-specific adsorption.[95] Indirect detection can overcome many of these shortcomings. In an indirect microarray, a capture strand which is complimentary to approximately half the target is covalently attached to the surface, the target is then added, without the need for prior sample separation.[87] The surface is rinsed to remove non-specifically bound RNA, and a second nucleic acid strand, complementary to the free portion of the target is introduced- a sandwich assay. This "probe" strand can be modified in advance with a wide variety of dyes, complexes and other detection moieties. This system allows for a much greater degree of control over the detection strategy, as the probe strand can be produced with a binding site such as an amine or thiol for easy modification.[88]

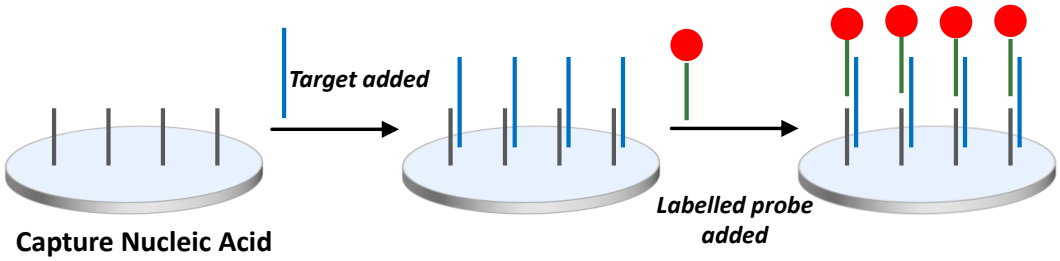

Figure 1.15: Diagram of a nucleic acid microarray with labelled probe strand.

One such system was created using Locked nucleic acids, which has the advantage of improved binding efficiency and improved differentiation from mismatched sequences. This is important when using shorter capture strands.[96] The capture and probe strands were 10 -12 nucleoids in length, with five sets designed to target five different miRNA. The target miRNA were attached to a surface via a capture LNA strand, a biotin functionalised probe strand was then introduced, and Cy3 dye labelled streptavidin was added. Using this system, a limit of detection of 1 Amole or 10 fM was achieved. By adjusting the temperature during the capture and probe hybridisation, this system was also capable of discriminating a single mismatched base.[97]

1.5.4 Electrochemical Detection

Electrochemical detection of miRNA has a number of benefits over optical methods. The signal produced for a single electrochemical event can be significantly higher than optical methods can achieve, a light source is not required and the instrumentation is significantly more robust. A study by Marija et al used nanopores to sensitively detect miRNA in a solution. [98] In this research, a strand of RNA complimentary to the miRNA target was added to the solution to form a stable duplex. A protein, p19, which specifically binds only to double stranded RNA, was linked to a magnetic nanoparticle. This complex was added to the solution where it is bound to the target duplex, and could then be removed from the solution by the application of a magnetic field. This achieved a significant enrichment by a factor of 100,000-fold of the target duplex. The duplex was then separated from the p19 and detected using a nanopore. This nanopore is 3-nm in diameter and less than 10 nm thick. It is capable of detecting single molecules of miRNA by measuring ion conductance though the pore. As the Target miRNA duplex moves through the membrane, the flow of ions though the channel is reduced, which causes a decrease in the observed current. The transit time of the analyte though the pore is dependent on its nature, with DNA transiting in 20 µs, whereas RNA takes 50 µs. Discrimination is also possible by examining the current profile of the molecule, with RNA producing a greater current differential.

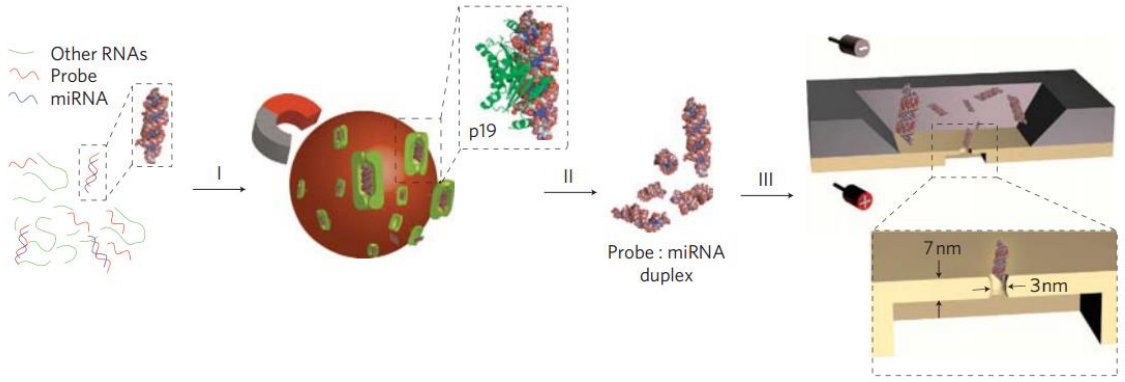

Figure 1.16: Detection strategy for the detection of miRNA. Step (I), DNA complimentary to miRNA target added. (II)Enrichment of miRNA target using a protein, P19, which selectively binds to duplexed nucleic acid. Protein attached to a magnetic nanoparticle to allow for separation. (III) miRNA:probe duplex is released from protein. (IV) Detection of duplex by decrease in ion conductance when passing through nanopore.[98]

Overall, this method allows for the detection of a single molecule of miRNA, however its specificity is based solely on the attachment of the p19 protein, which detects all miRNA duplexes present in the solution. In addition, this pre-processing step is labour intensive, and greatly increases the detection time. This method is also unsuitable for multiplexed detection, as the discrimination at the point of detection is reasonably insensitive.[98]

Some of the limitations of the nanopore approach have been solved by Gu et al.[99] In this study, the target miRNA is identified using a polycationic peptide-peptide nucleic acid probe, which contains a region completely complimentary to the target. Peptide nucleic acids (PNA) are synthetic polymers which are similar to DNA and RNA. They have the benefit of higher binding affinity for the target, forming more stable PNA/miRNA duplexes. PNAs are also stable over a greater range of pH and temperature and are more resistant to breakdown by nucleases and proteases.[100]

A membrane of similar size is used, which can detect the presence of duplexed miRNA, but not single stranded miRNA. A potential is applied across the membrane which attracts the positively charged PNA/Target duplex into the pore, while repulsing other negatively charged single stranded miRNA. As before, when the duplex enters the pore, the ions flowing through are blocked, causing a decrease in the current.

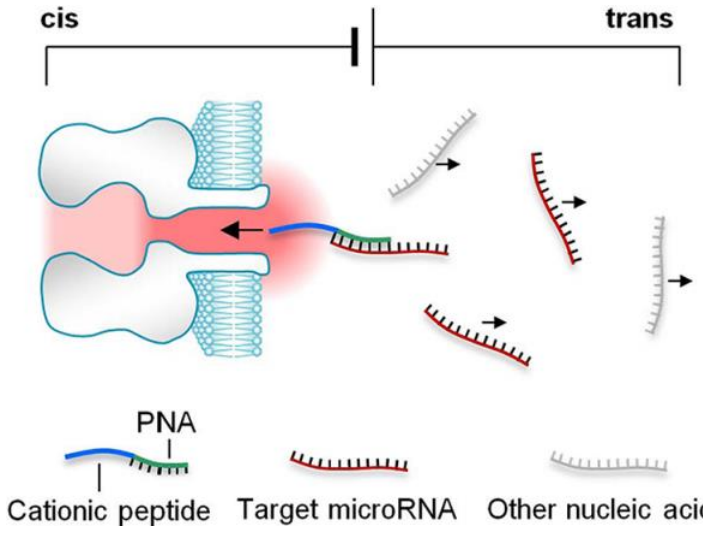

Figure 1.17: Detection of miRNA using a positivity charged PNA probe strand. After hybridisation to miRNA target, detection occurs by drop in current when duplex transits through nanopore. [99]

The limit of detection for the miRNA Let-7b was measured as 50 pM using this system, although data suggests that this might be improved with better data analysis techniques to remove non-specific signals. This method has a number of advantages over earlier approaches. The use of a PNA probe adds target sequence - dependent specificity to the capture probe, and improves the selectivity of the assay due to the high binding affinity of PNA for the perfectly matched target. The potential differential also ensures that only positively charged species will pass through the pore.

Another method which has been shown to have excellent capabilities in detection is based on a neutralizer displacement. In this assay, a capture strand is bound to a nano-structured microelectrode surface. A secondary strand, the neutralizer, which is partially complimentary to the capture, is manufactured with a PNA conjugate and cationic amino acids. When the target is introduced, it displaces the positively charged neutralizer. This binding event can then be detected in two ways, the neutralizer displacement causes a significant change in the charge at the capture strand, and the neutralizer is now free in solution to be detected.[101]

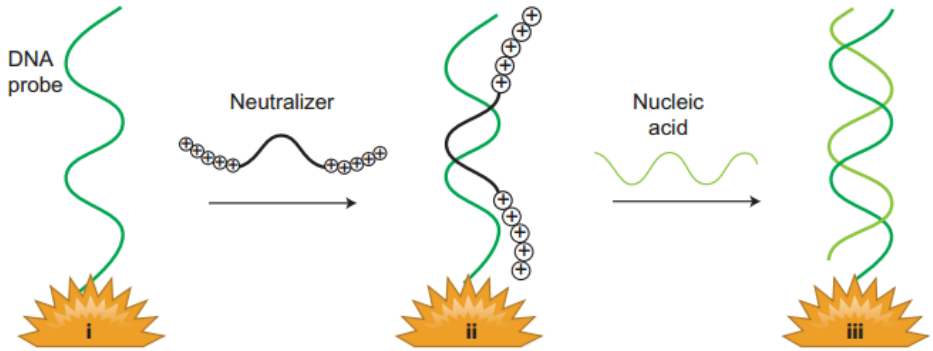

Figure 1.18: detection of nucleic acid by displacement of a partially complementary, positively charged strand.[101]

In this experiment, the primary detection was performed at the electrode surface by measuring the current associated with loss of the neutralizer strand. After the addition of the capture strand, the current was high, and this was reduced after the addition of the neutralizer. When the target DNA was added at 1 pM, the current increased by more than 300%. Further investigation established that, the limit of detection was 100 aM for a 20-mer DNA target. The ability of this system to detect RNA was also examined where it achieved good sensitivity. While miRNA was not directly detected in this study, the ability to detect short DNA sequences suggests that this method would be

suitable, although a slight decrease in the sensitivity would be expected due to the weaker binding efficiency of RNA. This could potentially be overcome however by using LNA based capture strands.

An assay based on direct electrical detection has been developed by Fan et al.[102] In this work, a capture strand was immobilised between a nano-gapped array. The array contained 150 -200 fingers, with each being 700 mn wide and 200 µm long. The capture strand was composed of PNA to improve binding efficiency and to reduce non-specific interactions. The target miRNA was added to the array, forming a duplex with the PNA capture. The duplex was then incubated at pH 4.0 with aniline, hydrogen peroxide and a protein, HPR. The acidic pH caused the aniline molecules to become protonated, and they were then attracted to the negatively charged miRNA/PNA duplex. This resulted in a local increase in acidity which promoted the polymerization of the aniline to form nanowires. The sample was then doped with HCl vapour to improve the conductivity of the aniline.

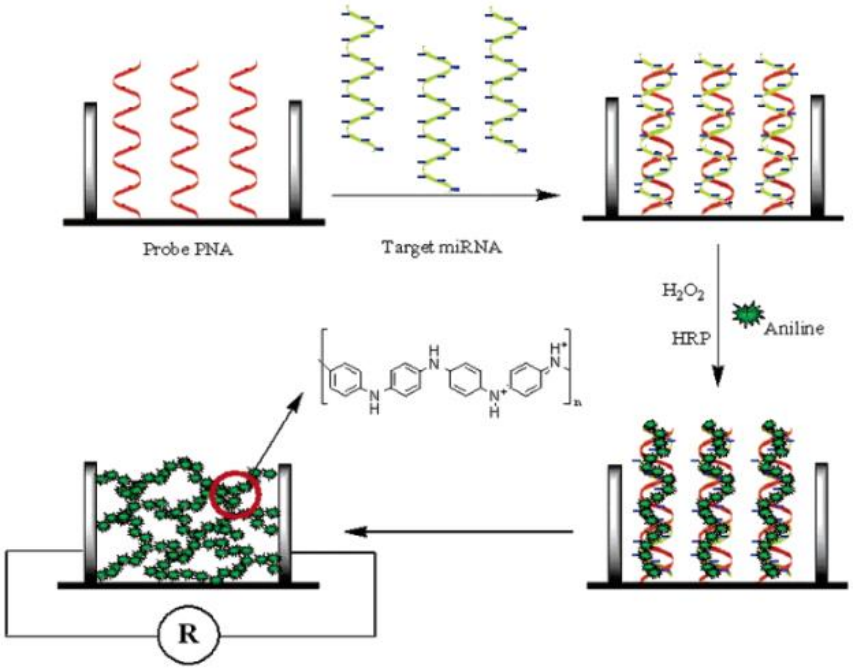

Figure 1.19: Detection of miRNA by capturing with probe PNA in a nano-gapped array, followed by growth of a conductive polymer.[102]

Using this method the limit of detection was determined as 5 fM. To check the selectivity of this method, a miRNA with single base mismatch to the target was examined, and showed only 5 % signal strength when compared to the target. One

major benefit of this system is its suitability for multiplexed analysis, as each finger can be labelled with a different miRNA capture, and the same procedure can then be applied to analyse multiple miRNA simultaneously. This method is highly complicated, requiring a number of steps to achieve detection, which limits the practicality of this system for point of care miRNA detection.

Another platform technology based on the bridging of an electrode was developed by Swager et al.[103] for the detection of DNA. In this work, a capture strand of DNA complimentary to 15 bases of the target nucleic acid was synthesised. This capture strand was then modified on each end with a carbon nanotube (CNT) by covalent attachment. These nanowires were then suspended in a non-conductive nanogap between two gold electrodes to form DNA-CNT network. When the DNA target was added, it hybridised to the capture DNA. A probe strand, modified with the enzyme horseradish peroxidase, was added which bound to the target DNA. This enzyme could then be stimulated to catalyse the reduction of a conductive silver layer, which bridged the non-conductive gap between the two CNTs. This caused a significant increase in the conductivity, which acted as the analytical signal.

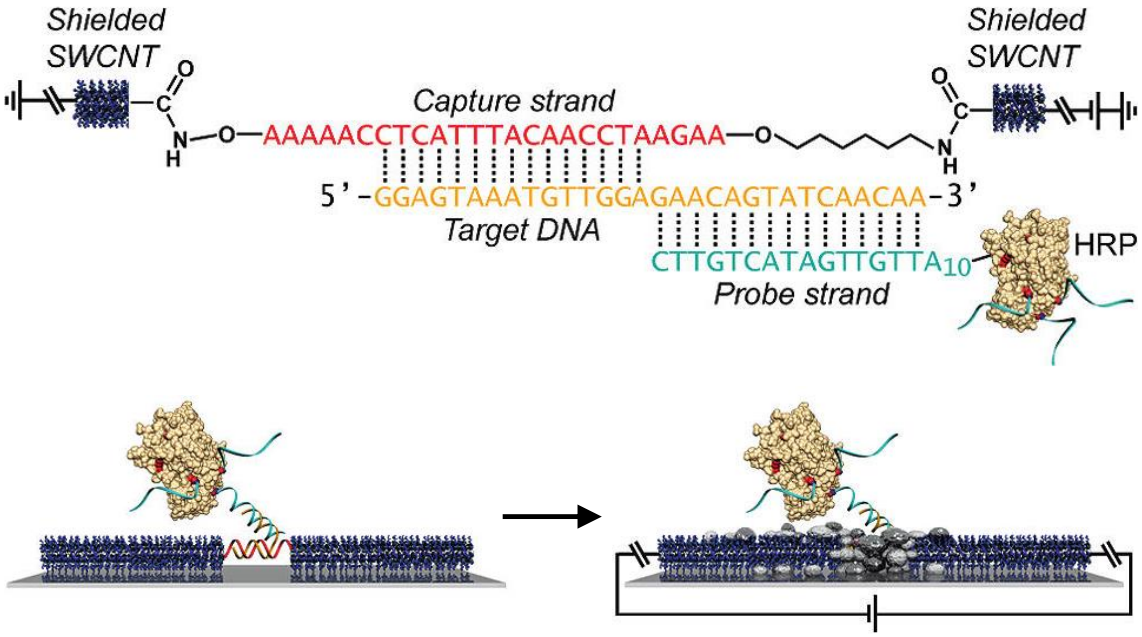

Figure 1.20: Conductivity-based DNA detection method utilizing capture DNA covalently attached to two SWCNT. After hybridisation with target DNA, a HRP labelled probe strand is added, which catalyses the reduction of silver to increase the conductivity between the SWCNT.[103]

The detection limit of this platform was approximately 10 fM for DNA. This method is suitable for miRNA detection, however a decrease in sensitivity would be expected if a DNA capture sequence was used due to the lower binding affinity for DNA/DNA hybrids compared to DNA/miRNA. This technology is not suited to a multiplexed assay presently, and the time required from sample input to measurement may make use of this device in a point of care system challenging.

miRNA detection using a photoelectrochemical system was developed by Dai et al.[104] In this work, single walled carbon nanotubes (SWCNT) are combined with DNA modified with CdS Quantum Dots. The DNA is complimentary to the miRNA target, and remains attached to the SWCNTs based on π-π interactions. The mixture is deposited onto an electrode and light applied to the surface. The quantum dots then generate a measurable photocurrent. DNase I is then added, which breaks down the accessible DNA, while leaving the DNA bound to the SWCNTs unaffected. When the miRNA target is added, hybridisation to the DNA increases the separation between the DNA and SWCNTs, resulting in breakdown of the DNA by DNase I. This causes quantum dots to be released into solution, causing a measurable drop in the photocurrent at the electrode.

Using this method, a limit of detection of 34 fM was achieved, with a linear detection range from 50 fM to 100 pM. This method benefits from simplicity of use, and has potential for use in a point of care setting, since the modified electrode surface can be produced in advance.

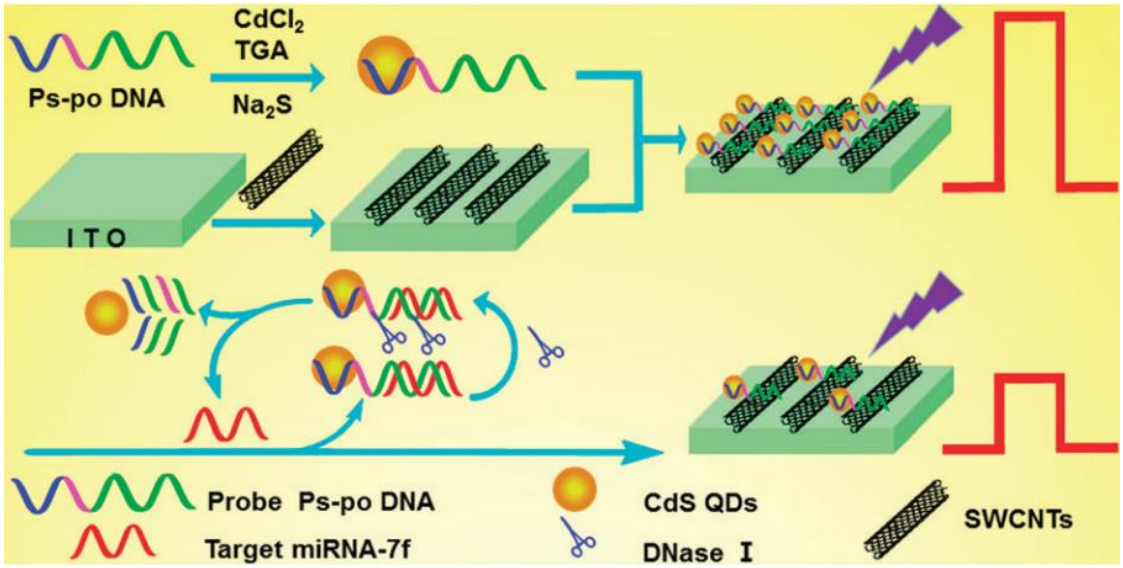

Figure 1.21: Photoelectrochemical detection of miRNA based on displacement of QDs from a SWCNT modified electrode. An electrode is modified with SWCNT, and QD

labelled capture DNA is added, giving rise to a measurable photocurrent. DNase I breaks down accessable DNA. Addition of target causes hybridisation to capture DNA, resulting in DNase I degredation, loss of QD from surface, and a reduction in photocurrent. [104]

1.5.5 Live Cell miRNA Detection

1.5.5.1 Genetic Modification

Live cell imaging of miRNA allows for the visualisation and analysis of miRNA expression levels and alterations. This is important for disease detection and for the elucidation of intercellular processes by studying the dynamics of miRNA expression.[105]

The first live-cell imaging of miRNAs was performed using green fluorescent protein (GFP). In a study by Naldini et al.,[106] cells were transfected with GFP plasmids labelled with DNA complimentary to the miRNA of interest. In the presence of the target miRNA, binding to this DNA resulted in downregulation of GFP production. The level of the miRNA target could then be elucidated by the difference in intensity between cell lines with differential miRNA expression. This system was capable of detecting a number of endogenous miRNA. Significantly, when miR142-3p levels in hematopoietic and non-hematopoietic cell lines were examined, a greater than 100-fold deference in green FP expression was measured.

A more advanced version of this method was developed by Inoue et al.[107]. In this work, miR-133, which is upregulated during myogenic differentiation, was examined in mouse embryos. Cells were transfected with genes for GFP and red fluorescent protein (RFP). As in the previous work, the GFP gene was modified with a capture DNA strand which caused down regulation of protein production upon hybridisation to the miRNA target, in this case miR-133. The RFP was unmodified, and so its expression was independent of mIR-133 concentration. The expression level of miR-133 could then be calculated based on the differential emission intensity between GFP and RFP. This system was capable of detecting the increase in miR-133 expression during differentiation towards muscle cells, see Figure 1.22.

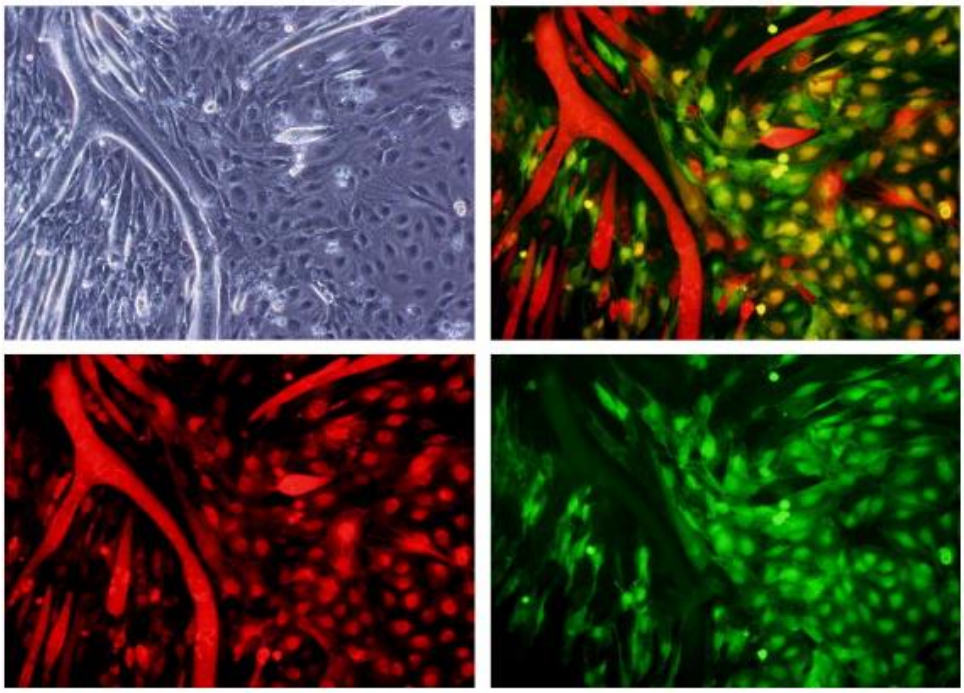

Figure 1.22: Two colour measurement of miR-133. Downregulation of green fluorescent protein caused by miR-133. Red fluorescent protein acts as endogenous control.[107]

While this method was somewhat successful for the detection of miRNA in live cells, it suffers from a number of issues. The poor penetration of the exciting light by tissue significantly reduces the signal to noise ratio.[108] The autofluorescence of cells further obscures the available signal, resulting is significant background.[109] This limits usefulness for this technique for monitoring miRNA for disease detection.

Another approach which has been examined for the *in vivo* detection of miRNA is bioluminescence imaging. This involves the use of photo-active enzymes that emit light when a specific substrate is available, known as luciferases.[110] Bioluminescence imaging benefits from a lack of background bioluminescence signal since no external excitation source is required.[111] A wide range of luciferases are also available at a variety of different wavelengths, including Firefly luciferase (Fluc) which emits at 560 nm[112] and Gaussia luciferase (Gluc) with emission at 480 nm[113]. The higher wavelength Fluc is useful for imaging applications due to increased tissue penetration; however the Gluc produces a considerably stronger light emission.[114]

In a study by Lee at al. [115], a Fluc plasmid was combined with a promoter for pre-miR-23a, which caused an upregulation of Fluc upon pre-miR-23a binding. A second luciferase probe using a Gluc plasmid was modified with a capture strand for mature

miR-23a was also prepared. This probe causes downregulation of Gluc production upon miR-23a binding. This dual probe system was used to monitor premature and mature miR-23a in HeLa, 293 cells and P19 cells. Implantation of these cells into nude mice showed differences in miR-23a concentration in 239 and P19 cells, see Figure 1.23.

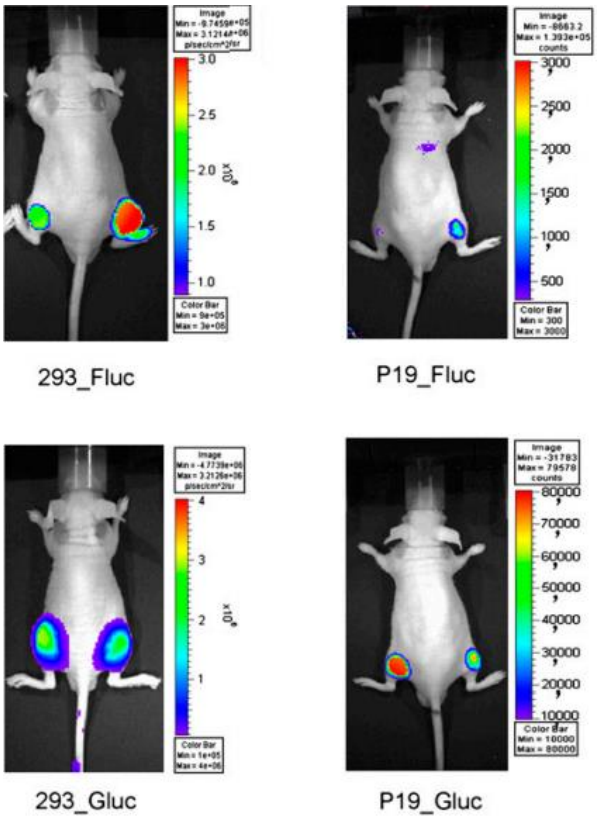

Figure 1.23: Nude mice implanted with 239 and P19 cells transfected with Fluc, which is upregulated in the presence of pre-miR-23a, and Gluc, which is downregulated upon binding to mature miR-23a.[115]

While the use of luciferases overcomes many of the issues with fluorescent proteins, including decreasing the background signal due to autofluorescence and improved tissue penetration for higher wavelength luciferases, a number of issues remain. The use of plasmids for the detection of miRNAs requires genetic modification of the host cells. This makes analysis of the results questionable, since genetic modification may cause changes in the endogenous miRNA concentration. Additionally, these systems rely on the synthesis of the reporter by the cell, meaning the results are strongly dependent on cellular metabolism. A decrease in the observed signal may be due to target miRNA binding, or as a result of apoptosis. These issues make implementation of these genetic techniques in a clinical setting problematic.

1.5.5.2 Molecular Beacons

In a molecular beacon (MB) a strand of nucleic acid which is complementary to the miRNA target is produced. The strand has an additional 4 to 7 bases at one end, with self-complementarity to its opposite end.[116,117] The nucleic acid is modified on one end with a dye and on the other with a quencher molecule. In the absence of the miRNA target, self-binding occurs, which brings the dye and quencher molecules into close proximity. This allows for transfer of the excited state via FRET. When the miRNA target is added, the MB opens up, due to the high affinity for the target. This separates the dye and quencher "switching on" emission. This system has the benefit of very low background signal in the absence of miRNA target, since ideally the dye should be completely quenched.[118] This approach allows for a significant degree of control over the sensitivity and selectivity of the detection.

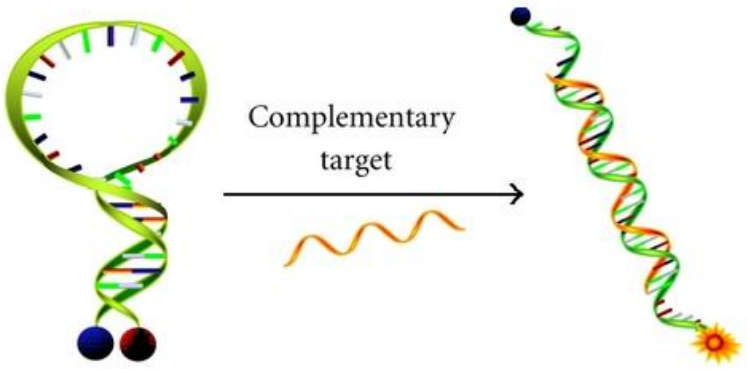

Figure 1.24: Scheme of molecular beacon unwinding when bound to target nucleic acid [119]

Another benefit of MBs is the speed of detection. Since the probe is complimentary to the entire 22 – 25 bases of a miRNA, the binding affinity of the target to the molecular beacon is high, with chemical equilibrium being established in minutes.[120] This is a significant advantage over the genetic methods previously discussed.

1.5.5.2.1 Design Considerations

One issue with plasmid based monitoring of miRNA expression is the limited penetration of light into tissue. Dyes with longer emission wavelengths are capable of improving this penetration. MBs allow for the addition of a number of dyes, with the only limiting factor being the brightness of a dye and availability of a quencher with high efficiency FRET. The dabcyl quencher is widely used for quenching of fluorescent molecules due to its broad absorbance typically giving extensive spectral overlap.[121-123] This allows for quenching of a wide range of dyes such as 6-FAM (em. 520 nm), HEX (em.533 nm) and Cyanine 3 (em. 565 nm).[124] Black hole quenchers (BHQ) are also available a range of absorptions, for example BHQ3 with maximum absorbance at 672 nm[125] allows for higher wavelength dyes such as Texas Red (em. 615 nm) and Cyanine 5 (em. 667 nm) to be integrated into a MB.[124]

The length of the self- complimentary region (stem) of the molecular beacon allows for a significant degree of control over the sensitivity and selectivity of the beacon. If the stem is short, the MB will open more readily, which improves the sensitivity of detection, at the cost of selectivity. Alternatively, a longer stem sequence allows for greater discrimination from mismatched sequences, but lower sensitivity.[126,127]

Another issue when MBs are used for live cell imaging is protection from nucleases. MBs constructed from DNA are vulnerable to degradation by DNases.[128] This allows for an increase in the separation between the dye and quencher, resulting in a fluorescent response in the absence of the miRNA target. A number of strategies have been employed to protect MBs for these cellular nucleases. One example is Locked Nucleic Acids (LNA), whereby an RNA nucleotide is modified with an addition bridge between the 2' oxygen and 4' carbon.[96] LNA has been shown to be resistant to nucleases, and has the additional advantage of improved binding affinity compared to DNA or RNA. 2'-O-methyl-RNA[129] and Peptide nucleic acids[130] are also available.

Delivery of MBs through the cell membrane can be problematic due to the large size and negative charge, which limits passive diffusion.[30] A number of methods have been developed to overcome this issue. Electroporation involves the application of an electric field to the cell membrane.[131] This increases the permeability of the membrane by the formation of pores, which allow diffusion of the molecular beacon into the cell. This method is high efficient for the delivery of MBs but often has poor cell viability.[132] Lipofection is another method for the introduction of nucleic acids to cell. In this

approach, the molecular beacon is placed in a solution containing phospholipids, which spontaneously forms vesicles, encapsulating the MB.[133] These vesicles then merge with the cell membrane, delivering the MB into the cell. This method is capable of high efficient transfection with excellent cellular viability but is generally unsuitable for *in-vivo* detection.[134]

The modification of MBs with Cell penetrating peptides (CPPs) has also been successful. These CPPs facilitate the uptake of the MB through the cell membrane.[135] This method has significant potential for the uptake of MBs without the need for additional reagents, and is potentially suitable for *in vivo* detection, however the exact mechanisms for this process are poorly understood at present.[136]

One of the first attempts to quantify cellular miRNA using molecular beacons was performed by Kim et al.[137] In this work, C2C12 cells were transfected with a MB containing 6-FAM and BHQ1 for the detection of miR-26a, and a second MB for miR-206 with Texas red and BHQ2. Skeletal muscle differentiation of the C2C12 cells showed steadily increasing cellular concentration of miR-026a and miR-206, see Figure *1.25*, with good agreement between PCR results and fluorescent intensity. Significantly, transfection of HeLa cells with synthetic miR-26a and miR-206 resulted in a corresponding increase in fluorescence from 0.01 to 0.1 nmol.

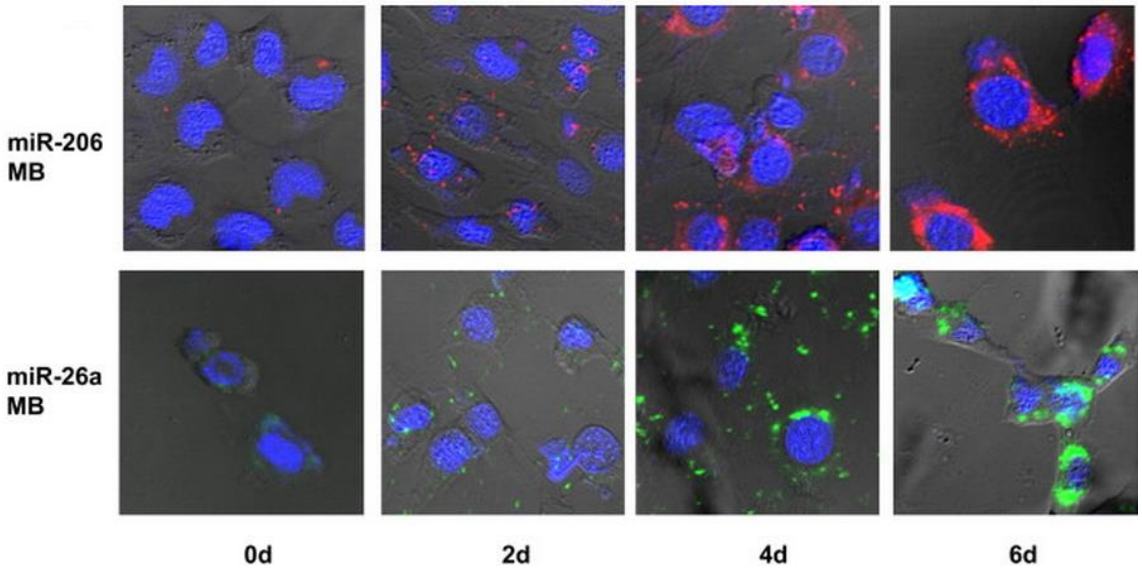

Figure 1.25*: Detection of miR-206 (Red) and miR-26a (Green) in differentiating C2C12 cells over 6 days. Overlaid with nucleus staining (blue) with 4',6-diamidino-2-phenylindole.*[137]

A study by Chen et al.[138] investigated the concentration of miR-155 in lung cancer cells. In this work, a MB for miR-155 was prepared with Cyanine5 and BHQ3 in a combination of LNA and DNA. The MB was additionally functionalised with chitosan, which conferred a positive charge to the MB to improve permeability. In this experiment three lung cancer cell lines, with known high expression of miR-155, were examined. The cells were treated with either the MB with a commercially available lipid based transfection (siPORT) or the chitosan modified MB, see Figure 1.26. The chitosan modified MB showed higher fluorescence in each of the cell lines tested, which suggests improved uptake of the MB compared to the lipofection. Significantly, when cells were transfected with a randomised MB, no significant signal was received, which suggests good stability and selectivity for the beacon. Analysis for the relative fluorescence signal from each of the cell lines showed good agreement with qRT-PCR results.

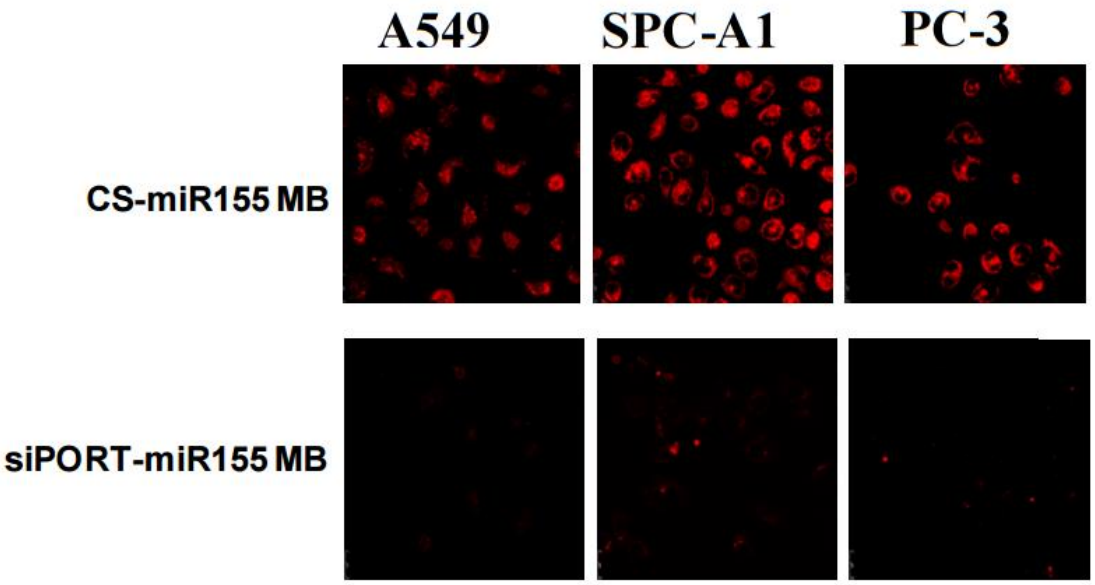

Figure 1.26: Detection of miR-155 in three lung cancer cell lines. Delivery of MB with chitosan (top) and lipid based transfection siPORT (bottom).[138]

One issue in the determination of cellular miRNA concentration using MBs is transfection efficiency. As seen in Figure 1.26, the intensity measured is highly dependent on the intercellular concentration of the MB. For electroporation, pores form in the membrane, which can remain open for up to 9 minutes, so the concentration of MB in the cell should equilibrate with the solution. [139] However, for lipid based transfection or cell penetrating moieties, the transfection efficiency can be difficult to

determine, making accurate miRNA measurement of concentration problematic. A recent study by Kim et al.[140] seeks to address this issue using a dual colour molecular beacon. In this work a strand of DNA complimentary to miR-9 was produced, modified on one end with Cyanine3 and Cyanine5.5 on the opposite end. A second short sequence with partial complementarity modified with a black hole quencher was also produced. The two strands were combined in solution, causing binding of the shorter sequence, and subsequent quenching of the Cyanine3 by BHQ1. In the absence of the target miRNA, a signal is received for the Cyanine5.5, but not Cyanine3. When the target was added, the shorter strand was displaced, switching on fluorescence of Cyanine3. This allowed for the concentration of the molecular beacon during live cell imaging to be determined independently of the miR-9 concentration.

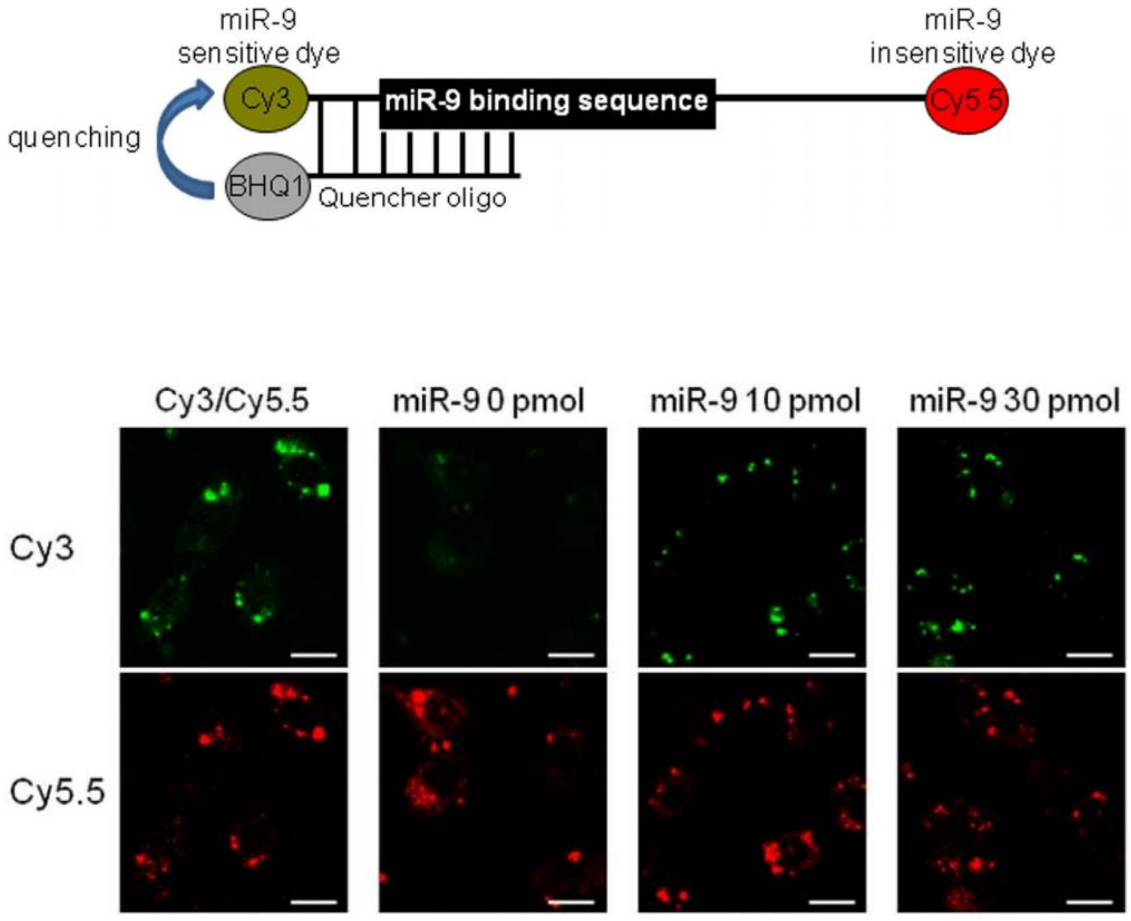

Figure 1.27: Dual colour molecular beacon, showing (top) design of the MB, and (bottom) miR-9 concentration dependent fluorescence of Cyanine3, and miR-9 concentration independent intensity of Cyanine5.5.[140]

Overall, molecular beacons are a highly efficient method for determination of intercellular miRNA concentration. The “switching on” of fluorescence upon target recognition provides a low background, allowing detection at considerably lower concentrations than genetic methods which rely on down regulation of fluorescence. Modified nucleic acids aid in resistance to cellular nucleases, and longer wavelength dyes have improved the overall performance by enhancing tissue penetration.

1.6 Scope of Thesis

The objective of this work is to achieve the ultrasensitive detection of miRNA, without amplification, in solution phase and in live cells. For solution phase detection, a method which is compatible with the development of a point of care diagnostic device was a major objective. To address this issue, two different approaches were investigated for the amplification free detection of miRNA, i.e., electrocatalytic platinum nanoparticles, and a displacement assay. For the live cell imaging of miRNA, the primary goal was to examine the concentration and localisation of a miRNA associated within neuroblastoma cells. To achieve this goal, a molecular beacon for the detection of miR-132 was designed and fully characterised.

Following a review of the relevant literature in Chapter 1, Chapter 2 details the production of regioselective platinum nanoparticles which are used for the detection of short DNA strands. The current state of the art for the detection of DNA and miRNA is PCR, whereby the nucleic acid of interest is amplified up to detectable limit. While this method provides highly sensitive detection, with a limit of detection of approximately 10 copies, the equipment and highly skilled personnel make this technology unsuitable for a point of care setting. Amplification free electrocatalytic nucleic acid detection has the potential to achieve the detection of nucleic acids at clinically relevant concentrations (fM), while also providing rapid detection which is suitable for integration into a point of care device.

In order to attach platinum nanoparticles to a detection assembly, the PtNPs must be modified. This modification is usually to the entire surface of the PtNP. This reduces the catalytic properties of these particles by reducing the surface area of platinum available for reaction. PtNPs that are functionalised with probe strand DNA only in particular regions, “regioselectively modified”, and have the potential to overcome this issue by allowing one side of the nanoparticles to attach to the detection assembly, and leaving another side clean for electrocatalysis.

The next objective of this work was the development of a molecular beacon (MB) for the detection of miR-132 in live cells. The environmental conditions within live cells vary greatly, e.g., with respect to pH, polarity etc., and so the photophysical properties of the dye, 6-FAM, and the quencher, dabcyl, which were integrated into the MB were examined in Chapter 3. In Chapter 4, the ability of the MB for the detection of miR-132

in solution phase was examined. This allowed for the binding kinetics of the MB to be studied, which allows for better interpretation of results from live cells. The ability of the MB to detect the presence of miR-132 isolated from a cellular source was also examined.

In Chapter 5, the MB was used for the detection miR-132 in live cells. As previously mentioned, negatively charged nucleic acids are incapable of diffusing through the cell membrane unassisted, and so methods for introducing the molecular beacon to the cells were examined. The intensity of the MB emission within individual cells was then used to examine the localisation of miR-132 in live cells, and to determine the total concentration in the cell. By imaging a large number of cells, the distribution of miR-132 concentration variation between individual cells was determined. The cellular concentration of miR-132 was also modulated using synthetic miRNA, and the impact on the observed intensity was examined.

In Chapter 6, an in vitro assay for the detection of mIR-132 is described based on the displacement of microspheres modified with probe strand DNA that are initially bound to a sensor surface. The objective of this work was to produce an assay, fully compatible with a microfluidic based system, which would allow rapid and highly sensitive detection of miRNA. A microsphere was modified with a probe DNA strand, which was complimentary to 11 of 22 bases of a capture DNA strand. This capture strand was complimentary to the full 22 bases of the miR-132 target. Hybridisation of the capture and target allowed capture of the microspheres to a gold surface, which could be released upon the addition of the miR-132 target. Conclusion and future recommendations arising from this thesis are given in Chapter 7.

1.7 References

1. Winter, J.; Jung, S.; Keller, S.; Gregory, R. I.; Diederichs, S. Many roads to maturity: microRNA biogenesis pathways and their regulation. *Nat. Cell Biol.* **2009**, *11*, 228-234.

2. Munker, R.; Calin, G. A. MicroRNA profiling in cancer. *Clin. Sci.* **2011**, *121*, 141-158.

3. Lu, J.; Getz, G.; Miska, E.; Alvarez-Saavedra, E.; Lamb, J.; Peck, D.; Sweet-Cordero, A.; Ebet, B.; Mak, R.; Ferrando, A.; Downing, J.; Jacks, T.; Horvitz, H.; Golub, T. MicroRNA expression profiles classify human cancers. *Nature* **2005**, *435*, 834-838.

4. Saumet, A.; Mathelier, A.; Lecellier, C. The potential of microRNAs in personalized medicine against cancers. *BioMed research international* **2014**, *2014*.

5. Bray, I.; Bryan, K.; Prenter, S.; Buckley, P. G.; Foley, N. H.; Murphy, D. M.; Alcock, L.; Mestdagh, P.; Vandesompele, J.; Speleman, F.; London, W. B.; McGrady, P. W.; Higgins, D. G.; O'Meara, A.; O'Sullivan, M.; Stallings, R. L. Widespread Dysregulation of MiRNAs by MYCN Amplification and Chromosomal Imbalances in Neuroblastoma: Association of miRNA Expression with Survival. *PLoS One* **2009**, *4*, e7850.

6. Levin, B.; Lieberman, D. A.; McFarland, B.; Andrews, K. S.; Brooks, D.; Bond, J.; Dash, C.; Giardiello, F. M.; Glick, S.; Johnson, D.; Johnson, C. D.; Levin, T. R.; Pickhardt, P. J.; Rex, D. K.; Smith, R. A.; Thorson, A.; Winawer, S. J.; Amer Canc Soc Colorectal Canc Ad; Amer Coll Radiology Colon Canc Screening and surveillance for the early detection of colorectal cancer and adenomatous polyps, 2008: A joint guideline from the American Cancer Society, the US Multi-Society Task Force on Colorectal Cancer, and the American College of Radiology. *Gastroenterology* **2008**, *134*, 1570-1595.

7. Catalona, W.; Richie, J.; Ahmann, F.; Hudson, M.; Scardino, P.; Flanigan, R.; Dekernion, J.; Ratliff, T.; Kavoussi, L.; Dalkin, B.; Waters, W.; Macfarlane, M.; Southwick, P. Comparison of Digital Rectal Examination and Serum Prostate-Specific Antigen in the Early Detection of Prostate-Cancer - Results of a Multicenter Clinical-Trial of 6,630 Men. *J. Urol.* **1994**, *151*, 1283-1290.

8. Frost, J.; Ball, W.; Levin, M.; Tockman, M.; Baker, R.; Carter, D.; Eggleston, J.; Erozan, Y.; Gupta, P.; Khouri, N.; Marsh, B.; Stitik, F. Early Lung-Cancer Detection - Results of the Initial (Prevalence) Radiologic and Cytologic Screening in the Johns-Hopkins-Study. *Am. Rev. Respir. Dis.* **1984**, *130*, 549-554.

9. Mitchell, P. S.; Parkin, R. K.; Kroh, E. M.; Fritz, B. R.; Wyman, S. K.; Pogosova-Agadjanyan, E. L.; Peterson, A.; Noteboom, J.; O'Briant, K. C.; Allen, A.; Lin, D. W.; Urban, N.; Drescher, C. W.; Knudsen, B. S.; Stirewalt, D. L.; Gentleman, R.; Vessella, R. L.; Nelson, P. S.; Martin, D. B.; Tewari, M. Circulating microRNAs as stable blood-based markers for cancer detection. *Proc. Natl. Acad. Sci. U. S. A.* **2008**, *105*, 10513-10518.

10. Bustin, S. Absolute quantification of mRNA using real-time reverse transcription polymerase chain reaction assays. *J. Mol. Endocrinol.* **2000**, *25*, 169-193.

11. Burns, M.; Valdivia, H. Modelling the limit of detection in real-time quantitative PCR. *Eur. Food Res. Technol.* **2008**, *226*, 1513-1524.

12. Bustin, S. A.; Benes, V.; Garson, J. A.; Hellemans, J.; Huggett, J.; Kubista, M.; Mueller, R.; Nolan, T.; Pfaffl, M. W.; Shipley, G. L.; Vandesompele, J.; Wittwer, C. T. The MIQE Guidelines: Minimum Information for Publication of Quantitative Real-Time PCR Experiments. *Clin. Chem.* **2009**, *55*, 611-622.

13. Alberts, B. *Molecular Biology of the Cell;* Garland Pub: **1989**; .

14. Shiloh, Y. ATM and related protein kinases: Safeguarding genome integrity. *Nat. Rev. Cancer* **2003**, *3*, 155-168.

15. Geacintov, N. E.; Broyde, S. *The Chemical Biology of DNA Damage;* Wiley: **2011**; .

16. Beljanski, M. *The Regulation of DNA Replication and Transcription;* Demos Medical Publishing, LLC: **2013**; .

17. Alberts, B.; Johnson, A.; Lewis, J.; Walter, P.; Raff, M.; Roberts, K. *Molecular Biology of the Cell 4th Edition: International Student Edition;* Routledge: **2002**; .

18. Roberts, M.; Reiss, M. J.; Monger, G. In *Advanced Biology;* Nelson: **2000**; pp 610.

19. Watson, J.; Crick, F. Molecular Structure of Nucleic Acids - a Structure for Deoxyribose Nucleic Acid. *Nature* **1953**, *171*, 737-738.

20. Kornberg, A.; Baker, T. A. In *DNA Structure and Function;* DNA Replication; University Science: 2005; pp 10.

21. Ghosh, A.; Bansal, M. A glossary of DNA structures from A to Z. *Acta Crystallogr. Sect. D-Biol. Crystallogr.* **2003**, *59*, 620-626.

22. Harper, D. R. In *Synthesis of Viral Genomes;* Viruses: Biology, Applications, and Control; Taylor \& Francis Group: **2011**; pp 55.

23. Karp, G. *Cell and Molecular Biology: Concepts and Experiments;* John Wiley & Sons: **2009**; .

24. Rosenberg, A. *The Structure of Biological Science;* Cambridge University Press: **1985**; .

25. Sancar, A.; Lindsey-Boltz, L.; Unsal-Kacmaz, K.; Linn, S. Molecular mechanisms of mammalian DNA repair and the DNA damage checkpoints. *Annu. Rev. Biochem.* **2004**, *73*, 39-85.

26. Khanna, K.; Jackson, S. DNA double-strand breaks: signaling, repair and the cancer connection. *Nat. Genet.* **2001**, *27*, 247-254.

27. Lindahl, T. Instability and Decay of the Primary Structure of Dna. *Nature* **1993**, *362*, 709-715.

28. McMurray, C. DNA secondary structure: A common and causative factor for expansion in human disease. *Proc. Natl. Acad. Sci. U. S. A.* **1999**, *96*, 1823-1825.

29. National Human Genome Research Institute Talking Glossary of Genetic Terms. *http://www.genome.gov/glossary/* (accessed 02/14, **2014**).

30. Lents, N. DNA II: The Structure of DNA. *http://www.visionlearning.com/en/library/Biology/2/DNA-II/160* (accessed 02/14, **2014)**.

31. Wartell, R.; Benight, A. Thermal-Denaturation of Dna-Molecules - a Comparison of Theory with Experiment. *Phys. Rep. -Rev. Sec. Phys. Lett.* **1985**, *126*, 67-107.

32. Schildkr.C; Lifson, S. Dependence of Melting Temperature of Dna on Salt Concentration. *Biopolymers* **1965**, *3*, 195-&.

33. Yakovchuk, P.; Protozanova, E.; Frank-Kamenetskii, M. Base-stacking and base-pairing contributions into thermal stability of the DNA double helix. *Nucleic Acids Res.* **2006**, *34*, 564-574.

34. Dove, W.; Davidson, N. Cation Effects on Denaturation of Dna. *J. Mol. Biol.* **1962**, *5*, 467-&.

35. Nirenber.M; Leder, P.; Bernfiel.M; Brimacom.R; Trupin, J.; Rottman, F.; Oneal, C. Rna Codewords and Protein Synthesis .7. on General Nature of Rna Code. *Proc. Natl. Acad. Sci. U. S. A.* **1965**, *53*, 1161-&.

36. Guttman, M.; Amit, I.; Garber, M.; French, C.; Lin, M. F.; Feldser, D.; Huarte, M.; Zuk, O.; Carey, B. W.; Cassady, J. P.; Cabili, M. N.; Jaenisch, R.; Mikkelsen, T. S.; Jacks, T.; Hacohen, N.; Bernstein, B. E.; Kellis, M.; Regev, A.; Rinn, J. L.; Lander, E. S. Chromatin signature reveals over a thousand highly conserved large non-coding RNAs in mammals. *Nature* **2009**, *458*, 223-227.

37. Steitz, J. A.; Jakes, K. How ribosomes select initiator regions in mRNA: base pair formation between the 3' terminus of 16S rRNA and the mRNA during initiation of protein synthesis in Escherichia coli. *Proc. Natl. Acad. Sci. U. S. A.* **1975**, *72*, 4734-4738.

38. Hurwitz, J. The discovery of RNA polymerase. *J. Biol. Chem.* **2005**, *280*, 42477-42485.

39. Tropp, B. E. In *RNA Synthesis and Processing;* Molecular Biology: Genes to Proteins; Jones and Bartlett Publishers: **2008**; pp 682.

40. Ryskov, A.; Saunders, G.; Farashyan, V.; Georgiev, G. Double-helical regions in nuclear precursor of mRNA (pre-mRNA). *Biochimica et Biophysica Acta (BBA)-Nucleic Acids and Protein Synthesis* **1973**, *312*, 152-164.

41. Izaurralde, E.; Mattal, I. W. RNA export. *Cell* **1995**, *81*, 153-159.

42. Filipowicz, W.; Bhattacharyya, S. N.; Sonenberg, N. Mechanisms of post-transcriptional regulation by microRNAs: are the answers in sight? *Nature Reviews Genetics* **2008**, *9*, 102-114.

43. Roberts, M.; Reiss, M. J.; Monger, G. *Advanced Biology;* Nelson: **2000**; .

44. Sharp, S.; Schaack, J.; Cooley, L.; Burke, D.; Soll, D. Structure and Transcription of Eukaryotic Transfer-Rna Genes. *CRC Crit. Rev. Biochem.* **1985**, *19*, 107-144.

45. Bartel, D. P. MicroRNAs: Target Recognition and Regulatory Functions. *Cell* **2009**, *136*, 215-233.

46. Filipowicz, W.; Bhattacharyya, S. N.; Sonenberg, N. Mechanisms of post-transcriptional regulation by microRNAs: are the answers in sight? *Nat. Rev. Genet.* **2008**, *9*, 102-114.

47. Vasudevan, S. Posttranscriptional upregulation by microRNAs. *Wiley Interdisciplinary Reviews: RNA* **2012**, *3*, 311-330.

48. National Institutes of Health. National Human Genome Research Institute. Talking Glossary of Genetic Terms. *http://www.genome.gov/glossary/* (accessed 02/10, **2015**).

49. Lee, Y.; Kim, M.; Han, J.; Yeom, K.; Lee, S.; Baek, S.; Kim, V. MicroRNA genes are transcribed by RNA polymerase II. *EMBO J.* **2004**, *23*, 4051-4060.

50. Han, J.; Lee, Y.; Yeom, K. H.; Kim, Y. K.; Jin, H.; Kim, V. N. The Drosha-DGCR8 complex in primary microRNA processing. *Genes Dev.* **2004**, *18*, 3016-3027.

51. Seila, A. C.; Sharp, P. A. Small RNAs tell big stories in Whistler. *Nat. Cell Biol.* **2008**, *10*, 630-633.

52. Gregory, R. I.; Chendrimada, T. P.; Shiekhattar, R. MicroRNA biogenesis - Isolation and characterization of the microprocessor complex. *Methods in Molecular Biology* **2006**, *342*, 33-47.

53. Yi, R.; Qin, Y.; Macara, I. G.; Cullen, B. R. Exportin-5 mediates the nuclear export of pre-microRNAs and short hairpin RNAs. *Genes Dev.* **2003**, *17*, 3011-3016.

54. Lund, E.; Guttinger, S.; Calado, A.; Dahlberg, J. E.; Kutay, U. Nuclear export of microRNA precursors. *Science* **2004**, *303*, 95-98.

55. Krol, J.; Sobczak, K.; Wilczynska, U.; Drath, M.; Jasinska, A.; Kaczynska, D.; Krzyzosiak, W. Structural features of MicroRNA (miRNA) precursors and their relevance to miRNA biogenesis and small interfering RNA/Short hairpin RNA design. *J. Biol. Chem.* **2004**, *279*, 42230-42239.

56. Gan, L.; Denecke, B. Profiling pre-microrna and mature microrna expressions using a single microarray and avoiding separate sample preparation. *Microarrays* **2013**, *2*, 24-33.

57. Schwarz, D. S.; Tomari, Y.; Zamore, P. D. The RNA-induced silencing complex is a Mg 2 -dependent endonuclease. *Current Biology* **2004**, *14*, 787-791.

58. Engels, B. M.; Hutvagner, G. Principles and effects of microRNA-mediated post-transcriptional gene regulation. *Oncogene* **2006**, *25*, 6163-6169.

59. Amsbio Trilencer-27 - Guaranteed knockdown for siRNA gene silencing. *http://www.amsbio.com/trilencer27.aspx* (accessed 06/28, **2015**).

60. Etheridge, A.; Lee, I.; Hood, L.; Galas, D.; Wang, K. Extracellular microRNA: a new source of biomarkers. *Mutation Research/Fundamental and Molecular Mechanisms of Mutagenesis* **2011**, *717*, 85-90.

61. Cho, W. C. S. OncomiRs: the discovery and progress of microRNAs in cancers. *Mol. Cancer* **2007**, *6*, 60.

62. Yang, H.; Kong, W.; He, L.; Zhao, J. J.; O'Donnell, J. D.; Wang, J.; Wenham, R. M.; Coppola, D.; Kruk, P. A.; Nicosia, S. V.; Cheng, J. Q. MicroRNA expression profiling in human ovarian cancer: miR-214 induces cell survival and cisplatin resistance by targeting PTEN. *Cancer Res.* **2008**, *68*, 425-433.

63. Wu, X.; Weng, L.; Li, X.; Guo, C.; Pal, S. K.; Jin, J. M.; Li, Y.; Nelson, R. A.; Mu, B.; Onami, S. H. Identification of a 4-microRNA signature for clear cell renal cell carcinoma metastasis and prognosis. *PloS one* **2012**, *7*, e35661.

64. Weber, J. A.; Baxter, D. H.; Zhang, S.; Huang, D. Y.; Huang, K. H.; Lee, M. J.; Galas, D. J.; Wang, K. The microRNA spectrum in 12 body fluids. *Clin. Chem.* **2010**, *56*, 1733-1741.

65. D'Alessio, G.; Riordan, J. F. *Ribonucleases: Structures and Functions;* Elsevier Science: **1997**; .

66. Weickmann, J. L.; Glitz, D. G. Human ribonucleases. Quantitation of pancreatic-like enzymes in serum, urine, and organ preparations. *J. Biol. Chem.* **1982**, *257*, 8705-8710.

67. Valadi, H.; Ekström, K.; Bossios, A.; Sjöstrand, M.; Lee, J. J.; Lötvall, J. O. Exosome-mediated transfer of mRNAs and microRNAs is a novel mechanism of genetic exchange between cells. *Nat. Cell Biol.* **2007**, *9*, 654-659.

68. Gibbings, D. J.; Ciaudo, C.; Erhardt, M.; Voinnet, O. Multivesicular bodies associate with components of miRNA effector complexes and modulate miRNA activity. *Nat. Cell Biol.* **2009**, *11*, 1143-1149.

69. Heneghan, H. M.; Miller, N.; Lowery, A. J.; Sweeney, K. J.; Newell, J.; Kerin, M. J. Circulating microRNAs as novel minimally invasive biomarkers for breast cancer. *Ann. Surg.* **2010**, *251*, 499-505.

70. Mitchell, P. S.; Parkin, R. K.; Kroh, E. M.; Fritz, B. R.; Wyman, S. K.; Pogosova-Agadjanyan, E. L.; Peterson, A.; Noteboom, J.; O'Briant, K. C.; Allen, A.; Lin, D. W.; Urban, N.; Drescher, C. W.; Knudsen, B. S.; Stirewalt, D. L.; Gentleman, R.; Vessella, R. L.; Nelson, P. S.; Martin, D. B.; Tewari, M. Circulating microRNAs as

stable blood-based markers for cancer detection. *Proc. Natl. Acad. Sci. U. S. A.* **2008**, *105*, 10513-10518.

71. Vaca, L. Point-of-care Diagnostic Tools to Detect Circulating MicroRNAS as Biomarkers of Disease. *Sensors* **2014**, *14*, 9117-9131.

72. Pall, G. S.; Hamilton, A. J. Improved northern blot method for enhanced detection of small RNA. *Nature protocols* **2008**, *3*, 1077-1084.

73. Gilbert, S. F. *Developmental Biology;* Sinauer: **2014**; .

74. Várallyay, E.; Burgyán, J.; Havelda, Z. MicroRNA detection by northern blotting using locked nucleic acid probes. *Nature protocols* **2008**, *3*, 190-196.

75. Kim, S. W.; Li, Z.; Moore, P. S.; Monaghan, A. P.; Chang, Y.; Nichols, M.; John, B. A sensitive non-radioactive northern blot method to detect small RNAs. *Nucleic Acids Res.* **2010**, *38*, e98.

76. Schmittgen, T. D.; Lee, E. J.; Jiang, J.; Sarkar, A.; Yang, L.; Elton, T. S.; Chen, C. Real-time PCR quantification of precursor and mature microRNA. *Methods* **2008**, *44*, 31-38.

77. Bartlett, J. M. S.; Stirling, D. A short history of the polymerase chain reaction. *Methods Mol. Biol.* **2003**, *226*, 3-6.

78. Radonić, A.; Thulke, S.; Mackay, I. M.; Landt, O.; Siegert, W.; Nitsche, A. Guideline to reference gene selection for quantitative real-time PCR. *Biochem. Biophys. Res. Commun.* **2004**, *313*, 856-862.

79. Erlich, H.; Gelfand, D.; Sninsky, J. Recent Advances in the Polymerase Chain-Reaction. *Science* **1991**, *252*, 1643-1651.

80. Yuan, J. S.; Reed, A.; Chen, F.; Stewart, C. N.,Jr Statistical analysis of real-time PCR data. *BMC Bioinformatics* **2006**, *7*, 85.

81. Holland, P. M.; Abramson, R. D.; Watson, R.; Gelfand, D. H. Detection of specific polymerase chain reaction product by utilizing the 5'----3' exonuclease activity of Thermus aquaticus DNA polymerase. *Proc. Natl. Acad. Sci. U. S. A.* **1991**, *88*, 7276-7280.

82. Livak, K. J.; Flood, S. J.; Marmaro, J.; Giusti, W.; Deetz, K. Oligonucleotides with fluorescent dyes at opposite ends provide a quenched probe system useful for detecting PCR product and nucleic acid hybridization. *PCR Methods Appl.* **1995**, *4*, 357-362.

83. Udvardi, M. K.; Czechowski, T.; Scheible, W. Eleven golden rules of quantitative RT-PCR. *Plant Cell* **2008**, *20*, 1736-1737.

84. Schefe, J. H.; Lehmann, K. E.; Buschmann, I. R.; Unger, T.; Funke-Kaiser, H. Quantitative real-time RT-PCR data analysis: current concepts and the novel "gene expression's C T difference" formula. *Journal of molecular medicine* **2006**, *84*, 901-910.

85. Dheda, K.; Huggett, J. F.; Bustin, S. A.; Johnson, M. A.; Rook, G.; Zumla, A. Validation of housekeeping genes for normalizing RNA expression in real-time PCR. *BioTechniques* **2004**, *37*, 112-119.

86. de Planell-Saguer, M.; Rodicio, M. C. Analytical aspects of microRNA in diagnostics: a review. *Anal. Chim. Acta* **2011**, *699*, 134-152.

87. Castoldi, M.; Schmidt, S.; Benes, V.; Noerholm, M.; Kulozik, A. E.; Hentze, M. W.; Muckenthaler, M. U. A sensitive array for microRNA expression profiling (miChip) based on locked nucleic acids (LNA). *RNA* **2006**, *12*, 913-920.

88. Erdmann, V. A.; Jurga, S.; Barciszewski, J. In *RNA and DNA Diagnostics;* Springer International Publishing: **2015**; pp 344.

89. Wang, H.; Ach, R. A.; Curry, B. Direct and sensitive miRNA profiling from low-input total RNA. *RNA* **2007**, *13*, 151-159.

90. Wiegant, J.; van Gijlswijk, R.; Heetebrij, R.; Bezrookove, V.; Raap, A.; Tanke, H. ULS: a versatile method of labeling nucleic acids for FISH based on a monofunctional reaction of cisplatin derivatives with guanine moieties. *Cytogenet. Cell Genet.* **1999**, *87*, 47-52.

91. England, T. E.; Uhlenbeck, O. C. 3′-terminal labelling of RNA with T4 RNA ligase. *Nature* **1978**, *275*, 560-561.

92. Thomson, J.; Parker, J.; Perou, C.; Hammond, S. A custom microarray platform for analysis of microRNA gene expression. *Nat. Methods* **2004**, *1*, 47-53.

93. Shingara, J.; Keiger, K.; Shelton, J.; Laosinchai-Wolf, W.; Powers, P.; Conrad, R.; Brown, D.; Labourier, E. An optimized isolation and labeling platform for accurate microRNA expression profiling. *RNA-Publ. RNA Soc.* **2005**, *11*, 1461-1470.

94. Shingara, J.; Keiger, K.; Shelton, J.; Laosinchai-Wolf, W.; Powers, P.; Conrad, R.; Brown, D.; Labourier, E. An optimized isolation and labeling platform for accurate microRNA expression profiling. *RNA-Publ. RNA Soc.* **2005**, *11*, 1461-1470.

95. Yin, J. Q.; Zhao, R. C.; Morris, K. V. Profiling microRNA expression with microarrays. *Trends Biotechnol.* **2008**, *26*, 70-76.

96. Vester, B.; Wengel, J. LNA (Locked nucleic acid): High-affinity targeting of complementary RNA and DNA. *Biochemistry (N. Y.)* **2004**, *43*, 13233-13241.

97. Lee, J. M.; Jung, Y. Two-Temperature Hybridization for Microarray Detection of Label-Free MicroRNAs with Attomole Detection and Superior Specificity. *Angew. Chem. -Int. Edit.* **2011**, *50*, 12487-12490.

98. Wanunu, M.; Dadosh, T.; Ray, V.; Jin, J.; McReynolds, L.; Drndic, M. Rapid electronic detection of probe-specific microRNAs using thin nanopore sensors. *Nat. Nanotechnol.* **2010**, *5*, 807-814.

99. Tian, K.; He, Z.; Wang, Y.; Chen, S.; Gu, L. Designing a Polycationic Probe for Simultaneous Enrichment and Detection of MicroRNAs in a Nanopore. *ACS Nano* **2013**, *7*, 3962-3969.

100. Egholm, M.; Buchardt, O.; Christensen, L.; Behrens, C.; Freier, S.; Driver, D.; Berg, R.; Kim, S.; Norden, B.; Nielsen, P. Pna Hybridizes to Complementary Oligonucleotides Obeying the Watson-Crick Hydrogen-Bonding Rules. *Nature* **1993**, *365*, 566-568.

101. Das, J.; Cederquist, K. B.; Zaragoza, A. A.; Lee, P. E.; Sargent, E. H.; Kelley, S. O. An ultrasensitive universal detector based on neutralizer displacement. *Nat. Chem.* **2012**, *4*, 642-648.

102. Fan, Y.; Chen, X.; Trigg, A. D.; Tung, C.; Kong, J.; Gao, Z. Detection of microRNAs using target-guided formation of conducting polymer nanowires in nanogaps. *J. Am. Chem. Soc.* **2007**, *129*, 5437-5443.

103. Weizmann, Y.; Chenoweth, D. M.; Swager, T. M. DNA− cnt nanowire networks for DNA detection. *J. Am. Chem. Soc.* **2011**, *133*, 3238-3241.

104. Cao, H.; Liu, S.; Tu, W.; Bao, J.; Dai, Z. A carbon nanotube/quantum dot based photoelectrochemical biosensing platform for the direct detection of microRNAs. *Chem.Commun.* **2014**, *50*, 13315-13318.

105. Wang, F.; Niu, G.; Chen, X.; Cao, F. Molecular imaging of microRNAs. *European journal of nuclear medicine and molecular imaging* **2011**, *38*, 1572-1579.

106. Brown, B. D.; Venneri, M. A.; Zingale, A.; Sergi, L. S.; Naldini, L. Endogenous microRNA regulation suppresses transgene expression in hematopoietic lineages and enables stable gene transfer. *Nat. Med.* **2006**, *12*, 585-591.

107. Kato, Y.; Sawata, S. Y.; Inoue, A. A lentiviral vector encoding two fluorescent proteins enables imaging of adenoviral infection via adenovirus-encoded miRNAs in single living cells. *J. Biochem.* **2010**, *147*, 63-71.

108. Troy, T.; Jekic-McMullen, D.; Sambucetti, L.; Rice, B. Quantitative comparison of the sensitivity of detection of fluorescent and bioluminescent reporters in animal models. *Mol. Imaging* **2004**, *3*, 9-23.

109. Aubin, J. E. Autofluorescence of viable cultured mammalian cells. *J. Histochem. Cytochem.* **1979**, *27*, 36-43.

110. Kricka, L. J. Clinical and biochemical applications of luciferases and luciferins. *Anal. Biochem.* **1988**, *175*, 14-21.

111. Contag, C. H.; Bachmann, M. H. Advances in in vivo bioluminescence imaging of gene expression. *Annu. Rev. Biomed. Eng.* **2002**, *4*, 235-260.

112. de Wet, J. R.; Wood, K. V.; DeLuca, M.; Helinski, D. R.; Subramani, S. Firefly luciferase gene: structure and expression in mammalian cells. *Mol. Cell. Biol.* **1987**, *7*, 725-737.

113. Tannous, B. A.; Kim, D.; Fernandez, J. L.; Weissleder, R.; Breakefield, X. O. Codon-optimized Gaussia luciferase cDNA for mammalian gene expression in culture and in vivo. *Molecular Therapy* **2005**, *11*, 435-443.

114. Inoue, Y.; Sheng, F.; Kiryu, S.; Watanabe, M.; Ratanakanit, H.; Izawa, K.; Tojo, A.; Ohtomo, K. Gaussia luciferase for bioluminescence tumor monitoring in comparison with firefly luciferase. *Molecular imaging* **2011**, *10*, 377.

115. Lee, J. Y.; Kim, S.; Hwang do, W.; Jeong, J. M.; Chung, J. K.; Lee, M. C.; Lee, D. S. Development of a dual-luciferase reporter system for in vivo visualization of MicroRNA biogenesis and posttranscriptional regulation. *J. Nucl. Med.* **2008**, *49*, 285-294.

116. Bonnet, G.; Tyagi, S.; Libchaber, A.; Kramer, F. Thermodynamic basis of the enhanced specificity of structured DNA probes. *Proc. Natl. Acad. Sci. U. S. A.* **1999**, *96*, 6171-6176.

117. Goel, G.; Kumar, A.; Puniya, A.; Chen, W.; Singh, K. Molecular beacon: a multitask probe. *J. Appl. Microbiol.* **2005**, *99*, 435-442.

118. Marti, A. A.; Jockusch, S.; Stevens, N.; Ju, J.; Turro, N. J. Fluorescent hybridization probes for sensitive and selective DNA and RNA detection. *Acc. Chem. Res.* **2007**, *40*, 402-409.

119. Wu, C. S.; Peng, L.; You, M.; Han, D.; Chen, T.; Williams, K. R.; Yang, C. J.; Tan, W. Engineering molecular beacons for intracellular imaging. *International journal of molecular imaging* **2012**, *2012*, 501579.

120. Baker, M. B.; Bao, G.; Searles, C. D. In vitro quantification of specific microRNA using molecular beacons. *Nucleic Acids Res.* **2012**, *40*, e13.

121. Nazarenko, I.; Bhatnagar, S.; Hohman, R. A closed tube format for amplification and detection of DNA based on energy transfer. *Nucleic Acids Res.* **1997**, *25*, 2516-2521.

122. Flechsig, G.; Peter, J.; Voss, K.; Grundler, P. Electrochemical DNA hybridization detection using the fluorescence quenching label dabcyl. *Electrochem. Commun.* **2005**, *7*, 1059-1065.

123. Parniak, M.; Min, K.; Budihas, S.; Le Grice, S.; Beutler, J. A fluorescence-based high-throughput screening assay for inhibitors of human immunodeficiency virus-1 reverse transcriptase-associated ribonuclease H activity. *Anal. Biochem.* **2003**, *322*, 33-39.

124. You, Y.; Tataurov, A. V.; Owczarzy, R. Measuring thermodynamic details of DNA hybridization using fluorescence. *Biopolymers* **2011**, *95*, 472-486.

125. Thompson, R. B. In *Fluorescence Sensors and Biosensors;* Taylor \& Francis: **2005**; pp 72.

126. Tsourkas, A.; Behlke, M.; Bao, G. Hybridization of 2 '-O-methyl and 2 '-deoxy molecular beacons to RNA and DNA targets. *Nucleic Acids Res.* **2002**, *30*, 5168-5174.

127. Wang, K.; Tang, Z.; Yang, C. J.; Kim, Y.; Fang, X.; Li, W.; Wu, Y.; Medley, C. D.; Cao, Z.; Li, J.; Colon, P.; Lin, H.; Tan, W. Molecular Engineering of DNA: Molecular Beacons. *Angew. Chem. -Int. Edit.* **2009**, *48*, 856-870.

128. Suck, D.; Oefner, C. Structure of Dnase-i at 2.0 a Resolution Suggests a Mechanism for Binding to and Cutting Dna. *Nature* **1986**, *321*, 620-625.

129. Tsourkas, A.; Behlke, M. A.; Bao, G. Hybridization of 2'-O-methyl and 2'-deoxy molecular beacons to RNA and DNA targets. *Nucleic Acids Res.* **2002**, *30*, 5168-5174.

130. Egholm, M.; Buchardt, O.; Nielsen, P. E.; Berg, R. H. Peptide nucleic acids (PNA). Oligonucleotide analogs with an achiral peptide backbone. *J. Am. Chem. Soc.* **1992**, *114*, 1895-1897.

131. Weaver, J.; Chizmadzhev, Y. Theory of electroporation: A review. *Bioelectrochem. Bioenerget.* **1996**, *41*, 135-160.

132. Chu, G.; Hayakawa, H.; Berg, P. Electroporation for the Efficient Transfection of Mammalian-Cells with Dna. *Nucleic Acids Res.* **1987**, *15*, 1311-1326.

133. Felgner, P.; Gadek, T.; Holm, M.; Roman, R.; Chan, H.; Wenz, M.; Northrop, J.; Ringold, G.; Danielsen, M. Lipofection - a Highly Efficient, Lipid-Mediated Dna-Transfection Procedure. *Proc. Natl. Acad. Sci. U. S. A.* **1987**, *84*, 7413-7417.

134. Felgner, P.; Ringold, G. Cationic Liposome-Mediated Transfection. *Nature* **1989**, *337*, 387-388.

135. Milletti, F. Cell-penetrating peptides: classes, origin, and current landscape. *Drug Discov. Today* **2012**, *17*, 850-860.

136. Tréhin, R.; Merkle, H. P. Chances and pitfalls of cell penetrating peptides for cellular drug delivery. *European journal of pharmaceutics and biopharmaceutics* **2004**, *58*, 209-223.

137. Kang, W. J.; Cho, Y. L.; Chae, J. R.; Lee, J. D.; Choi, K.; Kim, S. Molecular beacon-based bioimaging of multiple microRNAs during myogenesis. *Biomaterials* **2011**, *32*, 1915-1922.

138. Zhu, H.; An, J.; Yao, Q.; Han, J.; Li, X.; Jiang, F.; Chen, G.; Peng, L.; Li, Y.; Sun, J.; Chen, Z. Chitosan Combined with Molecular Beacon for Mir-155 Detection and Imaging in Lung Cancer. *Molecules* **2014**, *19*, 14710-14722.

139. Bier, M.; Hammer, S.; Canaday, D.; Lee, R. Kinetics of sealing for transient electropores in isolated mammalian skeletal muscle cells. *Bioelectromagnetics* **1999**, *20*, 194-201.

140. Ko, H. Y.; Lee, J.; Joo, J. Y.; Lee, Y. S.; Heo, H.; Ko, J. J.; Kim, S. A color-tunable molecular beacon to sense miRNA-9 expression during neurogenesis. *Sci Rep* **2014**, *4*, 4626.

CHAPTER 2

High Sensitivity Detection of DNA Using Regioselectively Modified Electrocatalytic Nanoparticles

2.1 Introduction

Micro RNAs (miRNA) are a class of short nucleic acids which post-transcriptionally modify the expression of genes by downregulating the production of proteins.[1] miRNA are essential in a wide variety of biological pathways.[2] Cells which have become cancerous tend to have differential expression of miRNA when compared to health cells.[3] This differential expression allows for the user of miRNA as a biomarker for cancer. Ideally, a biomarker should be capable of identifying a condition, provide information on the stage of the illness, be available via minimally invasive tests, and inform the treatment of the conditions.[4] miRNAs have the potential to fulfil each of these requirements.

Detection of short nucleic acid sequences is important in the diagnosis of a number of diseases, such as cancer[1-3] and a number of infections[4-6]. Early detection has been linked to improved survival rates for a number of cancers[7-9]. While at present a number of highly sensitive methods exist for the detection of short nucleic acid strands, many of these methods are not currently suitable for a point of care setting. In order to achieve the full potential of short nucleic acids as biomarkers, wide scale screening is necessary.

Currently, the state of the art detection strategy is polymerase chain reaction (PCR) which amplifies the nucleic acid target in the sample up to detectable limits.[9,10] This method is highly sensitive and capable of measuring a very small initial concentration.[11] Unfortunately, PCR requires highly purified samples, which is time consuming and requires highly skilled technicians.[12] These factors make PCR unsuitable for a point of care setting. Amplification free detection of nucleic acid sequences has the potential to provide rapid, reagent free detection, well suited to point of care measurement.

Optical methods are available, which are considerably faster than PCR, however these methods tend to have issues with sensitivity.[86] A simple optical detection methods is a sandwich assay, whereby a strand of capture DNA is immobilised to a surface. This strand is complimentary to half of the nucleic acid target. The capture strand binds to the target of interest. A second probe strand of DNA is then hybridised to the free end of the target.[87] This probe strand can be modified with a number of detection strategies including dyes and quantum dots.

Electrochemical detection of nucleic acids has a number of benefits over PCR or optical methods. A single electrochemical even can produce a significant signal. This allows for

the direct detection of the nucleic acid of interest, without amplification. This has the potential to significantly improve detection times since pre-processing of the sample is reduced. The instrumentation used for electrochemical detection is also significantly more robust, and has been successfully into a number of point of care devices, for example blood glucose monitoring.[17]

This work outlines a platform technology, which should be capable of detecting any short nucleic acid sequence with high sensitivity, not by increasing or amplifying the concentration of the target but by dramatically amplifying the current response associated with small numbers of binding events.

The objective of this work was to develop a high sensitivity detection strategy based on using electrocatalytic platinum nanoparticles (PtNPs) as labels in a DNA sandwich assay so as to determine the concentration of a nucleic acid target in solution. PtNPs have a number of attractive properties for analytical devices including electrocatalysis which can allow for high sensitivity detection.[13] Electrocatalysis of water or hydrogen peroxide is highly efficient, and has been integrated into a number of analytical devices.[14-16] Platinum is also highly stable, with no oxidation in air, or reaction with water acids or bases.[17] However, for efficient electrocatalysis, clean surfaces that are free of organic adsorbates are the most efficient. Simultaneously satisfying the needs of molecular recognition and electrocatalytic detection is challenging but one productive strategy is to physically separate the two functions in different regions of each nanoparticle.[18,19] Therefore, regio selective PtNPs were prepared, which separate the detection and attachment of the nanoparticle into two distinct regions.

As illustrated in Figure 2.1, regio selective PtNPs were prepared by functionalising a polycrystalline gold (Au) surface with an alkane thiol monolayer.[20] By controlling the concentration of the alkane thiol and the deposition time, imperfect monolayers can be formed in which the monolayers contain nanoscale defects. [21] Platinum was then electrodeposited into these defects to produce a mushroom shaped PtNP. The top surface of these PtNPs could then be functionalized with a thiol terminated DNA probe strand that is complementary to half of the DNA target. The PtNPs were then released into suspension by sonication, resulting in regio selective PtNPs, with the DNA attached to the top surface, and with the underlying surface clean for electrocatalytic detection.

These PtNPs could then be used as part of a sandwich assay, whereby a capture strand of DNA complementary to half the DNA target was attached to a Au surface. The target

was allowed to hybridize to one end of the capture, and then the probe modified PtNP was hybridized to the free end of this capture. The presence of the PtNP could then be detected electrocatalytically and the number of bound particles depends on the target concentration.

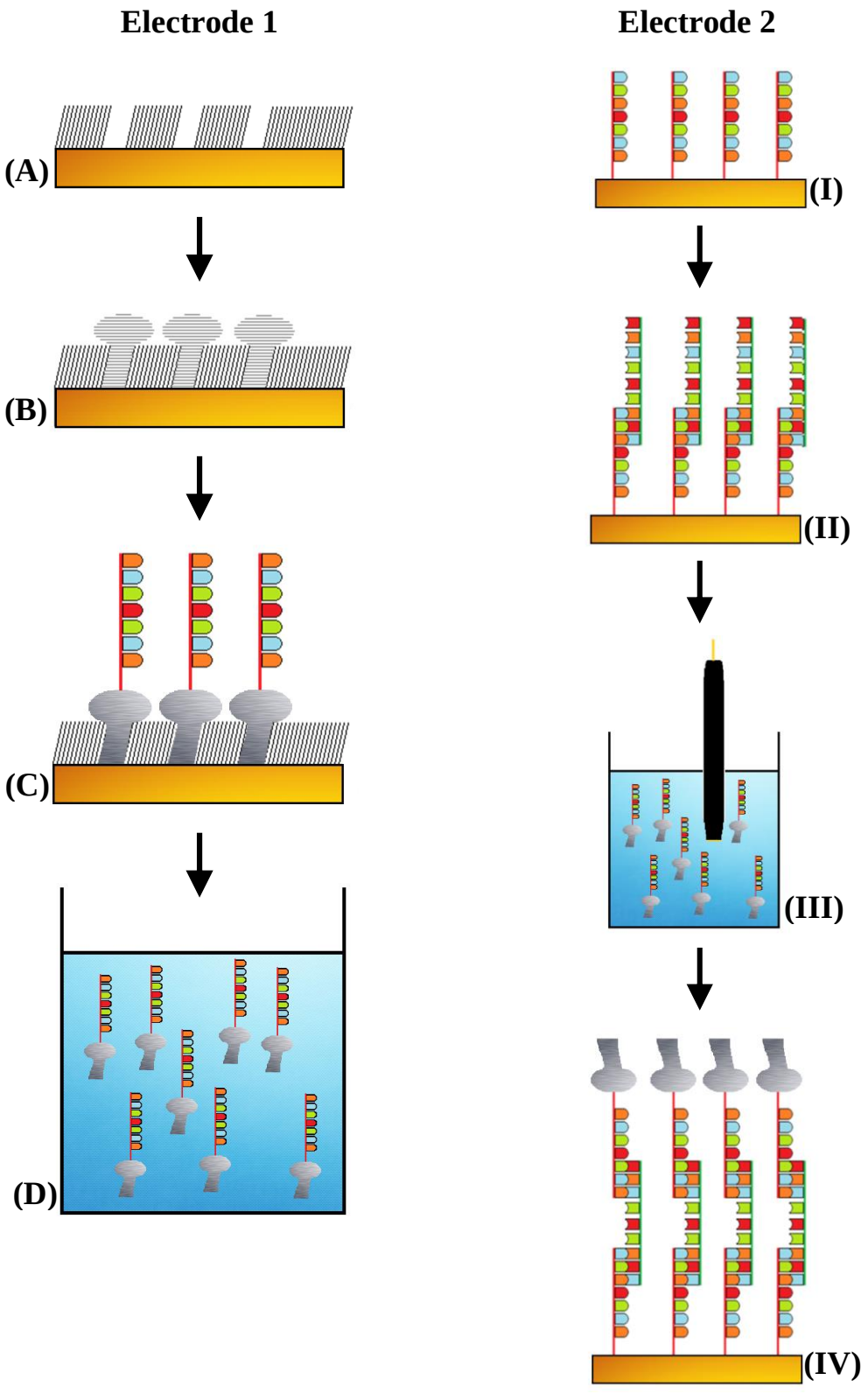

Figure 2.1: Scheme for the production of regio selective PtNPs. Showing (A) deposition of defective alkane thiol, (B) electrodeposition of PtNPs, (C) modification of PtNPs with probe DNA, and (D) release of PtNPs into solution by sonication. Detection of target DNA by (I) modification with capture DNA, (II) hybridization with target DNA,(III) immersion into suspension of probe functionalised PtNPs and (IV) electrocatalytic detection.

2.2 Experimental

2.2.1 Materials

Dodecanethiol was purchased from Sigma Aldrich. For DNA hybridization a buffer (1 M NaCl-TE) was prepared with 1.0 M NaCl, 10 mM Tris-HCl and 1 mM EDTA, and was adjusted to pH 7.0 with 1.0 M NaOH.

DNA was purchased from Eurogentec at ≥98 % purity. The target chosen was for the detection of Staphylococcus aureus bacteria, which causes mastitis. The following sequences were ordered:

Capture: 5'- CGG-CAG-TGT-TTA-TCA -3' – SH

Target:5'- TGA-TAA-ACA-CTG-CCG-TTT-GAA-GTC-TGT-TTA-GAA-GAA-ACT-TA-3'

Probe: SH-5'- TA-AGT-TTC-TTC-TAA-ACA-GAC- -3'

2.2.2 SEM Imaging

Scanning Electron Microscopy (SEM) was used to examine the surface morphology for the electrodeposition of PtNPs. Images were taken with a Hitachi S3000N scanning electron microscope with an accelerating voltage of 20 kV. Gold coated silicon wafer, 99.999 % Au, 100 nm thick, was purchased from Sigma Aldrich and used for all images.

2.2.3 Electrochemical Set-Up

Measurements were performed using a CH Instruments Model 660. A three-electrode electrochemical cell was used for electrochemical measurements. The working electrode was a 2 mm radius planar Au disk, the reference electrode was silver/silver chloride (Ag/AgCl in 3 M KCl), and the counter electrode was a Pt wire. Solutions were deoxygenated before use with nitrogen. Experiments were carried out at room temperature (~20 °C). All glassware was cleaned in an acidic solution comprised of three parts H_2O, one part HNO_3.

The working electrode was mechanically polished before experimentation to produce a smooth surface. Polishing was carried out using 0.3 µm alumina on a felt pad for approximately 10 to 20 minutes in a figure of eight motion. After polishing, the electrode was rinsed with water and ethanol and sonicated for at least five minutes. The working electrodes were cycled in a 0.1 M solution of H_2SO_4 between -0.2 and +1.5 V at a scan rate of 100 mVs^{-1} to electrochemically clean the electrode and to calculate the surface area, see Figure 2.2. The reduction of the Au oxidation peak, at approximately +0.8 V, was used to calculate the surface area of the electrode surface using Equation 2.2. The geometric area of the electrode is 0.0314 cm^2 for a planar 2 mm radius using Equation 2.1. The surface roughness could then be calculated as shown in Equation 2.3. All electrodes required to be at surface roughness of 1.6 or below to ensure consistency between experiments and an Au surface which was free from defects and absorbates.

$$A_G = \pi r^2$$

Equation 2.1: Geometric Area

$$EA = \frac{A_p}{3.9\ x\ 10^4\ Ccm^{-2}}$$

Equation 2.2: Electrochemical Area

$$R.F. = \frac{EA}{A_G}$$

Equation 2.3: Roughness Factor

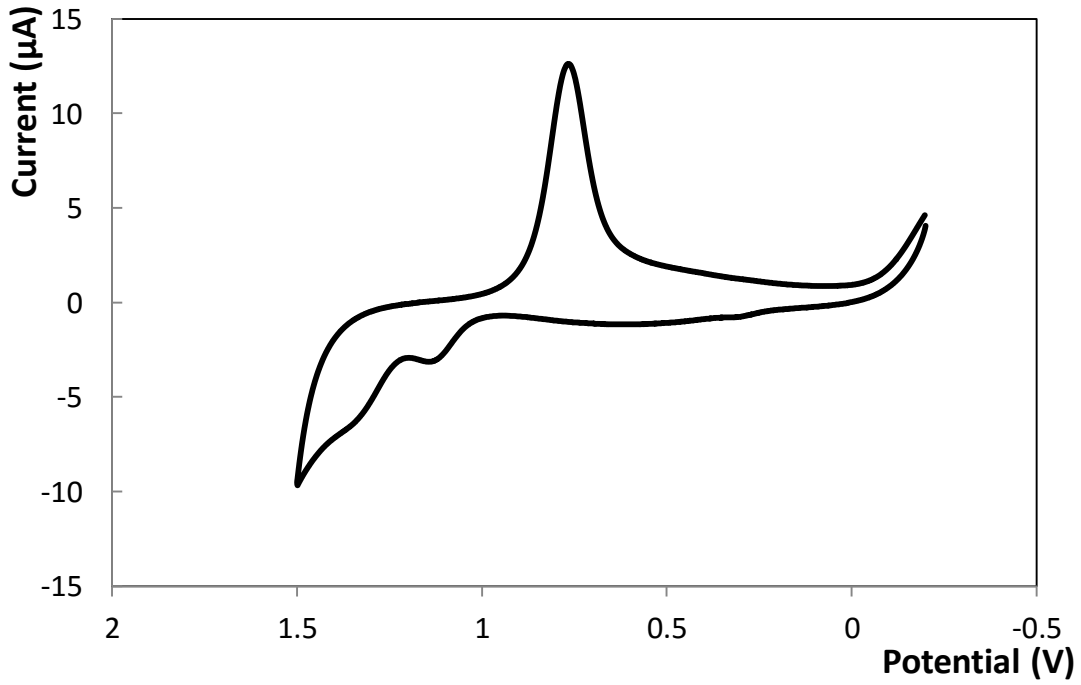

Figure 2.2: Cyclic voltammogram of a 2 mm diameter Au disk electrode in 0.1 M H_2SO_4 at a scan rate of 100 mVs^{-1}. The reference electrode was Ag/AgCl in 3 M KCl.

2.2.4 Monolayer Deposition

Gold disk electrodes were cleaned as previously described and immersed in a 1mM solution of dodecanethiol in ethanol for 1 to 12 hours. Electrodes were then rinsed with ethanol and dried under nitrogen. The monolayer deposition was monitored by CV in H_2SO_4 to calculate the available Au surface area.

2.2.5 DNA Immobilisation

After electrodeposition of PtNPs within the defects of the monolayers, the electrodes were immersed in a 10 µM solution of thiolated probe DNA in 1 M NaCl-TE buffer for 2 hours. Electrodes were then rinsed in deionised water to remove loosely attached oligos. The functionalised PtNPs were then removed by sonication in 0.01 M H_2SO_4.

Working electrodes were cleaned and polished as previously described and immersed in a 10 µM solution of thiolated capture strand DNA in 1 M NaCl-TE buffer for 2 hours. The electrodes were then rinsed with 1 M NaCl-TE buffer to remove loosely attached oligos.

Capture DNA functionalised electrodes were then immersed in a solution of target DNA at concentrations between 1 aM and 1 µM in 1 M NaCl-TE buffer at 37 °C for 90 minutes to hybridize. The electrodes were then rinsed with 1 M NaCl-TE buffer to remove loosely attached oligos.

The electrodes, functionalised with capture DNA and target strands, were then immersed in the PtNPs functionalised with probe for 2 hours at 37 °C. The electrodes were then rinsed with 1 M NaCl-TE buffer.

2.3 Results and Discussion

2.3.1 Monolayer Deposition

A monolayer with nanoscale defects is required in order to electrodeposit and regio selectively modify PtNPs. These defect sites act as nucleation sites for the growth of Pt.[22,23] When a Au surface is exposed to an alkane thiol, at first a highly disordered monolayer is formed.[24] Over time, this monolayer becomes more ordered, eventually becoming defect free.[21] The time for the monolayer to fully assemble depends on a number of factors, including the chain length of the alkane thiol[25], the concentration in solution[26] and the temperature of deposition[27]. Disorder in monolayers can take the form of missing rows[28], vacancy islands of low density monolayer[29], and defects where the monolayer is absent or disordered[30]. At shorter deposition times, a monolayer is formed with some highly ordered areas, and other areas with missing rows, islands and defect sites. As the deposition time is increased, the order of the monolayer increases by filling these islands and missing rows, and by decreasing the size of defect sites. For the production of regioselective PtNPs, a monolayer where these islands and missing rows are filled, but where nanoscale defects remain was required. In this experiment a 1 mM solution of dodecanethiol in ethanol was examined for suitability.

The area of the Au electrode can be determined using voltammetry in acid by measuring the charge associated with forming and then reducing the Au oxide. The microscopic area can be determined since reduction of an oxide monolayer[31] corresponds to 390 μC cm^{-2} of charge passed. The surface roughness factor can then be calculated as the ratio of the microscopic area to the geometric area.[32] The electrochemical area (EA) of the clean Au electrode was first calculated, working electrodes where then placed in the dodecanethiol solution for between 1 and 12 hours. The EA of the Au was then measured again. The results for this experiment are shown in Figure 2.3.

After 1 hour in the monolayer solution 73.3±22.7 % of the Au EA was available. As the time of deposition is increased the surface area decreases and after 4 hours only 12.7±4.6 % of the area was accessible. As the monolayer deposition time is further increased, the EA continues to decrease. At the 12 hour time point, the EA is 0.4±0.7 % of the initial Au area. These results suggest that from 1 to 4 hours the monolayer is highly disordered, with a large number of sizable defects and islands. From 4 to 9 hours the reduction in Au surface area is much lower, which is consistent with increasing

order via the filling of missing rows, islands and reducing defect size. From 9 to 12 hours the available surface area approaches 0, which suggest the monolayer is essentially defect free.

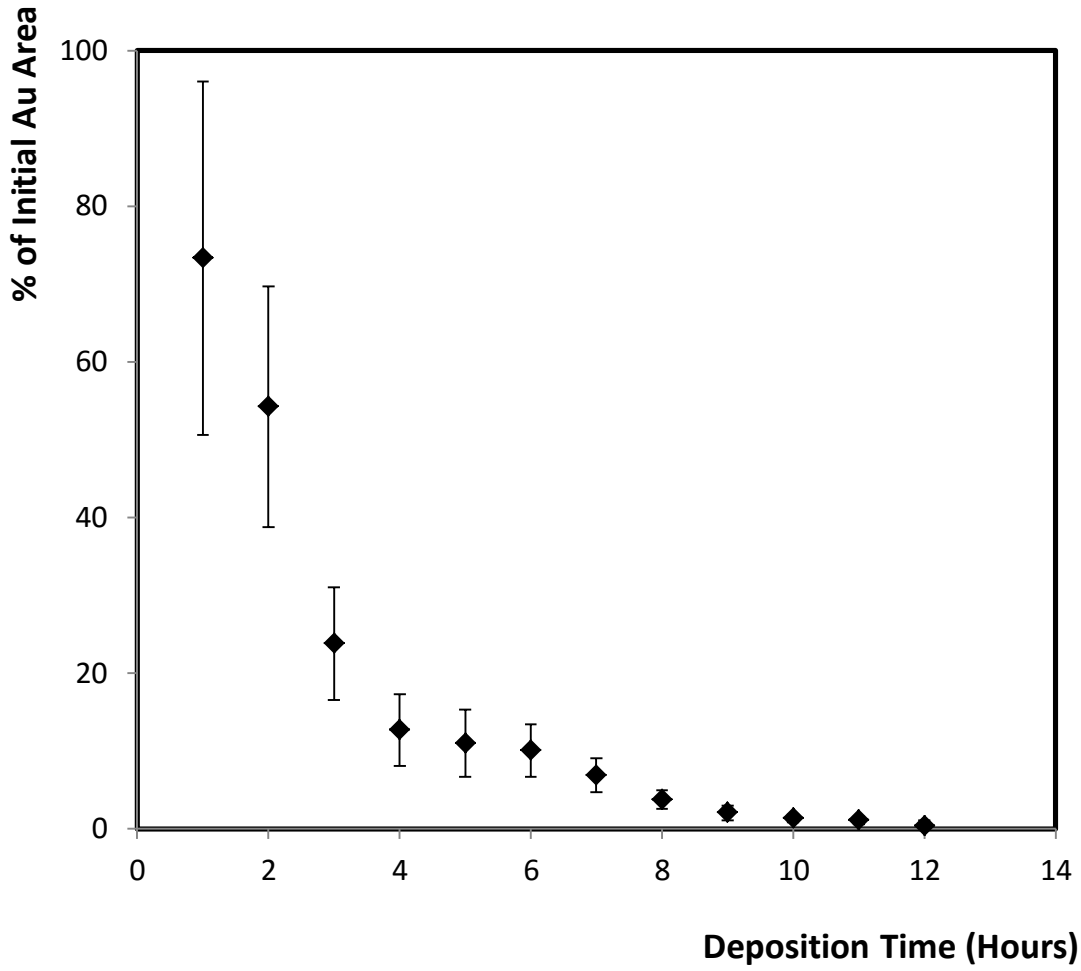

Figure 2.3: Percentage of initial electrochemical surface area of Au for 2 mm Au electrodes after immersion in a 1 mM solution of dodecanethiol in ethanol between 1 and 12 hours. Electrochemical area calculated by cyclic voltammetry in 0.1 M H_2SO_4 at a scan rate of 100 mVs^{-1}. 3 repeats were performed for each experiment. The reference electrode was Ag/AgCl in 3 M KCl.

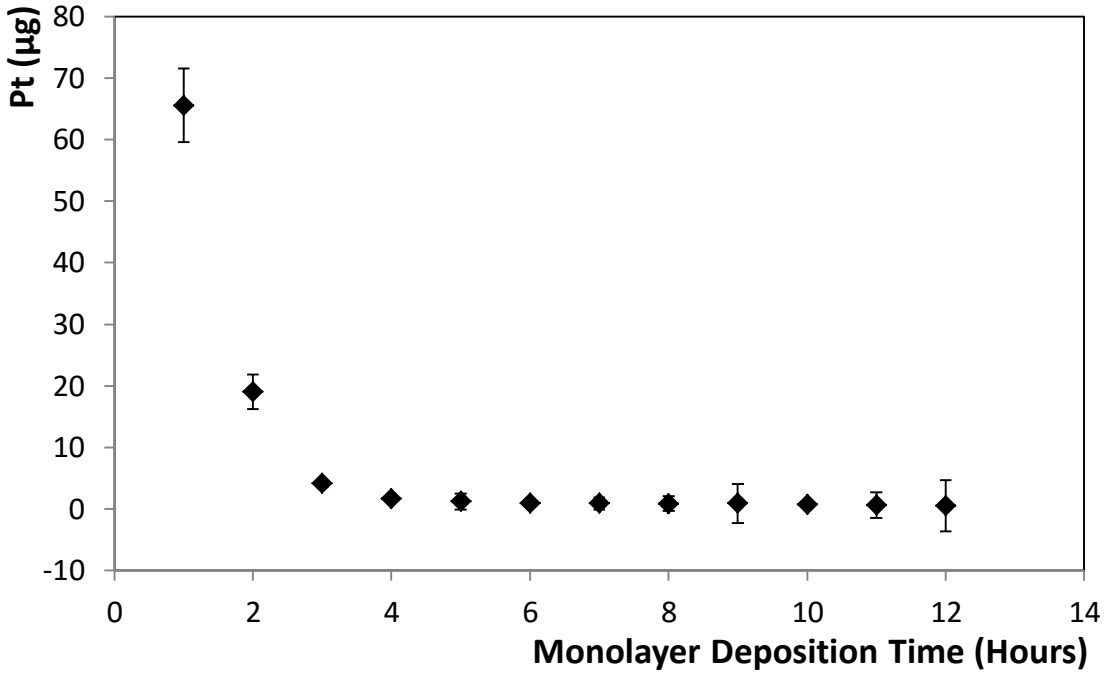

Figure 2.4: Mass of Pt deposited onto 2mm gold electrodes after immersion in a 1 mM solution of dodecanethiol in ethanol between 1 and 12 hours. Applied potential of -0.25V for 180 seconds in 1mM H_2PtCl_6 in 0.5M H_2SO_4.

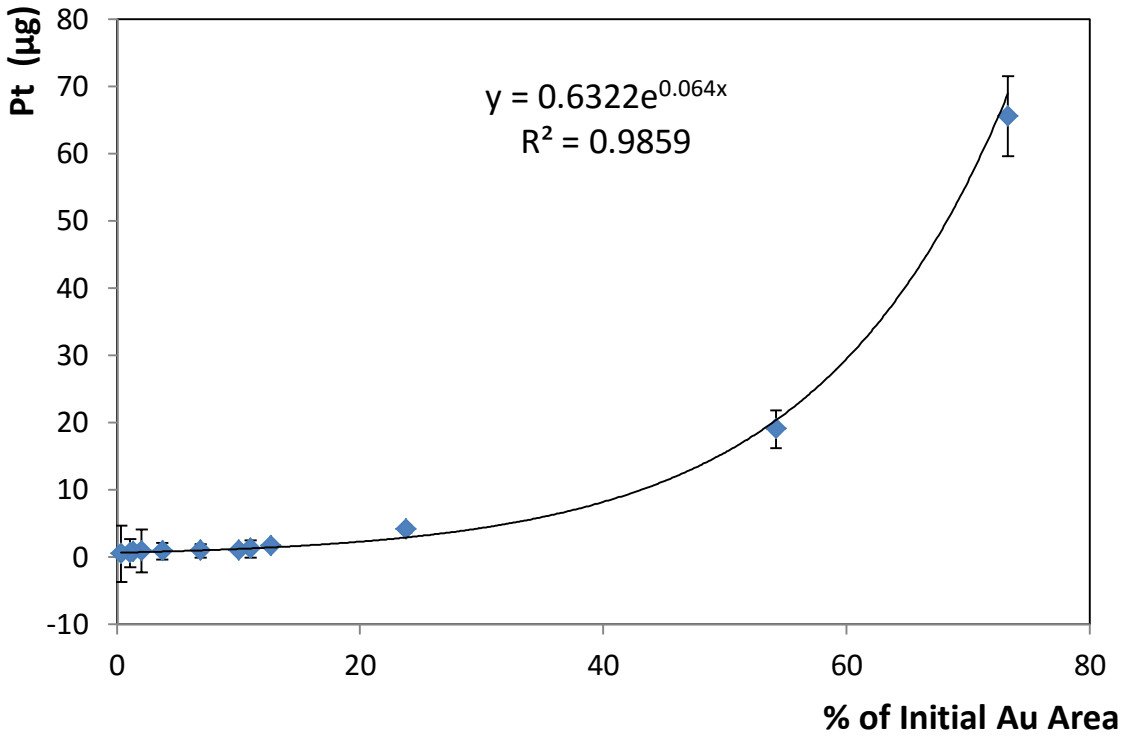

Figure 2.5: Mass of 2 mm Auplatinum deposited versus percentage of initial electrochemical surface area of gold for 2mm gold electrodes after immersion in a 1 mM solution of dodecanethiol in ethanol between 1 and 12 hours. Applied potential of -0.25 V for 180 seconds in 1 mM H_2PtCl_6 in 0.5 M H_2SO_4. The reference electrode was Ag/AgCl in 3 M KCl. 3 repeats were performed for each experiment.

To further probe the effect of the monolayer assembly time, Pt was electrodeposited onto each of the electrodes. The mass of Pt deposited was then calculated based on the charge passed during the deposition assuming that the electrodeposition process is 100 % efficient. The results for this experiment are shown in Figure 2.4. As the surface area available decreases, the mass of Pt also decreases.

The 1 hour monolayer shows significant Pt deposition of 65.6±6.0 µg. However after 4 hours this drops significantly to 1.6±0.2 µg. This corresponds to the EA with 26.7 % coverage after 1 hour, increasing to 87.3 % coverage after 4 hours. As the monolayer deposition time is further increased, the mass of Pt deposited continues to drop. At 7 hours the mass of Pt deposited is 0.9±1.0 µg, At deposition times of greater than 7 hours the mass of Pt drops further, reaching 0.5±4.2 µg at 12 hours. For the EA, after 7 hours, 93 % of the surface was covered and this increased to 99.6 % at 12 hours. If the Pt was only deposited onto the Au surface, then a smaller mass of Pt deposited on the 12 hour monolayer would be expected. This data suggests that at 7 hours and above, the available Au area is quickly covered, with further deposition occurring onto the Pt. This is promising for the goal of producing PtNPs at the defect sites.

Figure 2.5 shows a comparison of the Pt deposited versus the available EA. The mass of Pt decreases exponentially with decreasing available Au area. If the Pt was deposited only onto Au, a linear correlation would be expected. This exponential provides further evidence of the preferential deposition of Pt onto pre-existing Pt. When the monolayer is highly disordered, the available Au is quickly coated by a layer of Pt. As more Pt is deposited, the area available for deposition increases as the Pt grows in three dimensions. For highly ordered monolayers, only small defect sites are available. Even after 180 seconds, the mass of Pt deposited is very low, which provides a very small area for the further growth of Pt.

Based on these results it was decided that 8 hours would provide an ordered monolayer with nanoscale defects. This should give an EA of $1.5\pm0.5\times10^{-3}$ cm^2 which corresponds to 96 % coverage of the Au surface. Figure 2.6 shows an SEM image before and after the deposition of an 8 hour monolayer. Before deposition the Au appears dark due to the high conductivity of the surface. After monolayer deposition the majority of the surface appears to be considerably lighter most likely due to charging by the electron beam due to the non-conducting monolayer. The majority of the surface appeared to be covered, with a number of darker defect sites also visible. This dark colour indicated that the monomer is highly disordered in these areas, which allows the surface charging to

dissipate. While a number of large defect sites are visible, with diameters within the 0.17 to 0.3 µm range, a large number of smaller, nanoscale defects, should also be present. However, it is important to note that SEM is not an ideal technique for characterising defects in monolayers and provides limited insights.

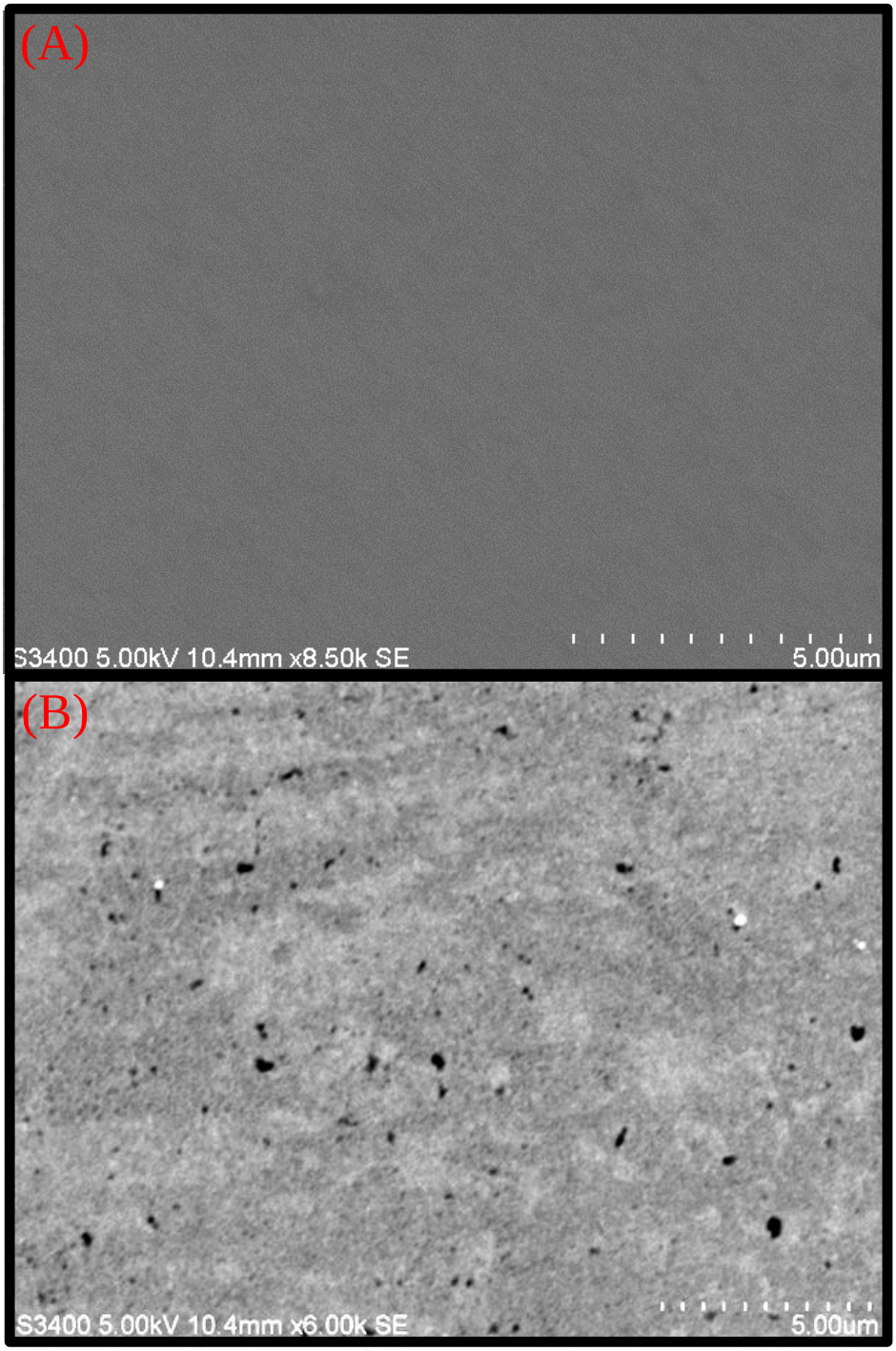

Figure 2.6: Scanning electron microscope image of Au wafer, (A) before, and (B) after, immersion in a 1 mM solution of dodecanethiol in ethanol for 8 hours.

Figure 2.7 shows CVs of each of the steps in the detection assembly. (A) shows a clean, unmodified 2mm Au electrode. It is characterised by an Au oxide peak at +0.87 V, with an Au surface area of 0.036 cm^2 (surface roughness factor of 1.14). After the electrode is templated with dodecanethiol for 8 hours (B), the Au oxide peak is significantly reduced in size and corresponds to an area of 0.002 cm^2. This is consistent with coverage of the Au surface with the alkanethiol monolayer, which blocks access to the underlying Au.[33] The CV's for Figure 2.7 (C) and (D) are discussed in sections 2.3.2 and 2.3.3 respectively.

Figure 2.8 shows voltammograms for the each of the steps in the production and release of the PtNPs. These have been recorded over a potential region where there are no faradaic reactions and the response is dominated by capacitance. The bare Au electrode initially shows a capacitance of 64.0 μFcm^{-2}, which is consistent with a clean electrode that is free of organic adsorbates.[34] Following monolayer deposition for 8 hours, the capacitance decreases to 5.5 μFcm^{-2} which is consistent with the formation of a low dielectric constant film. The low absolute value is consistent with a close packed film perhaps with a small number of widely separated defects.

Since a monolayer with appropriate defects had been identified, the next objective was to determine the optimal potential for the deposition of Pt into these defect sites.

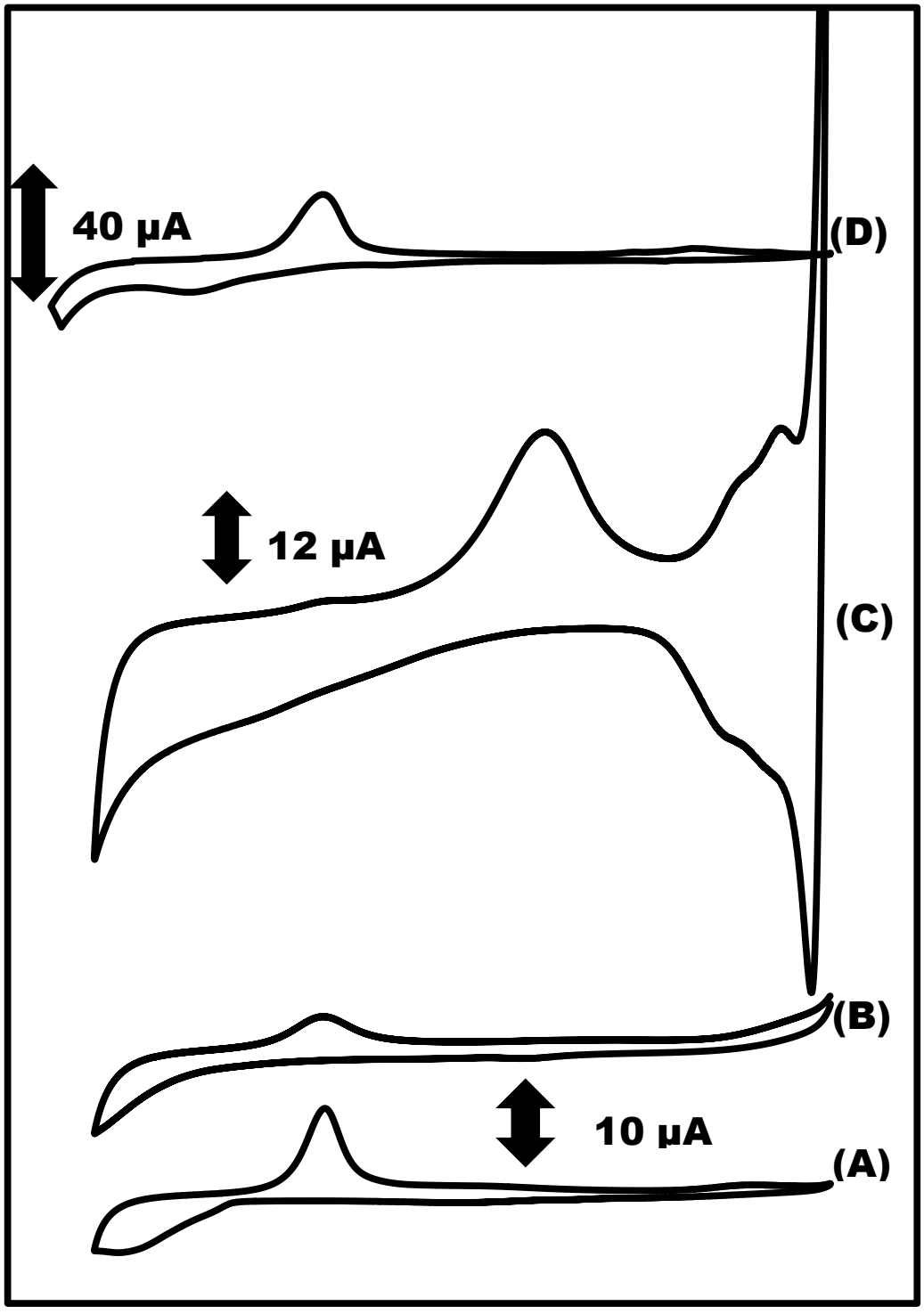

Figure 2.7: Cyclic voltammograms in 0.1 M H_2SO_4 of: (A) 2 mm unmodified Au electrode, (B) after deposition of a defective C_{12} monolayer, (C) following electrodeposition of PtNPs into the monolayer defects (D) after the PtNPs have been desorbed via sonication. The reference electrode was Ag/AgCl in 3 M KCl.

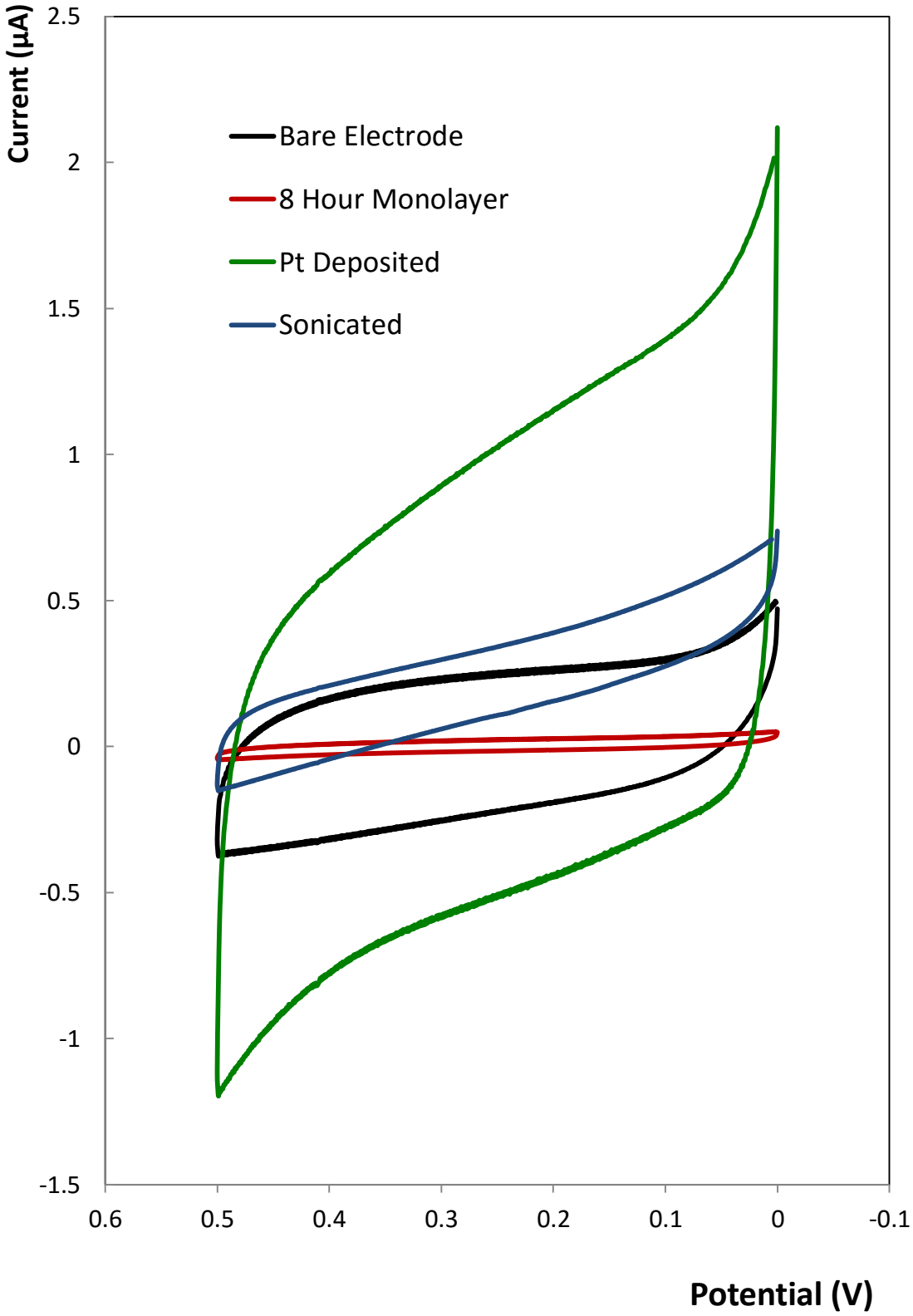

Figure 2.8: Cyclic voltammograms in 0.1 M H_2SO_4 of 2 mm unmodified Au electrode, after deposition of a defective C_{12} monolayer, following electrodeposition of PtNPs into the monolayer defects, and after the PtNPs have been desorbed via sonication. The reference electrode was Ag/AgCl in 3 M KCl.

2.3.2 Platinum Deposition Potential

The next objective was to determine the optimum potential for the deposition of PtNPs into these defects. Figure 2.9 shows a CV of a clean Au electrode in 0.5 M H_2SO_4 and in 1mM hydrogen hexachlorideplatinate (IV) hydrate (H_2PtCl_6) in 0.5 M H_2SO_4. The Pt solution is characterised by an increase in the oxidation current at +0.26 V, and a hydrogen production peak at -0.3 V. The reduction of Pt reaches a maximum at -0.25 V, with smaller current present until +0.1 V. Based on this CV it was decided to examine the voltammetric deposition of Pt from +0.2 V to -0.3 V. Electrodes were prepared with an 8 hour dodecanethiol monolayer and immersed in a 1 mM H_2PtCl_6 in 0.5 M H_2SO_4. A fixed potential was then applied for 180 seconds.

A typical current-time transient is shown in Figure 2.10. The current-time transient was then integrated to calculate the total charge passed. This charge was then used to calculate the mass of Pt deposited using Equation 2.4. This current-time transient shows a sharp rise in the charge passed initially, for approximately 30 seconds. This is consistent with rapid nucleation due to the large over potential at an applied potential of -0.25 V. The rate of increase of the charge then decreases, suggesting that at this point the electrodeposition is characterised by radial diffusion towards this particle.[35]

$$Mass = \frac{1}{\mathrm{F}} \; x \; \frac{Q\,\mathrm{MW}}{\mathrm{n}}$$

Equation 2.4 Mass of Pt deposited

Where F is faradays constant (96485 $Cmol^{-1}$), Q is the total charge, MW is the molecular weight of Pt (195.09 $gmol^{-1}$) and n is the number of electrons (4).

As expected from the voltammetry, -0.25 V gave the largest quantity of Pt deposited, see Figure 2.11, at 6.14±0.48 µg, which corresponds to 4.01±0.31 $mgcm^{-2}$ based on the area available after the deposition of an 8 hour monolayer. More negative potentials also resulted in a large amount of deposited Pt, with -0.3 V giving 5.71±0.90 µg and -0.35 V depositing 4.22±0.30 µg. While a more negative current should result in a larger volume of Pt deposited, vigorous hydrogen evolution at these potentials most likely impairs the growth of the PtNPs. At potentials more positive than -0.25 V the amount of Pt deposited dropped sharply, with only 0.91±0.31 µg deposited at -0.2 V,

which corresponds to 0.59±0.21 $mgcm^{-2}$, and 0.32±0.08 $mgcm^{-2}$ at a potential of 0.0 V. This decrease is consistent with an exponential decrease in driving force as the potential is increased

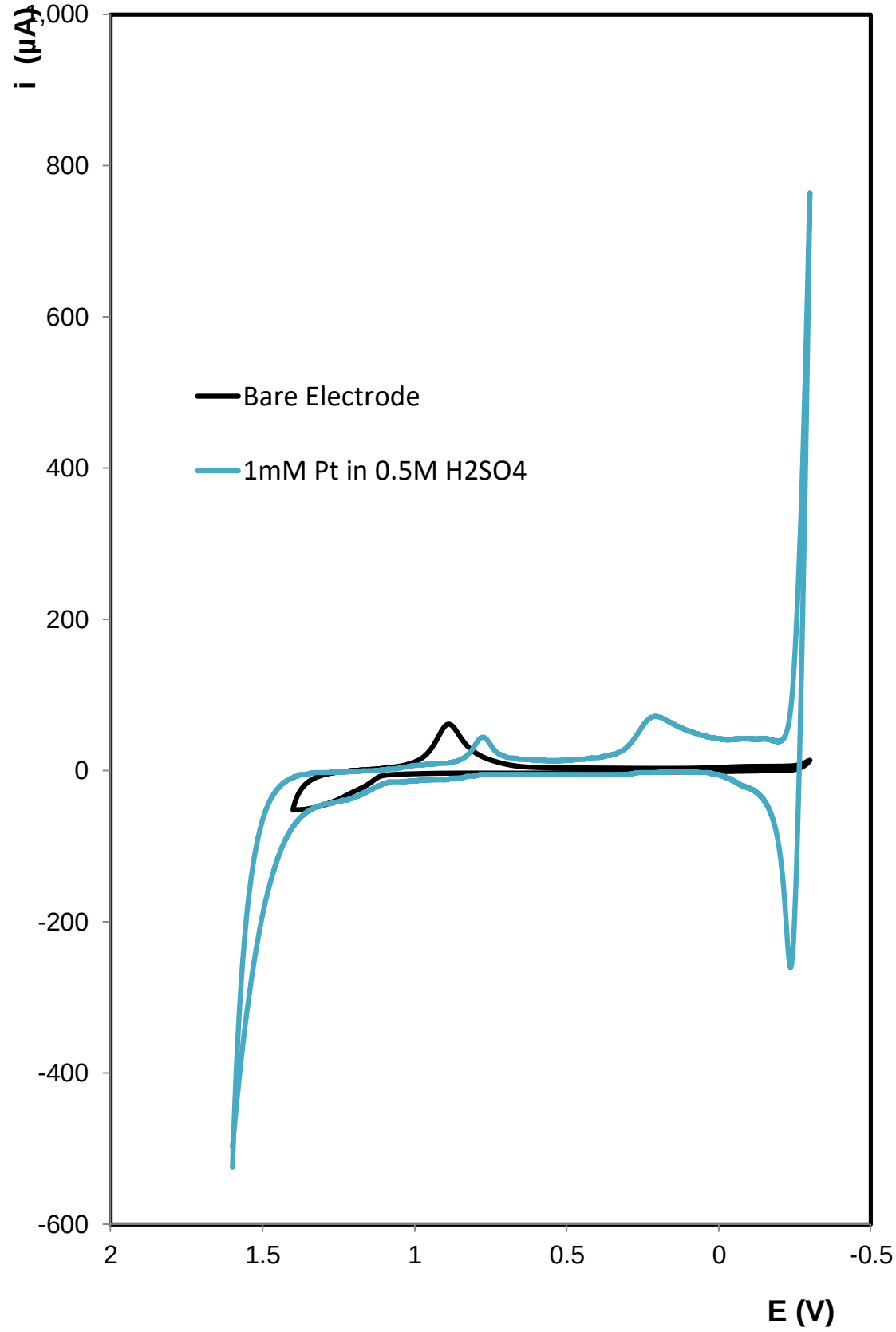

Figure 2.9: Cyclic voltammogram from -0.3 V to 1.6 V of a 2 mm Au electrode in 1 mM H_2PtCl_6 in 0.5 M H_2SO_4. The reference electrode was Ag/AgCl in 3 M KCl.

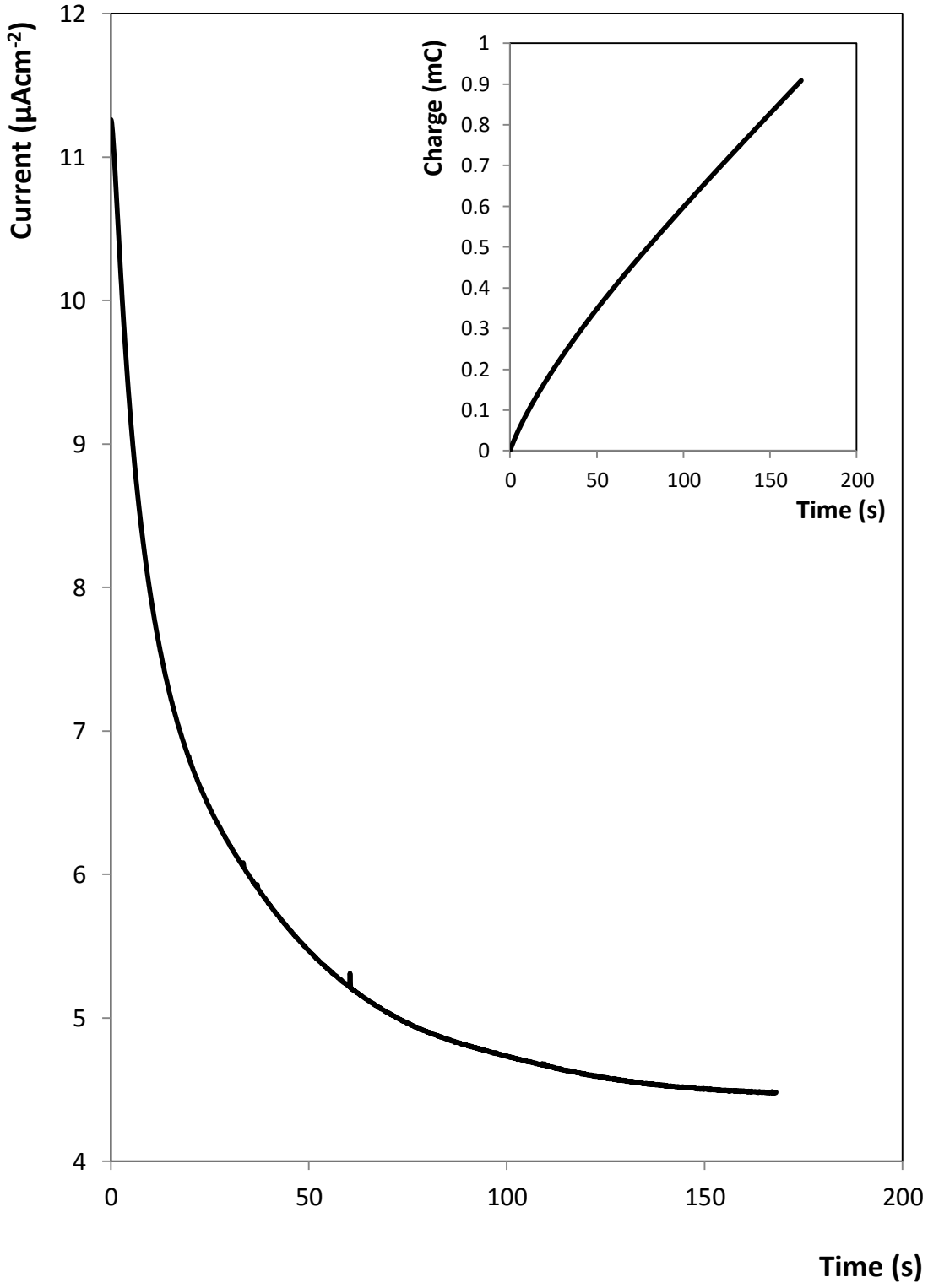

Figure 2.10: Current-time transient for growth of PtNPs in monolayer defects on a 2 mm Au electrode prepared in a 1 mM solution of dodecanethiol in ethanol for 8 hours. The applied potential was -0.25 V. The solution contains 1 mM H_2PtCl_6 dissolved in 0.5 M H_2SO_4. Inset showing integrated curve of charge passed vs. time. The reference electrode was Ag/AgCl in 3 M KCl.

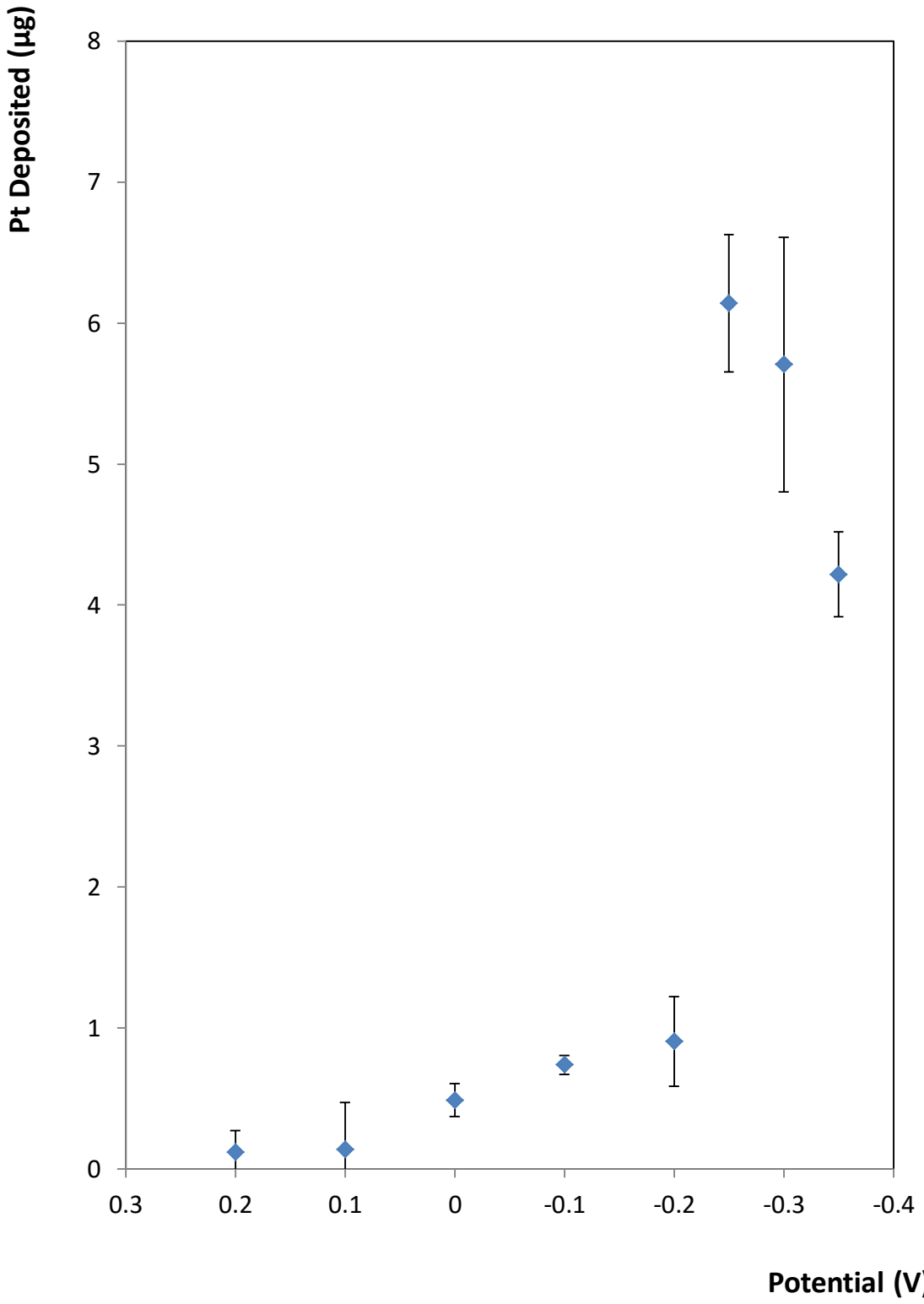

Figure 2.11: Mass of Pt deposited onto 2 mm Au electrodes after immersion in a 1 mM solution of dodecanethiol in ethanol for 8 hours. Applied potential between +0.2 V and -0.35 V for 180 seconds in 1 mM H_2PtCl_6 in 0.5 M H_2SO_4. 3 repeats were performed for each experiment. The reference electrode was Ag/AgCl in 3 M KCl.

Figure 2.12 shows SEM images following deposition at potentials from +0.2 V to -0.3 V. At each of the potentials, a number of PtNPs are visible with good dispersion throughout the area imaged. The average size of the PtNPs is shown in Figure 2.13, with the surface coverage in Table 2.1.

At 0.2 V PtNPs with a diameter of 119±26 nm are formed with high surface coverage, 25±9 %. The growth of these particles is consistent with rapid nucleation of the surface, followed by diffusion controlled growth. This gives rise to a large number of evenly sized PtNPs.

As the applied potential becomes more negative at 0.1 V, the size of the particles increases to 246±71 nm, however the surface coverage also drops significantly to 12.2±7.0 %. Consistent with the increased driving force, these results suggest that PtNPs rapidly nucleate, grow and coalesce giving rise to fewer, larger particles.

At a potential of 0.0 V, the particle size is 128±76 nm, and the surface coverage is 12.7±2.8 %. The smaller particle size and higher standard deviation is unexpected since the higher driving force would be expected to yield larger particles while instantaneous nucleation ought to lead to more uniform particles. This behaviour most likely arises due to the ability of the PtNPs to catalyse water reduction in this acidic electrolyte. Specifically, gas evolution is likely to slow the nanoparticle growth due to competition between water reduction and nanoparticle growth as well as non-diffusional mass transport. The increase in the standard deviation is consistent with this process since smaller PtNPs tend to be more catalytic than larger ones, i.e., the influence of water reduction on the growth rate depends on the absolute size of the particles leading to a greater standard deviation.

At -0.1 V the particles' diameter is 179±77 nm. The surface coverage increases significantly to 30.1±6.4 %, the highest value for the whole potential range investigated. The larger particle size suggests that the larger driving force for electrodeposition exerts a greater influence than gas evolution on the final particle size. The relative standard deviation for these particles is quite high at approximately 43 %. The mass of Pt was higher again at this potential at 0.74±0.07 µg.

From a potential of -0.20 V to -0.35 V the coverage is in the range of 12±0.6 % to 6.9±2.8 %. However, the charge passed was significant and would correspond to 6.14±0.48 µg at -0.25 V and 5.71±0.9 µg at -0.30 V if the coulometric efficiency was 100 %. Analysis of the particle size for this potential range shows large variation, with -0.2 V showing small particles at 94±47 nm, whereas -0.25 V is at 641±473 nm, -0.30 V at 422±378.12 nm and -0.35 V at 1.5±1.3 nm. Under these conditions, the PtNPs efficiently reduce water causing bubble formation and a very large relative standard deviation for the diameter of the particles.

As previously discussed, the rate of nanoparticle nucleation and growth depends on the applied potential and on transport of the Pt ions towards the growing PtNPs. If the applied overpotential is sufficiently negative and the solution is quiescent, once a nucleation site is formed, the growth and eventual size of the particles depends on the diffusion rate through the solution. However, at these more negative potentials, the PtNPs formed are highly efficient at the reduction of water to produce hydrogen. This hydrogen evolution acts to mix the solution, which ought to lead to a greater Pt^{2+} flux than is possible from diffusion alone giving rise to large PtNPs particles. However, gas evolution can also mechanically dislodge the PtNPs especially where their radius is small since these are the most catalytically active but have the smallest area of contact with the electrode and leads to a very low surface coverages of less than 7 %. This suggests that the majority of the PtNPs formed were removed from the surface. This explains the very small PtNPs at -0.35 V at 13±9 nm, the Pt detected by SEM is likely the "tails" of the PtNPs left behind on the surface after removal of the primary NP. For -0.3 V and -0.25 V the large relative standard deviation in the size suggests the loss of a large number of PtNPs also, with some very large particles remaining, but the majority being lost from the surface.

Based on these results it was decided that a potential of +0.1 V would be the most suitable. The particles produced, are large at 246±71 nm, with reasonably consistent size and a good surface coverage of 12±2.8 %.

Figure 2.7(C) shows a CV of PtNPs which were deposited into the monolayer with an applied potential of +0.1 V. After deposition of the monolayer, the available Au area is significantly reduced by 95 % to an area of 0.002 cm^2. When Pt is electrodeposited, the Au oxide peak becomes undetectable, suggesting coverage of the defect sites in the monolayer with Pt. A Pt oxide peak also becomes visible at +0.38 V, with an electrochemical surface area of 0.132 cm^2. This large EA for Pt is consistent with the growth of PtNPs in the monolayer defect sites.[36] The CV also shows hydrogen adsorption/desorption and hydrogen evolution at -0.3 V.

After the deposition of Pt into the defective monolayer, the EA of Pt was calculated from the Pt oxide reduction peak as 0.132 cm^2. Using the SEM images shown in Figure 2.14, and assuming that all of the PtNPs are hemispheres, the total area would be 0.024 cm^2. This shows that the actual area of Pt is approximately 20 % of that calculated by CV. This result may suggest that the particles may have a rough surface but given the assumptions made and the likely errors involved in estimating the quantities involved, this level of agreement is acceptable. To achieve an accurate measurement of the mass of platinum, methods such as inductively coupled plasma mass spectroscopy (ICP-MS) or atomic force microscopy (AFM) would yield considerably more accurate results.

Voltammograms which were recorded over a potential range where the response is dominated by capacitance are shown in Figure 2.8. After the deposition of an 8 hour monolayer onto the working electrode the capacitance was 5.5 μFcm^{-2}, based on the EA of a bare electrode of 0.036 cm^2. When Pt was electrodeposited at +0.1 V the capacitance increased significantly to 221.6μFcm^{-2}. This suggests the growth of a large number of PtNPs on the surface of the electrode. This value is larger than the 64.0 μFcm^{-2} capacitance received for the clean Au electrode, and is consistent with the increase in electrochemical surface area seen in Figure 2.7.

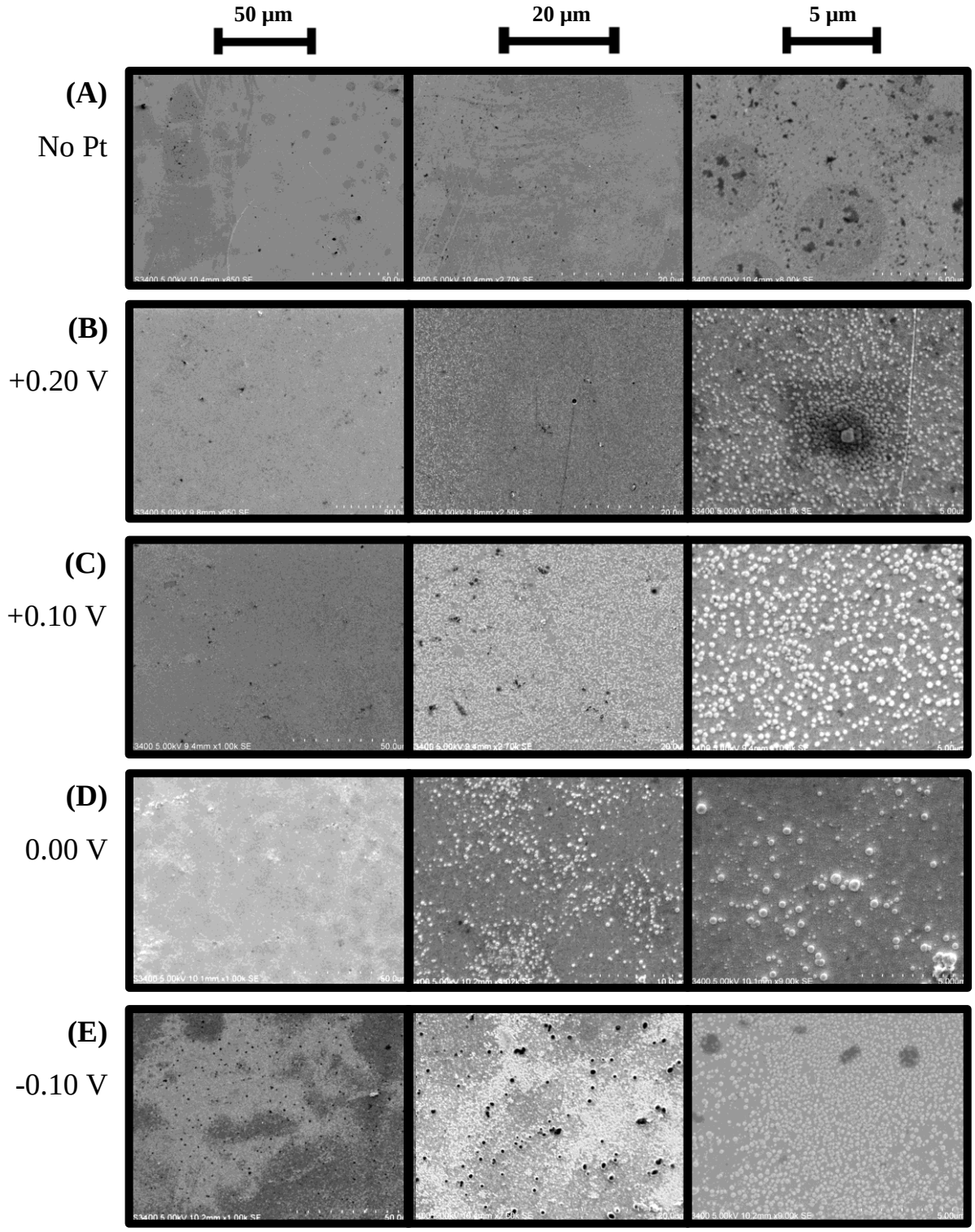

(Continues on next page)

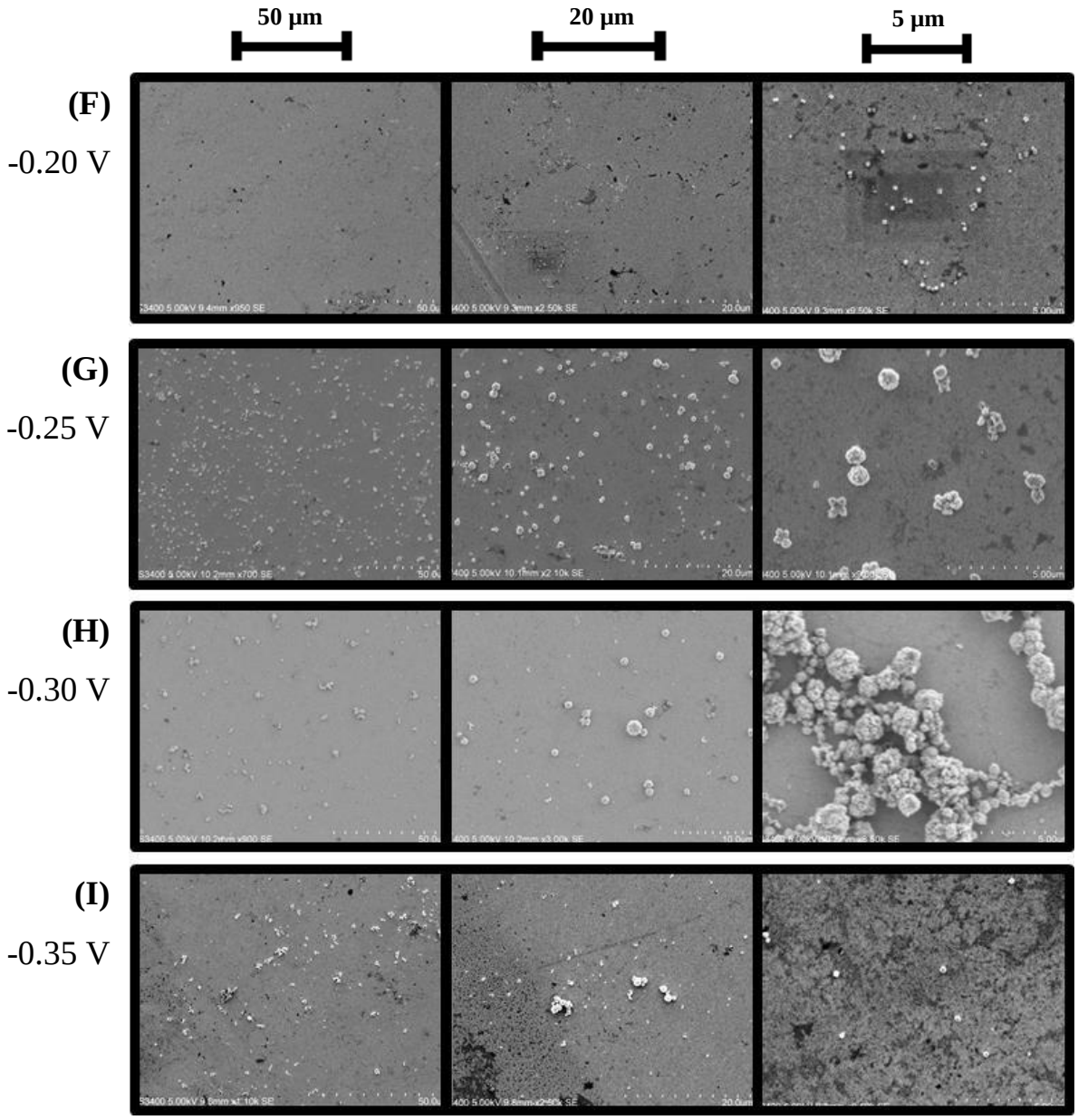

Figure 2.12: Scanning electron microscopy of Pt deposited onto an Au wafer after immersion in a 1 mM solution of dodecanethiol in ethanol for 8 hours. Applied potential between +0.2 V and -0.35 V (A to I) for 180 seconds in 1 mM H_2PtCl_6 in 0.5 M H_2SO_4. The reference electrode was Ag/AgCl in 3 M KCl.

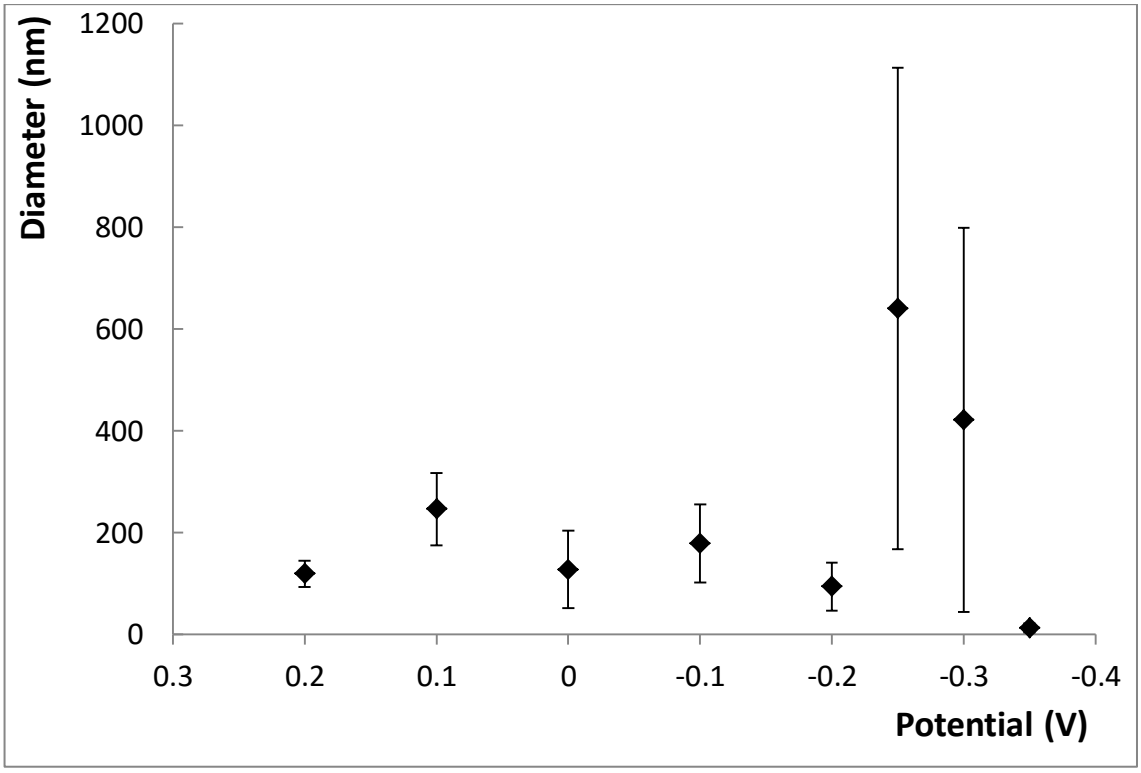

Figure 2.13: Average nanoparticle diameter from scanning electron microscopy of Pt deposited onto Au wafer after immersion in a 1 mM solution of dodecanethiol in ethanol for 8 hours. Number of particles measured between 41 and 814. Applied potential between +0.2 V and -0.35 V for 180 seconds in 1 mM H_2PtCl_6 in 0.5 M H_2SO_4. 3 repeats were performed for each experiment. The reference electrode was Ag/AgCl in 3 M KCl.

Table 2.1: Summary of results for nanoparticle diameter and surface coverage from SEM and mass of Pt deposited from charge passed during deposition. 3 repeats were performed for each experiment.

Potential (V)	Pt Deposited (µg)	Diameter (nm)	% Surface Coverage
0.20	0.12±0.15	119±26	25.8±8.9
0.10	0.14±0.33	246±71	12.2±7.0
0.00	0.49±0.12	128±76	12.7±2.8
-0.10	0.74±0.07	179±77	30.1±6.4
-0.20	0.91±0.32	94±47	1.2±0.6
-0.25	6.14±0.48	641±473	6.9±2.8
-0.30	5.71±0.90	422±378	1.2±0.6
-0.35	4.22±0.30	13±9	1.5±1.3

2.3.3 Nanoparticle Desorption

The next objective was to desorb the PtNPs from the electrode surface while preserving the functionality of the adsorbed probe strand DNA. Sonication is frequently used to break up aggregates[37], mix nanomaterials[38], and other solution phase processing of PtNPs[39-42]. It has also been shown to effectively remove nanosphere masks and surface confined PtNPs [43,44]. For these reasons, sonication represented an attractive method for the release of the electrodeposited PtNPs.

As seen in Figure 2.14, after electrodeposition a large number of PtNPs were visible on the surface of the electrode. (B) shows the electrode after 1 hour of sonication in 0.01 M H_2SO_4. The majority of the PtNPs have been removed from the surface, with only traces of Pt visible. It is believed that these traces occur as a result of PtNPs that fail to fully desorb from the surface. This image suggests that sonication is highly efficient at removal of the PtNPs.

The PtNPs which were removed by sonication were then drop cast onto an Au wafer and imaged by SEM, see Figure 2.14 (C). In order to minimise dying induced aggregation effects, the nanoparticle suspension is sufficiently dilute so that a fully dispersed nanoparticle array can be obtained. Significantly, the particles are well separated with no major clustering visible. The size of the PtNPs is 80±12 nm, compared to 123±35 nm before sonication, this decrease in the apparent size may be due to preferential settling of larger PtNPs causing smaller particles pre-concentrate in the desorbed suspension and the standard deviation decreases to 14.6 % compared to 28.7 % before sonication.

The CV of the working electrode after sonication is shown in Figure 2.7(D). The large Pt peak at +0.38 V present after the deposition of Pt is significantly reduced from 0.132 cm^2 to 0.004 cm^2.This suggests that the majority of the PtNPs have been successfully removed from the surface. A Au oxide peak is also visible at +0.87 V with a surface area of 0.003 cm^2. This is a somewhat higher available area than after the deposition of the monolayer of 0.002 cm^2, which suggests that the sonication procedure may remove a small amount of the monolayer in addition to the PtNPs.

Figure 2.8 shows voltammograms where the response is dominated by the interfacial capacitance. Based on the EA of the bare Au electrode, after electrodeposition of Pt the

capacitance was 221.6 μFcm^{-2}. When the particles are removed by sonication, the capacitance decreased to 23.7 μFcm^{-2}. This value is significantly higher than the monolayer only value of 5.5 μFcm^{-2}, which provides further evidence of the loss of some monolayer coverage for this step.

Since PtNPs that were suitable for DNA detection had been successfully produced, the next objective was to measure the ability of the assay to determine the concentration of DNA in solution, i.e., to confirm that the particles retained their molecular recognition functionality.

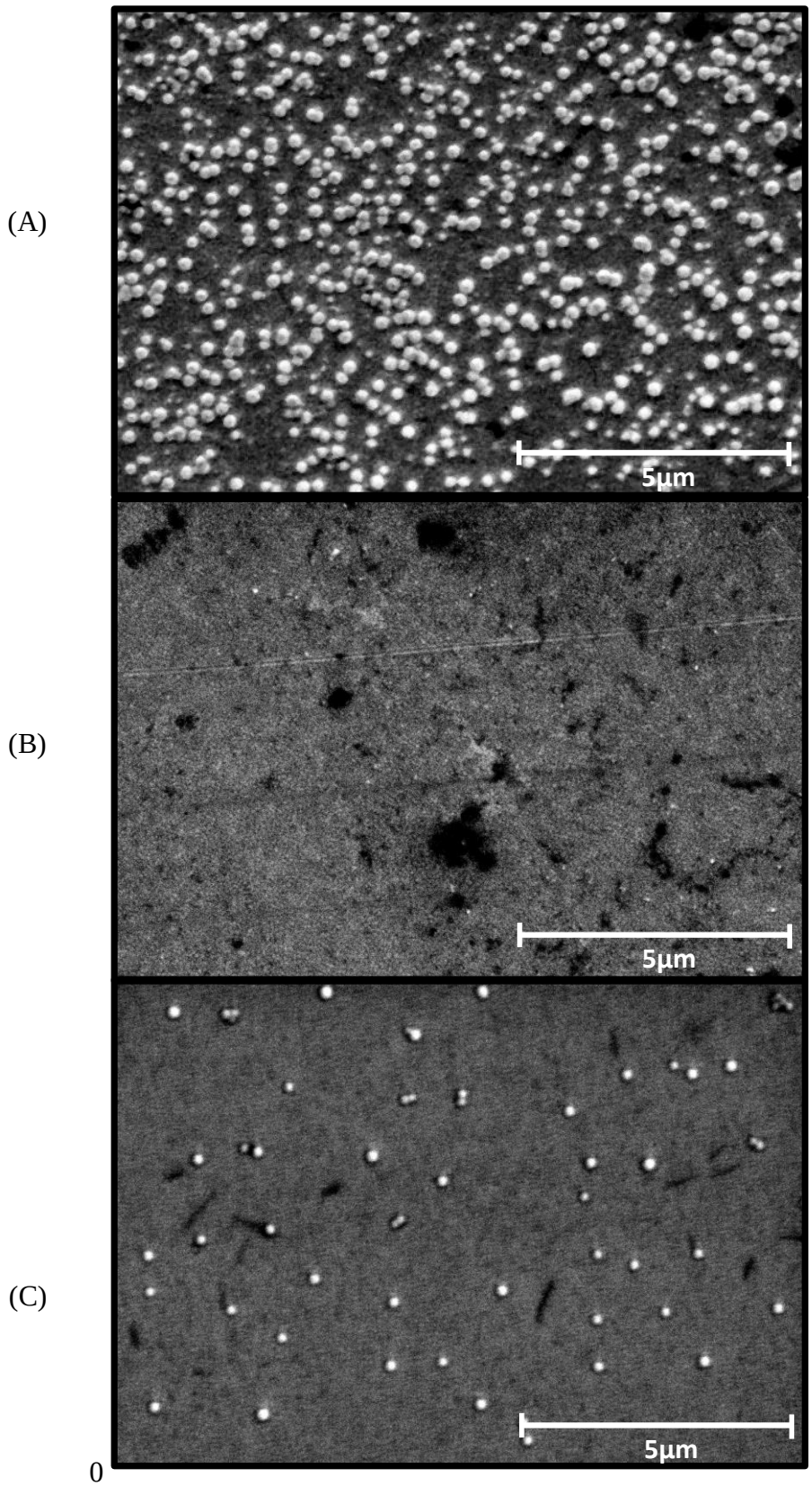

Figure 2.14: SEM images of (A) PtNPs electrodeposited onto an Au wafer after immersion in a 1 mM solution of dodecanethiol in ethanol for 8 hours using applied potential of +0.1 V for 180 seconds in 1 mM H_2PtCl_6 in 0.5 M H_2SO_4. (B) after the PtNPs have been desorbed via sonication. (C) desorbed PtNPs drop cast film onto Au wafer. The reference electrode was Ag/AgCl in 3 M KCl.

2.3.4 DNA Detection

The detection of DNA relies on the attachment of a thiolated capture strand to a clean Au electrode.[45] This capture strand then selectively hybridises with a section of the target and finally the probe strand labelled electrocatalytic PtNPs hybridise with the remaining section of the target in a sandwich assay format. The surface density of the capture strands on the electrode[46] and the surface area of the Au have a significant impact on the number of target binding sites available on the surface[47]. In order to maintain a consistent number of attached particles, the surface roughness was monitored by CV, and the deposition time of 2 hours was rigorously maintained.

After the electrode was modified with the capture surface, it was then immersed in a solution containing the target nucleic acid sequence. DNA hybridization is both highly temperature and time dependent. As the temperature approaches the melting temperature of the DNA/DNA duplex, the binding rate increases[20] but at the melting temperature, 50 % of the duplex will spontaneously disassociate.[48] The melting temperature of the target / capture hybrid was calculated as 39.2 °C.[49,50] A temperature of 37 °C was chosen as this allows for rapid hybridisation, and good discrimination against mismatched DNA.

Following hybridisation of the capture and target, the electrode was then immersed in a suspension of the PtNPs functionalised on one side with the probe strand. While it is difficult to determine the concentration of the PtNPs, it is sufficiently high so that all targets captured on the electrode can be labelled. The hybridization was carried out at 37 °C for 3 hours. The fully assembled detection assay was measured by CV. Figure 2.15 shows the CV obtained for a clean Au electrode functionalised with capture strand DNA, bound to target DNA, and then to the nanoparticle via the probe strand. Well-defined peaks are visible in the -0.05 V to -0.3 V range for hydrogen adsorption/desorption. This provides clear evidence for the expected DNA detection assembly. Control experiments, where the nanoparticle was not functionalised with the probe, or where no capture were present showed no hydrogen adsorption/desorption which suggests this signal is not due to non-specific absorption of the PtNPs onto the Au surface. Voltammetry of the assembly surface was expected to be a destructive process, and so electrodes used for these CV's were not used in the detection of DNA.

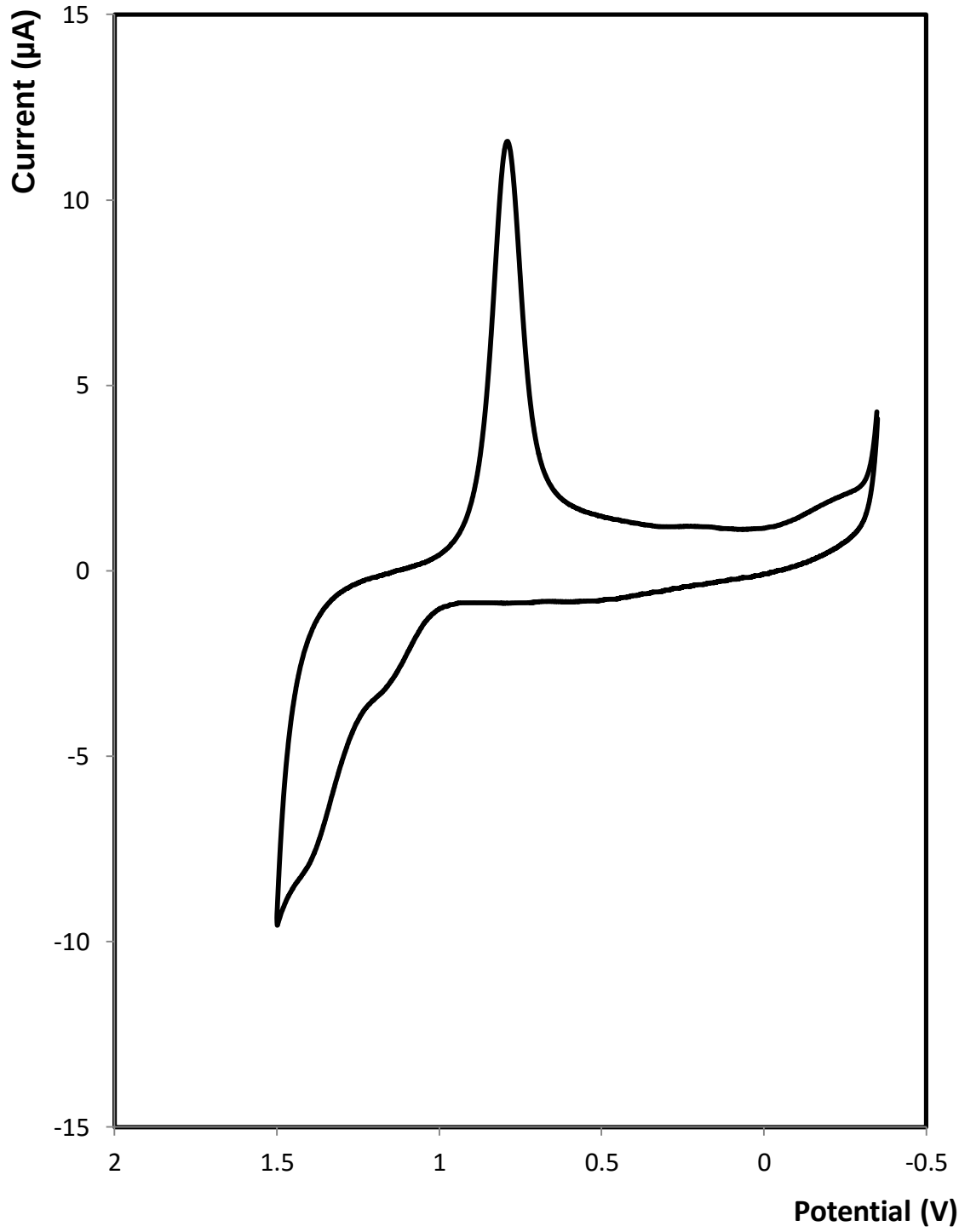

Figure 2.15: Cyclic voltammogram of a 2 mm radius Au disc electrode after modification with capture strand DNA and hybridization with the target and nanoparticle labelled probe sequence where the target strand concentration is 1 μM. The supporting electrolyte is 0.01 M H_2SO_4 and the scan rate is 100 mV s^{-1}. The reference electrode was Ag/AgCl in 3 M KCl.

2.3.5 Detection of DNA by Hydrogen Peroxide Electrocatalysis

PtNPs have previously been shown to catalyse the reduction of hydrogen peroxide.[14,51] To analyse the ability of the sensor to detect the DNA target, electrodes were modified with capture DNA, and then immersed in a target containing solution between 1 µM and 1 am. The capture/target duplex was then hybridised with probe functionalised PtNPs. The completed sensor was then placed in a 0.01 M H_2SO_4 solution, and a fixed potential of -0.25 V was applied. The current was measured for 10 minutes to allow the system to equilibrate. Hydrogen peroxide was then added to give a final concentration of 200 µM. The difference in current before and after the addition of hydrogen peroxide, Δi, was taken as the analytical signal. A representative example is shown in Figure 2.16. The large increase in the measured current is after the addition of hydrogen peroxide.

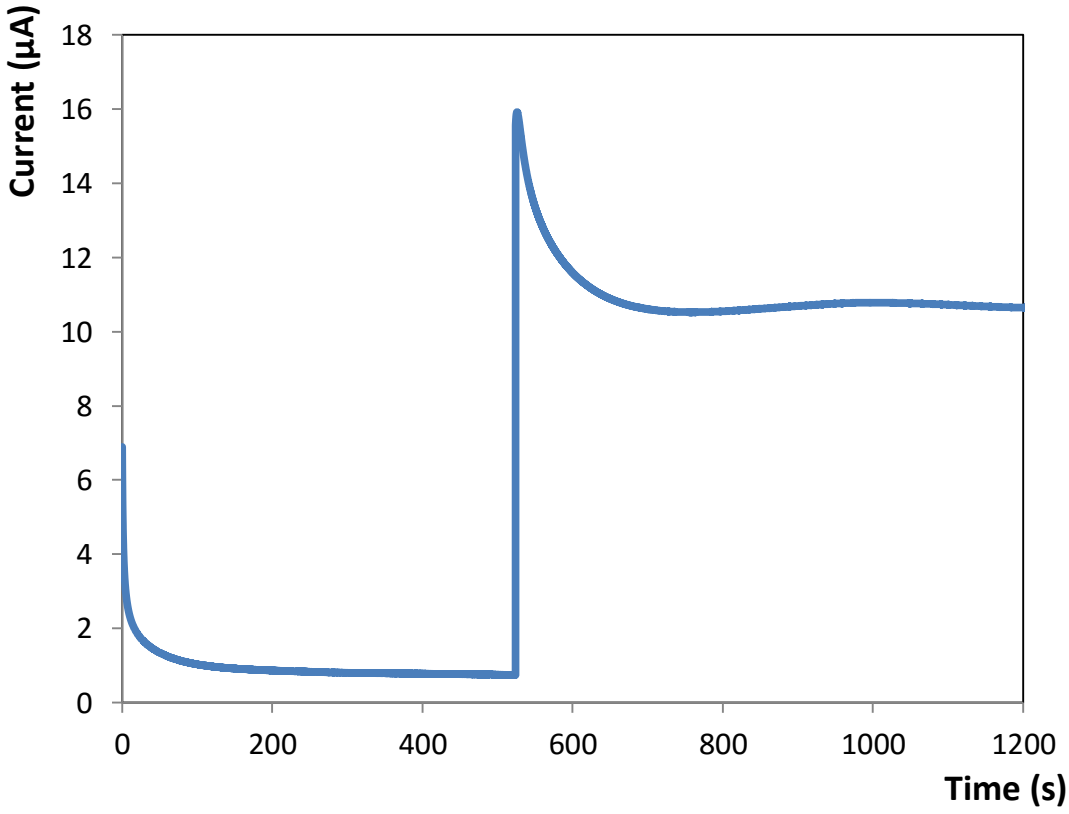

Figure 2.16: Current-time response for the detection of 10 nM target DNA in 0.01 M H_2SO_4. H_2O_2 added at 10 minutes to give a concentration of 200 µM. The applied potential was -0.25 V. The reference electrode was Ag/AgCl in 3 M KCl.

Figure 2.17 shows the dependence of Δi as the target concentration is systematically varied from 1 aM to 1 µM. The change in current is proportional to the log concentration of DNA, and an acceptable linear response was achieved from 10 pM to 1 µM.

Ideally, the addition of hydrogen peroxide would be unnecessary, since PtNPs are capable of reducing water. This would allow for the use of a reagent free detection strategy since water in the sample, e.g., blood, could be used to generate the current response. Analysis of the signal received before addition of peroxide resulted in a correlation between concentration of the DNA target and the signal received, however the variability was significant As previously discussed, when working electrodes are cleaned, a surface roughness in the range of 1 to 1.3 is desired. Gold is also capable of the reduction of hydrogen peroxide[52], and of oxygen in solution[53].

If electrodes with such large variation in the available surface area were used, then this would result in a significantly higher level of error for a given detection. However, in this experiment, the change in current after the addition of hydrogen peroxide was used as the analytical signal, which had the added benefit of controlling for differences in the Au surface area available, since the magnitude of the current before peroxide addition is not used directly. One possible approach that could be applied here, would be to block the Au surface with a closely packed monolayer after modification with capture DNA and target DNA hybridization. This may reduce the background signal, making single point detection with water feasible.

As a control experiment, PtNPs were uniformly functionalised with capture DNA, and the assay was performed again. The response for these particles is shown in Figure 2.17. A good linear response is again observed from 10 pM to 1 µM, however the sensitivity is significantly lower at 4.9×10^{-2} μA^{-1}. This poorer sensitivity is thought to arise from the lower electrocatalytic properties of the particles, since peroxide must pass through the DNA monolayer before reaching the Pt surface and being reduced. This difference is sensitivity suggests that the regioselective particles were successfully produced, i.e. part of the nanoparticle is unmodified, which improves the catalytic properties of the particle, giving rise to a higher current.

As an additional control experiment, the assay was performed in the absence of Pt, using an unlabelled probe strand. The signal for this control was less than 2 % of that

observed in the presence of PtNPs. Based on a signal to noise ratio of 3:1, the limit of detection (LOD) for this assay is approximately 0.1 aM.

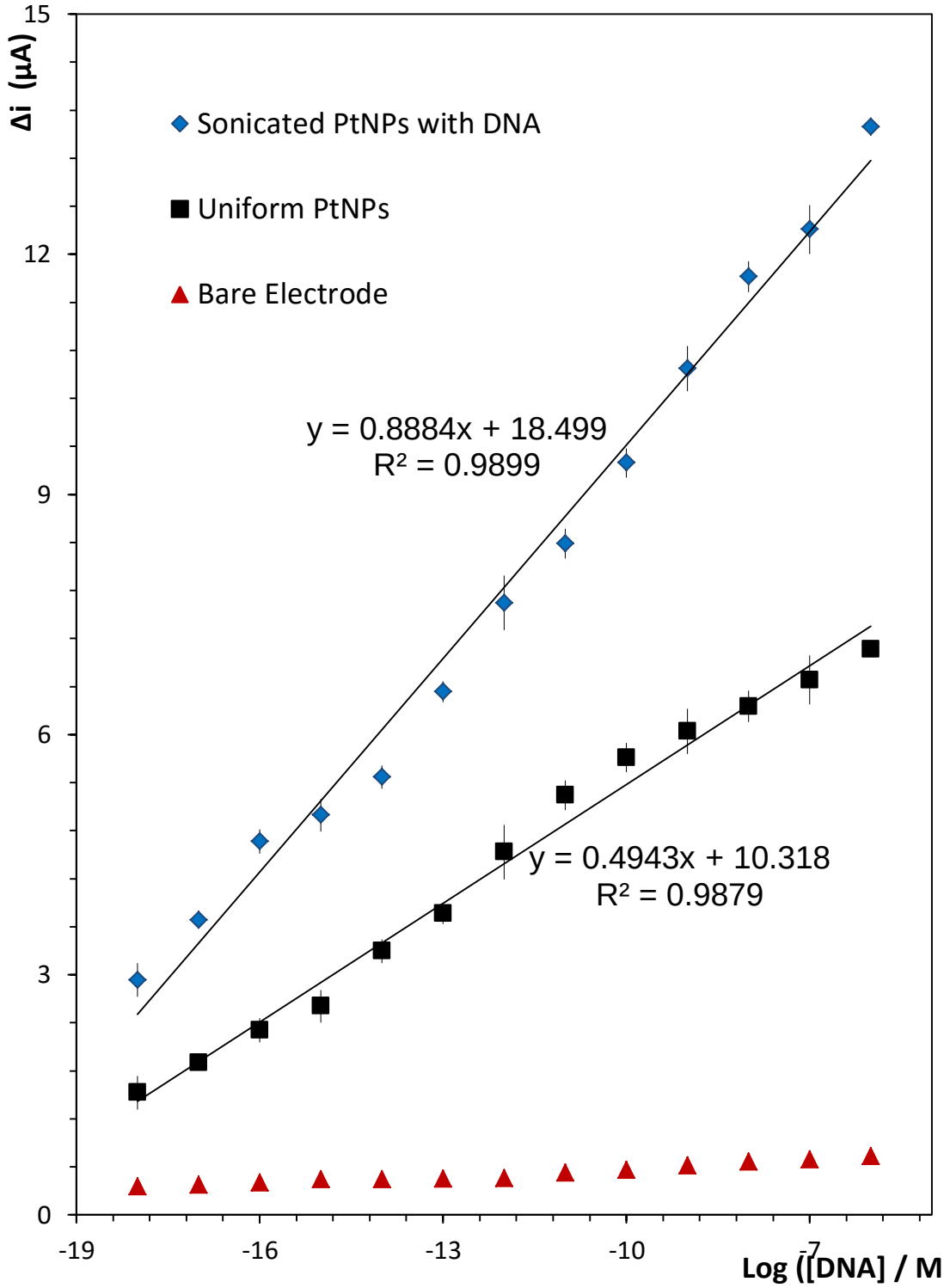

Figure 2.17: Calibration plots for the electrochemical detection of Staph. aureus mastitis DNA on a 2 mm diameter bare electrode following hybridization with probe DNA immobilized regio selectively on PtNPs (♦) and where the probe is unlabelled (▲). A control experiment showing the response of the electrode with uniform PtNPs functionalized with a homogenous full DNA monolayer is also illustrated (■)3 repeats were performed for each experiment. The reference electrode was Ag/AgCl in 3 M KCl.

2.4 Conclusions

The objective of this chapter was the detection of short nucleic acids, suitable for a point of care setting. To achieve this, regio selectively modified PtNPs were produced and used in the subsequent detection of DNA at low concentrations. PtNPs were produced by the electrodeposition of Pt into defects within an alkanethiol monolayer. For the growth of nanoparticles, a monolayer with nanoscale defects was required. A range of monolayer deposition times from 1 to 12 hours was examined using a solution 1mM dodecanethiol. From 1 to 4 hours a highly defective monolayer was formed, as the deposition time was further increased, the available surface are decreased in a manner consistent with increasing order of the monolayer. After 7 hours, the available surface are approached zero. By depositing platinum into defects from 1 to 12 hours it was found that an 8 hour monolayer deposition time with in ethanol gave a monolayer with nanoscale defects that acted as a suitable template.

The optimal deposition potential for the PtNPs was also investigated. Based on the CV of the Pt solution, the potential used during the electrodeposition step was varied between +0.2 V and -0.35 V. At lower potentials, a large amount of platinum was deposited onto the electrode, however SEM images shoed that the vast majority of the platinum was lost from the surface due to hydrogen gas production which mechanically removed the PtNPs. At higher potentials, the reduced driving force allowed for controlled growth of nanoparticles. A deposition potential of +0.1 V was chosen as optimal based on the particle size, monodispersity and yield. The diameter of these particles was 246±71 nm.

Removal of the particles from the working electrode was then investigated. Sonication was investigated based on previous reports of nanoparticles processing and nanoscale mixing using this technique. SEM images of the Au electrode after sonication showed that the vast majority of the PtNPs were successfully removed. Images of the drop cast, desorbed particles showed the particles were still intact, however the size dropped to 79±12 nm suggesting that some preferential enrichment of the smaller particles occurred. This is believed to be due to preferential settling of larger PtNPs in solution, which decreases the average size of the available PtNPs.

After the successful production and release of the PtNPs, the detection of DNA was examined. PtNPs were modified with probe DNA with complimentarily to one end of the DNA target and released into solution. A clean Au electrode was modified with capture DNA complimentary to the opposing end of the DNA target. This capture DNA strand was then hybridized with the DNA target at 37 ºC, and immersed in the PtNP solution. After hybridization of the probe to the target DNA, the presence of Pt was confirmed by CV in dilute sulphuric acid. A distinctive Pt oxidation was apparent at +0.3 V, with peaks in the -0.05 V to -0.3 V range for hydrogen adsorption/desorption. This cyclic voltammetry was believed to be destructive, so electrodes used for CV were not subsequently used for the detection of DNA.

Detection of target DNA was then performed by application of a fixed potential of -0.25 V in H_2SO_4. The system was allowed to equilibrate, and then H_2O_2 was added to give a concentration of 200 µM. The difference in current before and after the addition of hydrogen peroxide was taken as the analytical signal. Detection was possible at as low as 1 aM, with a linear response from 10 pM to 1 µM. Based on a signal to noise ratio of 3:1, the LOD for this assay is 0.1 aM. This extremely low concentration highlights the sensitivity of this approach.

To analyse whether the regio selective PtNPs were more effective that uniformly decorated PtNPs, a second calibration was carried out. The sensitivity of the regio selective PtNPs was significantly higher with 8.8×10^{-2} μA^{-1}, compared with 4.9×10^{-2} μA^{-1} for uniformly decorated particles. This provides good evidence for the successful production of regioselective PtNPs, where one area of the particles is clean, allows for efficient electrocatalysis.

This work contained in the chapter has been published in Electrochimica Acta, and has been included at the end of this thesis.

2.5 References

1. Iorio, M. V.; Visone, R.; Di Leva, G.; Donati, V.; Petrocca, F.; Casalini, P.; Taccioli, C.; Volinia, S.; Liu, C.; Alder, H.; Calin, G. A.; Menard, S.; Croce, C. M. MicroRNA signatures in human ovarian cancer. *Cancer Res.* **2007**, *67*, 8699-8707.

2. Harris, L.; Fritsche, H.; Mennel, R.; Norton, L.; Ravdin, P.; Taube, S.; Somerfield, M. R.; Hayes, D. F.; Bast, R. C., Jr. American society of clinical oncology 2007 update of recommendations for the use of tumor markers in breast cancer. *J. Clin. Oncol.* **2007**, *25*, 5287-5312.

3. Mitchell, P. S.; Parkin, R. K.; Kroh, E. M.; Fritz, B. R.; Wyman, S. K.; Pogosova-Agadjanyan, E. L.; Peterson, A.; Noteboom, J.; O'Briant, K. C.; Allen, A.; Lin, D. W.; Urban, N.; Drescher, C. W.; Knudsen, B. S.; Stirewalt, D. L.; Gentleman, R.; Vessella, R. L.; Nelson, P. S.; Martin, D. B.; Tewari, M. Circulating microRNAs as stable blood-based markers for cancer detection. *Proc. Natl. Acad. Sci. U. S. A.* **2008**, *105*, 10513-10518.

4. Monao, M.; Jensen, P.; Hou, J.; Durham, L.; Major, E. Detection of JC virus DNA in human tonsil tissue: Evidence for site of initial viral infection. *J. Virol.* **1998**, *72*, 9918-9923.

5. Schneider, A.; Kraus, H.; Schuhmann, R.; Gissmann, L. Papillomavirus Infection of the Lower Genital-Tract - Detection of Viral-Dna in Gynecological Swabs. *Int. J. Cancer* **1985**, *35*, 443-448.

6. Blum, H.; Haase, A.; Vyas, G. Molecular Pathogenesis of Hepatitis-B Virus-Infection - Simultaneous Detection of Viral-Dna and Antigens in Paraffin-Embedded Liver Sections. *Lancet* **1984**, *2*, 771-775.

7. Levin, B.; Lieberman, D. A.; McFarland, B.; Andrews, K. S.; Brooks, D.; Bond, J.; Dash, C.; Giardiello, F. M.; Glick, S.; Johnson, D.; Johnson, C. D.; Levin, T. R.; Pickhardt, P. J.; Rex, D. K.; Smith, R. A.; Thorson, A.; Winawer, S. J.; Amer Canc Soc Colorectal Canc Ad; Amer Coll Radiology Colon Canc Screening and surveillance for the early detection of colorectal cancer and adenomatous polyps, 2008: A joint guideline from the American Cancer Society, the US Multi-Society Task Force on Colorectal Cancer, and the American College of Radiology. *Gastroenterology* **2008**, *134*, 1570-1595.

8. Catalona, W.; Richie, J.; Ahmann, F.; Hudson, M.; Scardino, P.; Flanigan, R.; Dekernion, J.; Ratliff, T.; Kavoussi, L.; Dalkin, B.; Waters, W.; Macfarlane, M.; Southwick, P. Comparison of Digital Rectal Examination and Serum Prostate-Specific Antigen in the Early Detection of Prostate-Cancer - Results of a Multicenter Clinical-Trial of 6,630 Men. *J. Urol.* **1994**, *151*, 1283-1290.

9. Frost, J.; Ball, W.; Levin, M.; Tockman, M.; Baker, R.; Carter, D.; Eggleston, J.; Erozan, Y.; Gupta, P.; Khouri, N.; Marsh, B.; Stitik, F. Early Lung-Cancer Detection - Results of the Initial (Prevalence) Radiologic and Cytologic Screening in the Johns-Hopkins-Study. *Am. Rev. Respir. Dis.* **1984**, *130*, 549-554.

10. Bustin, S. Absolute quantification of mRNA using real-time reverse transcription polymerase chain reaction assays. *J. Mol. Endocrinol.* **2000**, *25*, 169-193.

11. Burns, M.; Valdivia, H. Modelling the limit of detection in real-time quantitative PCR. *Eur. Food Res. Technol.* **2008**, *226*, 1513-1524.

12. Bustin, S. A.; Benes, V.; Garson, J. A.; Hellemans, J.; Huggett, J.; Kubista, M.; Mueller, R.; Nolan, T.; Pfaffl, M. W.; Shipley, G. L.; Vandesompele, J.; Wittwer, C. T. The MIQE Guidelines: Minimum Information for Publication of Quantitative Real-Time PCR Experiments. *Clin. Chem.* **2009**, *55*, 611-622.

13. Kwon, S. J.; Bard, A. J. DNA Analysis by Application of Pt Nanoparticle Electrochemical Amplification with Single Label Response. *J. Am. Chem. Soc.* **2012**, *134*, 10777-10779.

14. Polsky, R.; Gill, R.; Kaganovsky, L.; Willner, I. Nucleic acid-functionalized Pt nanoparticles: Catalytic labels for the amplified electrochemical detection of biomolecules. *Anal. Chem.* **2006**, *78*, 2268-2271.

15. Hrapovic, S.; Liu, Y.; Male, K.; Luong, J. Electrochemical biosensing platforms using platinum nanoparticles and carbon nanotubes. *Anal. Chem.* **2004**, *76*, 1083-1088.

16. Markovic, N.; Gasteiger, H.; Ross, P. Oxygen Reduction on Platinum Low-Index Single-Crystal Surfaces in Sulfuric-Acid-Solution - Rotating Ring-Pt(hkl) Disk Studies. *J. Phys. Chem.* **1995**, *99*, 3411-3415.

17. Craig, B. D.; Anderson, D. S.; International, A. *Handbook of Corrosion Data;* ASM International: 1994; .

18. Loweth, C.; Caldwell, W.; Peng, X.; Alivisatos, A.; Schultz, P. DNA-based assembly of gold nanocrystals. *Angew. Chem. -Int. Edit.* **1999**, *38*, 1808-1812.

19. Spain, E.; Miner, B.; Keyes, T. E.; Forster, R. J. Regio selective functionalisation of gold nanoparticles with DNA. *Chem. Commun.* **2012**, *48*, 838-840.

20. Nuzzo, R. G.; Fusco, F. A.; Allara, D. L. Spontaneously Organized Molecular Assemblies .3. Preparation and Properties of Solution Adsorbed Monolayers of Organic Disulfides on Gold Surfaces. *J. Am. Chem. Soc.* **1987**, *109*, 2358-2368.

21. Bain, C.; Troughton, E.; Tao, Y.; Evall, J.; Whitesides, G.; Nuzzo, R. Formation Of Monolayer Films By The Spontaneous Assembly Of Organic Thiols From Solution Onto Gold. *J. Am. Chem. Soc.* **1989**, *111*, 321-335.

22. Liu, H.; Favier, F.; Ng, K.; Zach, M. P.; Penner, R. M. Size-selective electrodeposition of meso-scale metal particles: a general method. *Electrochim. Acta* **2001**, *47*, 671-677.

23. Scharifker, B. R.; Mostany, J. Three-dimensional nucleation with diffusion controlled growth: Part I. Number density of active sites and nucleation rates per site. *Journal of Electroanalytical Chemistry and Interfacial Electrochemistry* **1984**, *177*, 13-23.

24. Kato, H.; Noh, J.; Hara, M.; Kawai, M. An HREELS study of alkanethiol self-assembled monolayers on Au(111). *J Phys Chem B* **2002**, *106*, 9655-9658.

25. Azzaroni, O.; Fonticelli, M.; Benitez, G.; Schilardi, P.; Gago, R.; Caretti, I.; Vazquez, L.; Salvarezza, R. Direct nanopatterning of metal surfaces using self-assembled molecular films. *Adv Mater* **2004**, *16*, 405-+.

26. Allara, D.; Nuzzo, R. Spontaneously Organized Molecular Assemblies .1. Formation, Dynamics, and Physical-Properties of Normal-Alkanoic Acids Adsorbed from Solution on an Oxidized Aluminum Surface. *Langmuir* **1985**, *1*, 45-52.

27. Lavrich, D.; Wetterer, S.; Bernasek, S.; Scoles, G. Physisorption and chemisorption of alkanethiols and alkyl sulfides on Au(111). *J Phys Chem B* **1998**, *102*, 3456-3465.

28. Noh, J.; Hara, M. Molecular-scale desorption processes and the alternating missing-row phase of alkanethiol self-assembled monolayers on Au(111). *Langmuir* **2001**, *17*, 7280-7285.

29. Poirier, G. Mechanism of formation of Au vacancy islands in alkanethiol monolayers on Au(111). *Langmuir* **1997**, *13*, 2019-2026.

30. Vericat, C.; Vela, M.; Salvarezza, R. Self-assembled monolayers of alkanethiols on Au(111): surface structures, defects and dynamics. *Phys. Chem. Chem. Phys.* **2005**, *7*, 3258-3268.

31. Trasatti, s.; petrii, O. Real Surface-Area Measurements in Electrochemistry. *Pure Appl. Chem.* **1991**, *63*, 711-734.

32. Hoogvliet, J.; Dijksma, M.; Kamp, B.; van Bennekom, W. Electrochemical pretreatment of polycrystalline gold electrodes to produce a reproducible surface roughness for self assembly: A study in phosphate buffer pH 7.4. *Anal. Chem.* **2000**, *72*, 2016-2021.

33. Shen, H.; Mark, J.; Seliskar, C.; Mark, H.; Heineman, W. Blocking behavior of self-assembled monolayers on gold electrodes. *J. Solid State Electrochem.* **1997**, *1*, 148-154.

34. Bard, A. J.; Faulkner, L. R. In *Electrochemical Methods: Fundamentals and Applications;* Wiley: 1980; pp 718.

35. Miranda-Hernández, M.; Palomar-Pardavé, M.; Batina, N.; González, I. Identification of different silver nucleation processes on vitreous carbon surfaces from an ammonia electrolytic bath. *J Electroanal Chem* **1998**, *443*, 81-93.

36. Spain, E.; McArdle, H.; Keyes, T. E.; Forster, R. J. Detection of sub-femtomolar DNA based on double potential electrodeposition of electrocatalytic platinum nanoparticles. *Analyst* **2013**, *138*, 4340-4344.

37. Sanganwar, G. P.; Gupta, R. B. Nano-mixing of dipyridamole drug and excipient nanoparticles by sonication in liquid CO2. *Powder Technology* **2009**, *196*, 36-49.

38. Niesz, K.; Morse, D. E. Sonication-accelerated catalytic synthesis of oxide nanoparticles. *Nano Today* **2010**, *5*, 99-105.

39. Kim, Y. -.; Jun, G. K.; Lim, S. -.; Jae, H. S. Facile synthesis of monodispersed PdO nanoparticles within mesoporous silica with sonication. *Bulletin of the Korean Chemical Society* **2005**, *26*, 1129-1131.

40. Ma, X.; Shen, Y.; Wu, G.; Wu, Q.; Pei, B.; Cao, M.; Gu, F. Sonication-assisted sequential chemical bath deposition of CdS nanoparticles into TiO2 nanotube arrays for application in solar cells. *J. Alloys Compounds* **2012**, *538*, 61-65.

41. Zhang, G. Q.; Wu, H. P.; Ge, M. Y.; Jiang, Q. K.; Chen, L. Y.; Yao, J. M. Ultrasonic-assisted preparation of monodisperse iron oxide nanoparticles. *Mater Lett* **2007**, *61*, 2204-2207.

42. Basarir, F.; Yoon, T. Sonication-assisted layer-by-layer deposition of gold nanoparticles for highly conductive gold patterns. *Ultrason. Sonochem.* **2012**, *19*, 621-626.

43. Whitney, A.; Elam, J.; Zou, S.; Zinovev, A.; Stair, P.; Schatz, G.; Van Duyne, R. Localized surface plasmon resonance nanosensor: A high-resolution distance-dependence study using atomic layer deposition. *J Phys Chem B* **2005**, *109*, 20522-20528.

44. Haes, A.; Zhao, J.; Zou, S.; Own, C.; Marks, L.; Schatz, G.; Van Duyne, R. Solution-phase, triangular Ag nanotriangles fabricated by nanosphere lithography. *J Phys Chem B* **2005**, *109*, 11158-11162.

45. Herne, T.; Tarlov, M. Characterization of DNA probes immobilized on gold surfaces. *J. Am. Chem. Soc.* **1997**, *119*, 8916-8920.

46. Steel, A.; Herne, T.; Tarlov, M. Electrochemical quantitation of DNA immobilized on gold. *Anal. Chem.* **1998**, *70*, 4670-4677.

47. Demers, L.; Mirkin, C.; Mucic, R.; Reynolds, R.; Letsinger, R.; Elghanian, R.; Viswanadham, G. A fluorescence-based method for determining the surface coverage and hybridization efficiency of thiol-capped oligonucleotides bound to gold thin films and nanoparticles. *Anal. Chem.* **2000**, *72*, 5535-5541.

48. SantaLucia, J.; Hicks, D. The thermodynamics of DNA structural motifs. *Annu. Rev. Biophys. Biomol. Struct.* **2004**, *33*, 415-440.

49. Wallace, R.; Shaffer, J.; Murphy, R.; Bonner, J.; Hirose, T.; Itakura, K. Hybridization of Synthetic Oligodeoxyribonucleotides to Phi-Chi-174 Dna - Effect of Single Base Pair Mismatch. *Nucleic Acids Res.* **1979**, *6*, 3543-3557.

50. Rychlik, W.; Spencer, W.; Rhoads, R. Optimization of the Annealing Temperature for Dna Amplification Invitro. *Nucleic Acids Res.* **1990**, *18*, 6409-6412.

51. You, T.; Niwa, O.; Tomita, M.; Hirono, S. Characterization of platinum nanoparticle-embedded carbon film electrode and its detection of hydrogen peroxide. *Anal. Chem.* **2003**, *75*, 2080-2085.

52. Kolthoff, I.; Jordan, J. Oxygen Induced Electroreduction of Hydrogen Peroxide and Reduction of Oxygen at the Rotated Gold Wire Electrode. *J. Am. Chem. Soc.* **1952**, *74*, 4801-4805.

53. El-Deab, M.; Ohsaka, T. An extraordinary electrocatalytic reduction of oxygen on gold nanoparticles-electrodeposited gold electrodes. *Electrochem. Commun.* **2002**, *4*, 288-292.

CHAPTER 3

Photophysical Characterisation of 6-FAM and Dabcyl for Detection of miR-132 Using a Molecular Beacon

3.1 Introduction

Live cell imaging of miRNAs allows for the analysis and visualisation of miRNA expression levels within cells. This can potentially aid in the identification of cancerous cells, and provide information on the specific cancer subtype. This type of analysis is particularly important as it can provide rapid results with very small volumes of cells, which minimises the impact to the patient.

Molecular beacons (MB) are a method of examining cellular miRNA concentration based on the strong recognition of complimentary nucleic acids.[1,2] In a MB, a strand of nucleic acid complimentary to the target of interest is produced. This strand is produced with a four to six base overhang with complementarity to bases on the opposing end of the strand. The strand is also modified with a dye molecule and a quencher. When the target is absent, self-binding of the MB occurs. This brings the dye and quencher molecules into close proximity. Forster resonance energy transfer (FRET) then allows transfer of the excited state from the dye to the quencher which "switches off" emission of the dye. This method benefits low background, since the dye should be non-emissive in the absence of the target. By varying the length of the self-complimentary region of the MB, the sensitivity and selectivity can be adjusted.[3]

In order to accurately determine the localisation and concentration of miRNA in live cells, the environmental impacts on the dye and quencher molecules must be fully characterised. Within a live cell, the pH can vary greatly. With the intercellular fluid of the cell is generally in the region of pH 7.2, some areas of the cell can be significantly different. Lysosomes can have a pH as low as 4.7[4], whereas the mitochondria are pH 8.0[5].

As illustrated in Figure 3.1, the main objective of this work was to determine the extent of localisation and concentration of miR-132 in live cells. To achieve this goal a MB was constructed using 6-carboxyfluorescein (6-FAM), a targeting strand of nucleic acid and a dabcyl quencher molecule. Solution phase testing of the dye was carried out to fully characterise the impact of environmental factors on the properties of the dye, for example the emission intensity.

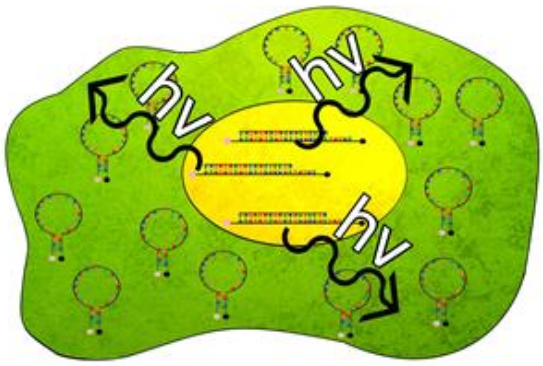

Figure 3.1: Cartoon of the cell containing MB for the detection of miR-132.

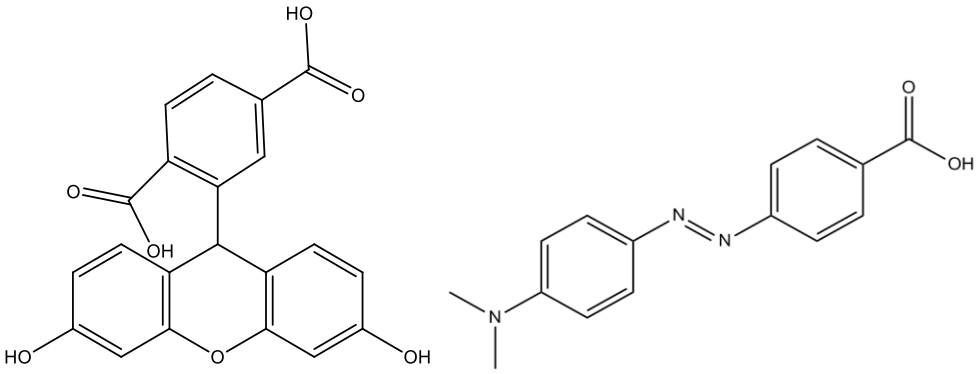

Figure 3.2: Structure of 6-FAM (left), and Dabcyl (right).

Figure 3.2 shows the structure of the fluorescein dye and dabcyl quencher. It is important to note that while the structures above were incorporated into the final MB, they were modified by attachment to the nucleic acid (NA) strand. The 6-FAM contains only a single carboxylic acid group in the MB, and the Dabcyl contains no free carboxylic acid group in the final MB.

The 6-FAM dye was found to have significant sensitivity to changes in the polarity of the solvent and the pH environment, both causing significant changes to the intensity of the dye. The concentration dependent self-quenching of the dye and the ability of the dabcyl quencher were investigated. The introduction of the 6-FAM dye to a neuroblastoma cell line was also investigated. Passive uptake of the dye was not observed, even with the addition of permeabilizing agents. The efficiency of electroporation of the dye into the cells was investigated as well as its effect on the cell viability.

3.2 Experimental

3.2.1 Materials

6-Carboxylfluorisin (6-FAM) was purchased from Sigma Aldrich at ≥97 % purity as determined by HPLC. 4-([4-(Dimethylamino)phenyl]-azo)-benzoic acid (Dabycl) was purchased from Sigma Aldrich at ≥90 % purity as determined by HPLC. Phosphate buffered saline (PBS) was prepared at a phosphate buffer concentration of 0.01 M and a sodium chloride concentration of 0.154 M using PBS tablets (Sigma Aldrich) in RNase free water.

Nucleic acids were synthesised by Exiqon at 85 % purity.

Molecular Beacon: 5'-6FAM+CGA+CCA+TGG+CTG+TAG+ACT+GTT+AGT+CG-DAB-3' (DNA/ LNA where the + is a Locked Nucleic Acid) In the absence of target, the 5' 6-Carboxyfluorescein (6FAM) was held in close proximity to the 3' Dabcyl, 4-((4-(dimethylamino)phenyl)azo)benzoic acid (DAB)

3.2.2 Emission Spectroscopy

Emission spectrums were obtained using a Jasco V-670. Emission and excitation slits were typically 20 nm. Solvents used were 1 % DMSO in PBS unless otherwise stated.

3.2.3 Time Correlated Single Photon Counting

Lifetime results were determined using a PicoQuant Fluotime 100 TCSPC system with excitation at 450 nm. In each case, an instrument response function (IRF) was collected using ludox AM 30 colloidal silica solution (Sigma Aldrich), and the lifetime was fitted by using an exponential model with reconvolution, whereby the IRF contribution to the signal is subtracted. Data was fitted to a single exponential providing it gave a good quality fit, i.e. a χ^2 value of below 1.2 and no systematic residual. Where this was not possible, two exponentials were fitted to the data.

The model used for performing multi exponential reconvolution fits was:

$$I(t) = \int_{-\infty}^{t} IRF(t') \sum_{i=1}^{n} A_i \, e^{-\frac{t-t'}{\tau_i}} \, dt'$$

Equation 3.1: Lifetime fitting

Where A_i = Amplitude of the i^{th} component in counts at time 0.

τ_i = Lifetime of the i^{th} component

3.2.4 Cell Culture

The adherent human neuroblastoma cell line, SK-N-AS, was obtained from the American Type Culture Collection (ATCC). The cells were cultured in Minimum Essential Media, with 10 % foetal bovine serum, 0.5 % L-glutamine and 0.5 % non-essential amino acids, with 100 µg/mL Gentamicin at 37 ˚C and 5 % CO_2.

The cells were split at three day intervals, and seeded at a ratio of 1:3. Prior to splitting, the cells were rinsed with 5 mL of PBS. 1mL of trypsin was added over a five minute period. Approximately 5 mL of cell culture media was then added to neutralise the trypsin. 2 mL of this solution was then added to a new cell culture flask with 8 mL of media. The mixture was gently mixed by pipetting and replaced in the incubator.

3.2.5 Imaging

Cellular imaging was performed using a Zeiss LSM 510 confocal microscope, which was used for dye visualisation, with an argon ion laser at 458 nm and with an LP560 nm filter at 6 % for 6-FAM. For DRAQ-7 a HeNe laser at 633 nm with an LP650 nm filter at 100 % was used. A 63 x oil emersion objective lens (NA 1.4) was used, with a further 4 x zoom obtained using the scanning software. Experiments were run for periods of up to 60 minutes.

3.2.6 Electroporation

Prior to experiments with the MB, the ability to deliver the 6-FAM dye into live cells by electroporation was investigated. A technical bulletin from Bio-Rad "Transfection of Neuroblastoma Cell Lines Using the Gene Pulser MCcell Electroporation System" was used as a starting point for the method development. The parameters initially used were a cell density of 3 x 10^6 cells per mL, square wave pulse of 200 V peak amplitude and 20 ms pulse width. An electroporation cuvette (Sigma Aldrich) with a 0.2 cm gap was used for all experiments.

Electroporation experiments were performed using the Bio-Rad GenePulser Xcell. Cells were incubated for 48 hours, which achieved approximately 75 % confluency. Cells were then rinsed with PBS three times to remove the media, and trypsinised for 10 minutes. Cells were then resuspended in 1 mL of media, and counted using a haemocytometer. Cells were diluted to achieve a cell density of 3 x 10^6 cells per mL. 400 µL of this suspension was loaded into an electroporation cuvette. 6-FAM was added to achieve a concentration of 50 µM. The cuvette was then placed in the Bio-Rad GenePulser Xcell and electroporated as previously described. The cells were then immediately transferred to a cell culture dish, post electroporation, and media was added to bring the final volume to 2 mL. The cells were then incubated for 24 hours. This allowed the cells which survived the procedure to attach to the surface. Cells were then imaged by confocal microscopy to determine viability.

3.3 Results and Discussion

3.3.1 6-Carboxyfluorescein

The photophysics of 6-carboxyfluorescein (6-FAM) were investigated to determine its suitability for use as part of a MB biosensor. It contains a fluorescein molecule with an additional carboxylic acid group. This COOH provides the attachment point for a targeting moiety, i.e., a nucleic acid sequence. Fluorescein has an exceptional quantum yield of 95 %[6], reasonable photostability[7], and has high compatibility with the 488 nm argon laser line[8]. Fluorescein derivatives have been used extensively for the detection of nucleic acids.[9,10,11,12]

Figure 3.3 shows the absorption and emission spectra for 10 µM 6-FAM in 1 % DMSO and PBS. The maximum absorbance was found at 491 nm, which closely matches the literature value of 492 nm in 0.1 N NaOH[13]. A shoulder is visible at approximately 460 nm, this may be due to the protonation state of the dye which is discussed later.

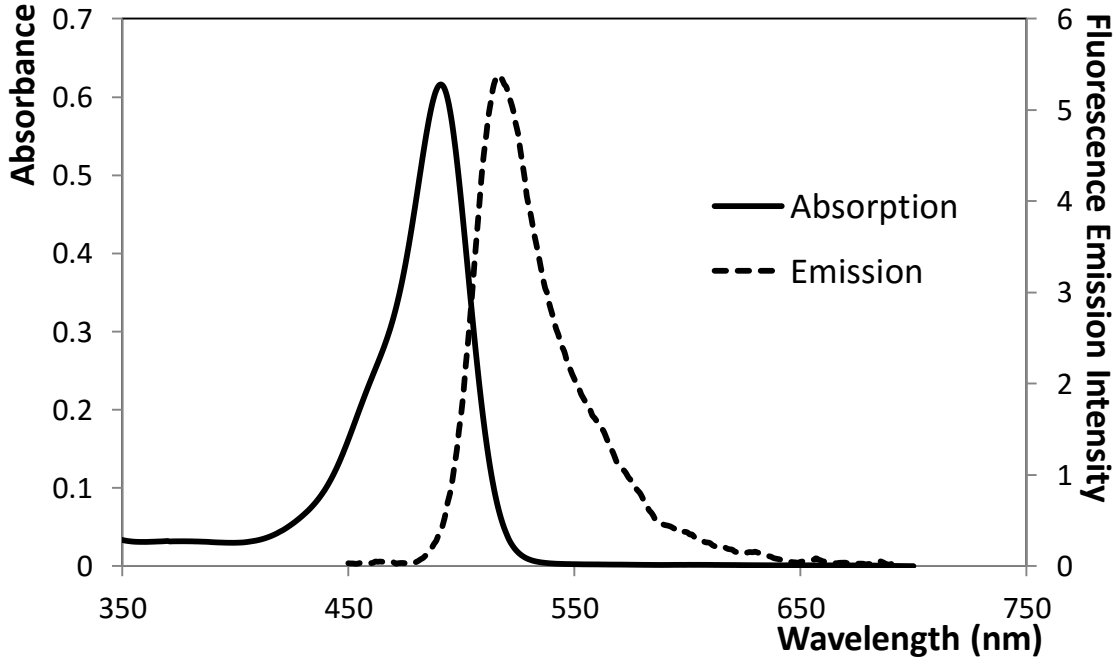

Figure 3.3: Absorbance and emission spectra of 10 µM 6-FAM in 1 % DMSO with PBS. Excitation at 395 nm with excitation and emission slits at 2.5 nm.

3.3.2 Solubility Effects

In order to examine environmental impacts on 6-FAM, a solvent study was carried out. The dye is poorly soluble in water, and so ethanol (ε=24.5) and DMSO (ε=46.7) were investigated. The 6-FAM was highly soluble in both solvents. In ethanol, a strong colour was observed after the addition of the dye, whereas in DMSO the colour was less intense. Figure 3.4 shows the absorption spectra for 10 µM solutions in these two solvents. No absorbance is observed in DMSO at this concentration.

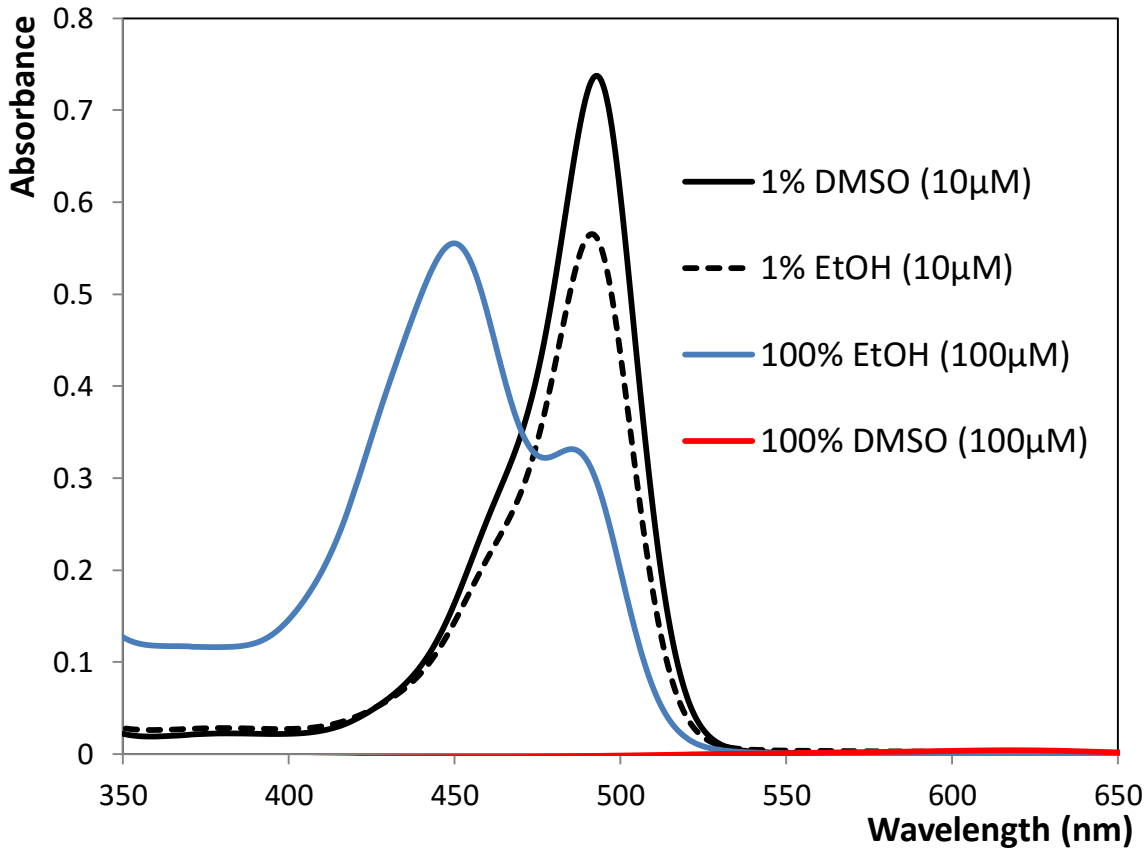

Figure 3.4: Absorption spectra for 100 µM 6-FAM in DMSO and ethanol 10 µM 1 % DMSO in PBS and 1 % EtOH in PBS.

However, since the purpose of further work was live cell imaging and RNA analysis, a pure organic solvent was not appropriate. It was found that by first dissolving the 6-FAM in either DMSO or EtOH, and then diluting in water to give a 1 % organic solvent system, a stable solution was achieved. To maintain a controlled pH, PBS was used instead of pure water. When the dye in DMSO was added to water, a very strong colour was observed compared to the stock. Previous studies of fluorescein have shown that at concentrations of higher that 1 % in DMSO, significant quenching of the fluorescent

signal occurs due to rapid relaxation of the excited state due to H-bonding with the solvent.[14]

Figure 3.4 shows the absorption spectra of a 1 % solution of 10 µM 6-FAM with DMSO or EtOH in PBS and reveals that the absorbance is significantly larger than in the pure solvent. The absorbance of the 1 % DMSO solution was greater than that displayed in the 1 % EtOH solution. In each case, the dye was fully dissolved with no particulate matter visible after centrifugation, so this effect is not due to incomplete dissolution. These spectral changes in different solvent systems suggest that the dye is environmentally sensitive, which may be problematic for miRNA quantitation in live cells. Fluorescein has been show previously to be sensitive to the polarity of the solvent used, showing higher intensities in more polar solvents.[15] The results obtained here are consistent with the previous reports, with the relatively non-polar DMSO displaying the smallest signal, the somewhat polar EtOH displaying a slightly higher signal, and polar water showing the highest signal.

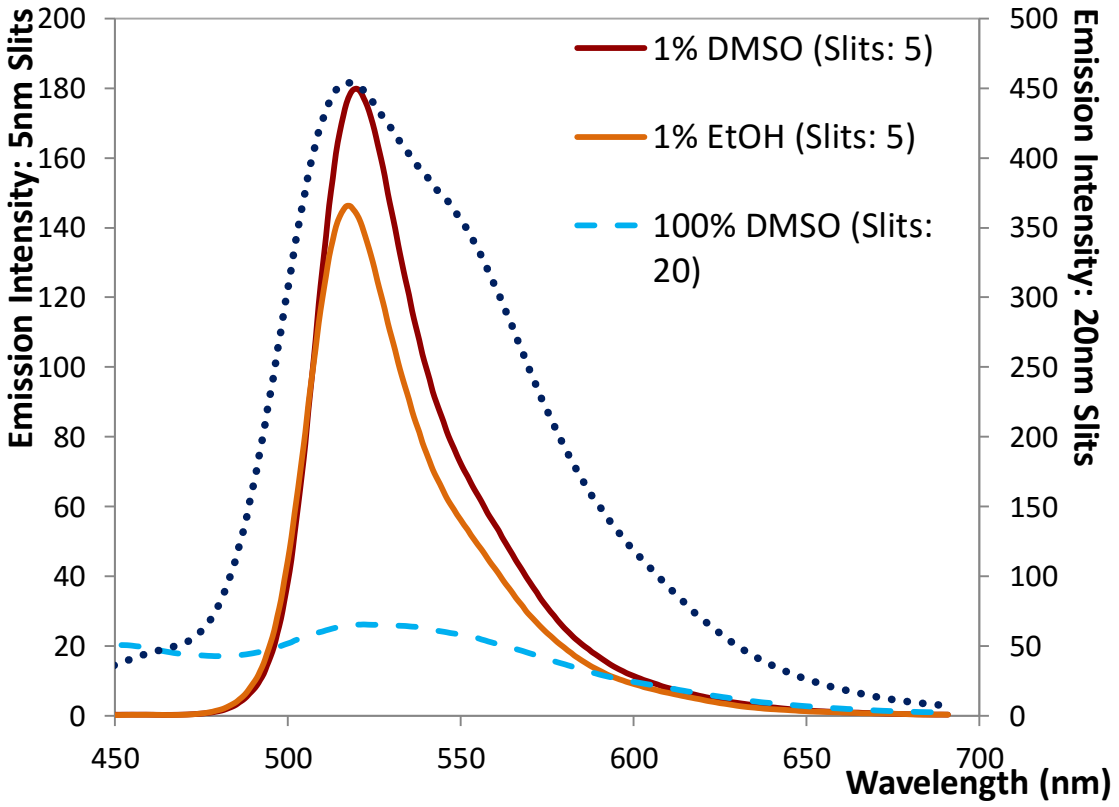

Figure 3.5: Emission spectra of 10 µM 6-FAM after excitation at 395 nm. 1 % DMSO and 1 % EtOH in PBS with 5 nm excitation and emission slits. 100 % DMSO and 100 % EtOH with 20 nm excitation and emission slits.

Figure 3.5 shows the emission spectra for these solutions. As seen in the absorption spectra, where DMSO had a negligible absorbance, the emission spectrum for this solution is also undetectable at this concentration. The water containing solutions have significantly higher intensities, with a more than 10 fold enhancement from 100 % ethanol to 1 % ethanol which agrees with the increase in absorbance. The shape of the 1 % DMSO and 1 % EtOH responses are similar, with a primary peak at approximately 515 nm and a secondary shoulder peak around 550 nm. The 100 % EtOH spectrum shows two peaks of similar intensity.

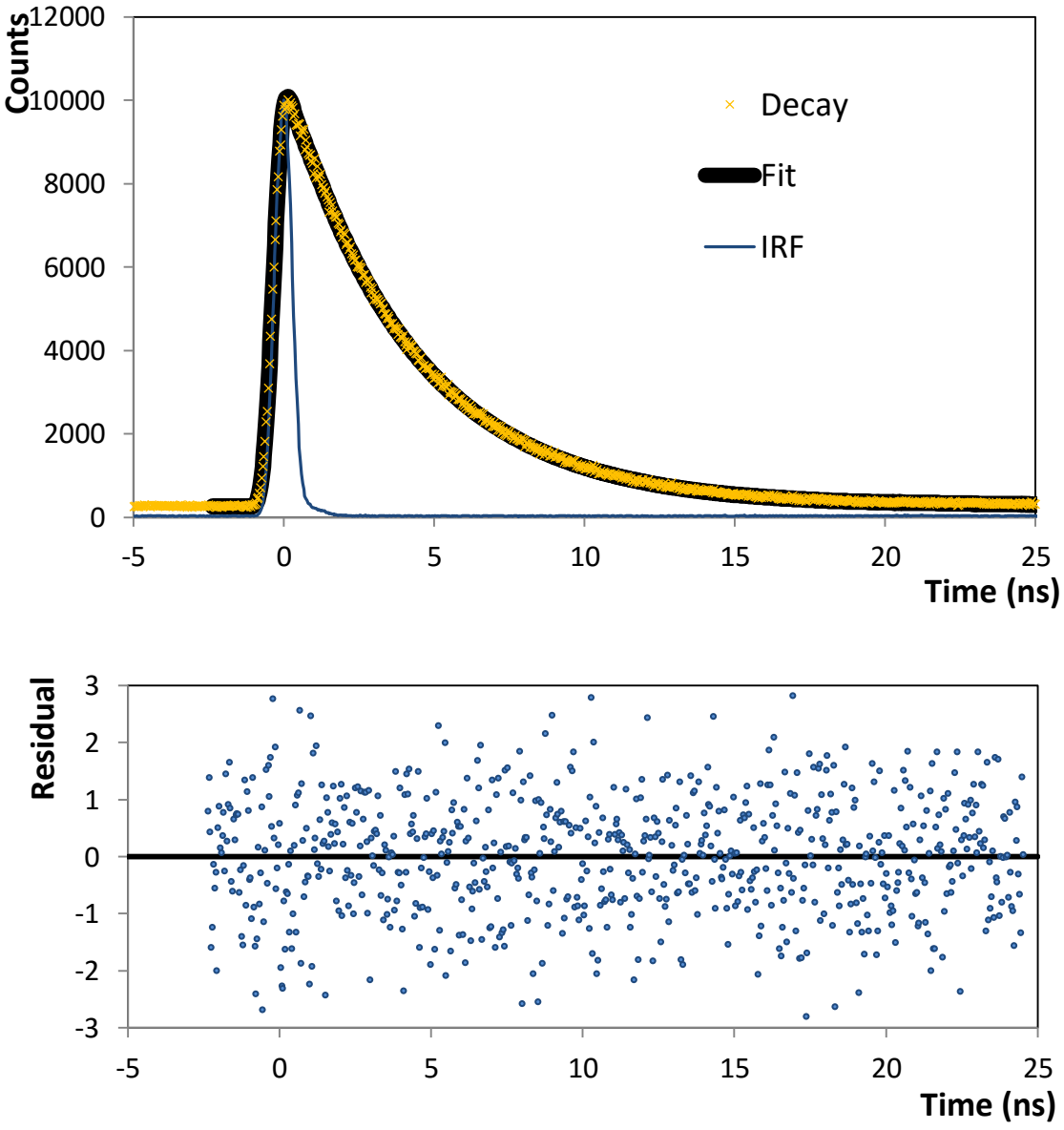

Figure 3.6: Time correlated single photon counting lifetime for 10 µM 6-FAM in 1 % DMSO in PBS with single exponential decay fit (top) and residual plot (bottom).

Table 3.1: Showing the time correlated single photon counting lifetime for 10 µM 6-FAM in DMSO, ethanol, 1 % DMSO in PBS and 1 % ethanol in PBS (n=3).

	Lifetime (ns)	χ^2
100 % DMSO	2.5±0.4	1.02±0.07
1 % DMSO	4.1±0.0	1.07±0.02
100 %EtOH	4.3±0.3	1.22±0.12
1 % EtOH	4.1±0.0	1.14±0.09

Figure 3.6 shows a representative fit to the TCSPC data for the lifetime determination. In this case, a single exponential provided a high quality fit, with a high degree of agreement between the decay and fitted exponential. The residual plot shows an even distribution over the analysed range, suggesting that a single exponential is sufficient to describe this decay. Table 2.1 shows the lifetimes of 6-FAM in each of the solvent mixtures analysed. The 1 % DMSO, 1 % EtOH and 100 % EtOH show similar lifetimes of 4.2±0.2 ns. The 100 % DMSO is significantly shorter, at 2.5±0.4 ns, which is consistent with the lower emission intensity observed.

Overall, the DMSO emission intensity and lifetime are significantly lower than in water containing solvent systems. One possible explanation for these results is that dimerisation of the dye in the ground state is mediated by the solvent, with DMSO promoting this self-association. Another possibility is that the excited state is coupled to the vibrational modes of the solvent causing more rapid destabilisation of the excited state. Based on previous reports[15], the latter mechanism is considered more likely.

This data also suggests that the dye has significant environmental sensitivity, with DMSO and ethanol causing significant changes in both the absorption and emission spectra. This may be an issue for cellular imaging, as the various environments of the cell can have significantly different properties. To further examine the environmental effects on the 6-FAM dye, the effects of pH on the dye were examined since different regions of the cells can have somewhat different pH values.

3.3.3 pH Study

The pH within a cell can vary significantly, while the intercellular fluid is generally pH ~7.2[5], some organelles can be significantly different, with mitochondria at pH 8.0[16] and lysosomes as low as 4.7[4]. Fluorescein is known to be pH sensitive, being used previously as a pH sensor[17,18,18]. Fluorescein contains a number of different pH dependent forms, see Figure 3.7, with only two of the forms contributing to a fluorescent signal[19]. The monoanion form emits near 450 nm while the dianion form emits at 495 nm. 6-FAM is structurally similar to fluorescein.

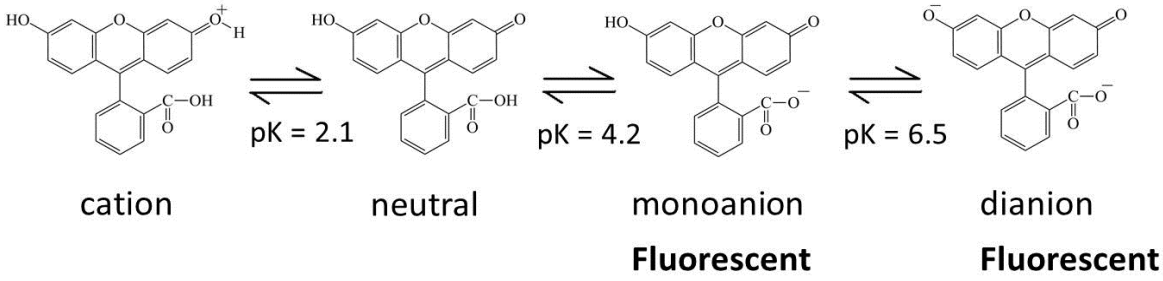

Figure 3.7: pH dependent ionisation of fluorescein.

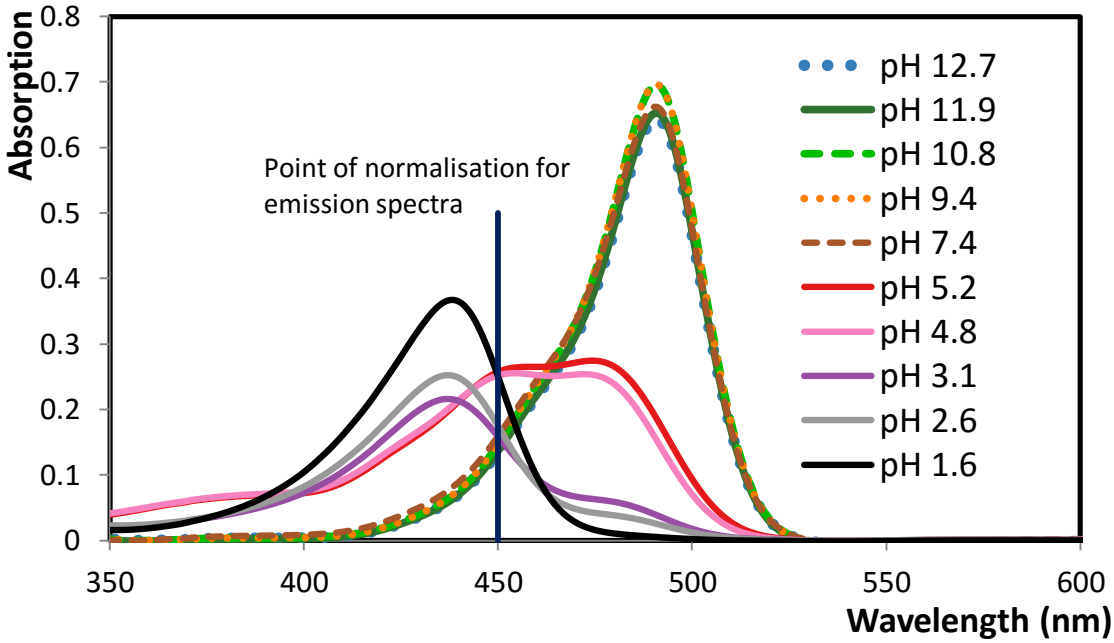

Figure 3.8: Absorbance spectra for a range of pH adjusted samples of 10 µM 6-FAM in 1 % DMSO and PBS, at a starting pH of 7.4, adjusted with NaOH and HCl.

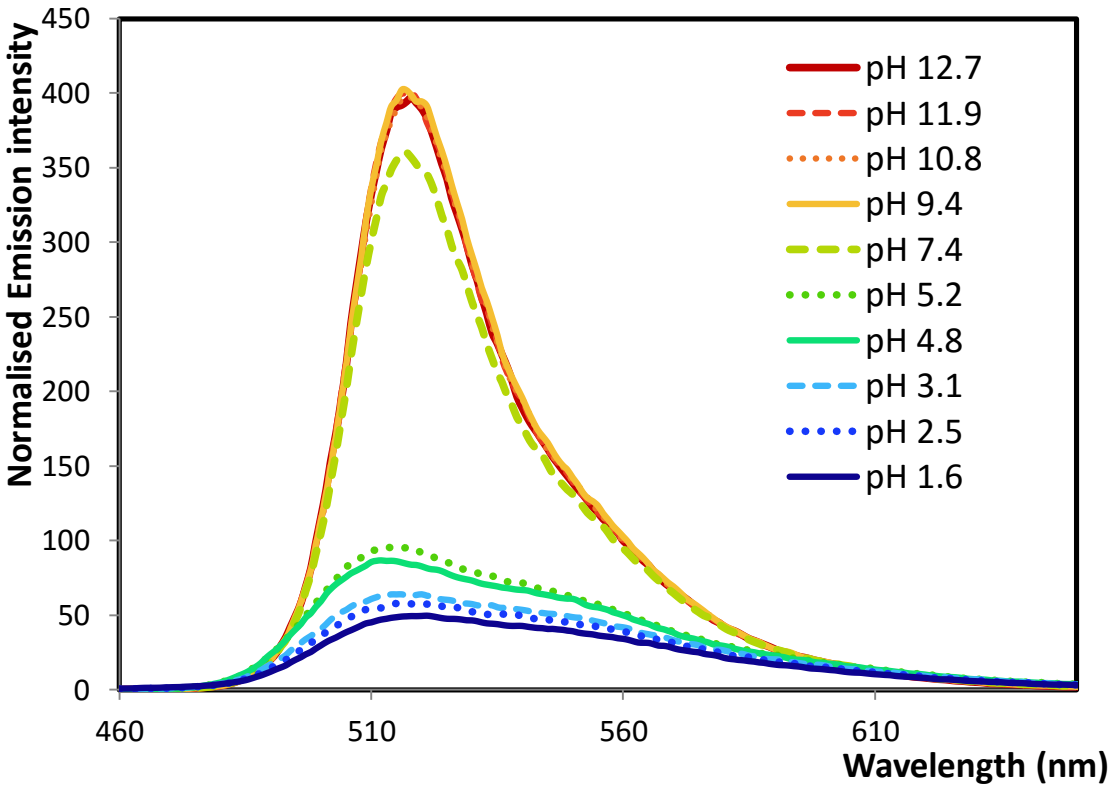

Figure 3.9: Emission spectra for a range of pH adjusted samples of 10 µM 6-FAM in 1 % DMSO and PBS, normalised for absorption at 450 nm. Excitation at 450 nm with excitation slit 2.5 nm and emission slit 5 nm, at a starting pH of 7.4, adjusted with NaOH and HCl.

A solution of 10 µM 6-FAM with 1 % DMSO in PBS was prepared and the pH adjusted using HCl and NaOH solutions. The initial pH in PBS was 7.4, the pH was then adjusted up and down from this point, with fresh solutions used to collect data for the acidic and basic ranges. Figure 3.8 shows the absorbance spectra for this experiment. At pH 7.4 a primary peak is observed with max absorbance at 495 nm with a shoulder visible at approximately 460 nm. As the pH is increased, this shoulder becomes less pronounced, and the intensity of the primary peak is enhanced to 0.68 at pH 12.7. The acidic pH range causes much more significant changes to the absorption peak shape and intensity. At pH 5.2, the intensity of the primary absorption peak at 495 nm is significantly decreased from 0.56 at pH 7.4 to 0.26 at pH 5.2, and the shoulder peak at approximately 450 nm is enhanced from 0.2 to 0.25. As the pH is decreased further to pH 3.1, a peak at 440 nm becomes dominant, and the 495 nm peak continues to decrease in size. This 440 nm peak continues to increase in absorbance, up to a maximum of 0.35 at pH 1.6.

Fluorescein has an isosbestic point at 460 nm where the absorbance at all pH values is equal, however 6-FAM does not show a sharp isosbestic point. A number of the absorbance spectra converge at approximately 450 nm, however the spectra for pH 1.6, 4.8 and 5.2 deviate significantly. To minimise the effect of pH induced changes, the emission spectra were recorded using excitation at 450 nm. The emission spectra were then numerically normalised based on the absorbance value at 450 nm to allow for an accurate comparison.

Figure 3.9 shows the emission spectra for the pH range. The max intensity at pH 7.4 is at 513 nm, and a slight shoulder is seen at approximately 560 nm. As the pH is increased the maximum emission increases from 340 A.U. at pH 7.4 up to 380 A.U. at pH 9.4. As the pH is further increased no significant change to the peak shape or intensity is observed. This is in keeping with the absorption data, with little change observed in the 495 nm absorption peak as pH increases. This behaviour is strongly reminiscent of fluorescein.

Conversion between 6-FAM in the monoanion and dianion form can be described as

$$HA \rightarrow A^- + H^+$$ *Equation 3.2: Acid dissociation*

$$K_a = \frac{[A^-][H^+]}{[HA]}$$ *Equation 3.3: Association constant*

where HA represents the monoanion form and A^- represents the dianion form. The pK_a of 6-FAM is 6.45[20], which corresponds to a K_a of approximately 2.8×10^6. At a pH of 7.4, the $[H^+]$ is 2.5×10^7 M. Based on Equation 3.2 it can be calculated that approximately 90 % of the dye is in the dianion form, with 10 % in the monoanion form. When the pH is further increased, the remaining monoanion is converted to dianion, and the maximum possible emission intensity is then observed.

In the absorption spectrum, the acid range caused significant change to the peak shapes and intensities, and this is reflected in the emission spectra. When the pH is decreased from pH 7.4 to pH 5.2, the emission intensity drops from 340 to 96 A.U. The absorption spectra also show a similar change from 0.56 to 0.14 at 495 nm. The peak shape is also affected, with a shoulder peak at 560 nm then becoming visible. When the pH is decreased the emission intensity drops further from 98 A.U. at pH 5.2 to 56 A.U. at pH 2.5, and this is also reflected in the absorption spectra at 495 nm as a drop from 0.14 to 0.02 occurs.

These results again closely match fluorescein. As the pH is decreased, the monoanion becomes favoured over the dianion, causing both the absorption and emission peaks to change shape. As the pH is further lowered, the non-fluorescent forms of the dye become more prevalent, which causes a decrease in emission intensity.

Table 3.2: Lifetime data based on 3 repeats for a range of pH adjusted samples of 10 µM 6-FAM in 1 % DMSO and PBS, at a starting pH of 7.4, adjusted with NaOH and HCl.

Sample	**Lifetime t_1**	**χ^2**
pH 1.6	2.3 ± 0.0	1.07 ± 0.08
pH 2.6	2.6 ± 0.0	1.09 ± 0.05
pH 3.1	2.8 ± 0.0	1.10 ± 0.06
pH 4.8	3.3 ± 0.0	1.09 ± 0.06
pH 5.2	3.3 ± 0.0	1.03 ± 0.05
pH 7.4	4.1 ± 0.0	1.08 ± 0.06
pH 8.4	4.0 ± 0.0	1.13 ± 0.02
pH 9.4	4.0 ± 0.0	1.11 ± 0.00
pH 10.8	4.2 ± 0.0	1.12 ± 0.02
pH 11.9	4.1 ± 0.0	1.12 ± 0.01
pH 12.7	4.2 ± 0.0	1.07 ± 0.06

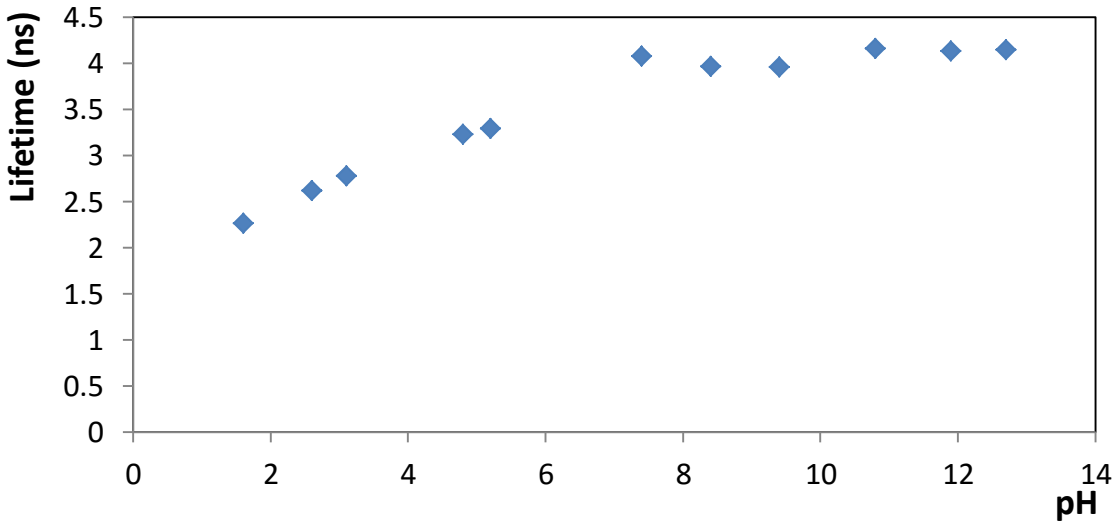

Figure 3.10: Lifetime data for a range of pH adjusted samples of 10 µM 6-FAM in 1 % DMSO and PBS, at a starting pH of 7.4, adjusted with NaOH and HCl. Lifetimes are reproducible to within 2 %. Error bars present but not visible.

Table 3.2 shows the TCSPC lifetime results for this pH range. All of these lifetimes could be fitted to a single exponential. At pH 7.4 the lifetime is 4.1±0.0 ns. As the pH is increased, this value remains unchanged. The acidic pH range caused a measurable drop in the lifetime of the dye, from 4.1±0.0 ns at pH 7.4, to 3.3±0.0 ns at pH 5.2. This reflects the significant peak changes seen in the absorption spectra with the monoanion becoming favoured over the dianion. As this pH is further decreased to 2.6, the lifetime drops to 2.6±0.0 ns. This pH induced change agrees with the absorption spectra, see Figure 3.8, which shows the monoanion form at 440 nm becoming the primary peak at pH 3.1 and below, with a significant reduction in the dianion peak at 495 nm.

Overall, the TCSPC data suggests that the ionic state of the dye has a significant impact on the lifetime of the dye, with the dianion form having a longer lifetime of approximately 4.0 ns, and the monoanion form having a significantly shorter lifetime of approximately 2.6 ns. This again underlines the pH sensitivity of the dye.

The pH sensitivity of the dye is potentially an issue for the detection of the miRNA target if it occurs in different regions of the cells due to variations occurring in cellular pH values. A second issue for consideration is the effect of dye concentration on the emission intensity. For example at high concentrations the small stokes shift could lead to trivial quenching and a lower emission intensity that would be interpreted incorrectly as arising from a low miR-132 concentration.

Concentration Study

The effect of changes in concentration on the absorption and emission spectra were examined. Figure 3.11 shows the emission spectra for a range of concentrations from 10 µM to 1000 µM. A linear enhancement in intensity is observed from 10 µM up to 50 µM, after which the rate of increase in intensity begins to level off, as shown in Figure 3.12. This data agrees with previous work which has shown that 6-FAM self-quenches via trivial quenching and dimerisation at higher concentrations[20].

Of note here is the shift in the peak maximum, which changes significantly with concentration, as shown in Table 2.3. At the 10 µM concentration, the position of maximum intensity is at 515 nm, and this value increases with the concentration up to 536 nm at 1000 µM. It is possible that this change is caused by FRET, with the dye molecules which would emit at an apparently lower wavelength having a spectral overlap with the 6-FAM absorption spectra causing a shift in the apparent maximum emission position. This process becomes more likely to occur as the concentration increases. The shape of the emission spectrum also changes with a greatly diminished signal below 518 nm at 500 µM and 1000 µM.

Figure 3.13 shows the absorption spectra for these samples. At concentrations above 10 µM, the absorbance values measured were above 1, and therefore this data cannot be accurately analysed as this data violates the Beer-Lambert law.

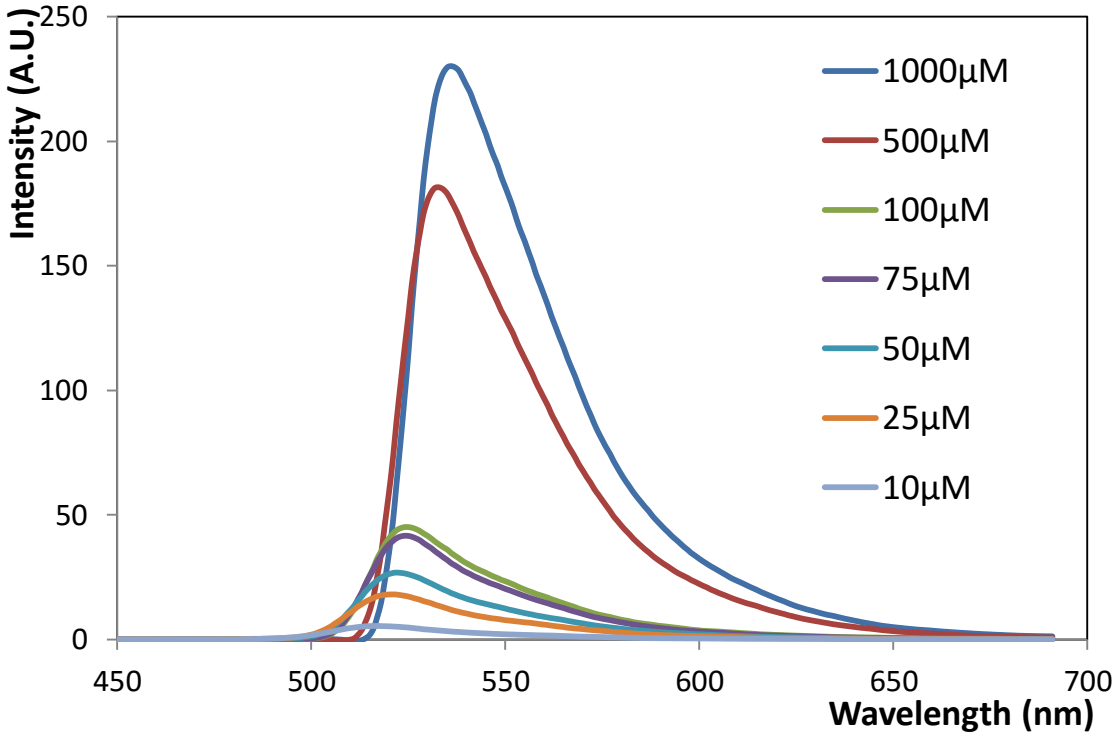

Figure 3.11: Emission spectra of 6-FAM in 1 % DMSO with PBS from 10 µM to 1000 µM after excitation at 395 nm with excitation slit at 2.5 nm and emission slit at 2.5 nm.

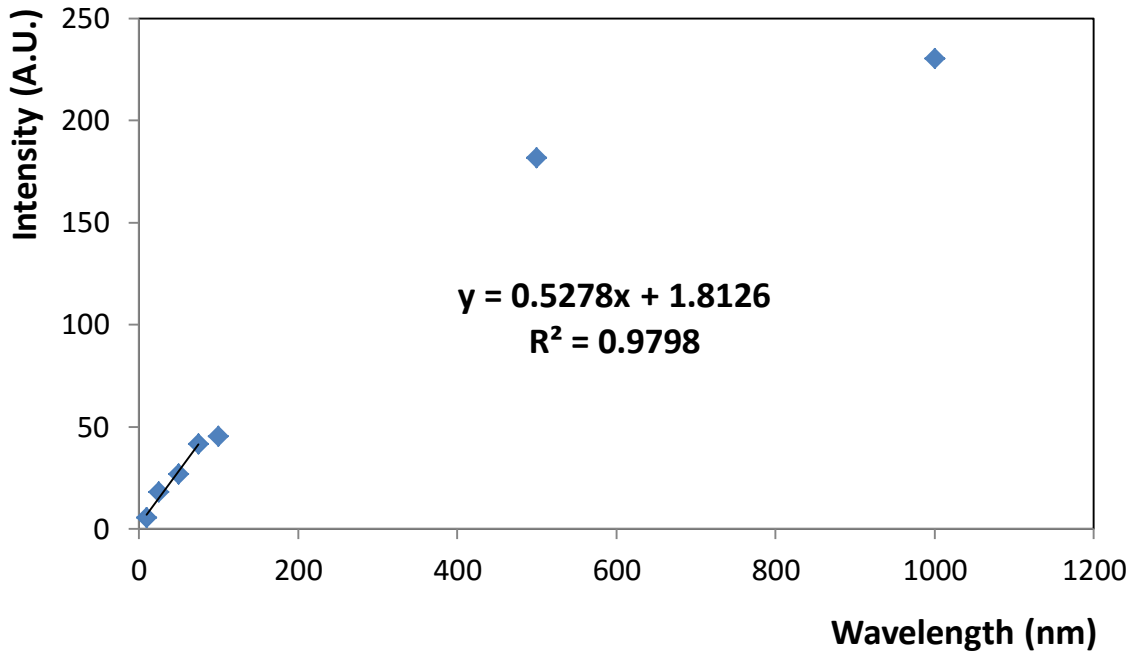

Figure 3.12: Max emission intensity versus concentration of 6-FAM in 1 % DMSO with PBS from 10 µM to 1000 µM.

Table 3.3: Effect of concentration on the position of max emission intensity with increasing 6-FAM concentration in 1 % DMSO with PBS from 10 µM to 1000 µM.

Concentration (µM)	Max Emission (nm)
100	536.0
500	533.0
100	525.1
75	524.0
50	521.9
25	521.9
10	515.0

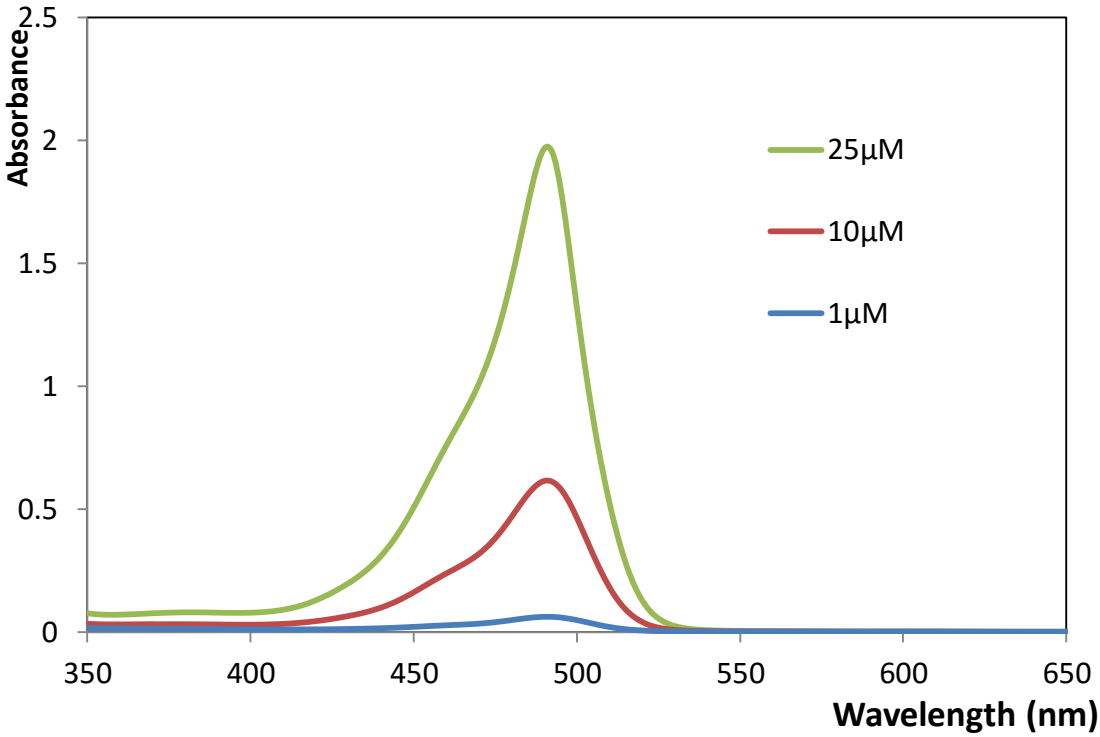

Figure 3.13: Absorbance spectra for 6-FAM with increasing concentration from 1 µM to 25 µM, in 1 % DMSO with PBS at pH 7.4.

Table 3.4: Lifetimes of 6-FAM from 10 µM to 1000 µM for three repeats after excitation at 450 nm in 1 % DMSO with PBS at pH 7.4.

Concentration (µM)	Lifetime (ns)	χ^2
10	4.1±0.0	1.08±0.00
25	4.2±0.0	1.08±0.02
50	4.4±0.0	1.17±0.05
75	4.5±0.1	1.18±0.10
100	4.7±0.1	1.09±0.08
500	5.6±0.3	1.16±0.08
1000	6.3±0.4	1.09±0.05

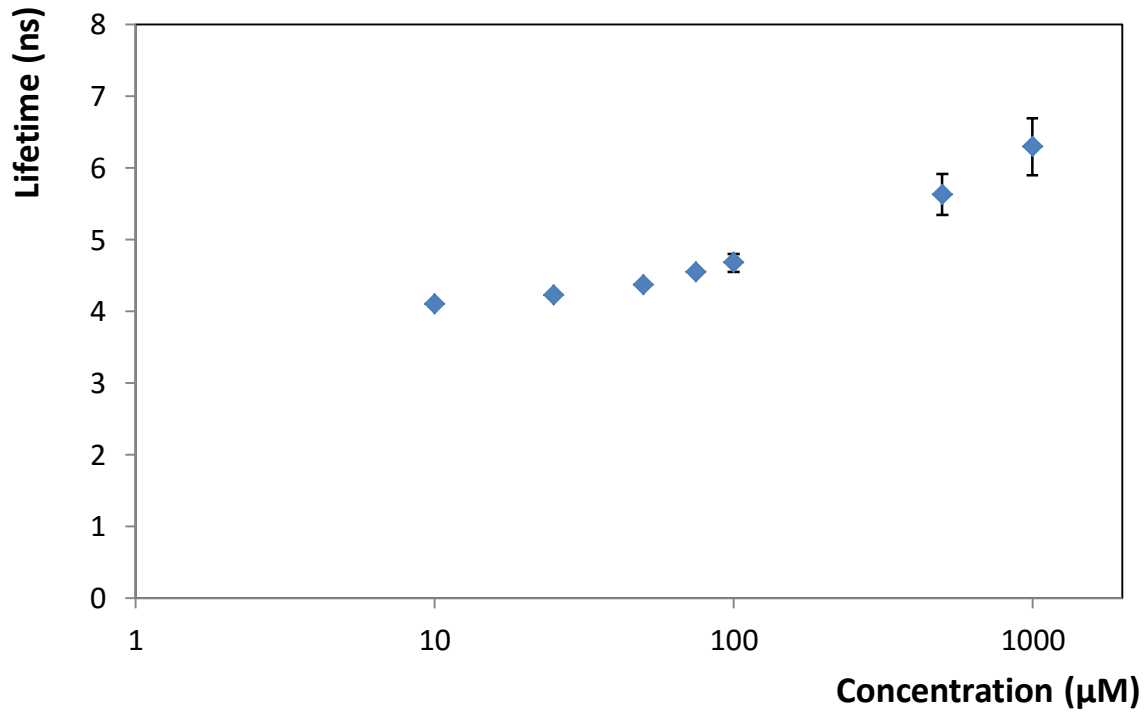

Figure 3.14: Effect of increasing concentration on 6-FAM lifetime in 1 % DMSO with PBS from 10 µM to 1000 µM for three repeats. Where error bars are not visible they are comparable to the size of the symbols.

Figure 3.14 shows the TCSPC results for the concentration range examined. From 10 µM to 100 µM the lifetime remains constant at approximately 4ns, which corresponds to the semi-linear enhancement seen in the emission spectra for this concentration range. At 500 µM the lifetime increases to 5.6±0.3 ns, and then to 6.3±0.4 ns at 1000 µM.

This increase in the observed lifetime at higher concentrations can arise from a number of possible mechanisms. Fluorescein has been shown previously to undergo aggregation at high concentration, which results in dimerisation.[20] This process would explain the decrease seen in emission intensity at high concentration, but is not sufficient on its own to explain the changes in lifetime as static quenching should result in a non-fluorescent complex. Due to the small spectral overlap between the absorption and emission bands of 6-FAM, Förster energy transfer of the excited state could be occurring. This process has been shown previously[20] to be significant at higher concentrations, however this would result in shorter lifetimes for 6-FAM. The cause of these longer lifetimes is not well understood.

The concentration data shows that at a high concentration significant quenching of the dye occurs, however as the effect does not become significant until 100 µM, this can be easily avoided by keeping the concentration low. As the photophysical properties of the dye had been fully characterised, the next step was to examine the MB in the presence of the quencher.

3.3.4 Dabcyl

Dabcyl is a dark quencher, i.e. it absorbs excitation energy from a dye molecule and releases this energy as heat[21]. Dabcyl has been widely used for the quenching of fluorescein derivatives based on its large spectral overlap.[22,23,23,24,24]

The photophysics of dabcyl were investigated to examine its quenching properties. The dabcyl was insoluble in water, and in water containing solvent systems, so all experiments were performed in 100 % DMSO. The absorption spectra for 10 µM of the dabcyl in DMSO is shown in Figure 3.15. A broad absorption peak is observed with peak maximum at 480 nm. The overlap between dabcyl and a 10 µM 6-FAM solution in 1 % DMSO is also shown. The graph shows a high degree of overlap which is desirable for fluorescence quenching.

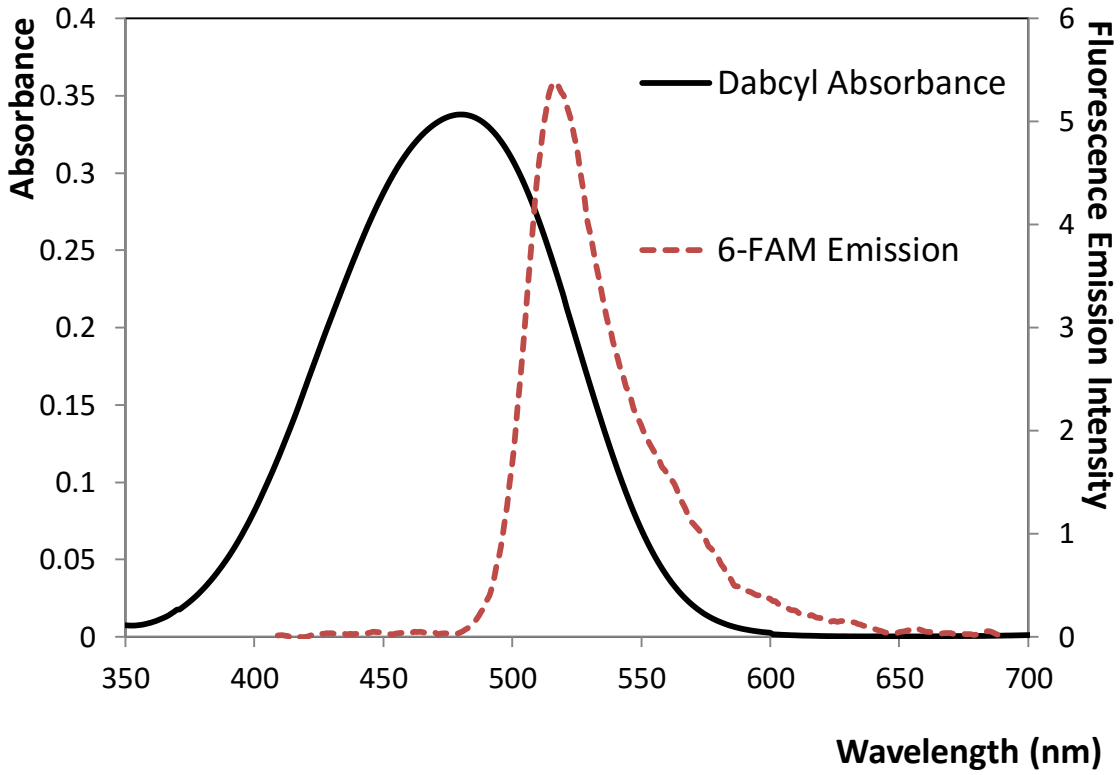

Figure 3.15: Absorbance spectra of 10 µM Dabcyl in DMSO (Black) and emission spectra of 10 µM 6-FAM with 1 % DMSO in PBS (Red). Excitation at 395 nm with excitation slit at 2.5 nm and emission slit at 2.5 nm.

Table 3.5: Calculated values for Förster energy transfer from the 6-FAM to the dabcyl.

Forster Distance (Å)	82.66
Rate of Electron Transfer (1/s)	7.78×10^{13}
Dexter Value (1/eV)	0.82
J value (cm^6)	2.82×10^{-12}

The distance between 6-FAM and dabcyl at which energy transfer is 50 % efficient (R_0) can be represented as:

$$R_0 = \frac{8.8 \times 10^{-25}\, K^2 \phi_D}{n^4} J$$

Equation 3.4: Critical Förster energy distance

Where K^2 = Orientation factor

ϕ_D = Fluorescence quantum yield

n = Refractive index

J = Spectral overlap integral

The orientation factor was assumed to be 2/3 for rapidly rotating randomly orientated donor and acceptor molecules.[25] The refractive index was 1.4, the average for DMSO (1.48)[26] and water (1.33)[27]. The quantum yield was 0.74, as previously reported.[20] The spectral overlap was calculated based on the spectra shown in Figure 3.15. Based on this calculation, the critical Förster energy distance was calculated as 82 Å. Therefore, efficient quenching is expected when the dye and quencher are in close proximity in the parent beacon. Based on the structure of the MB, a separation of <50 Å is expected.

The quenching of 6-FAM by dabcyl can potentially occur by two mechanisms. One is static quenching, whereby direct collision of a 6-FAM molecule and the dabcyl results

in quenching. The maximum distance that an excited 6-FAM molecule can diffuse within its excited state lifetime is given by:

$$d = (D\tau)^{1/2}$$ *Equation 3.5: Diffusion length*

Where d = diffusion length

D = Diffusion coefficient of the solvent

τ = Fluorescent lifetime

Assuming that the diffusion coefficient is approximately 5×10^{-6} cm^2 s^{-1}, and $\tau = 2.1 \times 10^{-9}$ s, then the diffusion length is 1×10^{-7} cm, i.e. 10 Å. This distance is so small that the probability of a collision occurring is very low. The second mechanism is by energy transfer. As shown previously, the critical energy transfer distance is 82.6 Å. This considerably longer distance suggests that FRET is the primary means of fluorescence quenching by dabcyl.

In order to experimentally examine the ability of the dabcyl to quench the 6-FAM, a quenching study was undertaken. As previously stated, dabcyl is insoluble in water containing solvent systems and so the experiment was performed in DMSO. In DMSO, the emission intensity of the 6-FAM is significantly reduced as shown previously, and so the concentrations were increased to 100 µM and the excitation wavelength was increased to 450 nm to provide adequate emission intensity. As illustrated in Figure 3.16, in the absence of dabcyl, an emission maximum was observed at 528±0 nm with intensity of 135±4.4 A.U. As the concentration of dabcyl is increased, the position of maximum emission intensity increases, as shown in Figure 3.18. The peak shifts from 528±0 nm in 5-FAM, to 565±1 nm at 50 µM dabcyl, and further to 596±1 nm in the presence of 500 µM dabcyl, see Figure *3.18*.

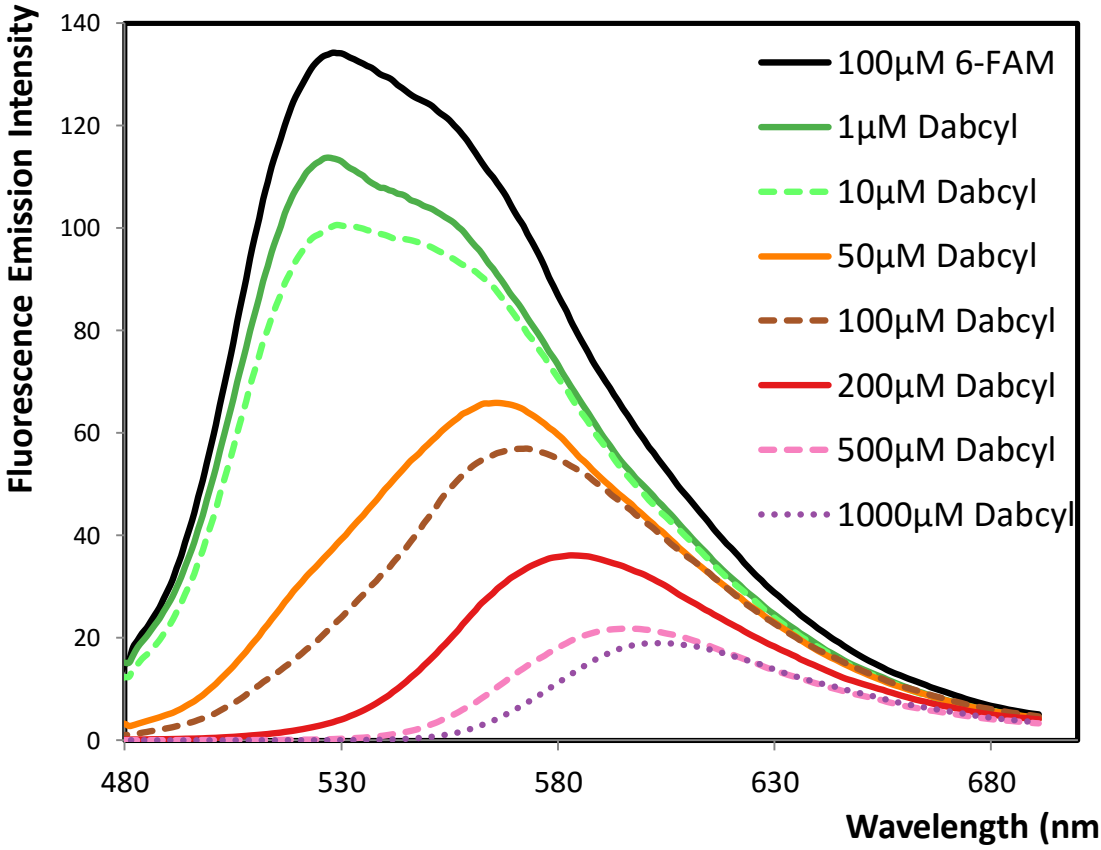

Figure 3.16: Emission spectra for 100 µM 6-FAM in DMSO with varying concentrations of Dabcyl quencher from 1 µM to 1mM after excitation at 450 nm with excitation slit at 20 nm and emission slit at 20 nm.

As seen in Figure 3.16, the intensity of the emission is also significantly reduced as the concentration of dabcyl is increased. In the absence of dabcyl the maximum emission is 135.3±4.4 A.U. As dabcyl is added, the emission drops sharply, with 1 µM resulting in a drop to 87±3 % of the initial signal. The addition of 50 µM dabcyl results in a decrease in intensity to 49±2 %., and then further to 27±1 % with 200 µM of dabcyl. At 1000 µM the emission intensity reduced to 12±2 % compared to 6-FAM alone.

Overall these results are promising, as the 6-FAM seems to be highly quenched by the addition of dabcyl, with even low concentrations causing a significant reduction in signal intensity. Figure 3.17 shows a Stern Volmer plot of the quenching experiment. For collisional quenching, a straight line is expected. This is not observed here which suggests a more complicated quenching mechanism.

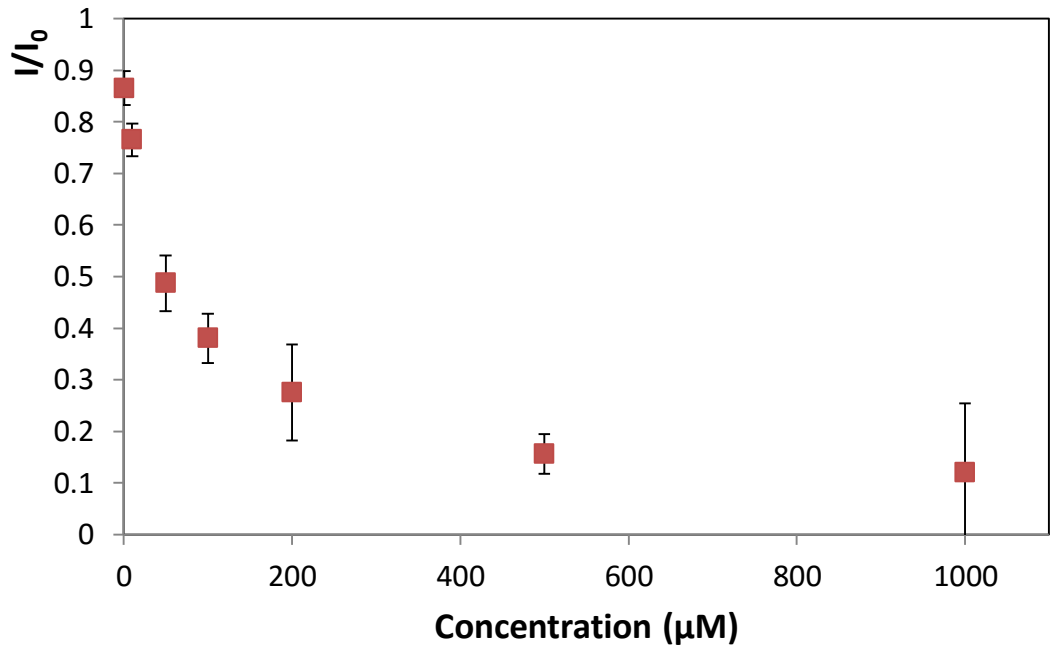

Figure 3.17: Stern Volmer plot of maximum emission intensity for 100 µM 6-FAM in DMSO with varying concentrations of dabcyl quencher from 1 µM to 1mM after excitation at 450 nm with excitation slit at 20 nm and emission slit at 20 nm

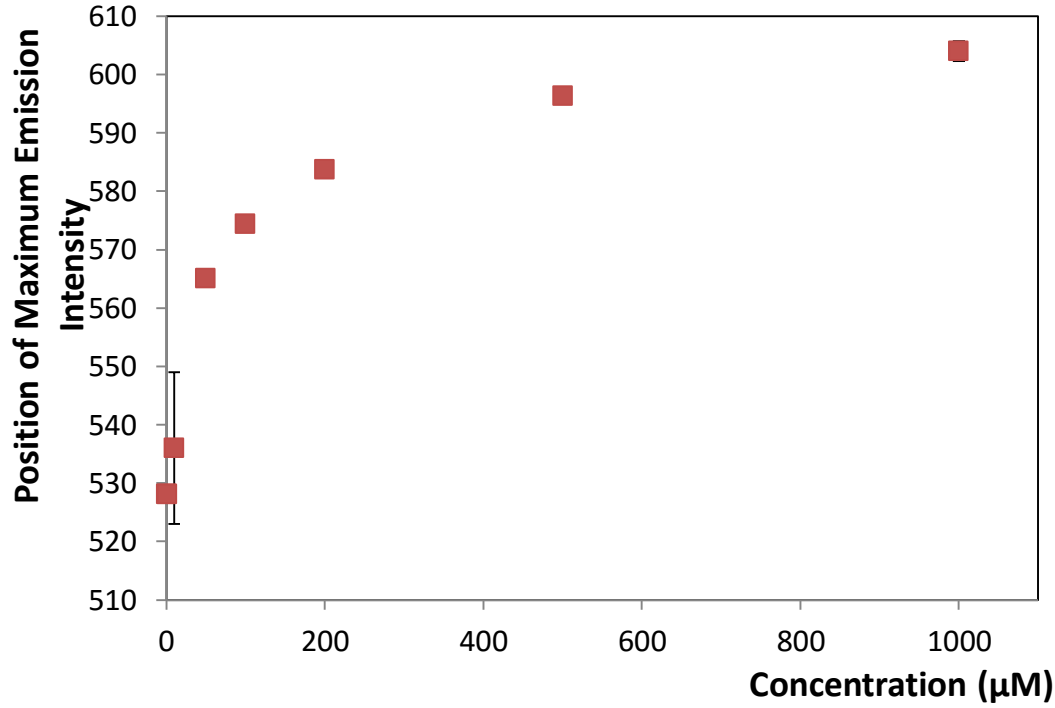

Figure 3.18: Wavelength of maximum emission intensity for 100 µM 6-FAM in DMSO with varying concentrations of dabcyl quencher from 1 µM to 1 mM after excitation at 450 nm with excitation slit at 20 nm and emission slit at 20 nm.

Figure 3.19 shows a representative TCSPC fit for 100 µM 6-FAM in DMSO. The lifetime could not be fitted to a single exponential but is adequately described by two components, a lifetime of 2.2±0.0 ns, which accounted for 26 % of the signal, and a second lifetime of 0.7±0.0 ns which accounted for 74 % of the signal. The shorter lifetime is most likely due to instrumental noise, as it remains consistent throughout the experiment and is present in different samples recorded under these conditions. Due to the low intensity of the emission in 100 % DMSO, this background signal becomes a more significant contributor to the signal.

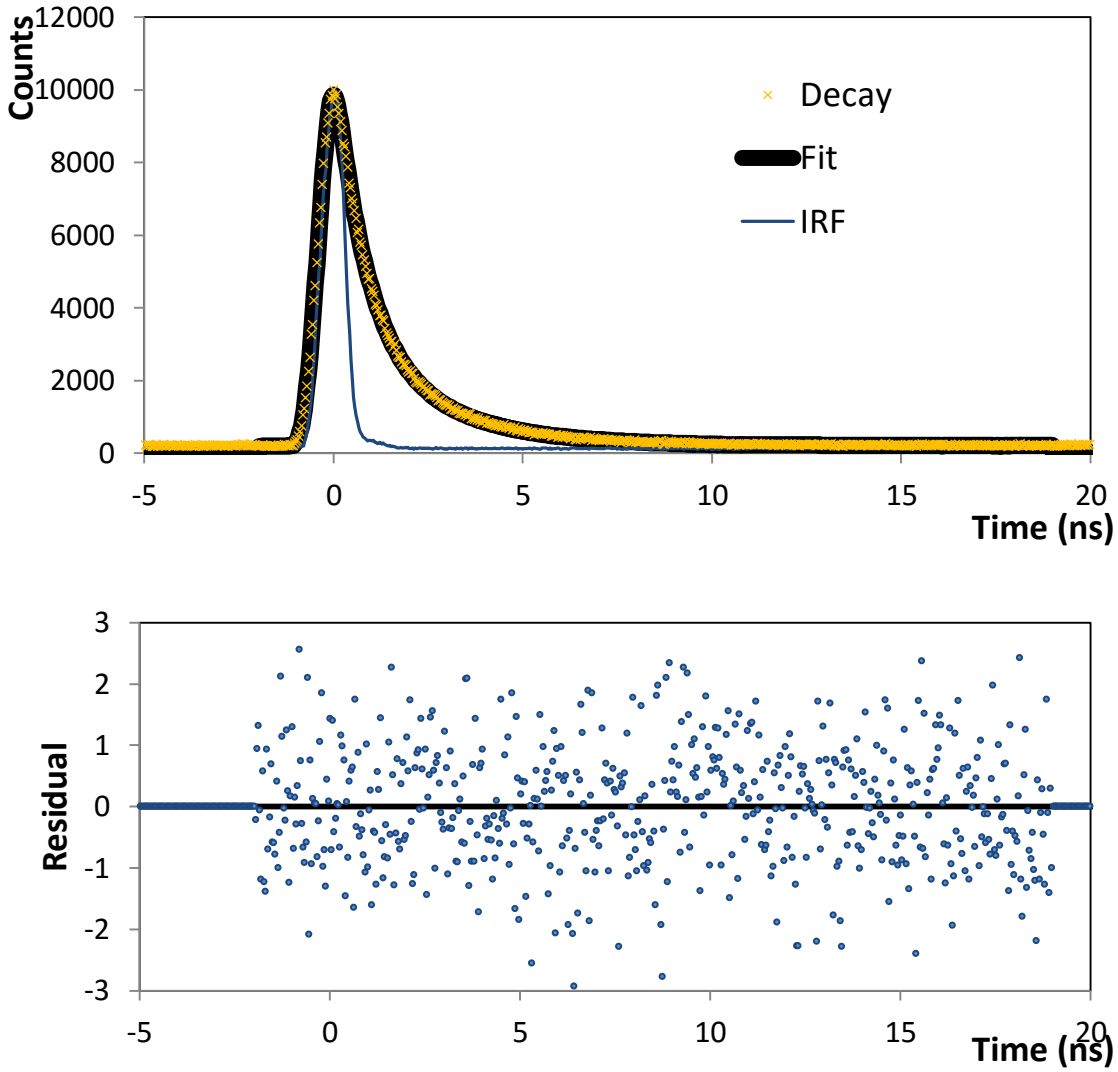

Figure 3.19: Time correlated single photon counting lifetime for 100 µM 6-FAM in DMSO with fit (top) and residual plot (bottom).

The lifetime results for the 6-FAM as the concentration of dabcyl is systematically varied are shown in Table 2.2. For this range of concentrations, the two lifetimes remain consistent at 2.1±0.1 ns and 0.6±0.1 ns.

The lifetime would be expected to decrease as the concentration of quencher is decreased for collisional quenching. This is not observed for the range of lifetimes, which suggest that static quenching may be the primary quenching mechanism under these conditions.

Table 3.6: Lifetime results for 100 µM 6-FAM in DMSO with varying concentrations of dabcyl quencher from 1 µM to 1 mM after excitation at 450 nm.

	τ_1 (ns)		τ_2 (ns)		χ^2
6-FAM	2.2±0.0	26.1±4.7 %	0.7±0.0	73.9±4.7 %	1.05±0.10
1 µM Dabcyl	2.2±0.1	22.3±4.4 %	0.7±0.0	77.7±4.4 %	1.15±0.08
10 µM Dabcyl	2.2±0.0	30.3±14.3	0.7±0.1	69.7±14.3 %	1.12±0.07
50 µM Dabcyl	2.1±0.0	25.6±2.6 %	0.7±0.0	74.4±2.6 %	1.14±0.06
100 µM Dabcyl	2.0±0.0	30.2±0.4 %	0.6±0.0	69.8±0.4 %	1.24±0.10
200 µM Dabcyl	1.9±0.0	39.4±2.0 %	0.5±0.0	60.6±2.0 %	1.19±0.09
500 µM Dabcyl	2.1±0.1	72.0±7.4 %	0.8±0.1	28.0±7.4 %	0.99±0.07
1000 µM Dabcyl	2.0±0.1	81.2±4.7 %	0.5±0.1	18.8±4.7 %	1.05±0.09

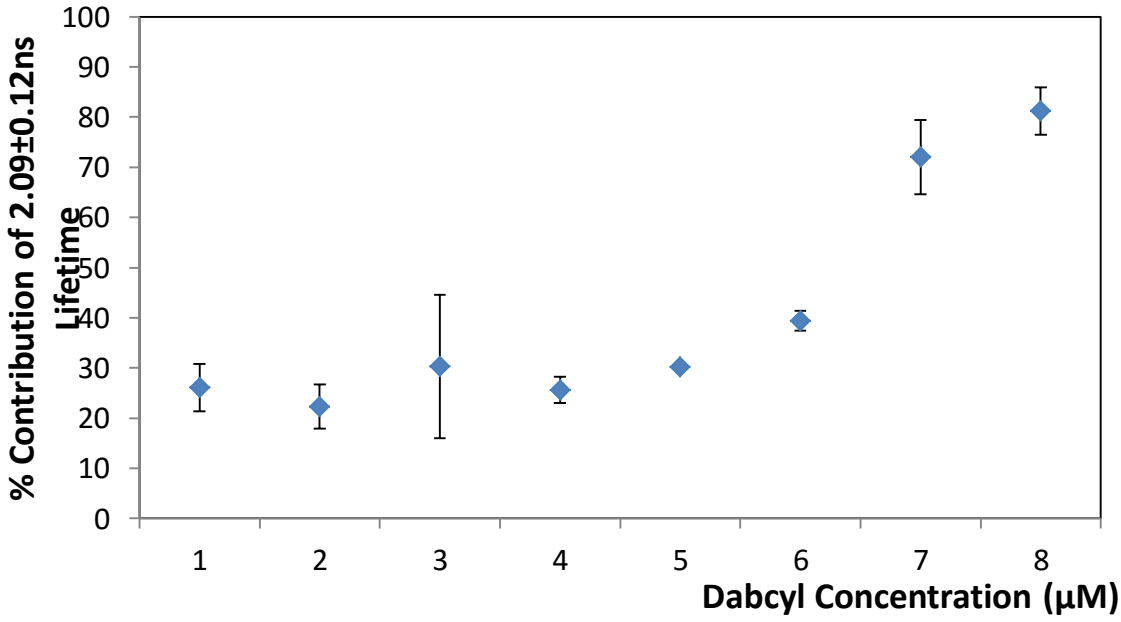

Figure 3.20: Percentage contribution of the 2.09±0.12 ns lifetime for 100 µM 6-FAM in DMSO with varying concentrations of dabcyl quencher from 1 µM to 1 mM after excitation at 450 nm.

3.3.5 Molecular Beacon

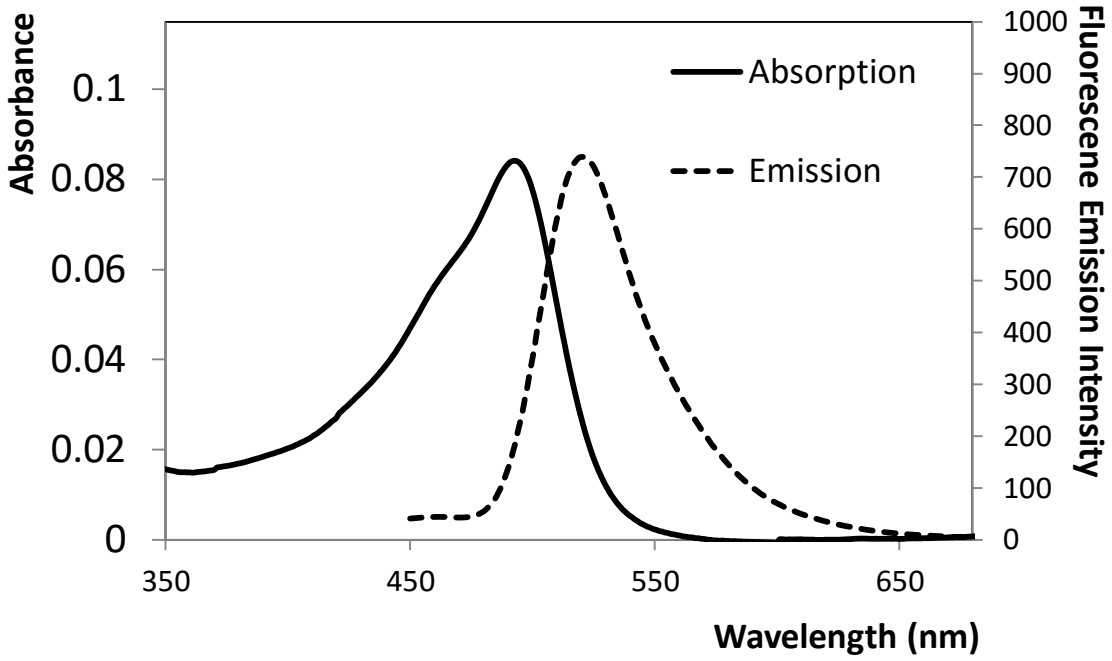

Figure 3.21: Absorbance and emission spectra of a 10 µM solution of the 6-FAM-dabycl MB in PBS. Excitation at 395 nm with excitation slit at 20 nm and emission slit at 20 nm.

The solubility of the MB (MB) was investigated, and it was determined that the MB was soluble in aqueous solutions, which is most likely due to the presence of the negatively charged DNA. A 50 µM stock of the MB was prepared and the UV and emission spectra acquired. The UV spectra exhibits maximum absorbance at 495 nm which is indistinguishable from that found for 6-FAM, however the absorbance intensity was significantly lower, being 0.616 for the free 6-FAM dye, compared with 0.084 for the same dye concentration bound within the hairpin. This lower absorbance is unexpected given that the MB also contains a dabcyl quencher that has wavelength of maximum absorbance of 480 nm, which should also be contributing to this absorbance signal. The reduced absorbance may be due to interaction with the nucleic acid or the loss of the carboxy functional group upon binding to the nucleic acid. The emission peak shape is similar for both the free 6-FAM dye and MB. However the emission intensity is much lower in the MB due to the FRET energy transfer to the dabcyl quencher. Ideally no emission would be observed, which would signify complete quenching of the 6-FAM by the dabcyl. The presence of this signal could cause a significant deterioration in the signal to noise ratio when trying to detect the miRNA target.

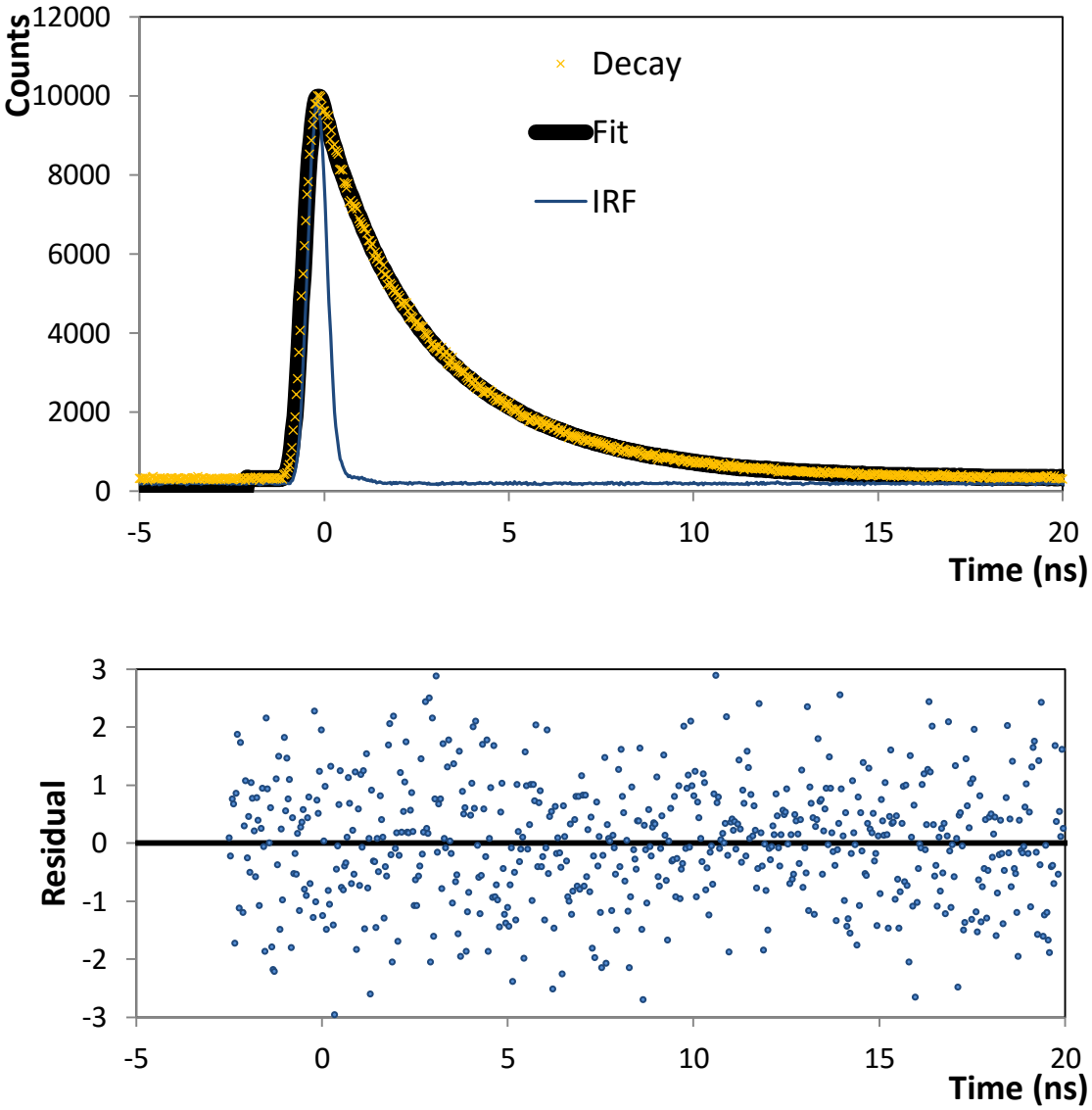

τ_1 (ns)		τ_2 (ns)		χ^2
3.5±0.0	77 %	1.1±0.0	23 %	1.144

Figure 3.22: Time correlated single photon counting lifetime for 10 µM MB in 1 % DMSO in PBS with fit (top) and residual plot (bottom).

Figure 3.22 shows the TCSPC data for the MB. The lifetime could not be fitted to a single exponential and was discovered to contain 2 components: a lifetime of 3.5±0.2ns, which accounted for 77 % of the signal, and a second lifetime of 1.1±0.0 ns which accounted for 23 % of the signal. 6-FAM[20] has a pK_a of 6.45, and so at a pH 7.4 in PBS approximately 90 % will be in the protonated form and 10 % will be in deprotonated form. However, on the basis of the investigations of the free dye both of these conformations are expected give rise to a lifetime in the 3 ns to 4 ns range, as shown in Table 2.2, which does not account for the 1.1±0.0 ns signal. As discussed above, the shorter lifetime is considered to arise from the instrument, e.g., filter emission.

3.3.6 Live Cell Imaging

3.3.6.1 Passive Uptake

One significant objective was to determine the concentration of miR-132 within the cells using live cell imaging. The SK-N-AS cell line was chosen as a source of miR-132 as it has been shown to highly express this miRNA.[28] However, getting the MB into the cells was a potential issue. As a starting point, the ability of 6-FAM dye to passively enter the cells was investigated. A simple passive uptake experiment was performed in which the cells were incubated overnight with a 50 µM solution of the 6-FAM. After incubation, the cells were rinsed with fresh media, and were imaged using a confocal microscope, see Figure 3.23. No emission from the dye was detected under confocal imaging and the cells appeared to be healthy and unaffected by the addition of 6-FAM to the media, with good attachment to the cell culture dish and normal morphology.

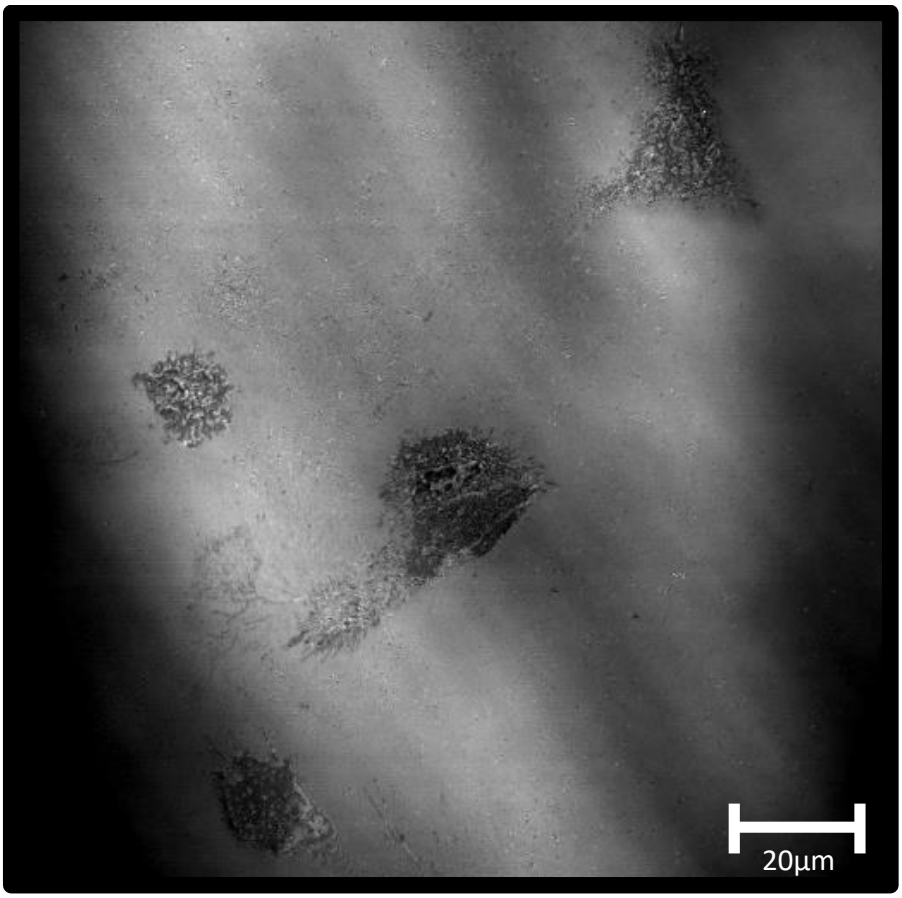

Figure 3.23: Confocal fluorescence microscopy of SK-N-AS cells after incubation with 50 µM 6-FAM, overnight, and after washing with fresh media. Excitation with argon ion laser at 458 nm and with an LP560 filter at 6 %.

As the dye was not taken up by the cells passively, the next attempted approach was the addition of solvents to the media to improve the permeability of the cells. DMSO has been shown to be non-toxic to cells at low concentrations[29,30,30], and to improve the permeability of lipid membranes[31]. A control experiment was performed, containing only SK-N-AS cells with 1 % DMSO in the media and the cells appeared to be healthy after 24 hours of incubation, showing normal shape and good attachment to the surface.

Cells were then incubated for 4 hours and 24 hours with 6-FAM in 1 % DMSO. The cells appeared to be healthy, with normal morphology and good attachment to the surface. The cells were imaged in the 6-FAM containing media, see Figure 3.24, as this provides contrast for the image. No signal was detected for 6-FAM within the cells, with a weak signal present in the media around the cells. This was the case for cells incubated for both 4 hours and 24 hours.

The concentration of DMSO was then increased from 1 % in the media, to 2 %, see Figure 3.25. Again, the viability of the cells was high at more than 90 %, with the control cells appearing healthy and having normal morphology. When the cells were incubated with 50 µM 6-FAM for 4 hours and 24 hours, no signal was present within the cells.

Ethanol has also been shown to increase the permeability of lipid membranes[32], and so ability of ethanol to improve the uptake of 6-FAM was also investigated. A batch of SK-N-AS cells were incubated with 5 % ethanol for 24 hours. In this case the viability of the cells was significantly reduced to approximately 70 % compared to a control population. When cells were incubated with ethanol and 50 µM 6-FAM, no significant uptake was observed.

Based on these experiments, the use of solvents to improve the uptake of 6-FAM was considered unsuccessful, and so alternative methods were then investigated.

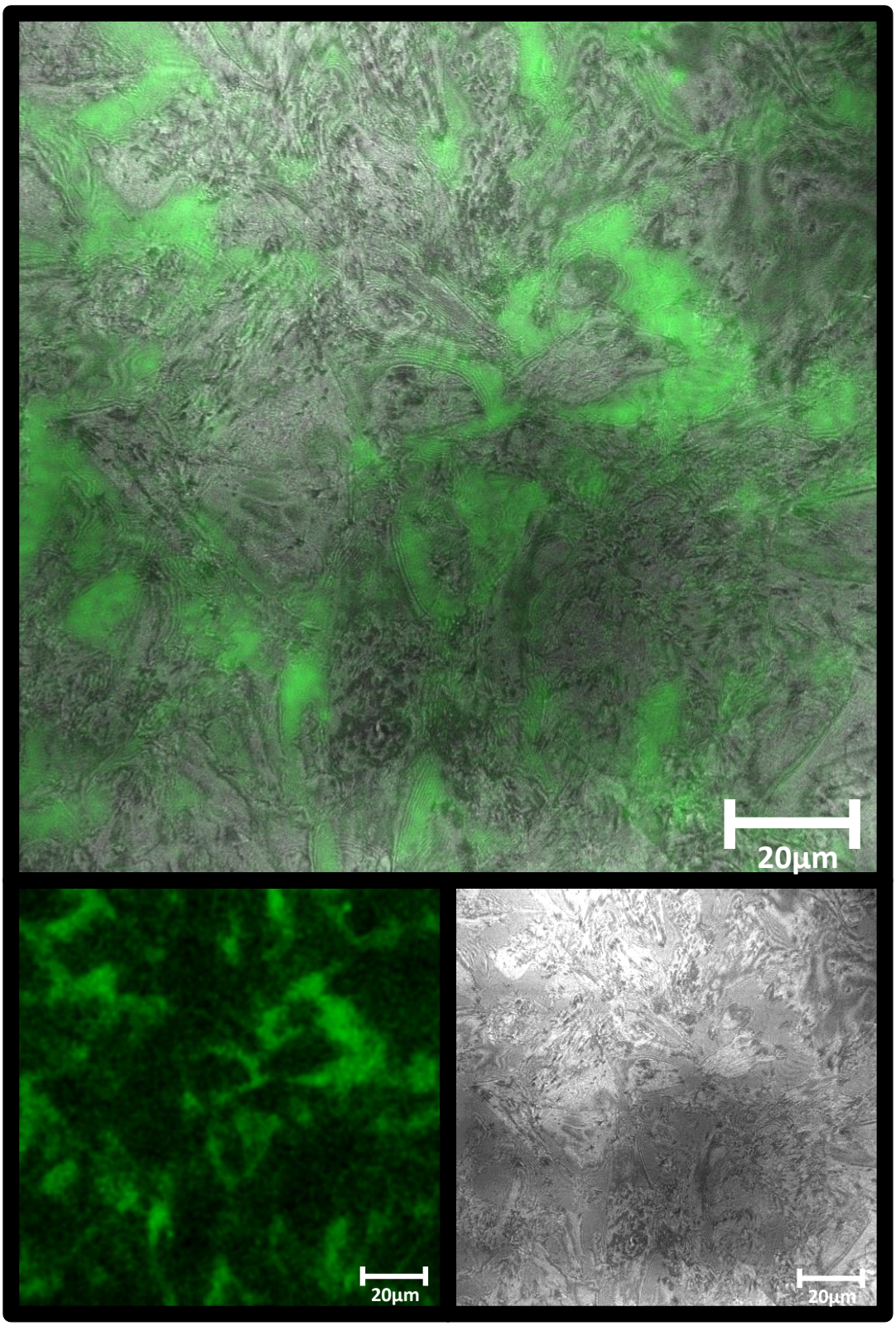

Figure 3.24: Confocal fluorescence microscopy of SK-N-AS cells after 24 hours with 50 µM 6-FAM in 1 % DMSO and media. Excitation with argon ion laser at 458 nm and with an LP560 filter at 6 %.

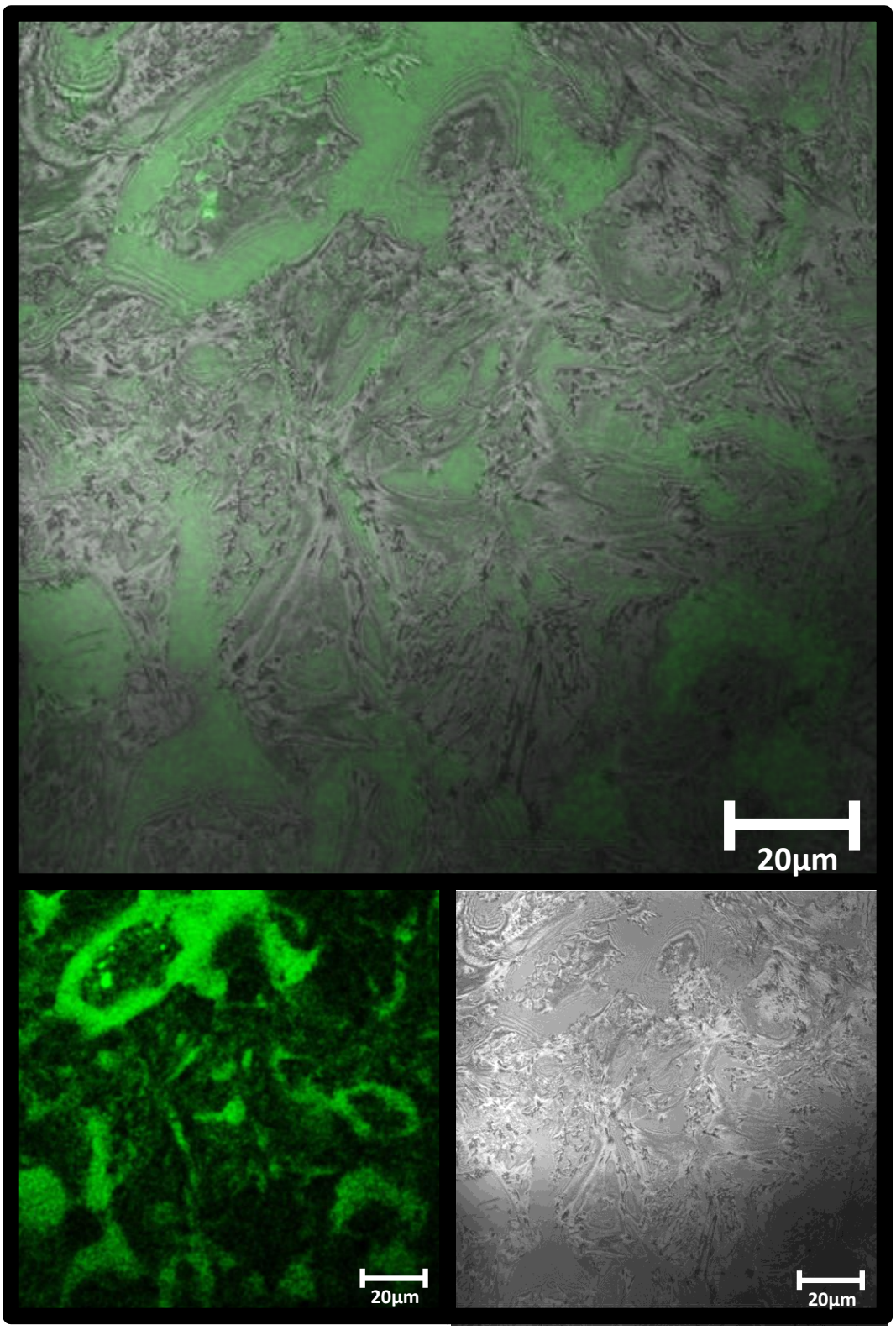

Figure 3.25: Confocal image of SK-N-AS cells after 24 hours with 50 µM 6-FAM in 2 % DMSO and media. Excitation with argon ion laser at 458 nm and with an LP560 filter at 6 %.

3.3.6.2 Electroporation

Since both passive and solvent assisted uptake of the dye were unsuccessful, an alternate method of getting the dye into the cells was investigated. Electroporation is a highly efficient technique which allows for the introduction of nucleic acids and other charged species to a cell by increasing the permeability of the cell membrane. This is achieved by the application of an electrical field across the cell membrane which causes the formation of pores in cell membranes[33], see Figure 3.26. This allows molecules usually excluded from the cell to diffuse in.[34]

Figure 2.27 shows a cell which has been electroporated with 50 µM 6-FAM, imaged in the dye containing media. A signal of higher intensity was observed in the cell, which suggests successful transfection. The viability of the cells however was very poor, i.e. below 5 %. When the media was removed and placed on a glass slide, a large number of dead cells can be seen as shown in Figure 3.28. The cells were treated with a viability stain, DRAQ7, (in red) which is only taken up by cells with ruptured cell membranes. As can be seen, all of the cells in suspension were dead. However for the small number of cells that remained alive after electroporation, emission from the 6-FAM can be observed. Interestingly, the 6-FAM was highly excluded from the cell nucleus, but was present in the rest of the cell. There are two possible explanations for these images. It is possible that at a concentration of 50 µM, that the 6-FAM is toxic to the cell, and that the cells which were efficiently transfected died as a result. The other possibility is that the cells died as a result of the electroporation procedure, caused by the catastrophic failure of the cell membrane, and that this, in turn, allowed the dye to diffuse into the cells. The backscatter image shows a significant amount of cell debris, for cells damaged in the electroporation procedure.

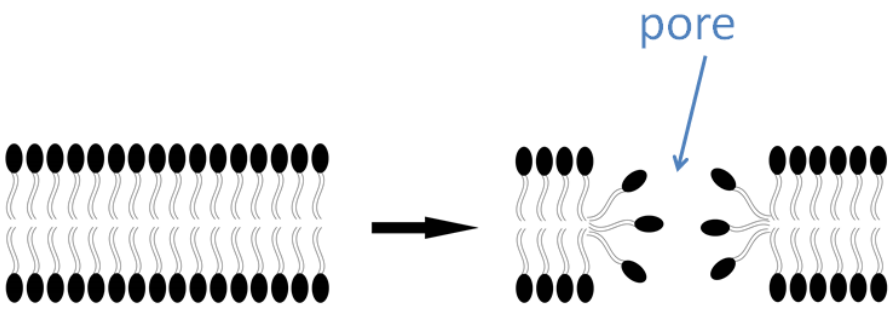

Figure 3.26 Formation of pores in cell membrane during electroporation

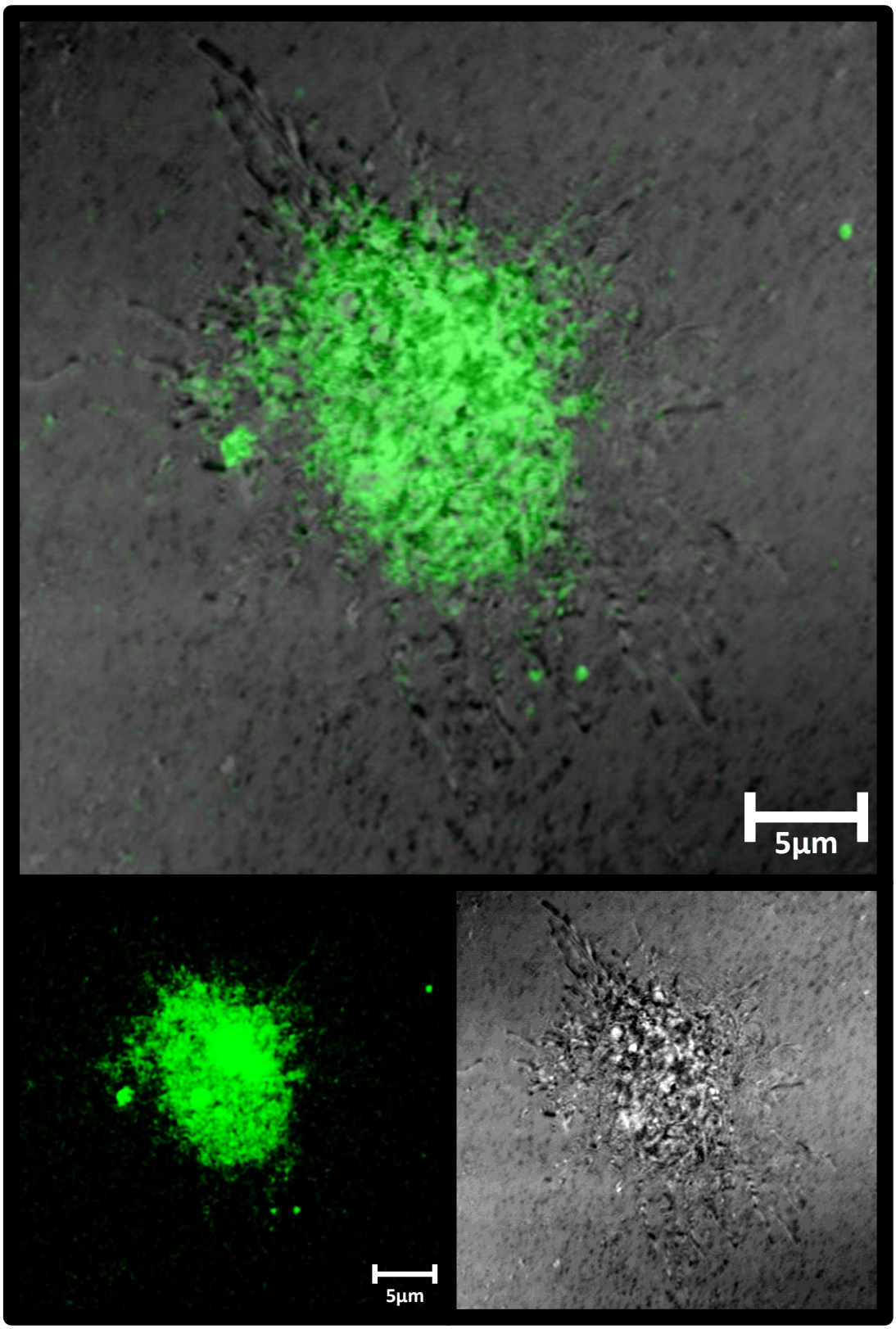

Figure 3.27: Confocal image of SK-N-AS cells after electroporation with 50 µM 6-FAM in media. Excitation with argon ion laser at 458 nm and with an LP560 filter at 6 %.

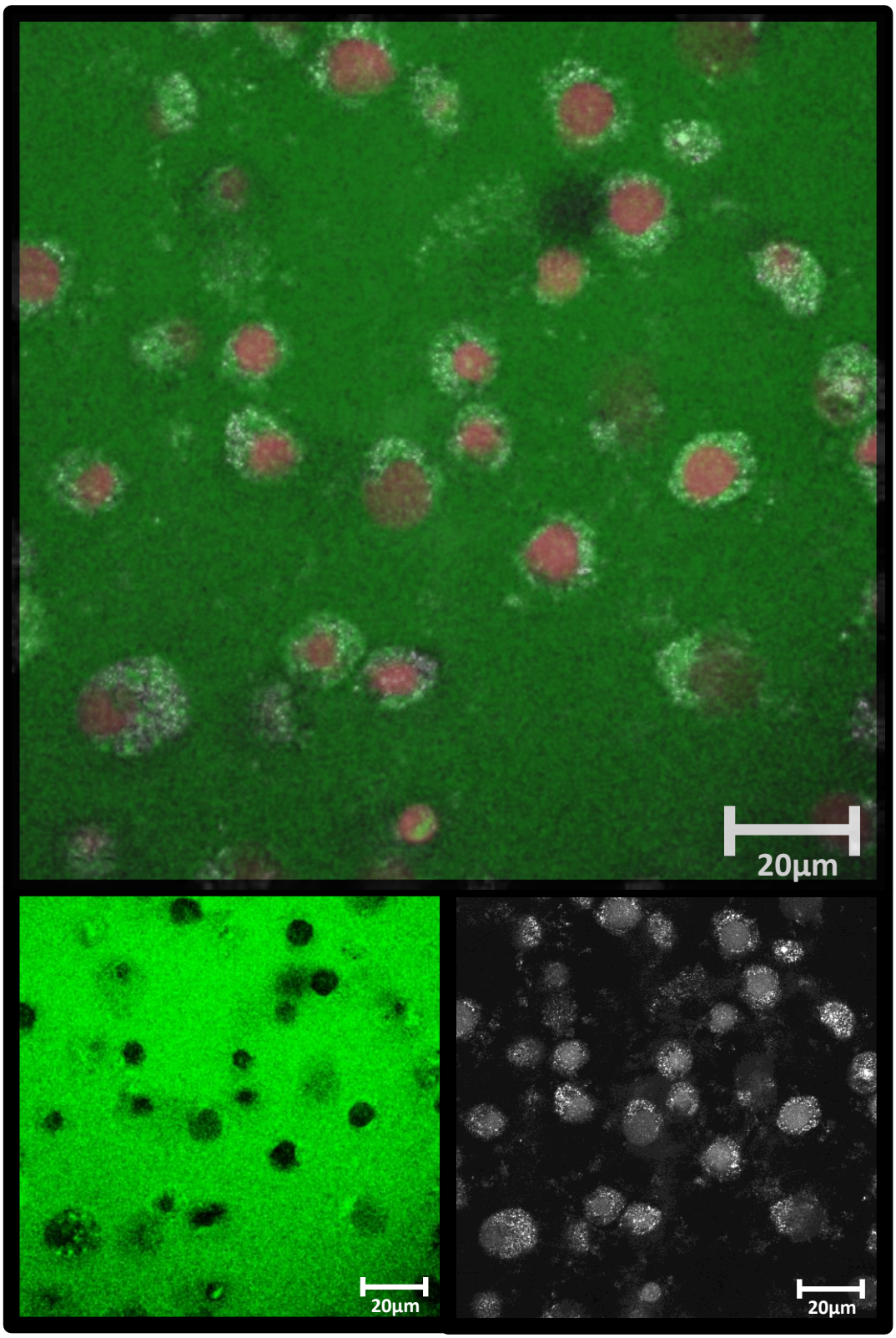

Figure 3.28: Confocal image of floating SK-N-AS cells after electroporation with 50 µM 6-FAM (Green) in media and with 1 µM DRAQ7 (Red) viability dye. Excitation with argon ion laser at 458 nm and with an LP560 filter at 6 %.

3.4 Conclusions

The goal of this chapter was to examine the environmental impacts of the cellular environment on the photophysics of the dye integrating into a MB for the detection of miR-132. This can inform the interpretation of results from live cells.

In this work, the dye 6-carboxyfluoresin was examined for suitability as part of a MB. The dye was found to be insoluble in water, but could be added to aqueous media by first dissolving in DMSO or ethanol and then transferring to water. 1 % organic solvent was found to be sufficient to maintain stable solubility in water.

The photophysics of the dye were examined using absorption and emission spectra, and the lifetime was examined using TCSPC. This lifetime was measured as 4.1±0.0 ns, which closely matches literature values for similar dyes. The effect of pH on the dye was also examined, and the absorbance data suggests significant changes to the dye as pH changes due to protonation and deprotonation of the dye. This results in different peaks at high and low pH, with both peaks contributing to the signal at intermediate levels of pH. This sensitivity of the dye to changes in pH may have an impact of the observed intensity of the MB in live cells. For example, in lysosomes where the pH is in the region of pH 4.7, it would be expected that the intensity of emission would decrease. No significant changes were observed at pH 7.4 and above. This is highly desirable for live cell imaging of cells, since the intercellular fluid, mitochondria, and nucleus are at or above pH 7.4.

The concentration study of the dye found that at higher than 100 µM significant self-quenching of the dye occurs. The emission was also affected, with a strong linear correlation with changes in concentration only from 10 µM to 100 µM, after which the emission intensity depends only weakly on the concentration. Since no significant self-quenching occurs at lower concentrations, future experiments with live cells can be performed at concentrations lower than 100 µM.

Basic characterisation of the MB was also carried out, with the emission, absorption and lifetime matching 6-FAM in terms of the position of maximum intensity, however the absorption and emission intensity was considerably reduced for the MB, which may be due to the 6-FAMs interaction with the nucleic acid strand. This lower than expected

emission intensity is also consistent with the expected quenching of the dye by the dacyl quencher.

The suitability of 6-FAM for use in live cell imaging was also examined. It was found that the dye does not passively enter the cells, and that the addition of solvents DMSO and ethanol displayed no improvement in this uptake. To overcome these issues, electroporation was investigated. This method was successful in delivering the 6-FAM to the cells, however it resulted in poor cell viability of approximately 5 %. Confocal fluorescence imaging reveals that the 6-FAM is highly excluded from the nucleus of the cell for both living and dead transfected cells.

3.5 References

1. Bonnet, G.; Tyagi, S.; Libchaber, A.; Kramer, F. Thermodynamic basis of the enhanced specificity of structured DNA probes. *Proc. Natl. Acad. Sci. U. S. A.* **1999**, *96*, 6171-6176.

2. Goel, G.; Kumar, A.; Puniya, A.; Chen, W.; Singh, K. Molecular beacon: a multitask probe. *J. Appl. Microbiol.* **2005**, *99*, 435-442.

3. Marti, A. A.; Jockusch, S.; Stevens, N.; Ju, J.; Turro, N. J. Fluorescent hybridization probes for sensitive and selective DNA and RNA detection. *Acc. Chem. Res.* **2007**, *40*, 402-409.

4. OHKUMA, S.; POOLE, B. Fluorescence Probe Measurement of Intralysosomal Ph in Living Cells and Perturbation of Ph by various Agents. *Proc. Natl. Acad. Sci. U. S. A.* **1978**, *75*, 3327-3331.

5. ROOS, A.; BORON, W. Intracellular Ph. *Physiol. Rev.* **1981**, *61*, 296-434.

6. BRANNON, J.; MAGDE, D. Absolute Quantum Yield Determination by Thermal Blooming - Fluorescein. *J. Phys. Chem.* **1978**, *82*, 705-709.

7. SONG, L.; HENNINK, E.; YOUNG, I.; TANKE, H. Photobleaching Kinetics of Fluorescein in Quantitative Fluorescence Microscopy. *Biophys. J.* **1995**, *68*, 2588-2600.

8. SJOBACK, R.; NYGREN, J.; KUBISTA, M. Absorption and Fluorescence Properties of Fluorescein. *Spectroc. Acta Pt. A-Molec. Biomolec. Spectr.* **1995**, *51*, L7-L21.

9. Abel, A.; Weller, M.; Duveneck, G.; Ehrat, M.; Widmer, H. Fiber-optic evanescent wave biosensor for the detection of oligonucleotides. *Anal. Chem.* **1996**, *68*, 2905-2912.

10. PATTERSON, B.; TILL, M.; OTTO, P.; GOOLSBY, C.; FURTADO, M.; MCBRIDE, L.; WOLINSKY, S. Detection of Hiv-1 Dna and Messenger-Rna in Individual Cells by Pcr-Driven Insitu Hybridization and Flow-Cytometry. *Science* **1993**, *260*, 976-979.

11. Nazarenko, I.; Bhatnagar, S.; Hohman, R. A closed tube format for amplification and detection of DNA based on energy transfer. *Nucleic Acids Res.* **1997**, *25*, 2516-2521.

12. Gibson, U.; Heid, C.; Williams, P. A novel method for real time quantitative RT PCR. *Genome Res.* **1996**, *6*, 995-1001.

13. Zhang, P.; Beck, T.; Tan, W. Design of a molecular beacon DNA probe with two fluorophores. *Angewandte Chemie* **2001**, *113*, 416-419.

14. Harris, D. L.; Mutz, M. Debunking the myth: validation of fluorescein for testing the precision of nanoliter dispensing. *Journal of the Association for Laboratory Automation* **2006**, *11*, 233-239.

15. Klonis, N.; Clayton, A.; Voss, E.; Sawyer, W. Spectral properties of fluorescein in solvent-water mixtures: Applications as a probe of hydrogen bonding environments in biological systems. *Photochem. Photobiol.* **1998**, *67*, 500-510.

16. Llopis, J.; McCaffery, J.; Miyawaki, A.; Farquhar, M.; Tsien, R. Measurement of cytosolic, mitochondrial, and Golgi pH in single living cells with green fluorescent proteins. *Proc. Natl. Acad. Sci. U. S. A.* **1998**, *95*, 6803-6808.

17. THOMAS, J.; BUCHSBAUM, R.; ZIMNIAK, A.; RACKER, E. Intracellular Ph Measurements in Ehrlich Ascites Tumor-Cells Utilizing Spectroscopic Probes Generated Insitu. *Biochemistry (N. Y.)* **1979**, *18*, 2210-2218.

18. Kim, H. N.; Swamy, K. M. K.; Yoon, J. Study on various fluorescein derivatives as pH sensors. *Tetrahedron Lett.* **2011**, *52*, 2340-2343.

19. Lee, D.; Sung, H.; Han, D.; Lee, M.; Ryu, G.; Aihara, M.; Takatori, K.; Park, J. In vitro bioassay of endotoxin using fluorescein as a pH indicator in a macrophage cell culture system. *Yonsei Med. J.* **2005**, *46*, 268-274.

20. CHEN, R.; KNUTSON, J. Mechanism of Fluorescence Concentration Quenching of Carboxyfluorescein in Liposomes - Energy-Transfer to Nonfluorescent Dimers. *Anal. Biochem.* **1988**, *172*, 61-77.

21. Kricka, L. J. In *Optical Methods: A Guide to the -escences;* AACC Press: 2003; pp 42.

22. Nazarenko, I.; Bhatnagar, S.; Hohman, R. A closed tube format for amplification and detection of DNA based on energy transfer. *Nucleic Acids Res.* **1997**, *25*, 2516-2521.

23. Flechsig, G.; Peter, J.; Voss, K.; Grundler, P. Electrochemical DNA hybridization detection using the fluorescence quenching label dabcyl. *Electrochem. Commun.* **2005**, *7*, 1059-1065.

24. Parniak, M.; Min, K.; Budihas, S.; Le Grice, S.; Beutler, J. A fluorescence-based high-throughput screening assay for inhibitors of human immunodeficiency virus-1 reverse transcriptase-associated ribonuclease H activity. *Anal. Biochem.* **2003**, *322*, 33-39.

25. Neckers, D. C.; von B\unau, G.; Jenks, W. S. In *Photophysical Probes of DNA Sequence-Directed Structure and Dynamics;* Advances in Photochemistry; Wiley: 2009; pp 174.

26. Sch\afer, F. P. In *Dye Lasers;* Springer Berlin Heidelberg: 2013; pp 41.

27. Rajadhyaksha, M.; Gonzalez, S.; Zavislan, J.; Anderson, R.; Webb, R. In vivo confocal scanning laser microscopy of human skin II: Advances in instrumentation and comparison with histology. *J. Invest. Dermatol.* **1999**, *113*, 293-303.

28. Stallings, R. L. SK-N-AS Expression Profile. **2012**.

29. Malinin, T. I.; Perry, V. P. Toxicity of dimethyl sulfoxide on HeLa cells. *Cryobiology* **1967***, 4*, 90-96.

30. Da Violante, G.; Zerrouk, N.; Richard, I.; Provot, G.; Chaumeil, J.; Arnaud, P. Evaluation of the cytotoxicity effect of dimethyl sulfoxide (DMSO) on Caco(2)/TC7 colon tumor cell cultures. *Biol. Pharm. Bull.* **2002***, 25*, 1600-1603.

31. Notman, R.; Noro, M.; O'Malley, B.; Anwar, J. Molecular basis for dimethylsulfoxide (DMSO) action on lipid membranes. *J. Am. Chem. Soc.* **2006***, 128*, 13982-13983.

32. Patra, M.; Salonen, E.; Terama, E.; Vattulainen, I.; Faller, R.; Lee, B.; Holopainen, J.; Karttunen, M. Under the influence of alcohol: The effect of ethanol and methanol on lipid bilayers. *Biophys. J.* **2006***, 90*, 1121-1135.

33. Joshi, R.; Schoenbach, K. Electroporation dynamics in biological cells subjected to ultrafast electrical pulses: A numerical simulation study. *Phys Rev E.* **2000***, 62*, 1025-1033.

34. NEUMANN, E.; SCHAEFERRIDDER, M.; WANG, Y.; HOFSCHNEIDER, P. Gene-Transfer into Mouse Lyoma Cells by Electroporation in High Electric-Fields. *EMBO J.* **1982***, 1*, 841-845.

CHAPTER 4

Solution Phase Detection of miR-132

4.1 Introduction

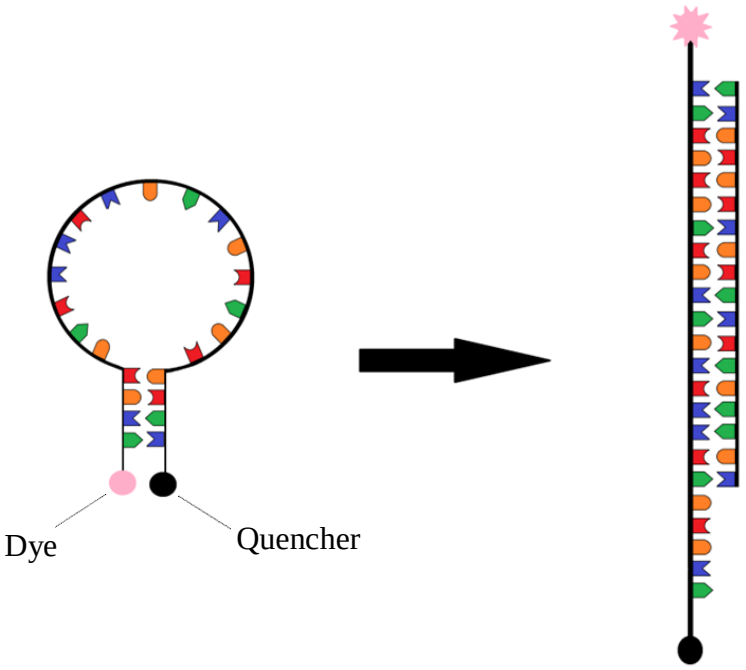

Figure 4.1 Scheme of MB attaching to miRNA target

The aim of this project was to detect the concentration and localisation of miR-132 in live neuroblastoma cells. In Chapter 3, the photophysics of the 6-FAM dye and dabcyl quencher were examined to characterise potential environmental impacts on the MB. An importation step in the process of live cell imaging was to fully understand the performance of the molecular beacon (MB) for the detection of the target in solution. The cellular environment contains a number of potential hazards for the detection of miRNA, including pH variation[1-3] and enzymes which can degrade DNA[4-6]. Solution phase testing allows for the performance of the MB to be probed without these potential complications which will aid in the interpretation of results from live cell imaging.

The emission of the dye in the absence of the target was examined also. This is important as the limit of detection of the MB is dependent on this background signal. This background can potentially be reduced by increasing the number of bases in the "stem" of the MB. This has the effect of increasing the relative stability of the self-bound form of the MB, which can result in a lower intensity signal. A second version of the MB was designed which aimed to improve the sensitivity of the assay by reducing the background emission in the absence of target.

Initially, solution phase testing was performed using a synthetic analogue of the target which allowed the detectable concentration range to be determined. This allows for the binding of the MB for the target to be calculated, which gives valuable information on the rate and reversibility of binding.

An important factor in the production of a MB for the detection of miRNA is specificity. A number of miRNA are present within cells which contain a number base matches with the target of interest. Detection of these sequences could lead to a higher signal, increasing the error associated the miRNA detection. To examine the specificity of the MB, a number of target sequences containing either one, two, or three mismatched bases were prepared. It is highly unlikely that miRNA are present within the cell with this high degree of similarity, so insensitivity to a single mismatch is indicative of a highly sensitive detection strategy.

Thermal cycling of the molecular beacon is also examined. This allows for the most stable conformer to become the predominant from. This provides information on the stability of the molecular bacon at varying temperature.

The ability of the MB to detect cellular miRNA target was then analysed using miRNA extracted from lysed neuroblastoma cells. This allowed the concentration of miR-132 within a single SK-N-AS cell to be estimated. This is important for future work with live cells, since the signal received from the MB should correspond to that seen in lysed cells.

4.2 Experimental

4.2.1 Materials

For DNA hybridisation, phosphate buffered saline (PBS) was prepared at a phosphate buffer concentration of 0.01 M and a sodium chloride concentration of 0.154 M using PBS tablets (Sigma Aldrich) in RNase free water.

Nucleic acids were synthesised by Exiqon at 85 % purity.

MB: 5'-6FAM+CGA+CCA+TGG+CTG+TAG+ACT+GTT+AGT+CG-DAB-3' (DNA/LNA where the + is a Locked Nucleic Acid)

miR-132 Mimic: 5'- UAA-CAG-UCU-ACA-GCC-AUG-GUC-G-3' (RNA)

1BMM: 5'- UAACAGUCUACAGCCAUGGUCC-3' (RNA)

2BMM: 5'- UAACAGUCUACAGCCAUGGUUC-3' (RNA)

3BMM: 5'- UAACAGUCUACAGCCAUGGGUC-3' (RNA)

4.2.2 Emission Spectroscopy

Emission spectra were obtained using a Jasco V-670. Emission and excitation slits were 20 nm for all experiments.

4.2.3 Time Correlated Single Photon Counting

Lifetime results were calculated using the PicoQuant FluoFit Pro version 4.6.6. In each case, an instrument response function (IRF) was collected, and the lifetime was fitted using an exponential model using reconvolution, whereby the IRF contribution to the signal was subtracted. Data was fitted to a single exponential providing it gave a good quality fit, i.e. a χ^2 value of below 1.2 with no systematic residual. Where this was not possible, two exponentials were fitted to the data.

The model used for performing multi exponential reconvolution fits is:

$$I(t) = \int_{-\infty}^{t} IRF(t') \sum_{i=1}^{n} A_i \, e^{-\frac{t-t'}{\tau_i}} \, dt' \qquad \textit{Equation 4.1: Lifetime fitting}$$

Where A_i = Amplitude of the i^{th} component in counts at time 0.

τ_i = Lifetime of the i^{th} component

4.2.4 RNA Extraction

A liquid-liquid extraction was used to selectively extract RNA from the cells. Cells were lysed with one volume of QIAzol reagent (Qiagen). Two volumes of chloroform were then added. The mixture was centrifuged for 15 minutes at 12,000 g to form two clearly defined layers. The RNA is retained in the colourless aqueous layer, whereas the DNA is retained in the pink organic layer. The upper phase, containing the RNA, was removed, 1.5 volumes of ethanol were added, and the solution was mixed well. The solution was added to an "RNeasy Spin Column". The column was then centrifuged at 13,000 rpm for 30 seconds. The RNA is retained on the column. The column was then washed with buffer RWT (Qiagen) and a further three times with buffer RPE (Qiagen). This removes impurities held in the column, leaving only purified RNA retained on the column. The RNA was then eluted out with 100 µL of RNase free water.

4.3 Results and Discussion

4.3.1 Concentration

The ability of the MB to detect the target miRNA, miR-132, in solution was investigated to allow calculation of the binding affinity of the MB to the target, and to calculate the linear detection range. The concentration of beacon was held constant at 1 µM, and the concentration of target was varied between 0.25 µM and 20 µM.

4.3.1.1 Absorption

Figure 4.2 shows the absorption spectra for the MB as the concentration of the miR-132 target in solution is increased. The shape of the absorption spectrum changes as the concentration of the target was varied, e.g., from 0 µM to 1 µM. Two distinct peaks were observed at 480 nm and 506 nm, but the relative intensity of the 480 nm peak decreased at higher target concentrations. The 506 nm peak was consistent with 6-FAM dye alone obtained at low concentrations, which had a peak at approximately 513 nm. The secondary peak at 480 nm was believed to have arisen from the dabcyl quencher which had a maximum absorbance at 453 nm. As the concentration increased, the 480 nm dabcyl peak remained constant, but the 506 nm peak increased, suggesting that opening of the MB was altering the absorption of the 6-FAM. If the excitation wavelength used was in the region of these peaks, then these changes in relative peak intensity would affect the expected linear dependence of the emission intensity on unfolded MB concentration. To avoid these issues, emission spectra were recorded using 395 nm excitation where the absorbance increases linearly with increasing concentration. While this did result in a lower overall signal intensity for the emission spectra, the brightness of the dye was still sufficient to provide an adequate signal.

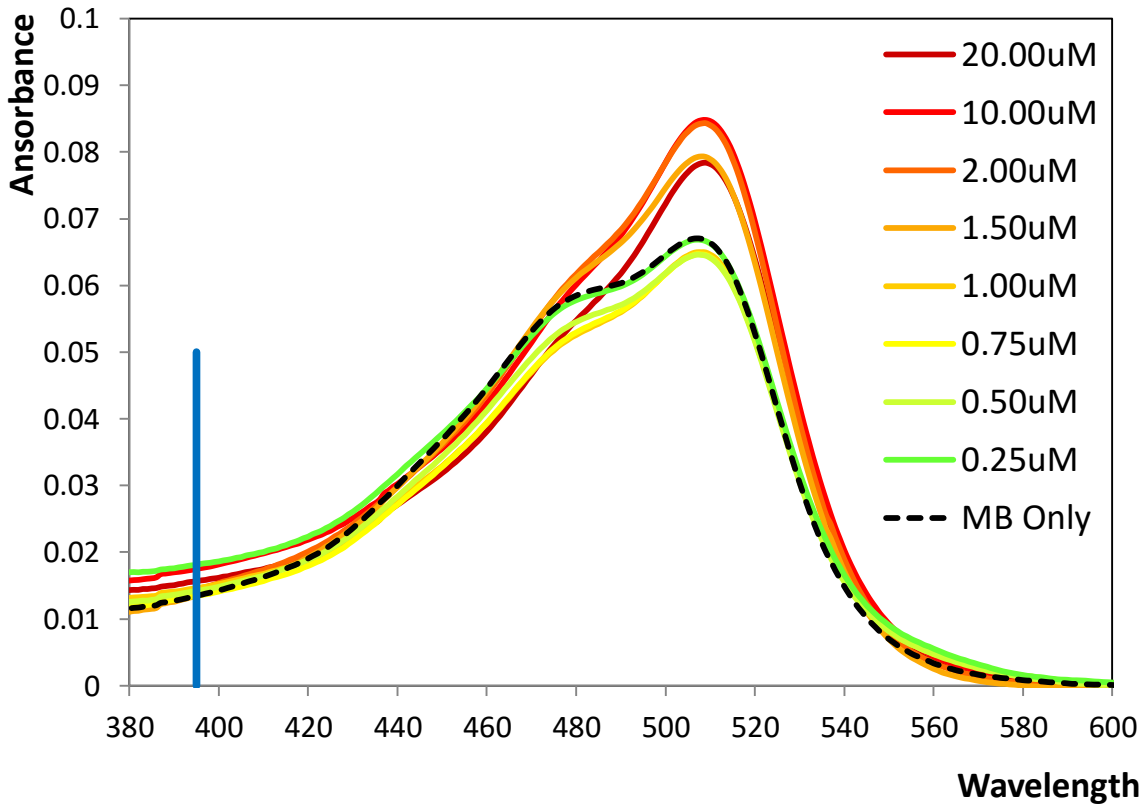

Figure 4.2: Absorption spectra of 1 µM MB in PBS with varying concentration of miRNA-132 between 0.25 µM and 20 µM, after a hybridisation time of 10 minutes.

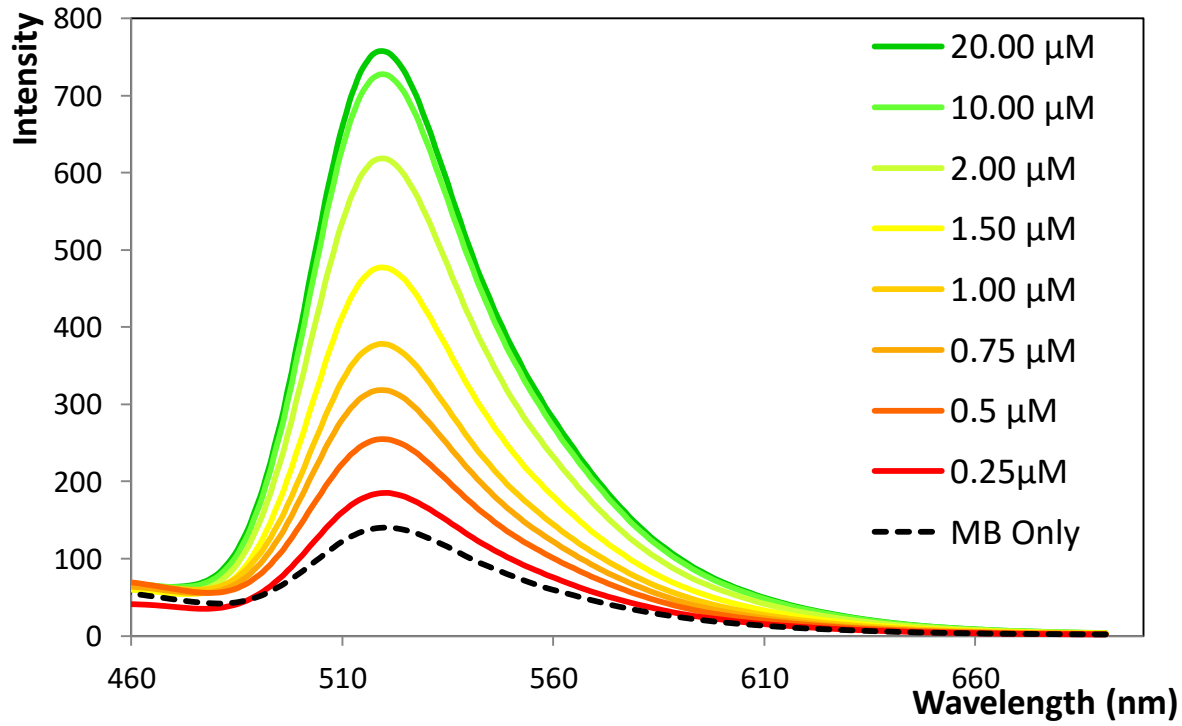

Figure 4.3: Emission spectra of 1 µM MB in PBS with varying concentration of miRNA-132 between 0.25 µM and 20 µM, after a hybridisation time of 10 minutes. Emission and excitation slits were 20 nm, excitation at 395 nm.

4.3.1.2 Emission

Figure 4.3 shows the emission intensity measured using 395 nm excitation. Following addition of the target, the emission increased rapidly but stopped increasing after less than 1 minute, indicating rapid opening of the stem-loop structure which is highly desirable for imaging applications.[7,8] This suggests that the beacon : target hybrid has excellent binding efficiency, which allows this method to provide very fast results, especially when compared with traditional techniques such as PCR[9,10] or Northern blotting[11,12].

As illustrated in Figure 4.3, the time independent emission intensity increases linearly with increasing target concentrations up to 2 µM (mole ratio MB:target, 1:2) before saturation is observed for concentrations above 10 µM (mole ratio MB:target, 1:10). This behaviour is consistent with target binding and unfolding of the stem loop which increases the separation between dye and quencher resulting in a turn on of the emission. Above this concentration of 2 µM, there is insufficient self-bound beacon and the emission intensity no longer increases with an increasing concentration of the target. The observation of a background emission from the beacon in the absence of target significantly increases the LOD.[13,14]

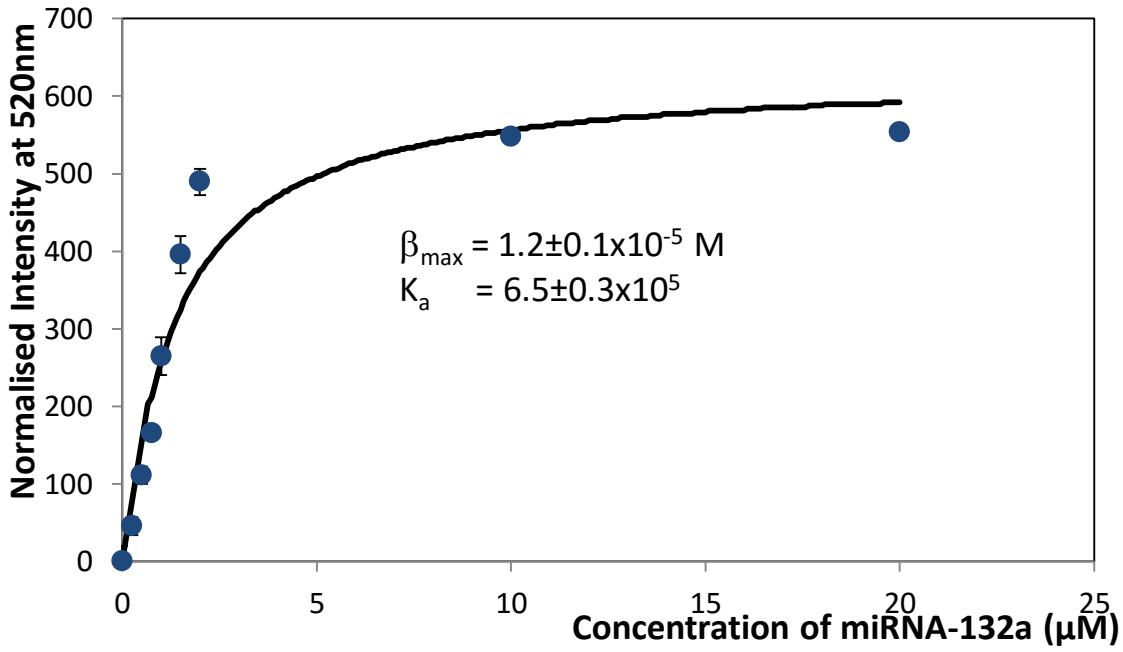

Figure 4.4 Dependence of the emission intensity of a 1 µM solution of the MB in PBS on the concentration of the miR-132 target after a hybridization time of 10 minutes. Corrected to remove background emission in the absence of target. The solid line is the least squares fit of Equation 4.2 to the experimental data. Emission and excitation slits were 20 nm excitation at 395 nm. 3 repeats were performed for each experiment.

Figure 4.4 shows the emission intensity at 520 nm as the concentration is increased. Binding at a single site can be described by the following equation[15]:

$$\frac{[Hairpin]}{[miR-132]} = \frac{\beta_{\max}[miR-132]}{K_a + [miR-132]}$$

Equation 4.2: Single site binding

where β_{max} and K_a are the maximum specific binding and equilibrium association constants, respectively. Figure 4.4 shows the best-fit obtained which yields an association constant of 6.5±0.4 x 10^5 indicating that the equilibrium strongly favours the formation of the hybridized product with a corresponding Gibbs free energy of -33.1±0.2 kJmol^{-1}, calculated using UNAFold software.

Table 4.1 Lifetime results based on three repeats for 1 µM MB in PBS with varying concentration of miRNA-132 between 0.25 µM and 20 µM, after a hybridisation time of 10 minutes when the emission is time independent.

	τ_1 (ns)	%	τ_2 (ns)	%	χ^2
MB	3.6±0.0	43.1±1.1	1.1±0.0	56.9±1.27	1.27±0.08
0.25 µM	3.4±0.0	57.5±2.8	1.1±0.0	42.5±1.16	1.16±0.03
0.50 µM	3.3±0.0	68.6±0.6	1.1±0.0	31.4±1.16	1.16±0.11
0.75 µM	3.3±0.0	70.7±1.7	1.1±0.0	29.3±1.14	1.14±0.02
1.00 µM	3.3±0.0	73.9±1.5	1.1±0.0	26.1±1.12	1.12±0.08
1.50 µM	3.3±0.0	76.3±1.7	1.1±0.0	23.7±1.11	1.11±0.06
2.00 µM	3.3±0.0	79.0±1.2	1.1±0.0	21.0±1.18	1.18±0.06
10.00 µM	3.3±0.0	81.5±1.4	1.1±0.0	18.5±1.15	1.15±0.04
20.00 µM	3.3±0.0	83.2±0.7	1.1±0.0	16.8±1.16	1.16±0.08

4.3.1.3 Lifetime

The lifetime results for this concentration study are presented in Table 4.1. The lifetime could not be fitted accurately to a single exponential, so a bi-exponential model was used to fit this data. The two lifetimes obtained are 3.3±0.1 ns and 1.1±0.0 ns. The long time component is similar to the lifetime for 6-FAM in 1 % DMSO of 4.1 ns, suggesting that it is associated with those conformations of the MB where the dye and quencher are insufficiently close to quench the emission. When the target is absent, the majority of the lifetime contribution is from the shorter lifetime, at 57±1.3 %. As the target is added, the shorter lifetime intensity drops, reaching 16.8±1.16 % at 20 µM target. As target is introduced the percentage of MB in the open position increases, resulting in enhancement of the 3.3±0.1 ns lifetime. The shorter lifetime is most likely due to instrumental noise[16], as it remains consistent throughout the experiment, with the apparent change in relative intensity caused by an increase in the intensity of 3.3±0.1 ns lifetime noise.

Noise in TCSPC can occur due to electronic interference. If the different components of the TCSPC are powered by different power outlets, as was the case in these experiments, RF radiation from external sources to be introduced into the set-up. This can also occur if the computer attached to the TCSPC is connected to a wired network.[17] This noise in exceptionally difficult to present. In this system, the noise only appears to become a significant issue when the intensity of the dye is low.

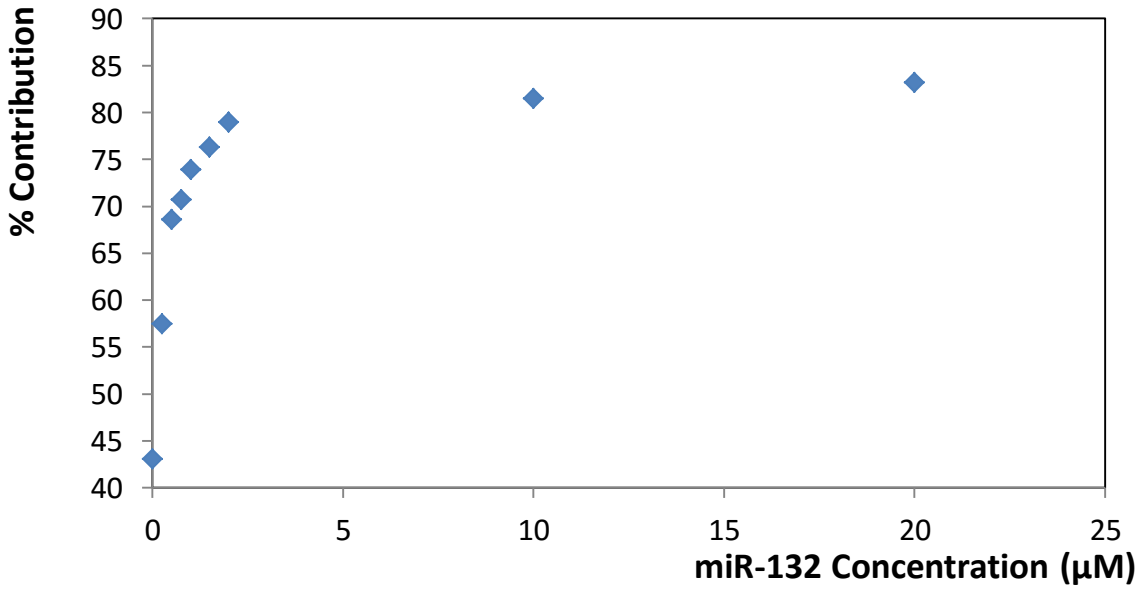

Figure 4.5 Change of 3.3±0.1 ns lifetime component of a 1 µM solution of the MB in PBS with miR-132 target between 0.25 µM and 20 µM, after a hybridisation time of 10

minutes. 3 repeats were performed for each experiment, error bars are smaller than the size of icons.

As illustrated in Figure 4.5, as the concentration of target is increased, a shorter lifetime contributed less to the signal, with the 3.3 ns lifetime becoming dominant contributing 73.9±1.5 % of the intensity where the target concentration is 1.0 µM. This transition from a bi-exponential decay towards a single decay at 3.3 ns was consistent with opening of the MB and with the dye's properties moving closer to those previously seen for free 6-FAM.

4.3.2 RNA Extraction from SK-N-AS Cells

As the MB had been successfully measured using a synthetic strand of miR-132 in solution, the next goal was to determine if detection was possible using a real sample containing miR-132. The SK-N-AS cell line was chosen as a source of miR-132 as it has been shown to highly express this miRNA.[18]

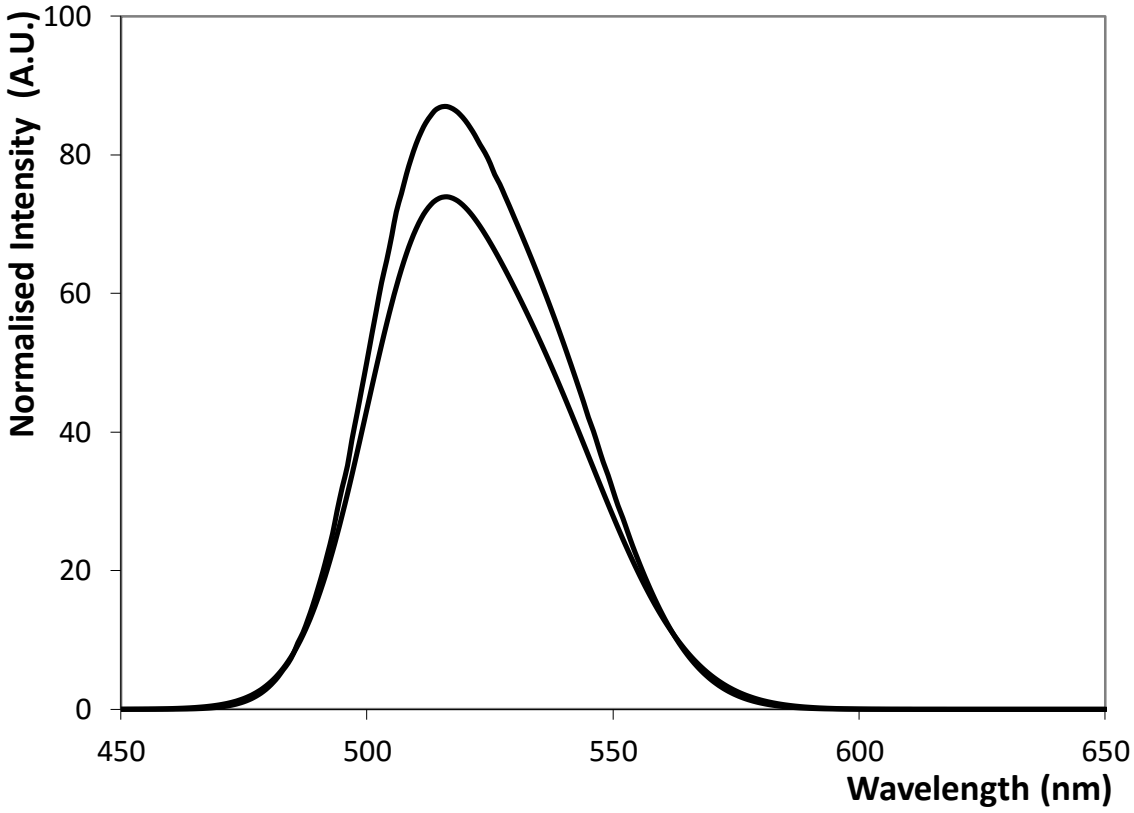

Figure 4.6: Emission spectra from the miRNA extracted from two independent batches of 10^7 SK-N-AS cells following addition of the MB to give a concentration of 1 µM. Emission and excitation slits were 20 nm, excitation at 395 nm.

The total RNA present in a suspension of SH-N-AS cells (10 mL, 1.6 x 10^6 cells per mL) was extracted, precipitated and taken up into 100 µL of buffer. The MB complex was then added to give a final concentration of 1 µM and allowed to equilibrate for 30 minutes. Figure 4.6 shows the emission for two extracted samples using 395 nm excitation. The wavelength of maximum emission was shifted to shorter wavelengths by approximately 7 nm for the cell extract compared to the calibration solutions, most likely due to solvatochromic effects due to the more complex nature of the extracted cells compared to the clean buffer calibration solutions.

Using the calibration data shown in Figure 4.4, the concentration of the miRNA target within the cell extract was approximately 0.45 µM. Given that the volume of a single SK-N-AS cell is approximately 20 pL, the concentration of an individual cell is approximately 0.14 µM. This figure was strikingly high compared to miRNA concentrations found in other cells[19-21], and suggests a high expression level in neuroblastoma cells. This higher than expected value may be due to the binding of the MB to the immature versions of miR-132, as these contain the same nucleic acid sequence.[22] A number of studies have shown that the concentration of immature miRNAs can be equal to or higher than the concentration of mature miRNA.[23,24] There are a number of possible errors in the calculation of this value. Cell counting was performed using a hemocytometer which has the potential to introduce error with regard to the total number of cells present in the sample. In addition, other RNA present in the sample may be capable of causing opening of the molecular beacon, which could cause higher than expected intensity. Further analysis would be required to achieve a definite conclusion on the cellular miRNA concentration. Significantly, the miR-132 concentration for two independently analysed batches of cells, cultured separately, agree to within 10 %. Overall, these *in vitro* experiments using lysed cells strongly suggest that the MB has attractive properties for live cell imaging which will be examined in a later section.

4.3.3 Base Mismatch

4.3.3.1 Emission

Beyond the issue of sensitivity, a key issue to be considered is the selectivity of the beacon:miR-132 interaction. Therefore, the emission response where the target contains one, two and three mismatches, was investigated. A number of miRNA are present in cells which have some structural similarity to miR-132, including miR-212[25] and let-7f[26] which each share 9 base pairs. Figure 4.7 shows the emission spectra for a 1 µM solution of the MB in the absence of miR-132 target as well as in the presence of 1 µM of targets that differ from the fully complementary sequence by 1, 2 or 3 bases. The signal due to one and two base mismatches was indistinguishable from that observed for the beacon in the absence of the target, i.e., even when the target contains only a single mismatch, no significant hybridization occurs and no increase in emission intensity was observed. The signal for 3 base mismatches was somewhat higher than that found for the 1-base mismatch but the response was still three times lower than that found for the fully complementary which suggests good selectivity for this assay.

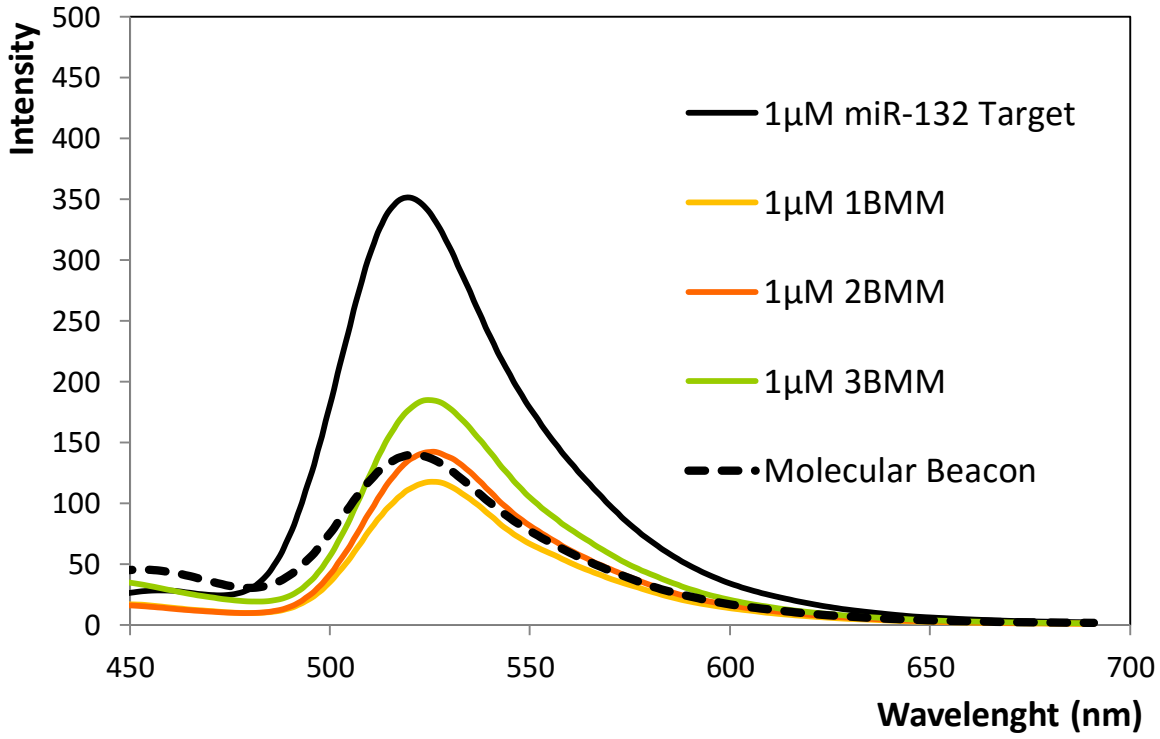

Figure 4.7: Emission spectra of 1 µM MB in the presence of 1 µM of fully complementary target and 1 µM of 1, 2 and 3 base mismatch. Emission and excitation slits were 20 nm, excitation at 395 nm.

4.3.3.2 Absorption

The absorption spectra for the MB with the fully complementary target and strands which contain mismatches are shown in Figure 4.8. As observed in the concentration study, the spectrum of the MB alone has a primary peak at 506 nm, with a secondary peak at 480 nm. The shape of the peak changes significantly upon the addition of target, with the 480 nm peak becoming less pronounced. This same trend is seen for the mismatched bases. Interestingly, the 1 base mismatch had the smallest 480 nm shoulder, and this increased in size for the 2 BMM, and larger again for the 3BMM. This represents further evidence that the binding of these additional strands is impacted by the number of mismatched bases present.

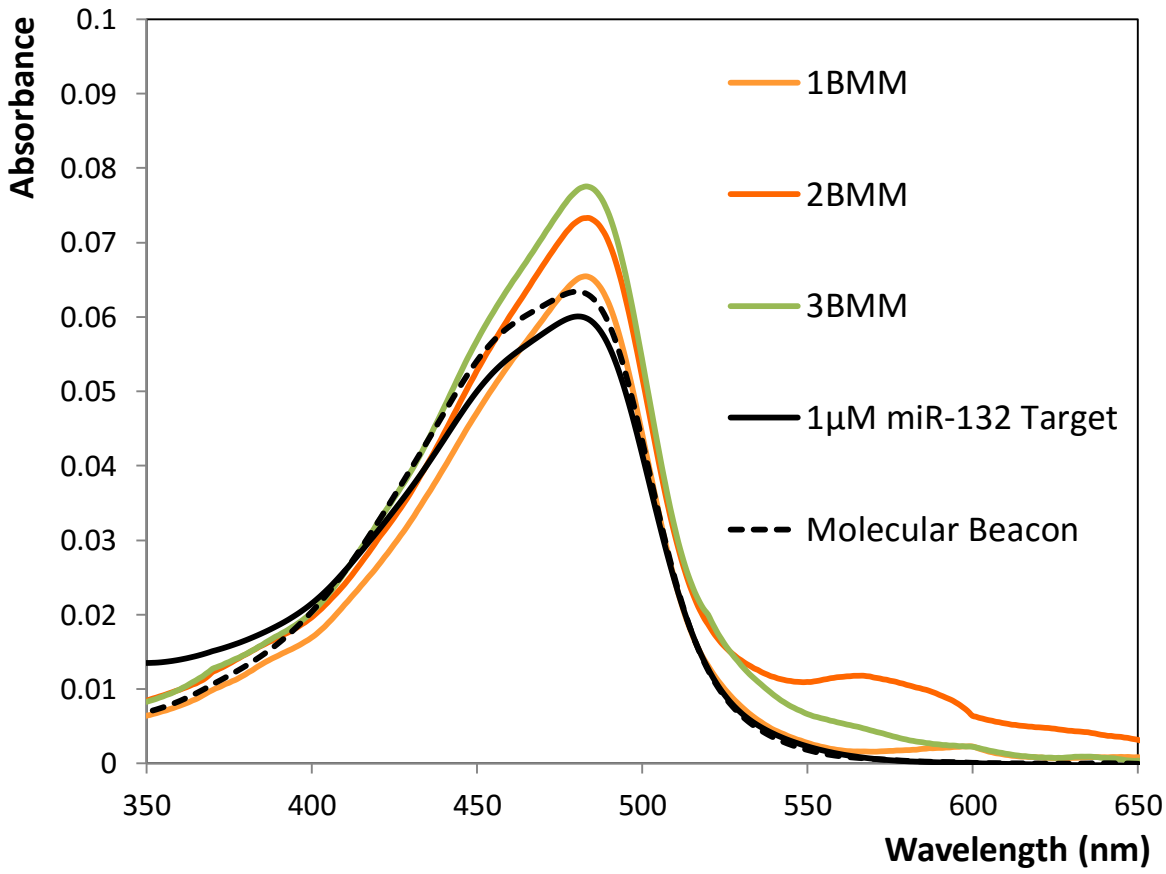

Figure 4.8: Absorption spectra of 1 µM MB in the presence of 1 µM of fully complementary target and 1 µM of 1, 2 and 3 base mismatch.

4.3.3.3 Lifetime

The TCSPC results for this experiment are shown in Table 4.2. As in the concentration study, two exponentials were required to fit this data. These two lifetimes were in the region of ~3 ns and ~1 ns. The MB only shows 45±1.74 % contribution from the longer lifetime, with the perfectly complementary target at 74±4.00 %, and so based on the emission results obtained, it was expected that the contribution from the ~3 ns component would fall between these two values for the base mismatched RNA. The 1BMM had a value of 63±5.1 % which while high, falls within the expected values. The 2BMM however, was 98±09 %, and the 3BMM was 91±27 %. These values were exceptionally high compared to the concentration curve lifetimes previously seen where the maximum ~3ns contribution was 84±2.2 % for 20 µM of target with 1 µM of MB. This data suggests that the contribution of the longer and shorter lifetime signal may not be a useful measure of the opening of the MB.

Table 4.2 Lifetime results of 3 repeats of 1 µM MB in PBS with 1 µM of fully complementary target and 1 µM of 1, 2 and 3 base mismatch.

	τ_1 (ns)	%	τ_2 (ns)	%	χ^2
MB	3.2 ± 0.25	45±1.7	0.8 ± 0.19	55 ± 1.7	1.20±0.01
1 BMM	3.7±0.12	63±5.1	1.5±0.10	37±5.1	1.03±0.05
2 BMM	3.9±0.02	98±0.9	1.1±0.01	2±0.9	1.12±0.05
3 BMM	3.8±0.09	91±2.7	1.3±0.50	9±2.7	1.07±0.11
Target	3.3±0.07	74±4.0	1.1±0.17	26±4.0	1.16±0.01

4.3.4 Alternate Conformers

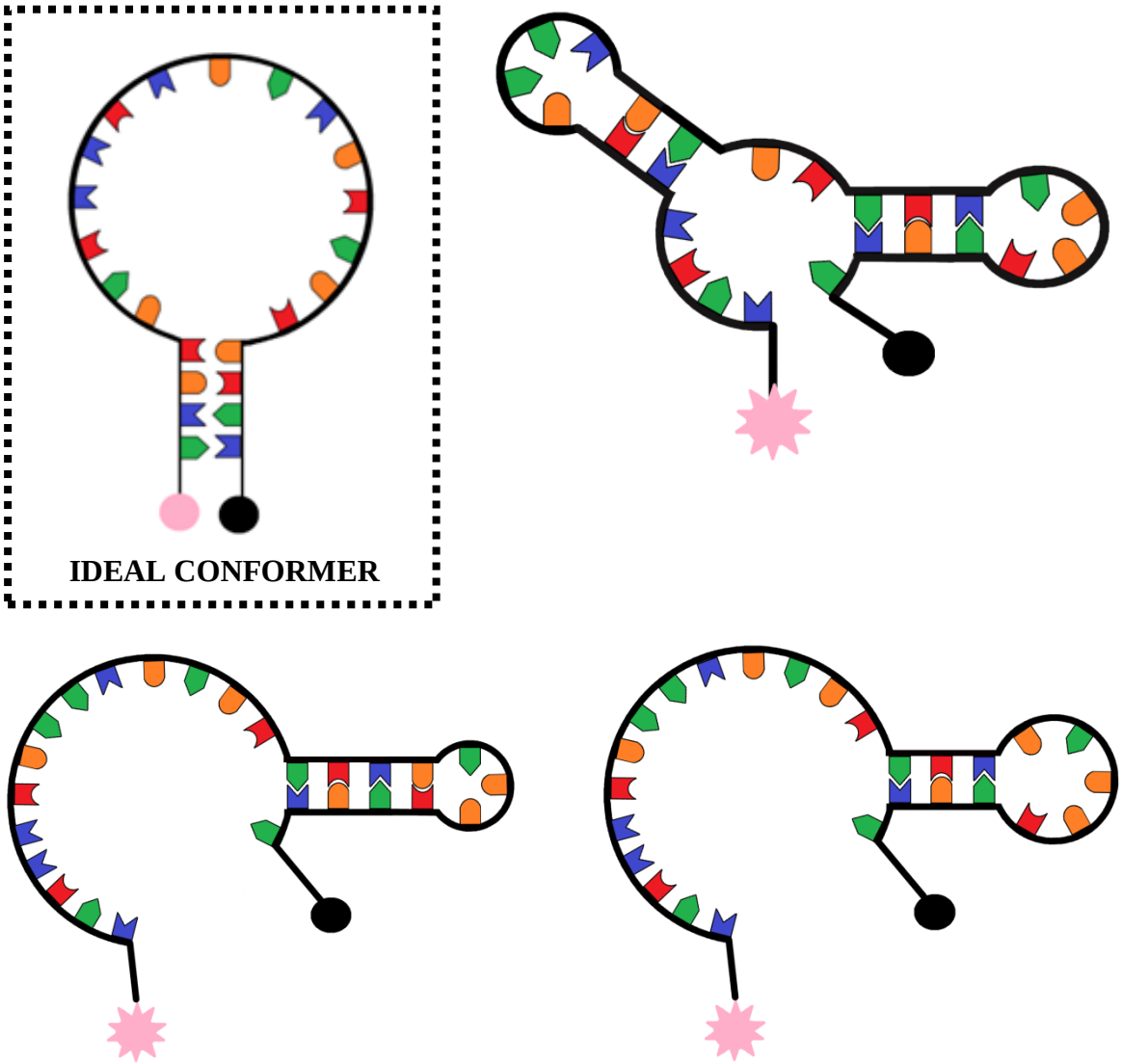

Figure 4.9 Preferred and potential alternate conformations of the MB in the absence of target.

Table 4.3 Calculated binding energies of preferred and possible alternate conformers of the MB in the absence of target.

	ΔG (kcal.mole^{-1})	**Melting Temperature (°C)**
Preferred Conformer (A)	-0.84	33.7
Alternate (B)	-0.45	27.9
Alternate (C)	-0.86	35.3
Alternate (D)	-1.18	39.0

As mentioned previously, when the MB was measured in the absence of target, a measurable emission is observed. To determine the possible causes for this signal, molecular modelling was performed using UNAfold solfware. This analysis found that three alternate conformers exist when the dye and quencher are separated by a distance greater than the FRET distance, see Figure 4.9. This modelling treats every base in the MB as DNA, and does not take into account the additional stability granted due to the LNA. The most stable other confirmer, (D), shown above, has a predicted melting temperature of 39.0 °C, whereas the preferred conformer had a predicted melting temperature of only 33.7 °C.

4.3.5 Temperature Study

To test the impact of these additional conformers on the background signal intensity, a temperature study was undertaken. Other work with MBs has used thermal cycling, which involves increasing the temperature of the solution to melt all of the various forms, and then allowing the solution to cool.[27,28] This should allow the most stable conformer to become the predominant form.

Figure 4.10 shows the results of this experiment. The sample was measured before heating and brought to 70 °C for 1 hour to ensure complete melting of the beacon. The sample was then placed in a fluorimeter and measured at 1 minute intervals as it cooled. Initially, a large signal was observed, with the maximum intensity increasing four-fold suggesting successful opening of the MB. This is consistent with the enhancement in intensity observed for saturation of the MB with miR-132, see Figure 4.3, which resulted in a 4.5 fold increase in intensity. As the sample cooled to room temperature the signal intensity dropped significantly and within 7 minutes had reached the same intensity to within 6.6 % of that observed before heating. The sample was allowed to cool for 2 hours in total, but no further drop in intensity was observed. This experiment suggests that despite the previous modelling undertaken, that the predominant form is the “ideal conformer”, based on the 4-fold decrease in signal intensity upon cooling. The presence of a signal after heating, however, suggests that in order to further reduce this background intensity, design changes would need to be made to the beacon.

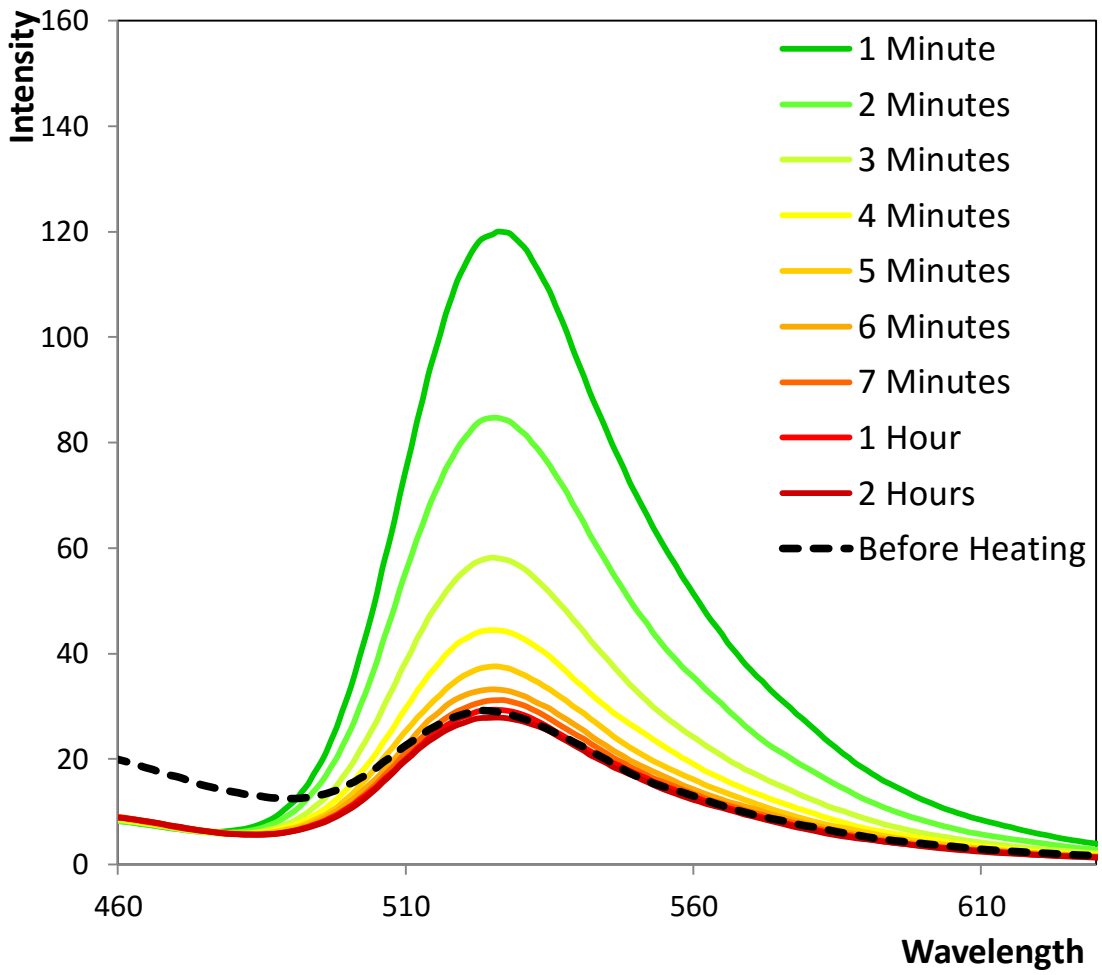

Figure 4.10 Emission spectra of 1 µM MB after being heated to 70 °C for 1 hour. Emission and excitation slits were 20 nm, excitation at 395 nm.

4.3.6 MB Version 2 (MB2)

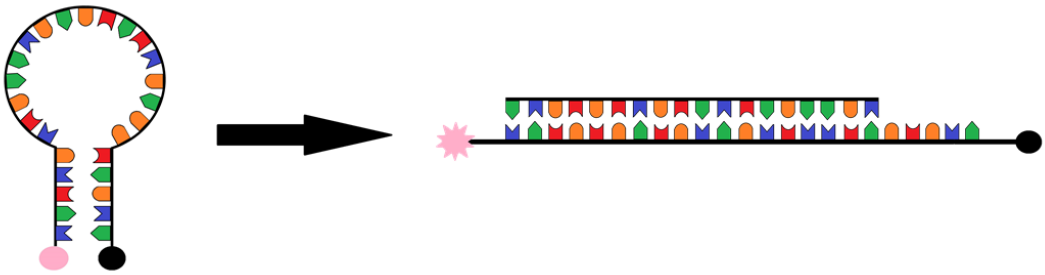

Figure 4.11 Scheme of MB version 2, with five bases in the stem section.

When designing the second iteration of the MB (MB2), the primary focus was to decrease the background signal present in the absence of target. To achieve this, the number of bases in the "stem" of the MB was increased from four to five. Previous work has shown that this can further stabilise the self-bound form in the desired conformer[29,30]. While an increase in the stability of the self-bound form was desirable to reduce the background, it also had the potential to reduce the absolute sensitivity of the beacon, as the self-bound form was less likely to be opened by the target.[31,32]

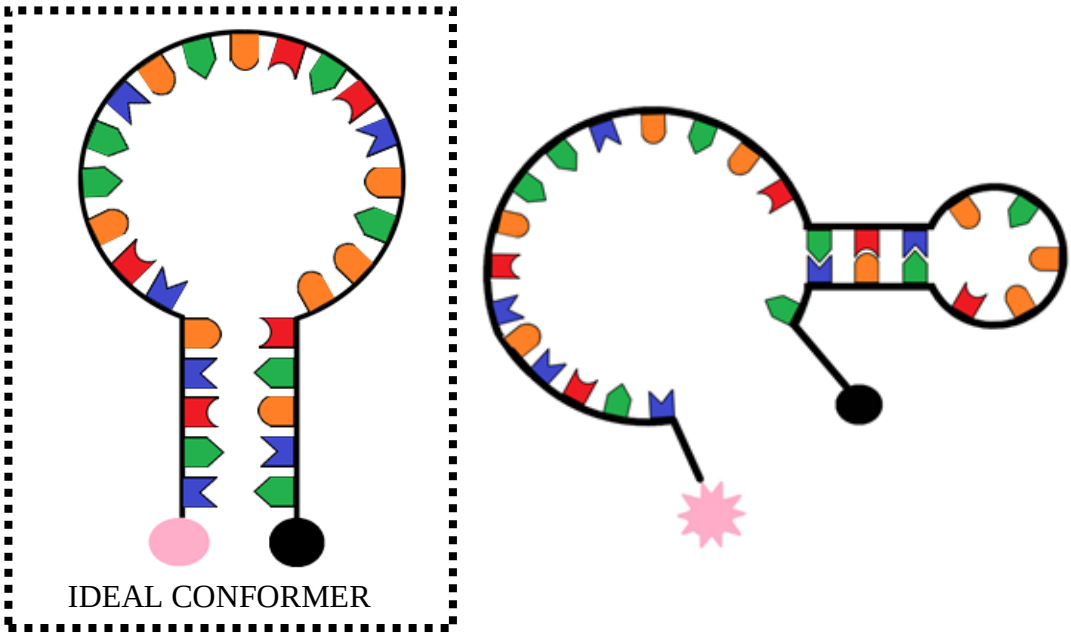

Figure 4.12 Preferred and potential alternate conformation of MB2 in the absence of target.

Table 4.4 Calculated binding energies of preferred and possible alternate conformers of MB2 in the absence of target.

	ΔG (kcal.mole^{-1})	**Melting Temperature (°C)**
Preferred Conformer (A)	-1.87	40.5
Alternate (B)	-1.18	39.0

Molecular modelling of the structure was performed before the synthesis of the new beacon, see Figure 4.12. The number of predicted alternate structures of significant stability was reduced to one with this new iteration. The melting temperature of the ideal form was predicted to increase to 40.5 °C, compared with 33.7 °C in the previous version. Importantly, the single predicted alternate conformer was predicted to occur at 39.0 °C, which should favour the ideal form.

Figure 4.13 shows the absorption matched emission spectra for the two versions of the MB in solution at 1 µM. The maximum emission intensity was reduced by approximately 20 % for the second iteration of the MB, suggesting that the preferred self-bound form of the beacon had become more favoured as a result of the stem length being increased. Based on the molecular modelling previously shown, it was expected that this decrease in signal in the absence of the miRNA target would be more significant due to the expected decrease in alternate conformers.

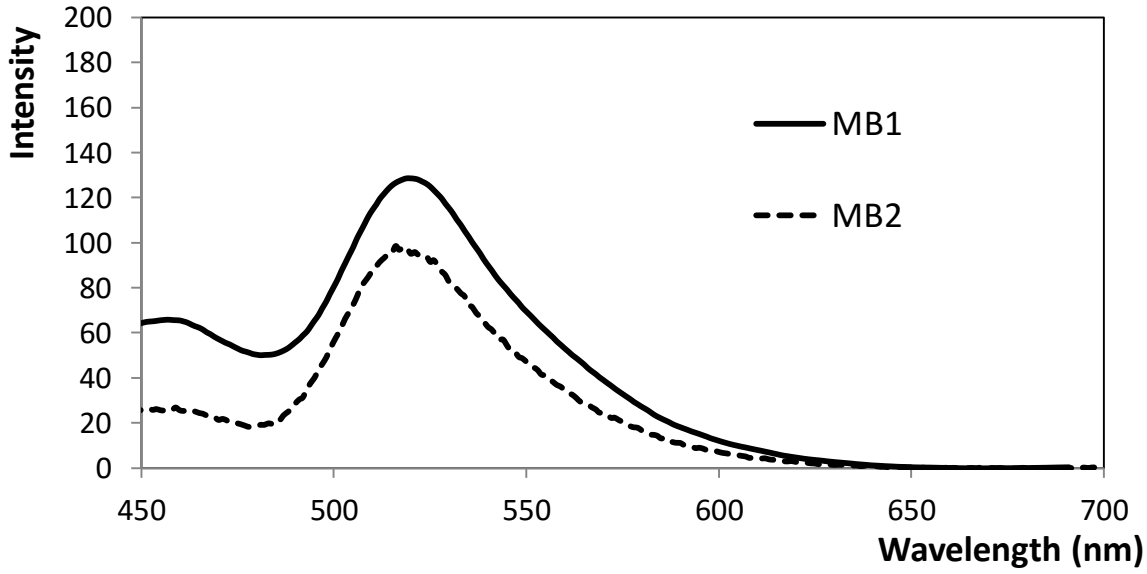

Figure 4.13 Emission spectra for 1 µM of MB1 and MB2 in PBS after excitation at 395 nm, absorbance matched. Emission and excitation slits were 20 nm.

The ability of the second MB (MB2) to detect the target miRNA, miR-132, in solution was investigated to allow comparison to the previous version. As before, the concentration of beacon was held constant at 1 µM, and the concentration of target was varied between 0.25 µM and 20 µM.

4.3.6.1 Absorbance

The absorbance spectra for MB2 is shown in Figure 4.14. Two peaks were observed at 496 nm and 461 nm. This is shifted slightly from MB1, which show maximum absorbance at 506 nm and a secondary peak at 480 nm. As the concentration was increased, the 461 nm peak remained constant and the 496 nm peak increased in size, suggesting that the opening of the beacon increased the amount of 6-FAM available to give rise to this signal. Based on this data, it was decided to use an excitation wavelength of 395 nm as before, as this region of the curve is not affected by changes in the concentration which could distort the emission spectra. Overall the absorption spectra for MB2 was highly consistent with MB1, as was expected based on the high structural similarity between the two structures.

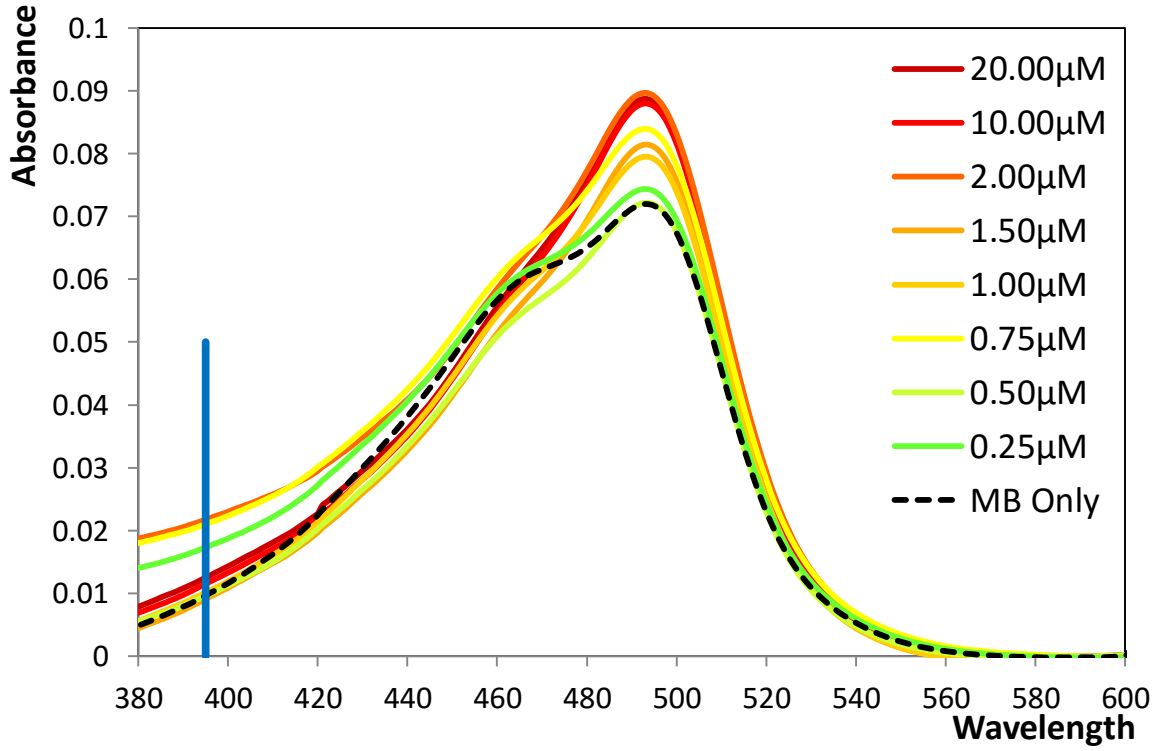

Figure 4.14 Absorption spectra of 1 µM MB 2 in PBS with varying concentration of miRNA-132 between 0.25 µM and 20 µM, after a hybridisation time of 10 minutes.

4.3.6.2 Emission

The emission spectra for 1 µM of the MB2 with a range of miR-132 concentrations are shown in Figure 4.15. The signal increased significantly with the addition of target, with a linear increase being observed from 0.25 µM to 2 µM of target. After this point the intensity begins to level out, signifying that there is insufficient self-bound beacon, resulting in a constant emission intensity. This data was highly similar to the MB1, which showed a similar linear range of detection.

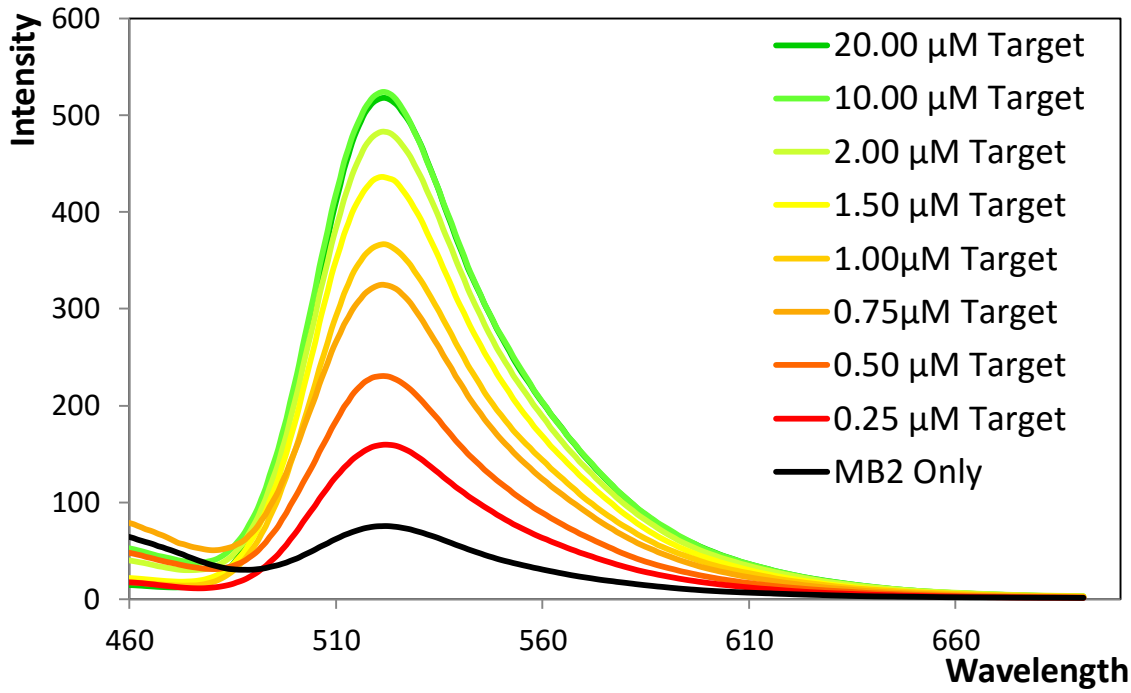

Figure 4.15: Emission spectra of 1 µM MB2 in PBS with varying concentration of miRNA-132 between 0.25 µM and 20 µM, after a hybridisation time of 10 minutes and after excitation at 395 nm with excitation slit 20 nm and emission slit 20 nm.

Figure 4.16 shows the best-fit obtained which yields an association constant of $1.34\pm0.4 \times 10^6$, with a corresponding Gibbs free energy of -34.4 $kJmol^{-1}$, indicating that the equilibrium strongly favours the formation of the hybridized product. The value observed is approximately double the $6.5\pm0.3 \times 10^5$ achieved for the original version of the beacon, which suggest the binding affinity is even higher for MB2. Based on simple modeling of the two beacons which assumes that all the bases are DNA[33], MB1 was calculated to have a Gibbs free energy of -33.39 $kcal.mol^{-1}$, with MB2 at -47.59 $kcal.mol^{-1}$. This is an increase of approximately 21 %. While both calculations show an increase in the association of MB2 to the miR-132 target, the size of this

increase is different between the two models. The calculated association value is believed to be more accurate, as it is based on experimental results.

Overall, this increase in the association of MB2 and the target proves attractive for detection at lower concentrations, as this suggests that the MB will be more likely to open with lower amounts of miR-132. This may however, prove to have implications for the selectivity of the beacon.[34]

The maximum intensity of the two beacons, normalized to remove the backroom signal, are shown in Figure 4.17. The two beacons were virtually indistinguishable at low concentrations from 0.25 µM to 2 µM, with very similar increases in intensity. The MB2 reached saturation at 2 µM, whereas the MB1 shows an increase up to 10 µM. This is consistent with the association constants previously discussed, with the MB2's higher affinity resulting in saturation being reached at a lower target concentration. Overall from these results, the two MBs behave very similarly, with no major improvement for the MB 2 in terms of limit of detection or the background emission.

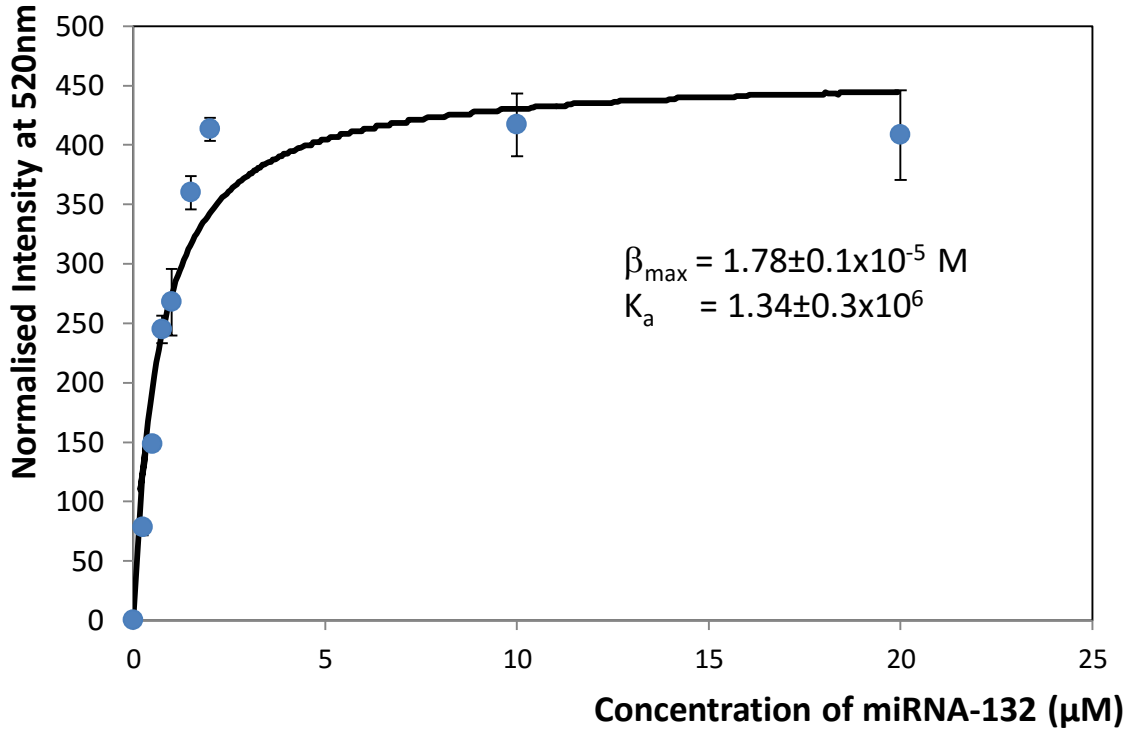

Figure 4.16 Dependence of the emission intensity of a 1 µM solution of the MB2 in PBS on the concentration of the miR-132 target after a hybridization time of 10 minutes. The solid line is the least squares fit of Equation 1 to the experimental data. Emission and excitation slits were 20 nm, excitation at 395 nm.

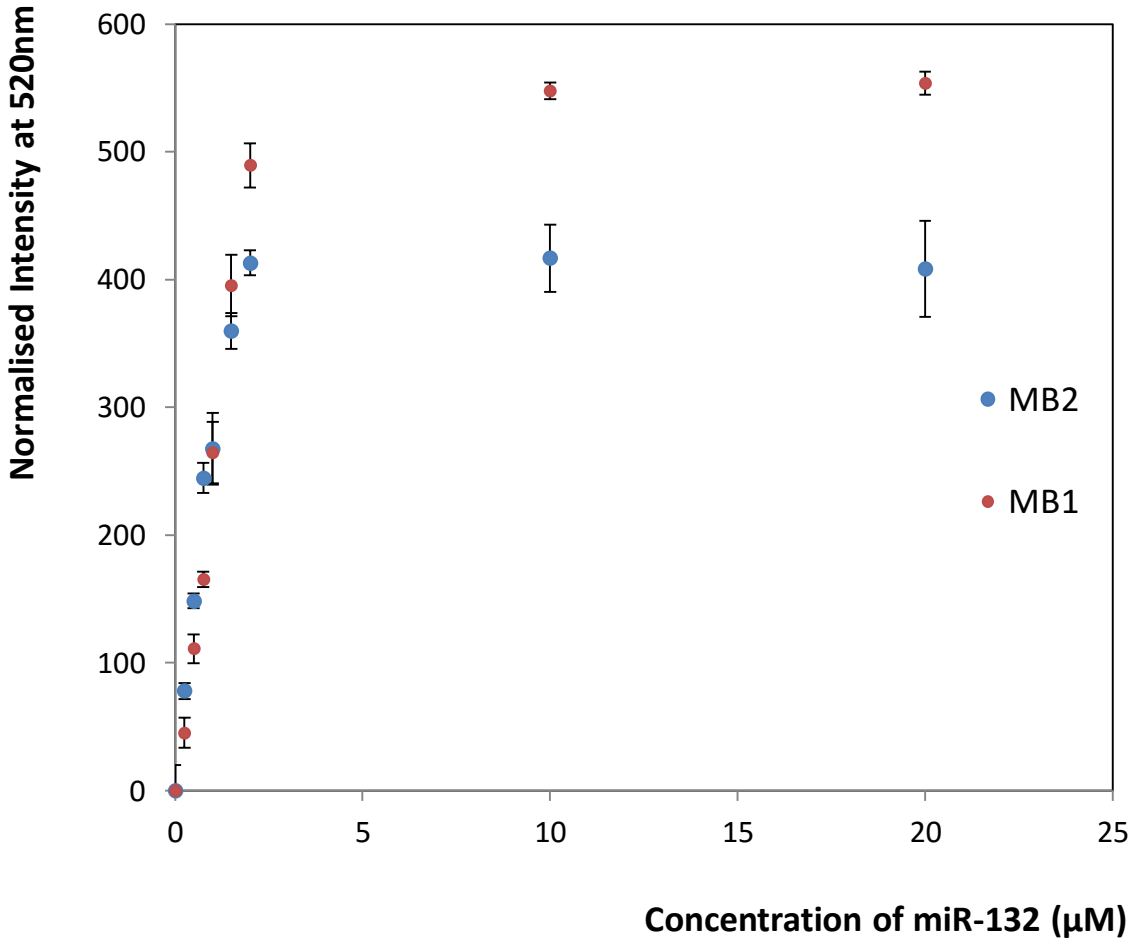

Figure 4.17 Comparison of the emission intensity of a 1 µM solution of the MB1 and MB2 in PBS on the concentration of the miR-132 target after a hybridization time of 10 minutes. Emission and excitation slits were 20 nm, excitation at 395 nm.

4.3.6.3 Lifetime

The TCSPC results for the concentration range investigated are shown in Table 4.5. Two lifetimes were observed in the absence of target at 3.1±0.0 ns and 0.6±0.1 ns. These two lifetimes were similar to those observed for MB1 at 3.6±0.0 ns and 1.1±0.0 ns. In MB1, the longer lifetime accounted for 43±1.1 % of the signal, whereas in MB2 this had increased to 72±0.9 % of the signal intensity. As the concentration was increased, the shorter lifetime contributed less to the signal and at 2 µM, where saturation of the MB2 was seen in the emission spectra previously, the lifetime decay became mono-exponential, with the shorter lifetime disappearing completely. In the MB1, the shorter lifetime also contributed less to the decay as the concentration increased, reaching 17±1.2 % at saturation. The MB2 did not show a residual short lifetime at saturation, which was consistent with the shorter lifetime arising from instrumental noise.

Table 4.5 Lifetime results of 3 repeats of 1 µM MB2 in PBS with varying concentration of miRNA-132 between 0.25 µM and 20 µM, after a hybridisation time of 10 minutes when the emission is time independent.

Concentration (µM)	**τ_1 (ns)**	**%**	**τ_2 (ns)**	**%**	**χ^2**
0.00	3.1±0.0	72±0.9	0.59±0.1	28±0.8	1.12±0.03
0.25	3.4±0.1	94±1.1	1.04±0.2	6±1.1	0.99±0.10
0.50	3.3±0.0	93±3.5	1.03±0.3	7±3.5	0.97±0.04
0.75	3.4±0.0	94±2.5	1.08±0.4	6±2.5	1.03±0.10
1.00	3.4±0.0	83±1.1	1.15±0.2	17±1.1	1.30±0.38
1.50	3.4±0.0	92±3.2	1.09±0.3	8±3.2	1.06±0.07
2.00	3.3±0.0	100±0.0	N/A	N/A	1.10±0.03
10.00	3.3±0.0	100±0.0	N/A	N/A	1.12±0.07
20.00	3.3±0.0	100±0.0	N/A	N/A	1.15±0.01

4.4 Conclusions

The goal of this work was to study the localisation and concentration of miR-132 in live neuroblastoma cells. An importation step towards this goal was quatification of the MB in solution phase, as this allows the binding of the miR-132 to the MB to be studied outside of the complexity of a live cell. This can inform the interpretation of results from live cells, which is presented in a later section.

The first objective of this chapter was to test the ability of the MB to detect its miRNA target in solution. The 1 µM MB was shown to be capable of detecting miR-132 with linear increase in the emission intensity as the target concentration is increased from 0.25 µM to 2.0 µM. Above this point the increase in intensity with increasing concentration of the miR-132 target began to decrease. This is consistent with the solution containing insufficient quantity of the molecular beacon in the self-bound form.

The MB was shown to be high selective, with excellent discrimination for one, two and three base mismatches. The intensity from 1BMM and 2BMM was lower than that seen for 3BMM. The reason for this difference is not known, however the intensity is considerably lower for all of the mismatches studied. Within a live cell, no miRNA have been detected with such high similarity, so the insensitivity of the MB to 3BMM should insure high specificity in the cellular environment.

The MB was also capable of detecting miR-132 from a neuroblastoma cell line, SK-N-AS, which gave a cellular concentration of miR-132 within the cell of approximately 0.14 µM. This value is an approximation of the cellular miR-132 concentration. One major source of error for this measurement is the counting of the cells. Cell were counted with a haemocytometer, for a more accurate cell count flow cytometry would be required. This may improve the accuracy of this cellular concentration result.

A significant signal was detected for the MB in the absence of target despite the use of a black hole quencher. Molecular modelling predicted the presence of three alternate conformers with similar association energies. The separation between the 6-FAM and the dabcyl quencher is larger in some of these conformers, which may explain this signal. Thermal cycling of the beacon resulted in no change in intensity, suggesting that the difference in energy between these conformers is either insufficiently large to drive the formation of a single conformer, or that a meta-stable state is formed kinetically.

In an attempt to reduce the background fluorescent from the beacon, a second iteration was designed. It was informed by molecular modelling which showed significantly higher stability of the self-bound form, and only a single alternate conformer. Testing of the MB2 showed a 20 % reduction in background fluorescence compared to the MB1. The linear detection range of the MB2 was found to be very similar to MB1, with no significant improvement in the signal to noise ratio.

Overall the second iteration of the MB was shown to have no significant improvements over the first version, and at higher target concentrations was found to be even less effective. It was decided based on these results to perform live cellular imaging with the first version of the beacon. It was also decided to refrain from designing further iterations of the beacon, because the primary alternate conformer is based on similarity in the sensing region of the beacon where no changes can be made, and that further lengthening of the stem portion of the beacon would result in poorer target binding and detection limits based on molecular modelling.

4.5 References

1. Roos, A.; Boron, W. Intracellular Ph. *Physiol. Rev.* **1981**, *61*, 296-434.

2. Madshus, I. Regulation of Intracellular Ph in Eukaryotic Cells. *Biochem. J.* **1988**, *250*, 1-8.

3. Smith, F. A.; Raven, J. A. Intracellular pH and its regulation. *Annual Review of Plant Physiology* **1979**, *30*, 289-311.

4. Peitsch, M.; Polzar, B.; Stephan, H.; Crompton, T.; Macdonald, H.; Mannherz, H.; Tschopp, J. Characterization of the Endogenous Deoxyribonuclease Involved in Nuclear-Dna Degradation during Apoptosis (Programmed Cell-Death). *EMBO J.* **1993**, *12*, 371-377.

5. Suck, D.; Oefner, C. Structure of Dnase-i at 2.0 a Resolution Suggests a Mechanism for Binding to and Cutting Dna. *Nature* **1986**, *321*, 620-625.

6. Hoffmann, P. J. Mechanism of degradation of duplex DNA by the DNase induced by herpes simplex virus. *J. Virol.* **1981**, *38*, 1005-1014.

7. Wu, C. S.; Peng, L.; You, M.; Han, D.; Chen, T.; Williams, K. R.; Yang, C. J.; Tan, W. Engineering molecular beacons for intracellular imaging. *International journal of molecular imaging* **2012**, *2012*, 501579.

8. Tyagi, S. Imaging intracellular RNA distribution and dynamics in living cells. *Nat. Methods* **2009**, *6*, 331-338.

9. Chen, C.; Ridzon, D.; Broomer, A.; Zhou, Z.; Lee, D.; Nguyen, J.; Barbisin, M.; Xu, N.; Mahuvakar, V.; Andersen, M.; Lao, K.; Livak, K.; Guegler, K. Real-time quantification of microRNAs by stem-loop RT-PCR. *Nucleic Acids Res.* **2005**, *33*, e179.

10. Gibson, U.; Heid, C.; Williams, P. A novel method for real time quantitative RT PCR. *Genome Res.* **1996**, *6*, 995-1001.

11. Li, W.; Ruan, K. MicroRNA detection by microarray. *Anal. Bioanal. Chem.* **2009**, *394*, 1117-1124.

12. Várallyay, E.; Burgyán, J.; Havelda, Z. MicroRNA detection by northern blotting using locked nucleic acid probes. *Nature protocols* **2008**, *3*, 190-196.

13. Long, G. L.; Winefordner, J. D. Limit of detection. A closer look at the IUPAC definition. *Anal. Chem.* **1983**, *55*, 712A-724A.

14. Shrivastava, A.; Gupta, V. B. Methods for the determination of limit of detection and limit of quantitation of the analytical methods. *Chronicles of Young Scientists* **2011**, *2*, 21.

15. Kenakin, T. In *Pharmacological Assay Formats: Binding;* A Pharmacology Primer: Techniques for More Effective and Strategic Drug Discovery; Elsevier Science: **2014**; pp 63-Pharmacological Assay Formats: Binding.

16. Rousseau, D. In *Optical Techniques in Biological Research;* Elsevier Science: **2012**; pp 206.

17. Stallings, R. L. SK-N-AS Expression Profile. **2012**.

18. Chen, C.; Ridzon, D.; Broomer, A.; Zhou, Z.; Lee, D.; Nguyen, J.; Barbisin, M.; Xu, N.; Mahuvakar, V.; Andersen, M.; Lao, K.; Livak, K.; Guegler, K. Real-time quantification of microRNAs by stem-loop RT-PCR. *Nucleic Acids Res.* **2005**, *33*, e179.

19. Degliangeli, F.; Kshirsagar, P.; Brunetti, V.; Pompa, P. P.; Fiammengo, R. Absolute and Direct MicroRNA Quantification Using DNA-Gold Nanoparticle Probes. *J. Am. Chem. Soc.* **2014**, *136*, 2264-2267.

20. Schmittgen, T. D.; Lee, E. J.; Jiang, J.; Sarkar, A.; Yang, L.; Elton, T. S.; Chen, C. Real-time PCR quantification of precursor and mature microRNA. *Methods* **2008**, *44*, 31-38.

21. Gregory, R. I.; Chendrimada, T. P.; Shiekhattar, R. MicroRNA biogenesis - Isolation and characterization of the microprocessor complex. *Methods in Molecular Biology* **2006**, *342*, 33-47.

22. Dosenko, V. E.; Gurianova, V. L.; Surova, O. V.; Stroy, D. A.; Moibenko, A. A. Mature and immature microRNA ratios in cultured rat cardiomyocytes during anoxia-reoxygenation. *Exp. Clin. Cardiol.* **2012**, *17*, 84-87.

23. Gan, L.; Denecke, B. Profiling pre-microrna and mature microrna expressions using a single microarray and avoiding separate sample preparation. *Microarrays* **2013**, *2*, 24-33.

24. Lim, L.; Glasner, M.; Yekta, S.; Burge, C.; Bartel, D. Vertebrate MicroRNA genes. *Science* **2003**, *299*, 1540-1540.

25. Lagos-Quintana, M.; Rauhut, R.; Lendeckel, W.; Tuschl, T. Identification of novel genes coding for small expressed RNAs. *Science* **2001**, *294*, 853-858.

26. Maksimenko, A.; Ishchenko, A. A.; Sanz, G.; Laval, J.; Elder, R. H.; Saparbaev, M. K. A molecular beacon assay for measuring base excision repair activities. *Biochem. Biophys. Res. Commun.* **2004**, *319*, 240-246.

27. Tsourkas, A.; Behlke, M.; Rose, S.; Bao, G. Hybridization kinetics and thermodynamics of molecular beacons. *Nucleic Acids Res.* **2003**, *31*, 1319-1330.

28. Bonnet, G.; Tyagi, S.; Libchaber, A.; Kramer, F. Thermodynamic basis of the enhanced specificity of structured DNA probes. *Proc. Natl. Acad. Sci. U. S. A.* **1999**, *96*, 6171-6176.

29. Goel, G.; Kumar, A.; Puniya, A.; Chen, W.; Singh, K. Molecular beacon: a multitask probe. *J. Appl. Microbiol.* **2005**, *99*, 435-442.

30. Tsourkas, A.; Behlke, M.; Bao, G. Hybridization of 2 '-O-methyl and 2 '-deoxy molecular beacons to RNA and DNA targets. *Nucleic Acids Res.* **2002**, *30*, 5168-5174.

31. Wang, K.; Tang, Z.; Yang, C. J.; Kim, Y.; Fang, X.; Li, W.; Wu, Y.; Medley, C. D.; Cao, Z.; Li, J.; Colon, P.; Lin, H.; Tan, W. Molecular Engineering of DNA: Molecular Beacons. *Angew. Chem. -Int. Edit.* **2009**, *48*, 856-870.

32. Zuker, M. Mfold web server for nucleic acid folding and hybridization prediction. *Nucleic Acids Res.* **2003**, *31*, 3406-3415.

33. Kim, Y.; Yang, C. J.; Tan, W. Superior structure stability and selectivity of hairpin nucleic acid probes with an L-DNA stem. *Nucleic Acids Res.* **2007**, *35*, 7279-7287.

CHAPTER 5

Live Cell Imaging of miR-132

5.1 Introduction

miRNA has been shown to have an important role to play in a wide variety of biological pathways.[1] Cells which have become cancerous tend to have differential expression of miRNA when compared with healthy cells.[2,3] By analysing the miRNA concentration of a cellular population, it is possible to identify the presence of cancer, and potentially to determine the cancer subset.[4] This can allow for earlier detection, since miRNA changes occur early in the disregulation of cells which leads to cancer.[5] This can also inform treatment of the disease.[6]

miR-132 has been shown to induce proliferation[7], and is upregulated in chronic lymphoblastic leukaemias[8], gastric cancer[9], pancreatic cancer[10] and neuroblastoma[11]. It has also been associated with neuronal differentiation[12,13]. miRNA primarily regulates cellular function by formation of the RNA induced silencing complex.[14] The complex is formed after the export of the RNA from the nucleus.[15] For this reason, the localisation of miRNA within the cell is an important indicator of cellular function, and disease state.

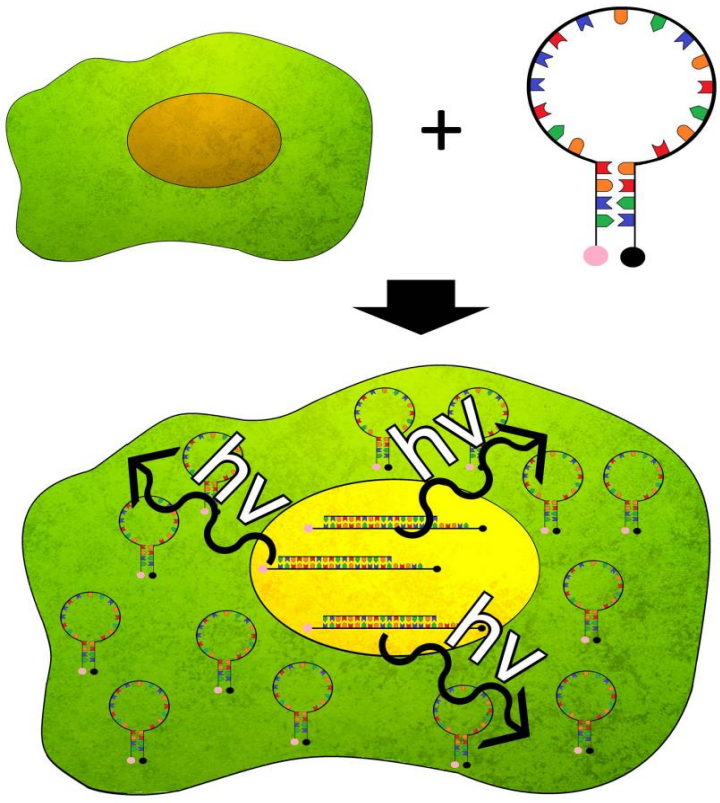

Figure 5.1: Scheme for the live cell imaging of miR-132 using the MB.

This chapter reports on the use of the MB (MB) to probe where miR-132 is localised within live neuroblastoma cells and its concentration. It was shown in Chapter 3 that the dye, 6-FAM, is sensitive to changes in pH, whereby acidic pH caused the intensity of the dye to decrease significantly. The intensity of the dye was stable with increasing pH. In the cellular environment, the intercellular fluid, microchondria and nucleus are at pH of 7.4 or above, so no major impact on the intensity of the dye is expected. Lysosomes within the cell can reach approximately pH 4, so it would be expected that fluorescence from these areas of the cell would be significantly reduced. The self-quenching of the dye was also examined, whereby significant quenching occurred at concentrations above 100μM. For this chapter, the concentration will be maintained below this level.

In chapter 4, the ability of the dye to detect the miR-132 target was investigated. From this work, the MB reaches maximum emission intensity in approximately 10 minutes. This should allow for rapid detection of miR-132 within the cells. The selectivity of the MB was also examined, where good discrimination was possible for a single mismatched base. Within the cell, no miRNA with this high degree of similarity have been identified, so the intensity received should be based solely on the presence of the miR-132 target.

The first challenge was to introduce the MB to the cells. A number of approaches were examined for suitability, including passive uptake, the use of solvents to improve permeability, electroporation, peptide based transfection, and lipid based transfection.

It was found that the MB was unable to passively enter the cell. The addition of permeabilizing agents such as 2 % DMSO, 2 % ethanol or 0.1 % triton-x also showed no measurable uptake of the beacon after 24 hours. Electroporation was investigated as a potential means of transferring the MB into cells. It was effective at introducing the MB; however the viability of the cell was very low, at approximately 5 %. The number of cells undergoing electroporation was increased to allow for a measurable population.

The variability of the fluorescence intensity received from the cells was very high; with a relative standard deviation of approximately 56 %. Treatment of the cells with retinoic acid, which has been shown to upregulate the expression of miR-132, caused an increase in the overall intensity, however the high variability of the intensity within individual cells, combined with the low sample number, made measurement of a statistical difference challenging.

An alternative method was investigated to introduce the MB to the cells, without causing significant cell damage. A lipid based transfection showed good uptake of the MB, with a viability of approximately 60 %. Transfection with anti-miR-132, followed by transfection with the MB caused a decrease in average intensity, however a statistical difference could not be measured due to the variability between individual cells. Overall, this work suggests that single cell determination of miR-132 concentration may not be a useful diagnostic tool.

5.2 Experimental

5.2.1 Materials

DMSO, EtOH, Triton-X and retinoic acid were purchased from Sigma Aldrich. For DNA hybridisation, phosphate buffered saline (PBS) was prepared at a phosphate buffer concentration of 0.01 M and a sodium chloride concentration of 0.154 M using PBS tablets (Sigma Aldrich) in RNase free water.

Nucleic acids were synthesised by Exiqon at 85 % purity. The following sequences were ordered:

Molecular Bacon: 5'-6FAM-+CGA+CCA+TGG+CTG+TAG+ACT+GTT+AGT+CG-DAB-3' (where the + is a Locked Nucleic Acid)

miR-132 Mimic: 5'- UAA-CAG-UCU-ACA-GCC-AUG-GUC-G-3'

anti-miR-132: 5'-CGA-CCA-TGG-CTG-TAG-ACT-GTT-A-3'

5.2.2 Cell Culture

The adherent human neuroblastoma cell line, SK-N-AS, were obtained from the American Type Culture Collection (ATCC). The cells were cultured in Minimum Essential Media, with 10 % foetal bovine serum, 0.5 % L-glutamine and 0.5 % non-essential amino acids, with 100 µg/mL Gentamicin at 37 ˚C and 5 % CO_2.

The cells were split at three day intervals, and seeded at a ratio of 1:3. Prior to splitting, the cells were rinsed with 5mL of PBS. 1 mL of trypsin was added for five minutes. Approximately 5mL of cell culture media was then added to neutralise the trypsin. 2 mL of this solution was then added to a new cell culture flask with 8 mL of media. The mixture was gently mixed by pipetting and then replaced in the incubator.

5.2.3 Electroporation

Electroporation experiments were performed using the Bio-Rad GenePulser Xcell. Cells were incubated for 48 hours which achieved approximately 75 % confluency. Cells were then rinsed with PBS three times to remove the media, and trypsinized for 10 minutes. Cells were resuspended in 1mL of media, and counted using a haemocytometer. Cells were diluted to achieve a cell density of 3 x 10^6 cells per mL. 400 µL of this suspension was loaded into an electroporation cuvette. MB or miR-132 mimic was added to achieve a concentration of 5 µM. The cuvette was then placed in the Bio-Rad GenePulser Xcell and electroporated as previously described (see Section 2.1.6). The cells were then immediately transferred to a cell culture dish, post electroporation, and media was added to bring the final volume to 2 mL. The cells were then incubated for 24 hours. This allowed the cells which survived the procedure to attach to the cell culture dish. Cells were then imaged by confocal microscopy to determine viability.

5.2.4 N-TER Transfection

20 µL of 50 µM MB was mixed with 80 µL of N-TER buffer. 100 µL of N-TER solution peptide (Sigma Aldrich) was then added to achieve a concentration of 5 µM MB. The mixture was incubated for 30 minutes at 37 °C, then added to 800 µL of media and added to cells. Cells were then incubated for 24 hours.

5.2.5 Escort IV Transfection

20 µL of 50 µM MB, miR-132 mimic or anti-miR-132, was added to 30 µL of media. 5 µL of Escort IV transfection reagent (Sigma Aldrich) was added to 45 µL of media. The two solutions were mixed to give a nucleic acid concentration of 5 µM, and incubated for 20 minutes at 37 °C. The mixture was added to 900 µL of media and added to the cells. Cells were then incubated for 24 hours.

5.2.6 Imaging

Cellular imaging was performed using a Zeiss LSM 510 confocal microscope, which was used for dye visualisation, with an argon ion laser at 458 nm and with an LP560 filter at 6 %. A 63x oil emersion objective lens (NA 1.4) was used, with a further 4x zoom obtained using the scanning software. Experiments were run for periods of up to 60 minutes.

5.3 Results and Discussion

This chapter describes the use of the MB to study the localisation and concentration of miR-132 within live cells. The first challenge was to deliver the MB into the cells. The first approach was passive uptake, whereby the cells were incubated with 5 μM MB in media. After 24 hours, the cells appeared to be healthy, with good attachment to the cell culture flask, normal morphology, and no significant cell debris visible. However, when the cells were imaged by confocal fluorescence microscopy, no signal was visible within the cells for the MB. This suggests that the MB is not capable of passive diffusion through the membrane.

The two primary means of diffusion through a cell membrane are passive and facilitated.[16] Only molecules which are small and non-polar are capable of passive diffusion through the lipid membrane.[17] The MB is slightly negatively charged which makes passive diffusion unlikely.[18] Facilitated diffusion proceeds via transmembrane proteins, however these channels require specific recognition or an external trigger, for example voltage-gated channels require a change in membrane potential.[19] Overall this makes the passive transport of the MB through the cell membrane unlikely.

Since passive uptake was unsuccessful, the use of agents to increase the permeability of the cells was then investigated. 2 % DMSO, 2 % EtOH and a surfactant, Triton-X, were investigated. Figure 5.2 shows the cells treated with 2 % DMSO after 4 hours and 24 hours. The normal morphology and good attachment of the cells suggested low toxicity from the 2 % DMSO, however no uptake of the MB could be detected. 2 % EtOH and Triton-X showed similar results, with good viability of the cells, but no apparent uptake. The confocal settings were optimised so that the MB at 5 μM in the absence of the target was undetectable. It is possible that the lack of detectable signal was due to a low concentration of either the target miRNA or the MB, either of which could result in an undetectable intensity value.

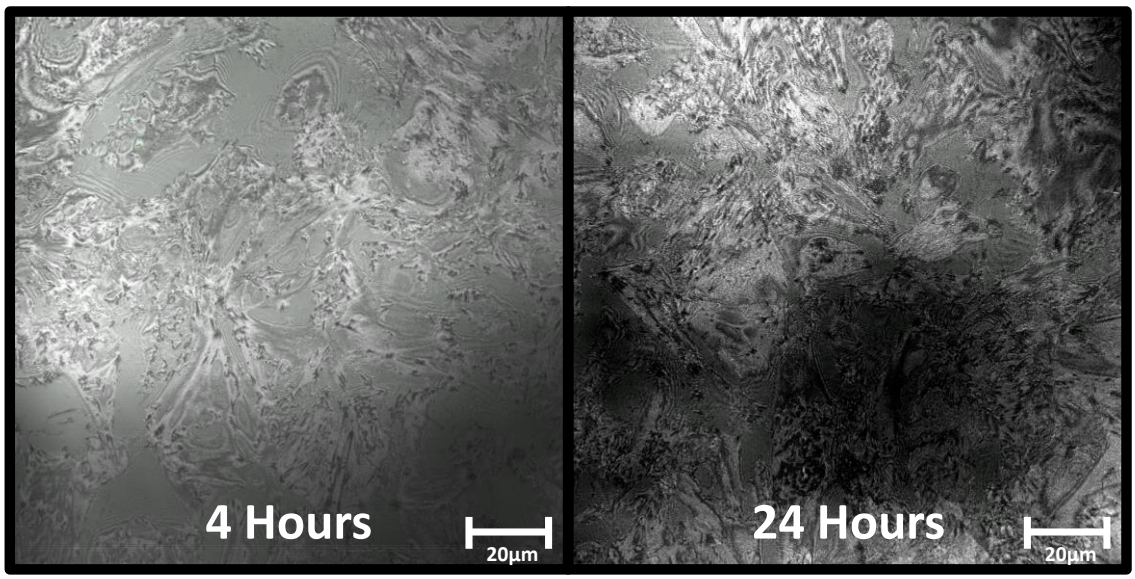

Figure 5.2: Confocal fluorescence microscopy of SK-N-AS cells after incubation with 5 µM MB in 2 % DMSO with media. Excitation with argon ion laser at 458 nm and with an LP560 filter at 6 %.

5.3.1 Electroporation

The next method attempted was electroporation, which had previously been successful at introducing the 6-FAM dye to cells, see Section 3.3.6.2. Electroporation has been shown to be highly effective for the introduction of nucleic acids into mammalian cells.[20,21] Initially 1 x 10^5 cells were treated with 5 µM MB in media and electroporated with a square wave pulse of 200 V peak amplitude and 20 ms pulse width in a 0.2 cm gap electroporation cuvette. Figure 5.3 shows a batch of SK-N-AS cells which were electroporated 3 hours prior to being imaged. The cells were imaged in the media containing the MB, as this provided contrast for the image. A large amount of cell debris was visible, which suggested poor cell viability for the method. While a significant portion of the cells appeared to be dead, a number of viable cells were also observed. These live cells showed high emission intensity. However, the viability of the cells was estimated at below 2 % for this experiment. Based on these results, it was decided to increase the number of cells electroporated from 1 x 10^5 to 3 x 10^6, so that a sufficient number of viable cells would still remain to allow for analysis.

Figure 5.4 shows a viable cell which was electroporated 24 hours prior to imaging. As in the previous experiment, a large amount of cell debris is viable in the media, which was due to the large number of cells destroyed during the electroporation procedure. Interestingly, these cells showed an area of very high intensity within the nucleus, with much lower intensity in the surrounding cytoplasm (500x difference). This was in contrast to the electroporation with 6-FAM seen previously, which showed that even in cells with ruptured cell membranes, the dye was still highly excluded from the nucleus.

There are a number of possible explanations for this higher intensity within the nucleus. One is that the MB is preferentially transported to the nucleus by an intercellular process, however access to the nucleus is tightly controlled by the nuclear pore complex[22]. This makes it highly unlikely for a given nucleic acid sequence to be actively transported into the nucleus.[23] Another possibility is that the beacon is electroporated into the entire cell and the portion in the cytoplasm is broken down or excluded, causing a reduction in signal intensity, however if the beacon was broken down, this would increase the separation between the 6-FAM and the quencher, which would cause an increase in signal. The third possibility is that the concentration of the beacon is consistent across the cytoplasm and nucleus, and that a higher concentration

of miR-132 within the nucleus is causing the beacon to open, resulting in a higher intensity signal.

The localisation of miR-132 within cells is not well understood, with different experiments resulting in different expression. A recent study examined the relative concentration of miR-132 in the nucleus and cytoplasm using a variety of methods including microarray, northern blotting and deep sequencing.[24] Cells were separated by centrifugation into a nucleus and cytoplasm fraction. The results varied depending on the measurement technique used, with deep sequencing showing a very high expression level in the nucleus compared to the cytoplasm, whereas northern blotting showed a slightly lower relative signal from the nucleus.

These published results broadly agree with the nuclear localisation observed in this experiment. Even if the number of miR-132 in the cytoplasm is slightly lower than in the nucleus; the volume of the nucleus is considerably smaller, which would result in a higher effective concentration.

Interestingly, miR-132 has been linked to neuronal cell survival, with miR-132 being upregulated in response to damage to the cell.[24] The electroporation procedure causes damage to the cell membrane which much be repaired by the cell, and so it is plausible that electroporation is activating this stress response, causing the miR-132 expression level to be increased.[21] This upregulation would involve production of miR-132 in the nucleus of the cell, which would explain the high signal observed.

Since the localisation of miR-132 in live cells had been achieved, the next objective was to determine the concentration within the cells.

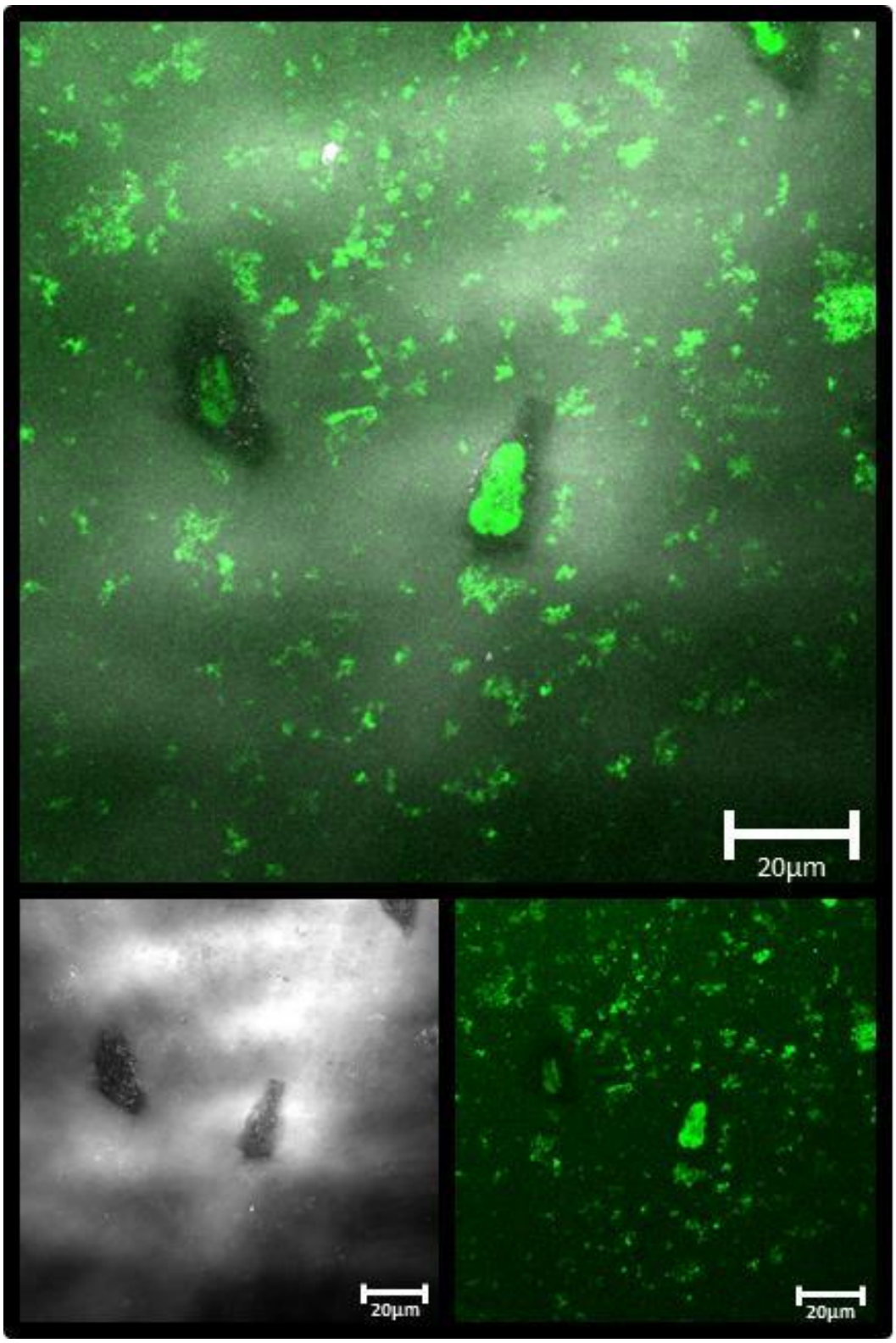

Figure 5.3: Confocal fluorescence microscopy of SK-N-AS cells 3 hours after electroporation with 5 µM MB. Excitation with argon ion laser at 458 nm and with an LP560 filter at 6 %.

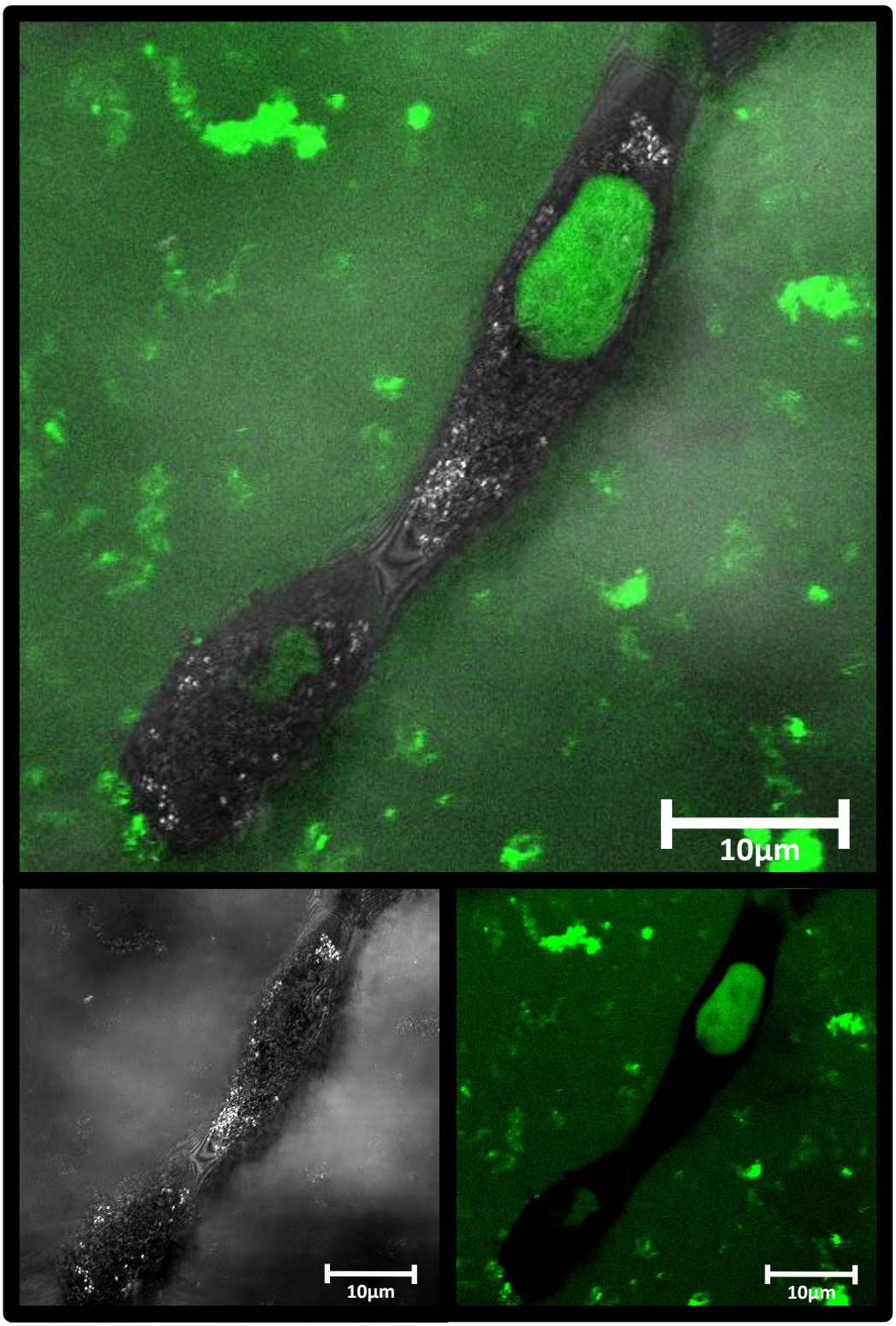

Figure 5.4: Confocal fluorescence microscopy of SK-N-AS cells 24 hours after electroporation with 5 µM MB. Excitation with argon ion laser at 458 nm and with an LP560 filter at 6 %.

5.3.2 Concentration of miR-132

The next objective was measurement of the concentration of miR-132 within the cell. When cells are electroporated, the cell works to actively repair the pores which form in the membrane. These pores can remain open for up to 9 minutes.[25] During this period of time, the concentration of MB should fully equilibrate between the solution and interior of the cell. This means that the concentration of MB within the cells should be approximately 5 µM. The confocal microscopy settings were optimised so that the background signal which was measured for the MB in the absence of target would not produce a measurable fluorescence. Thus, any signal detected in the confocal microscopy images should be due to opening of the MB.

The intensity values of the MB with a range of miR-132 conentrations were recorded in solution using the confocal microscope. When the settings in Figure 5.4 were used, the intensity received was very low. This resulted in significant noise, and made determination of an absolute intensity difficult. In an attempt to overcome this issue, the gain settings were increased so that the intensity of the MB with miR-132 gave a very high intensity, which had the effect of significantly reducing the noise associated with the measurement. The full concentration range was then performed at these increased gain settings. A single point calibration was then performed using the higher gain setting, and then with the lower gain setting used in Figure 5.4. This single point calibration was then used to numerically adjust the calibration curve down, by assuming a linear dependence of the intensity on gain, see Figure 5.6

As can be seen in Figure 5.5, the intensity increased steadily as the MB was added, giving similar relative intensities to the solution phase experiments in Chapter 2. As illustrated in Figure 5.6, when the intensity values were adjusted, the minimum detectable value was approximately 4.6 µM with the settings used to record the confocal images. The average intensity of the nucleus seen in Figure 5.4 corresponds to a concentration value of approximately 5.8 µM according to this calibration.

This value is significantly higher than expected based on the previous value achieved for lysed cells, which gave a concentration for the entire cell of 0.14 µM. Assuming that all of the miR-132 present within the cell is localised in the nucleus and the volume of the cell is taken as being approximately 20 pL, and the volume of the nucleus as being 2.3 pL, then the concentration within the nucleus would be approximately 1.2 µM. As

reported by other researchers, these data speak to the difficulties of precisely defining the absolute miRNA concentration in different regions of the cells. But the results strongly suggest that following electroporation the miR-132 concentration is in the micromolar range.

As previously discussed, miR-132 has been linked to the survival response of the cell, so it is possible that the miR-132 concentration for this experiment was higher than that in the lysed cells experiment, however the magnitude of the increase in the measured intensity was unexpected. It is also unlikely that all of the miR-132 was in fact located within the nucleus.

The cause for this increase in intensity value within the nucleus of the cell is not well understood. 6-FAM was shown in Chapter 2 to be sensitive to changes in pH, however the pH value in the nucleus is approximately 7.2, which is very similar to the pH 7.4 for the PBS used for the calibration, so this is not expected to cause any significant difference.

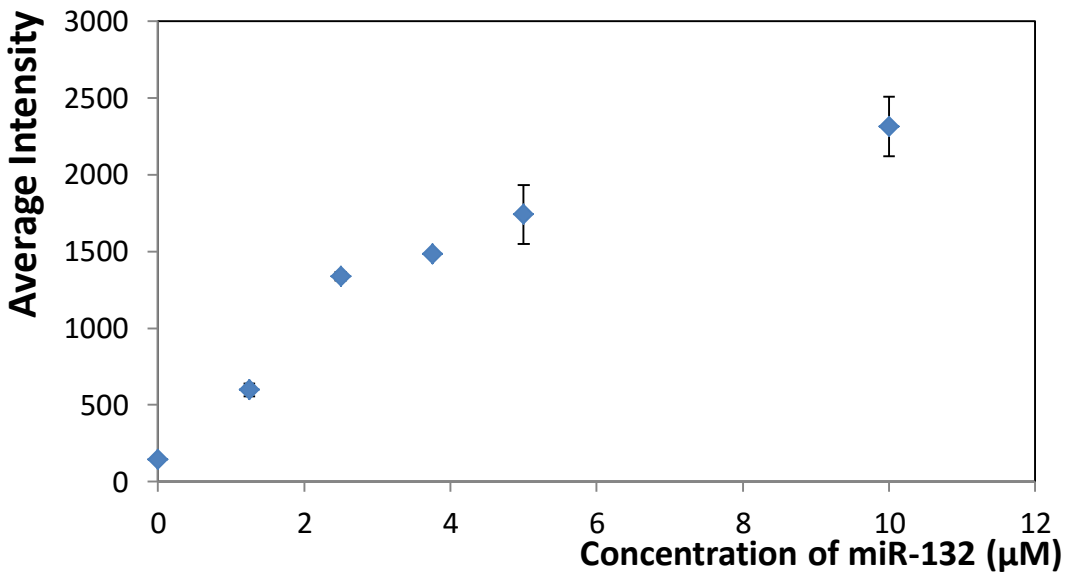

Figure 5.5: Average intensity measured by confocal microscopy for 5 µM MB with a range of miR-132 concentration from 0.25 µM to 10 µM in PBS. Gain increased to give maximum possible signal. 3 repeats of the experiment were performed.

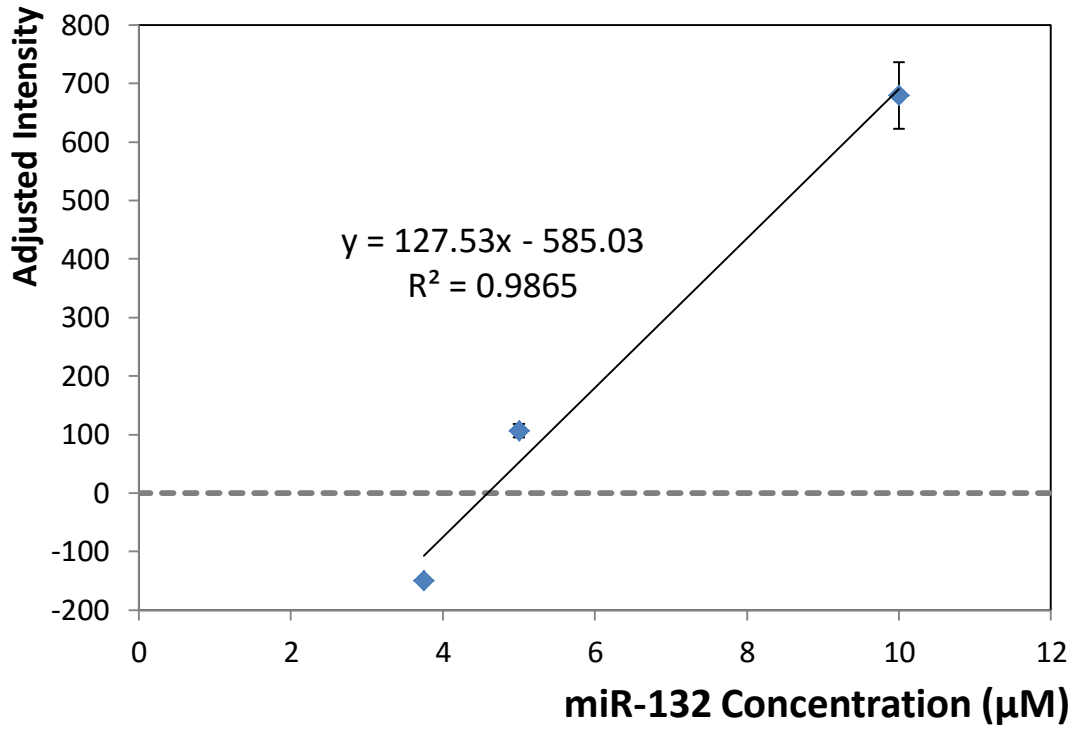

Figure 5.6: Average intensity measured by confocal microscopy for a 5 µM solution of the MB with a range of miR-132 concentration from 0.25 µM to 10 µM in PBS. Intensity numerically adjusted based on a single point calibration to match gain settings used in Figure 5.4. 3 repeats of the experiment were performed.

5.3.3 Electroporation of Target into Cells

Since delivery of the MB had been successfully achieved, the next objective was to examine the ability of the MB to monitor changes in the intercellular miRNA concentration. The goal was to introduce a miR-132 mimic to the cell, and then introduce the MB.

As a control experiment, 3 x 10^6 cells were initially electroporated in fresh media, and then incubated for 8 hours. The cells were then electroporated a second time with 5 µM of the MB and incubated for a further 12 hours.

Figure 5.7 shows the results for this experiment. The viability of the cells was very poor, with a large amount of cell debris visible in solution, and very few cells adhering to the glass slide. While it was technically possible to further increase the number of cells used in the experiment, the viability was so low that an acceptable sample size would have been unachievable. This experiment suggested that electroporation is too damaging to the cells for consecutive cycles to be performed.

This low viability was somewhat expected based on the mechanism of electroporation. Sealing of pores formed during electroporation requires active repair by the cell. This process involves the removal of water, reordering of membrane lipids, and use of ion pumps to restore ion gradients.[26,27] This is a time consuming and energy intensive process. In the case of even larger membrane defects, cytoplasmic transport vesicles must be actively transferred to the defect site.[28] It is probable that even after 12 hours, the resources used to repair the membrane are still depleted, and so the resealing of defects becomes more difficult, resulting in apoptosis.[29]

Since addition of miR-132 to the cells using electroporation was not a viable approach, alternate methods of modulating the cellular miR-132 concentration were then examined.

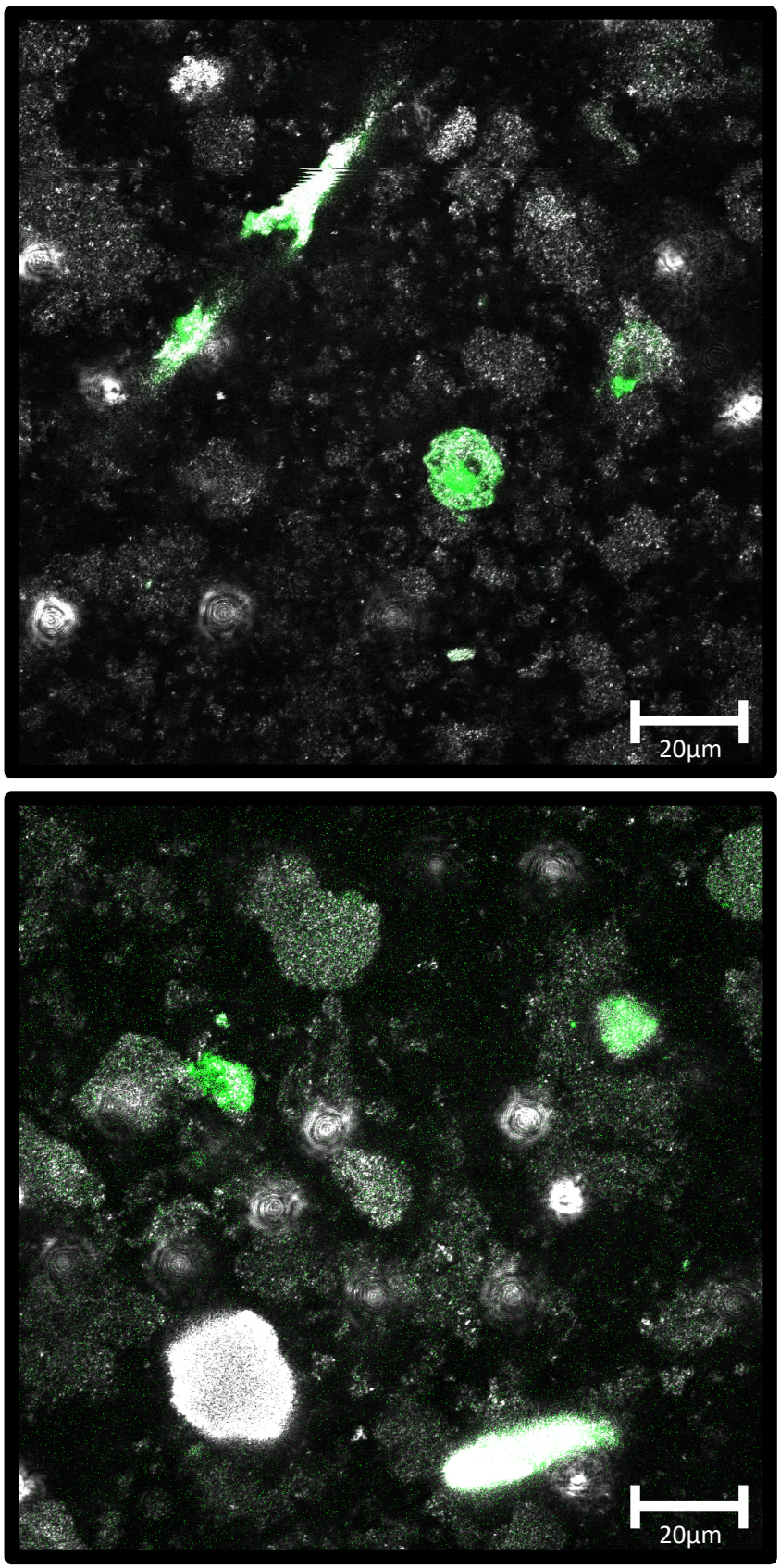

Figure 5.7: Confocal fluorescence microscopy of SK-N-AS cells after two electroporation cycles with 5 µM MB. Excitation with argon ion laser at 458 nm and with an LP560 filter at 6 %.

5.3.4 Retinoic acid Treatment

Retinoic acid had been show previously to upregulate the production of miR-132 in neuroblastoma cell lines.[29] It was hoped that by treating cells with retinoic acid for 24 hours, a measurable increase in the intensity would be observed, corresponding to upregulation of miR-132.

The retinoic acid was not soluble in water, or in a DMSO:water solvent system, and so a 5 % solution of ethanol was investigated. SK-N-AS cells were treated with 1 µM retinoic acid for 24 hours. Cells were then electroporated with 5 µM MB, and incubated for a further 12 hours. The results for this experiment are shown in Figure 5.8, alongside a 5 % ethanol only control. The viability of the retinoic acid treated cells was approximately 5 %, which was similar to the control population.

As illustrated in Figure 5.9, the average intensity in the retinoic acid treated cells is higher than the control population. Unfortunately, the intensity values for individual cells can vary significantly. For the control cells, the average intensity value was 73.13±41.10 A.U., (n=22), i.e., the relative standard deviation is approximately 56 %. This large variation between cells makes it challenging to confirm a statistically significant difference between populations of control and retinoic acid treated cells.

One possible cause for this large deviation seen between individual cells is that the natural expression level of miR-132 is significantly different. A recent study, which examined the miRNA concentration of individual cells, found that distribution among individual cells varied greatly depending on the miRNA measured and the cell line tested. For example, in the K652 cell line, miR-223 expression had a standard deviation of 79 % and the distribution was not log-normal, whereas miR-16 gave a standard deviation of 30 % with log normal expression.[30]

The distribution of the control population is shown in Figure 5.10. Unfortunately, the poor viability of the cells resulted in a relatively small number live of cells, which further complicated the analysis. In both the cytoplasm and nucleus, the distribution appears to be non-normal, however this may be due to the intensity threshold of the experiment, whereby low intensity signals corresponding to cells with a lower concentration of target are not detectable. This suggests a high level of difference between the expression of miR-132 in individual cells. As previously discussed,

miR-132 has been linked to the stress response of neuronal cells.[24] In this experiment, cells were electroporated and treated with 5 % ethanol, both of which are capable of activating a stress response. It is possible that the distribution of miR-132 may be different in a normal population of cells.

The next objective was to deliver the MB to the cells without causing significant disruption to the cells. A number of different transfection reagents were examined for suitability.

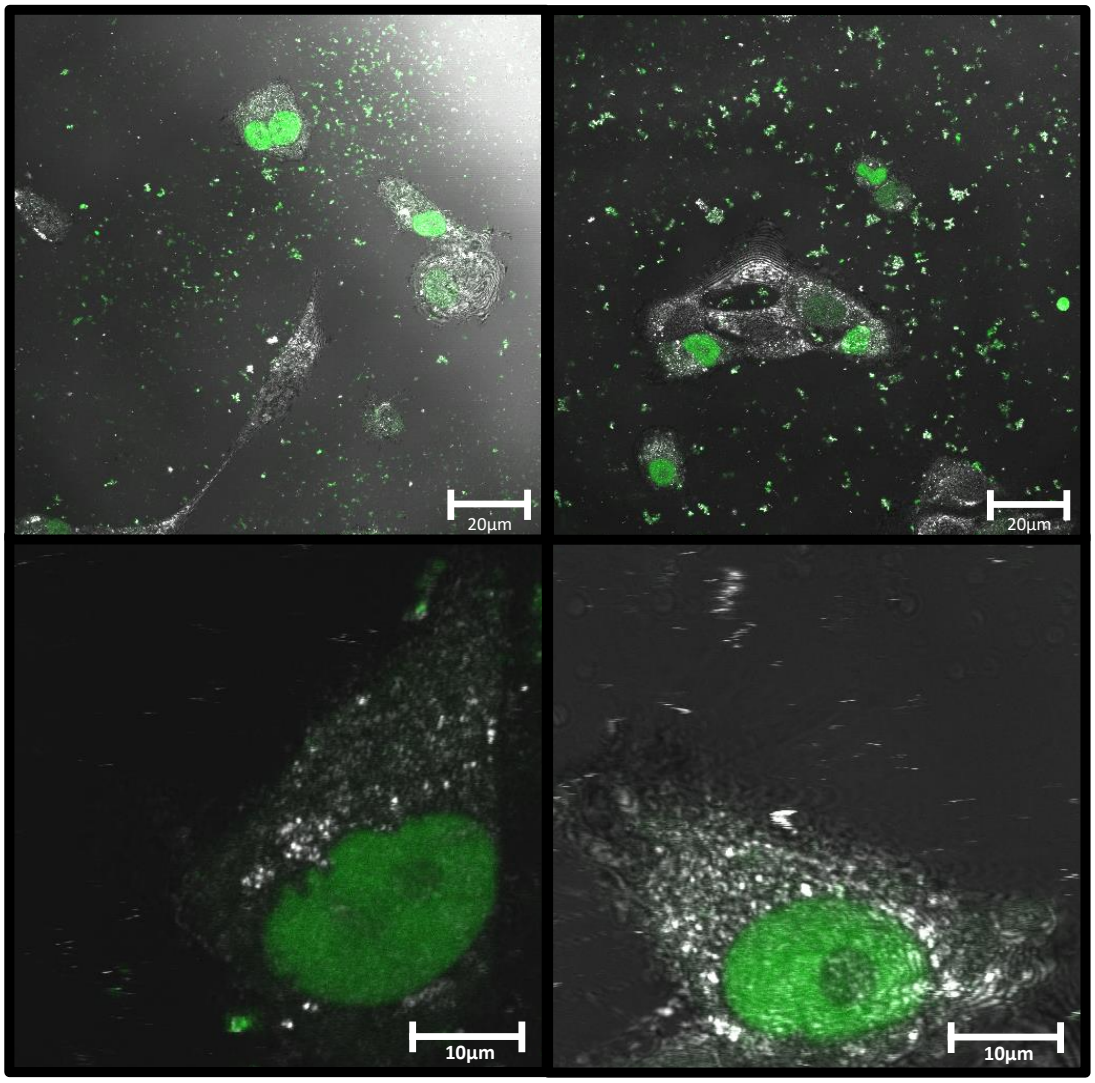

Figure 5.8: Confocal fluorescence microscopy of SK-N-AS cells treated with 1 µM retinoic acid for 24 hours (left), and 1 µM ethanol (right). Electroporated with 5 µM MB, and incubated for 12 hours before confocal microscopy. Excitation with argon ion laser at 458 nm and with an LP560 filter at 6 %.

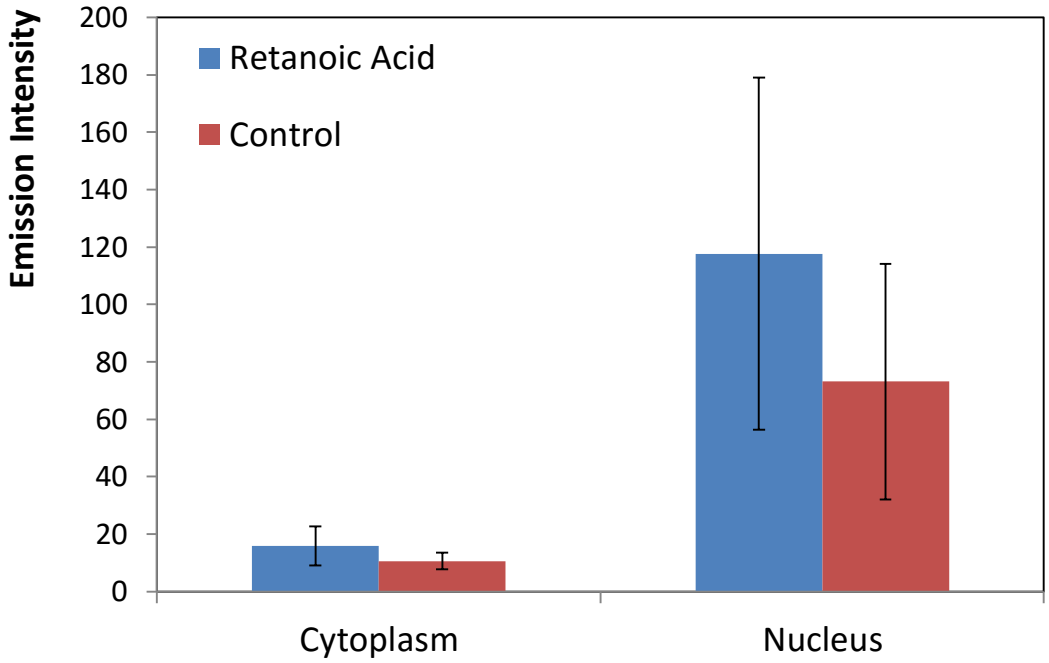

Figure 5.9: Average fluorescence intensity in the nucleus and cytoplasm of SK-N-AS cells treated with 1 µM retinoic acid for 24 hours, and 1 µM ethanol. Electroporated with 5 µM MB, and incubated for 12 hours before confocal microscopy.

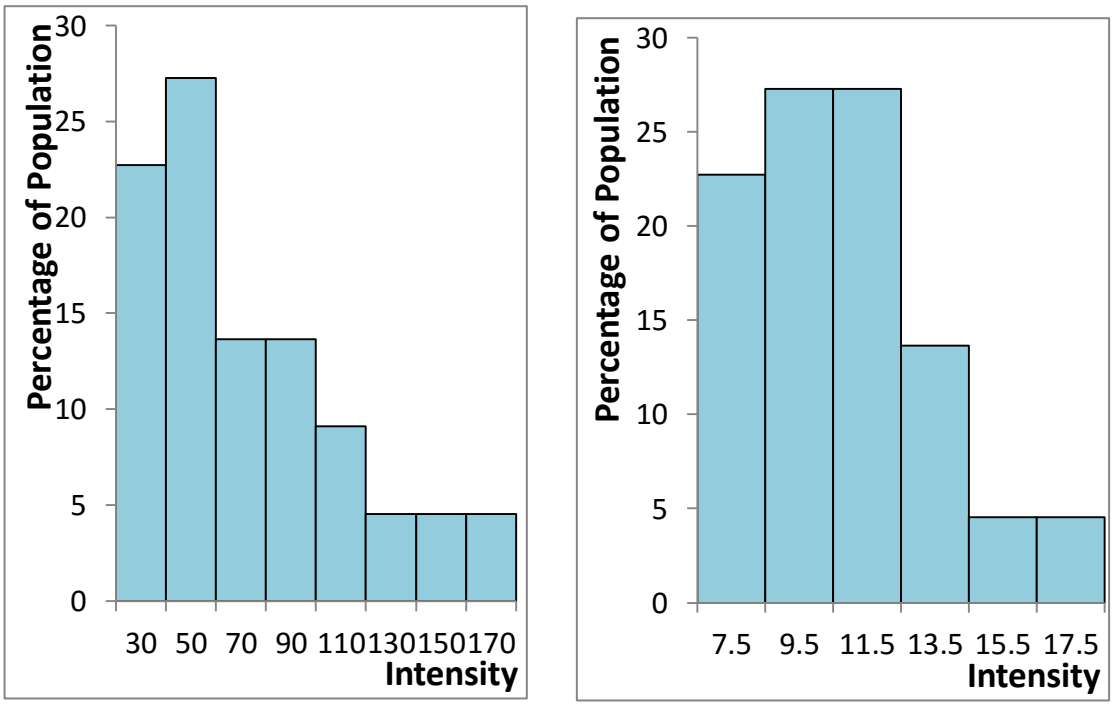

Figure 5.10: Fluorescence intensity in the nucleus (left) and cytoplasm (right) of SK-N-AS cells in 5 % EtOH. Electroporated with 5 µM MB, and incubated for 12 hours before confocal microscopy.

5.3.5 Transfection with N-TER

In an attempt to deliver nucleic acid to cells without causing the poor viability previously seen for electroporation, a peptide based delivery system called N-TER was examined. This transfection reagent had previously proved successful for delivery of nucleic acids to neuronal cell lines.[31] Cell-penetrating peptides are a class of short peptides which enable the uptake of molecules through the cell membrane.[32] The transfected molecule can be held by covalent bond or by non-covalent interactions. The peptides tend to gain access to the cell by direct translocation and endocytosis.[33]

The MB was mixed with N-TER, as previously described in Section 5.2.4, and added to the SK-N-AS cells. Figure 5.11 shows the results of the transfection after 4 hours. A significant amount of cell debris is visible; however the majority of the cells appeared to be healthy, with good attachment to the surface and normal morphology. A number of the cells showed high intensity in the nucleus, as previously seen with electroporation; however for the majority of the cells no significant fluorescence emission was detected.

24 hours after transfection, the cells were washed to remove dead cell debris and the cells were visualised under confocal, see Figure 5.12. The vast majority of the cells showed no emission, with a small number showing very low intensity emission. This suggests that the N-TER may be toxic to the cells which it efficiently transfects, as the percentage of cells with emission decreased from the 4 hour time point to the 24 hour time point. It is also possible that the cells had excluded the beacon over the 24 hour period, however no evidence of this was seen in the electroporation experiments previously performed.

Based on the poor uptake of the MB shown in this experiment, alternate transfection reagents were then investigated.

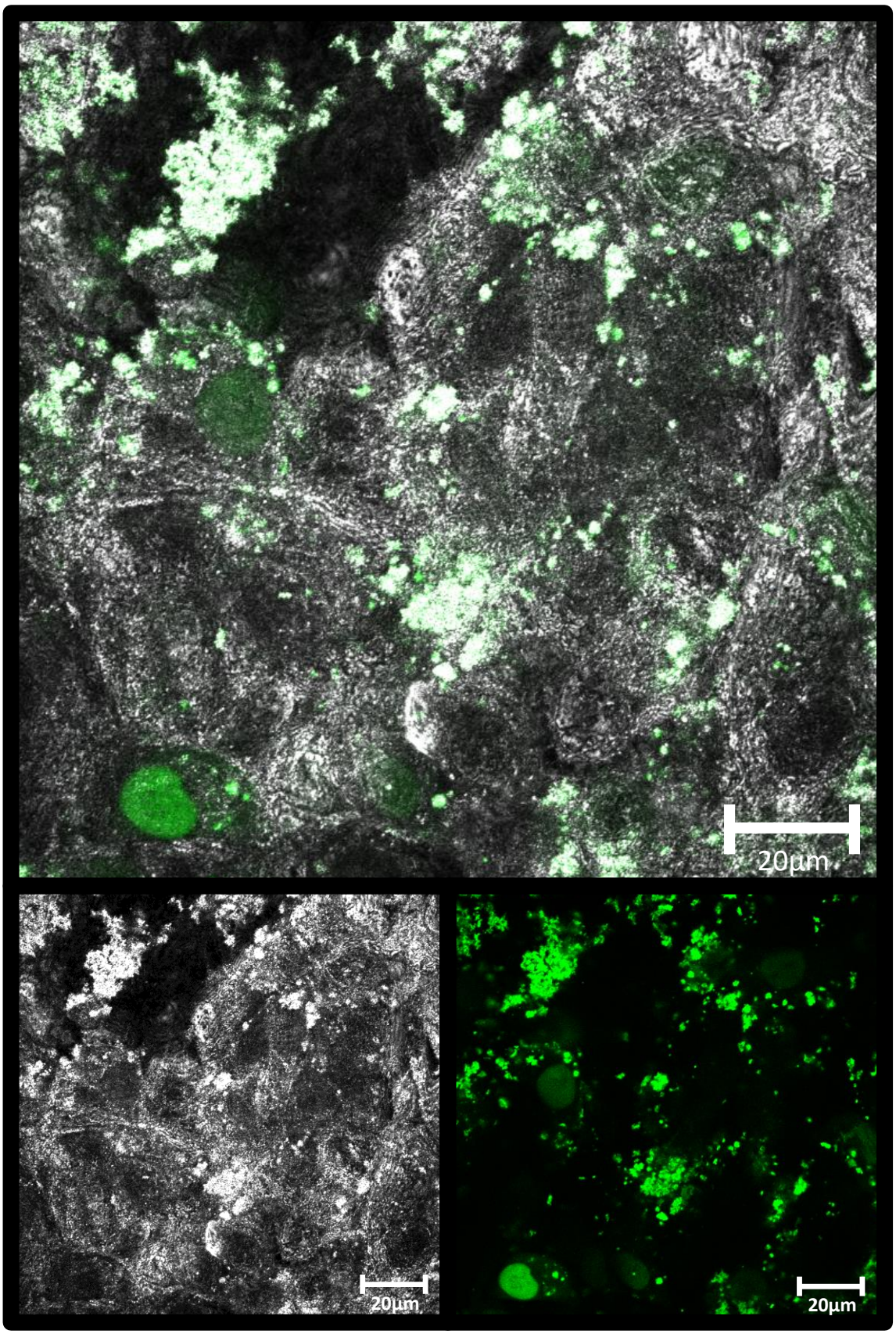

Figure 5.11: Confocal microscopy of SK-N-AS cells treated with 5 µM MB and N-TER transfection reagent for 4 hours in media. Excitation with argon ion laser at 458 nm and with an LP560 filter at 6 %.

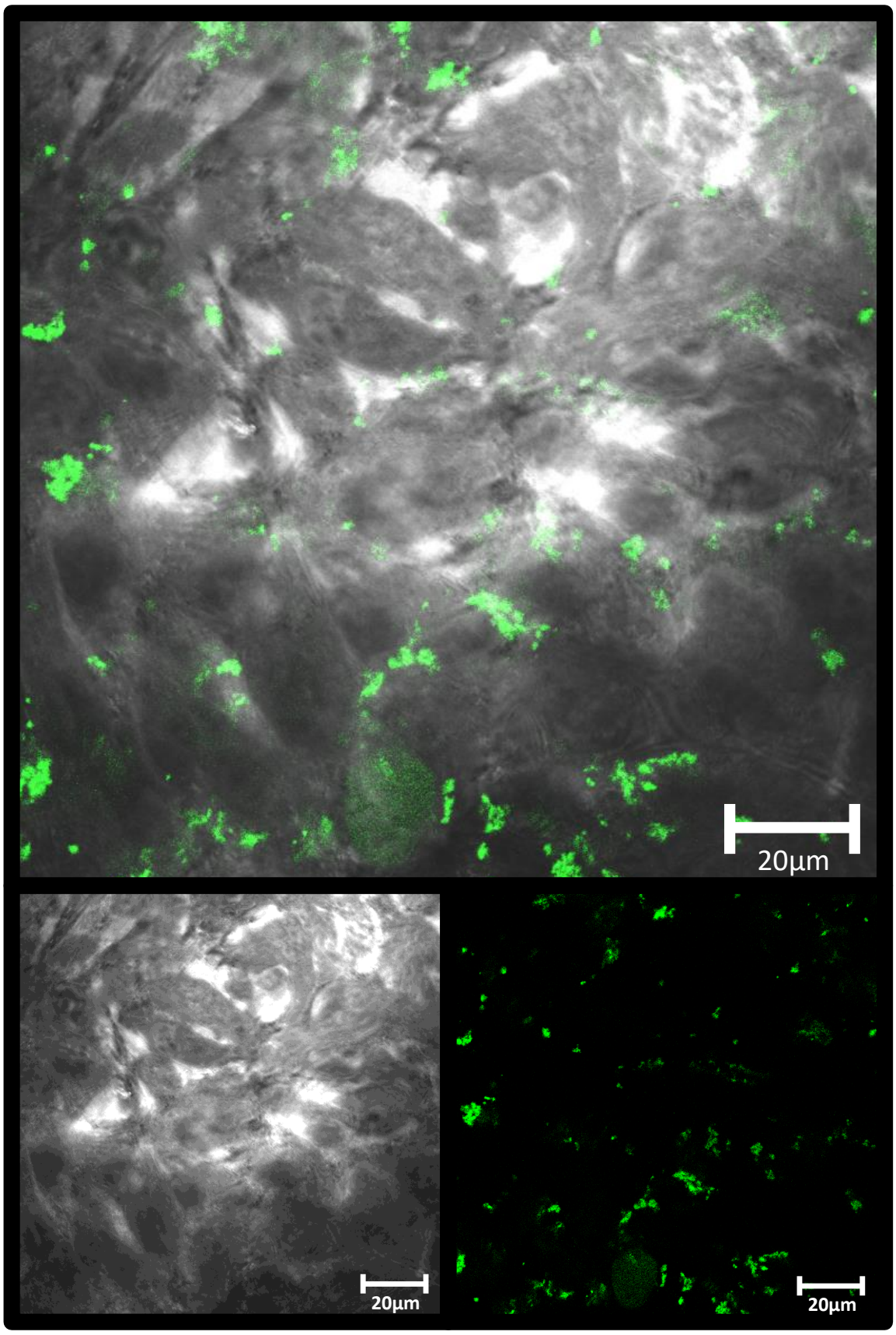

Figure 5.12: Confocal microscopy of SK-N-AS cells treated with 5 µM MB with N-TER transfection reagent for 24 hours in fresh media. Excitation with argon ion laser at 458 nm and with an LP560 filter at 6 %.

5.3.6 Transfection with Escort IV

Since the peptide based transfection was unsuccessful in delivering the MB into the cells, a lipid based transfection, Escort IV, was investigated. Lipid transfections involve the encapsulation of a negatively charged species, in this case DNA / LNA, to form micelles with a positively charged outer membrane.[34] These positively charged micelles are capable of passing through the negatively charged cell membrane.[35] Liposome transfections have been shown to have high efficiency and reproducibility with low toxicity.[36]

The MB was combined with Escort IV, as previously described in Section 5.2.5, and added to the SK-N-AS cells. After 4 hours the uptake was observed by confocal microscopy. As seen in Figure 5.13, a number of cells show a weak emission suggesting that a small amount of the MB has been uptaken. Also visible are a number of smaller areas showing a high intensity fluorescence signal. These are believed to be MB containing micelles that have not yet been uptaken into the cells.

After 24 hours the cells were visualised again, as seen in Figure 5.14. The number of micelles which were visible at the 4 hour time point was significantly reduced. The number of cells showing uptake of the MB was also significantly increased. As previously seen for electroporated cells, the area of the cell showing highest intensity is the nucleus. This is very promising, as it suggests this signal is not as a result to damage of the cell caused by electroporation. A weaker signal is also present in the cytoplasm, suggesting that miR-132 is predominantly nuclear localised.

The viability of the cells was approximately 65 %, which was a significant improvement over the 5 % viability achieved with electroporation.

Since a method of delivering nucleic acid to the cells without causing significant reduction in cell viability had been identified, modulation of the cellular miR-132 concentration was again attempted.

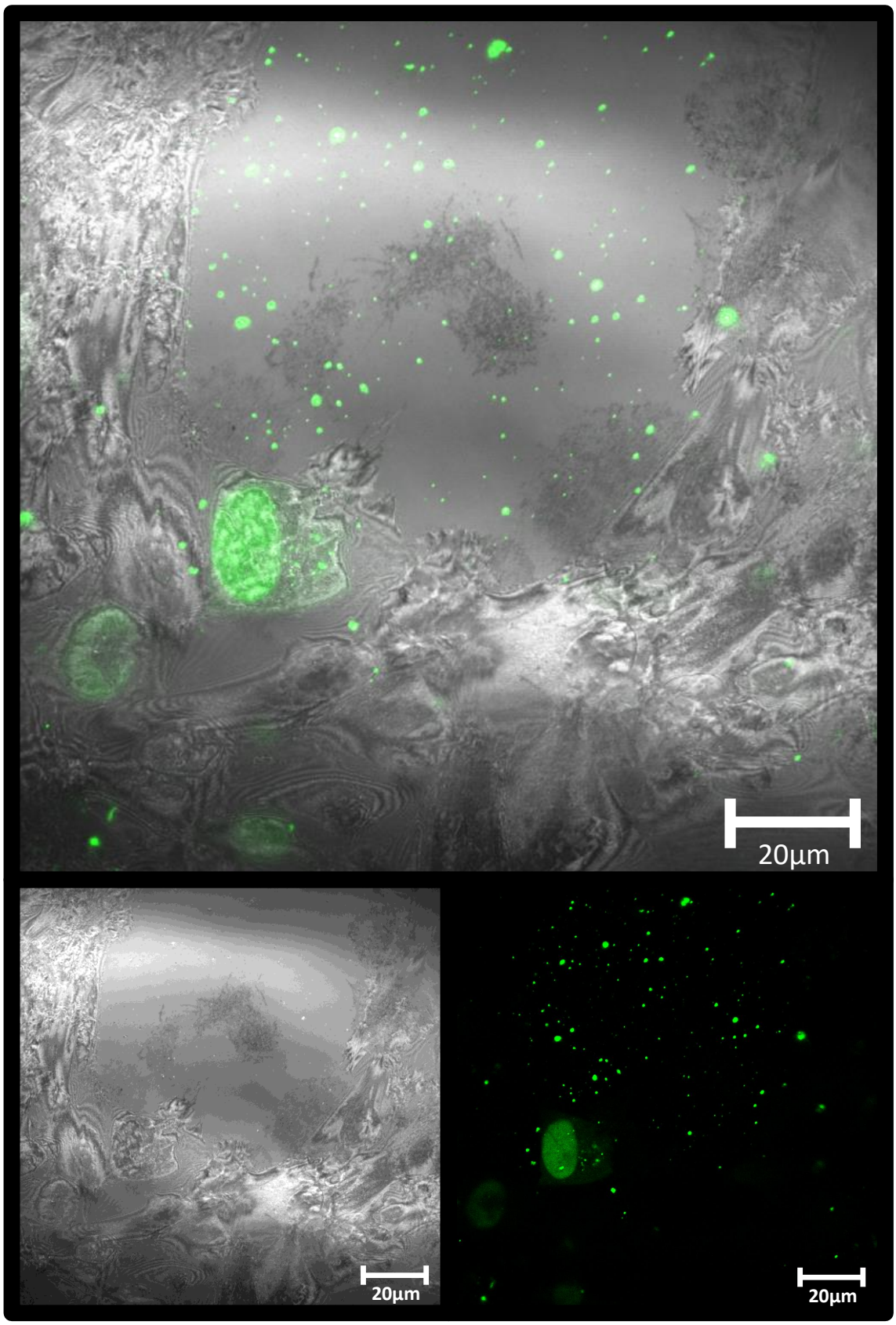

Figure 5.13: Confocal microscopy of SK-N-AS cells treated with 5 µM MB with Escort IV transfection reagent for 4 hours. Excitation with argon ion laser at 458 nm and with an LP560 filter at 6 %.

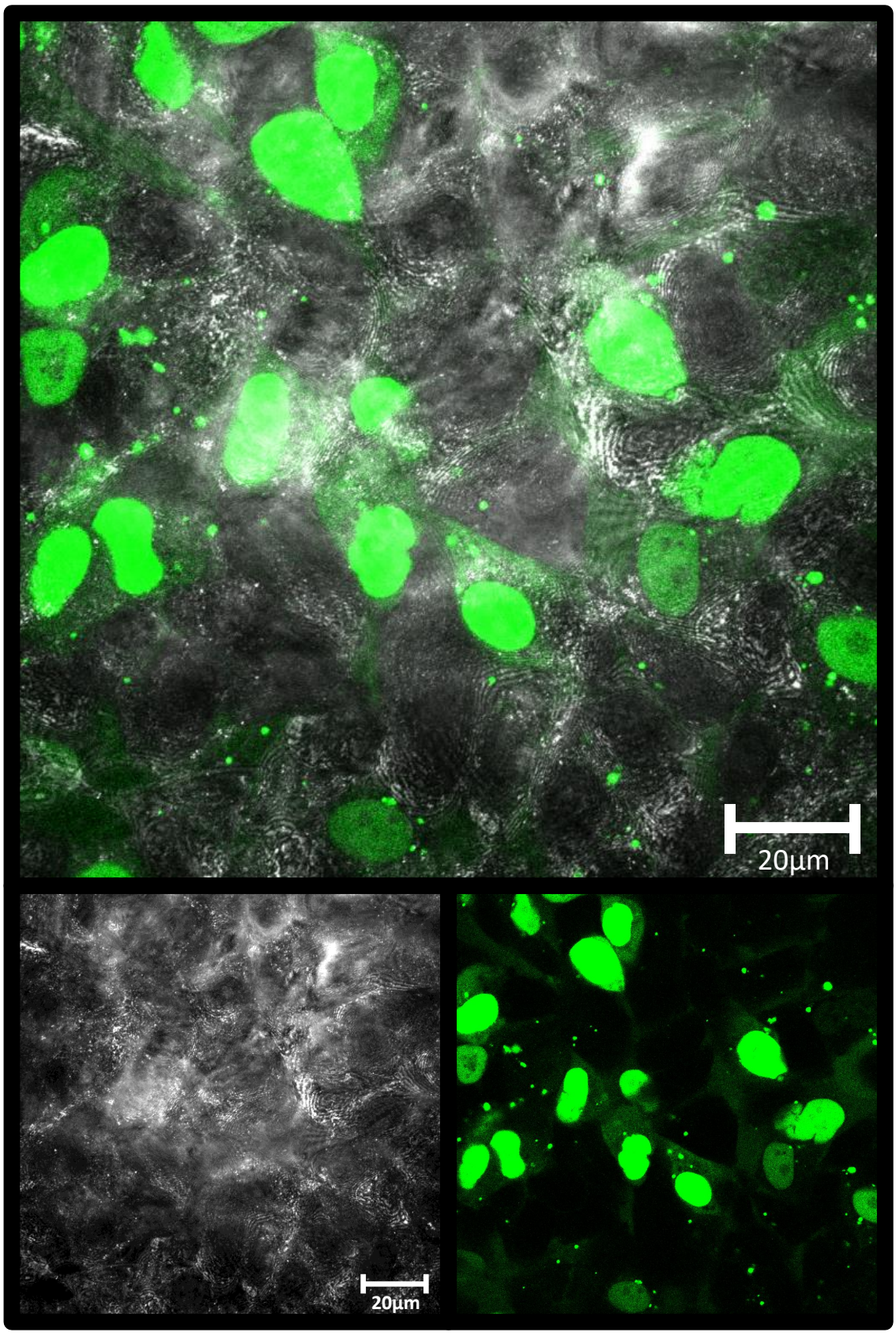

Figure 5.14: Confocal microscopy of SK-N-AS cells treated with 5 µM MB with Escort IV transfection reagent for 24 hours in fresh media. Excitation with argon ion laser at 458 nm and with an LP560 filter at 6 %.

5.3.7 Mimic and anti-miR

SK-N-AS cells were treated with either a miR-132 mimic, or anti-miR-132 using Escort IV for 24 hours. Cells were then treated with 5 µM MB for a further 24 hours, and the results were visualised by confocal microscopy.

Cells which were treated with the miR-132 mimic reacted poorly. No cells were attached to the surface of the cell culture dish, with only cells in suspension visible. Figure 5.15 shows a selection of these cells. The cell membrane is damaged for most of the cells, with death vacuoles visible. These images suggest that the cells transfected with miR-132 underwent apoptosis. While analysis of these cells is not possible, since the conditions within dead cells can be significantly different to live cells[37], these data suggest that the transfection was successful, and the miR-132 is toxic to the cells at high concentrations. Since no cells were found attached to the surface it also suggests that the transfection was successful at introducing miR-132 to a significant fraction of the entire population.

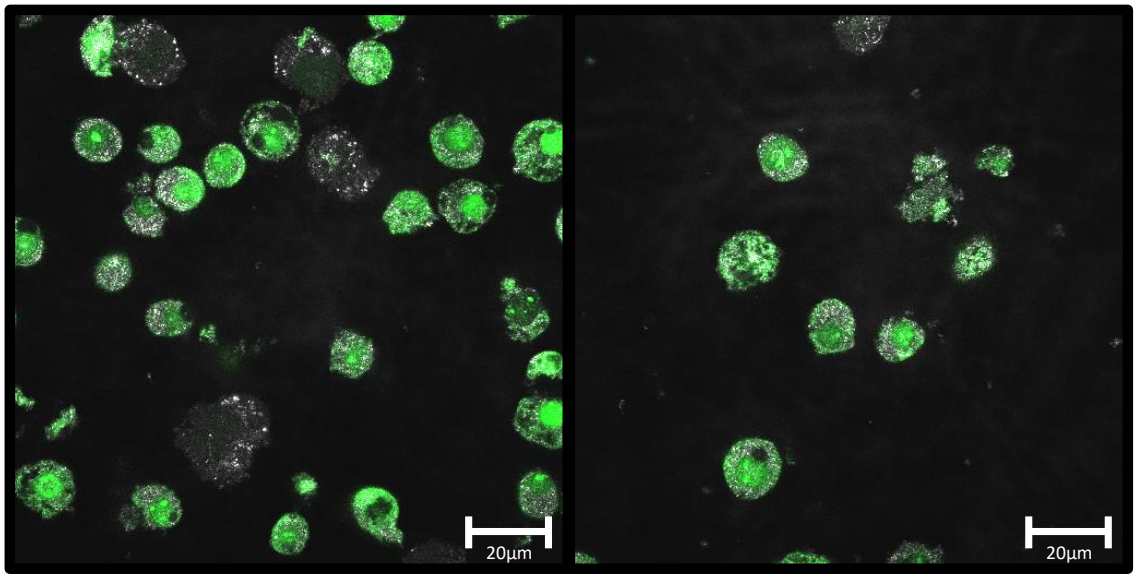

Figure 5.15: Confocal microscopy of SK-N-AS cells treated with 5 µM miR-132 mimic with Escort IV transfection reagent for 24 hours, followed by 5 µM MB with Escort IV for 24 hours. Excitation with argon ion laser at 458 nm and with an LP560 filter at 6 %.

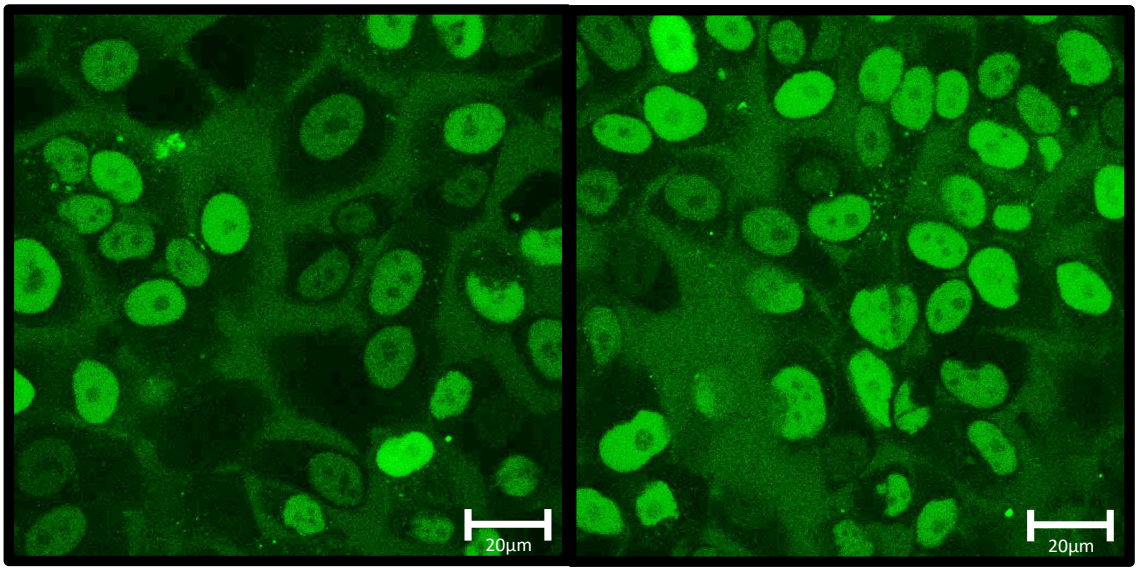

Figure 5.16: Confocal microscopy of SK-N-AS cells treated with Escort IV for 24 hours, followed by 5 µM MB with Escort IV for 24 hours. Excitation with argon ion laser at 458 nm and with an LP560 filter at 6 %.

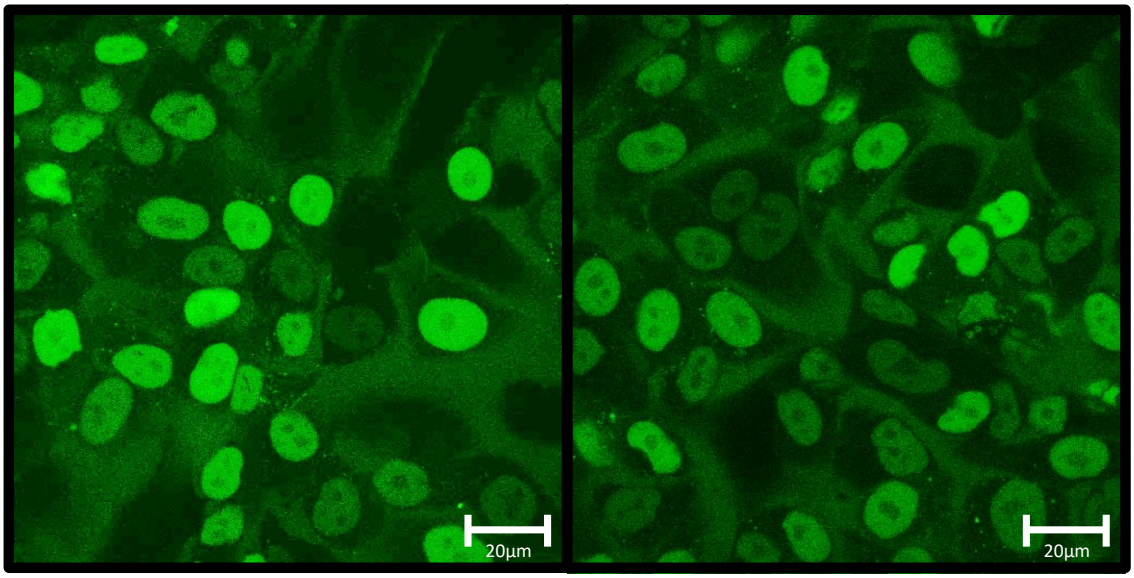

Figure 5.17: Confocal microscopy of SK-N-AS cells treated with 5 µM anti-miR-132 with Escort IV for 24 hours, followed by 5 µM MB with Escort IV for 24 hours. Excitation with argon ion laser at 458 nm and with an LP560 filter at 6 %.

Figure 5.16 shows the control population of cells for this experiment. These cells were treated with Escort IV for only 24 hours, and then with MB. The viability of the cells was very high, at approximately 80 %, with the majority of the cells showing normal morphology, with good attachment to the surface. The relative intensities of the various cells is significantly different, with some cells showing an intensity in the nucleus of 7

A.U., whereas others were as high as 123 A.U. Figure 5.18 shows the distribution of miR-132 within the nucleus of 307 cells. The average intensity was 20.5±13.3 A.U., which is a relative standard deviation of 163 %.

On possible reason for the high variability of these cells is the passage number. Cells were passaged a maximum of 25 times from the frozen stock, which may allow for significant divergence from the parent line. This could cause the cells examined to have the higher than expected variance in intensity shown in Figure 5.18.

Figure 5.17 shows images of cells transfected with anti-miR-132. As seen in the control population there is a large variation in the intensity from the cells. The viability of these cells was high at approximately 80 %, with cells showing good attachment and normal morphology. These cells were seeded at approximately 60 % confluency, and were highly confluent at the end of the experiment which suggests that the cells were capable of growing normally despite the addition of anti-miR-132. Figure 5.19 shows the distribution of the intensity in the nucleus of these cells. The average intensity was 16.8±7.0 A.U. which is a relative standard deviation of 41 %. It was expected that the addition of the anti-miR-132 would result in a significantly lower signal than that found for the control population. While the intensity is lower for these cells, the standard deviation makes it difficult to confirm a statistically significant difference.

The Shapiro-Wiki normality test[38] was used to analyse the distribution of the two populations. This is considered the most powerful normality test for all sample sizes and distributions[39,40], and is suitable for a sample size from 3 to 5000[41]. The control population had a calculated P value of 0.0871, assuming a significance interval of 95 %, this distribution is Gaussian. The anti-miR-132 treated cells however had a calculated P value of 0.0123, and as such is considered non Gaussian. This analysis suggests that the transfection of the anti-miR-132 did have a measurable impact on the cells, causing the loss of a normal distribution, but that the natural variation between the miR-132 concentration in individual cells makes direct comparison of the intensities difficult. The sample sizes used for this analysis are 238 for the control population and 307 for the anti-miR-132 treated cells.

The death of cells transfected with miR-132 mimic suggests that the transfections performed in this experiment were successful. While the change in the shape of this distribution suggests that the cells were impacted by the addition of the anti-miR-132,

no definitive conclusions can be drawn from this data. As previously mentioned, the passage number of the cells may be impact the variability of the population, so the wide distribution of miR-132 seen here may be as a result of this population drift. Alternatively, this distribution could be linked to the cell cycle or some other cellular process.

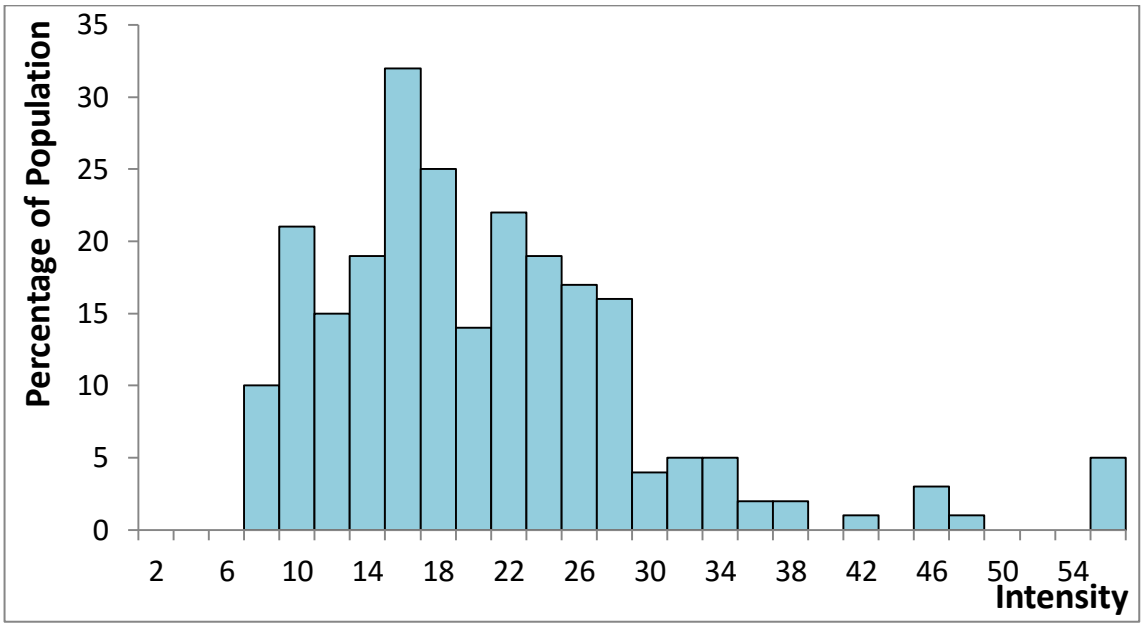

Figure 5.18: Fluorescence intensity in the nucleus of SK-N-AS cells treated with Escort IV for 24 hours, followed by 5 µM MB with Escort IV for 24 hours.

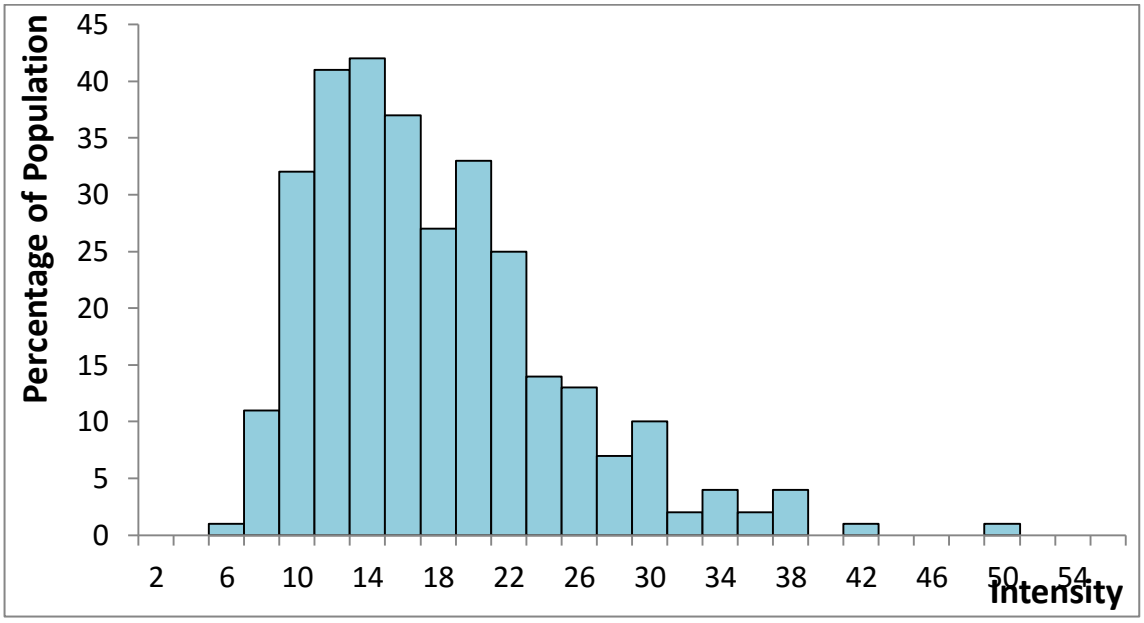

Figure 5.19: Fluorescence intensity in the nucleus of SK-N-AS cells treated with 5 µM anti-miR-132 with Escort IV for 24 hours, followed by 5 µM MB with Escort IV for 24 hours.

5.4 Conclusions

The objective of this chapter was to use the MB to study the localisation and concentration of miR-132 in a neuroblastoma cell line. The MB was successfully introduced to the cells by electroporation. The area of highest intensity was in the nucleus of the cell, suggesting a high nuclear concentration of miR-132. These high intensities are potentially as a result of a cellular survival mechanism which upregulate the production of miR-132.

The intensity values achieved by confocal microscopy were used to estimate the concentration of miR-132. The concentration within the nucleus was calculated as approximately 5.8 µM. Based on the lysed cell experiment from Chapter 2, the maximum concentration of miR-132 within the nucleus was 1.2 µM. The reason for the considerably higher value under confocal microscopy is not known but variations of this kind have been reported previously.

The ability of retinoic acid to modulate the intercellular miR-132 concentration was also investigated. Unfortunately, the poor viability of the cells after retinoic acid treatment and electroporation resulted in a small sample size, so a statistically significant difference could not be confirmed.

Modulation of the intercellular miR-132 concentration was then attempted by electroporation a miR-132 mimic into the cell, followed by the MB. Again, the poor viability caused by electroporation caused all of the treated cells to undergo apoptosis.

Alternate methods of delivering the MB to the cells were investigated. A peptide based transfection system resulted in poor uptake, however a lipid based transfection allowed for highly efficient transfection with viability of above 60 %. The MB was introduced to the cells via this method and, as with electroporation, the area of highest intensity was within the nucleus of the cell. This agreement between the two transfection approaches suggests that this is a real result.

The lipid based transfection was used in an attempt to vary the intercellular miR-132 concentration. Transfection of a miR-132 mimic resulted in 100 % cell death, which suggests that miR-132 is toxic to cells at high concentrations. Analysis of the control population showed the high variability in miR-132 between individual cells, which

fitted to a Gaussian distribution. This high variability may be due to the high passage number of the cells, which can allow the characteristics of the cells to drift, giving rise to a number of distinct cell populations with differing characteristics. This issue could be avoided by more frequent restoration of cells from frozen stocks.

Transfection with anti-miR-132 resulted in similar viability to the control population, however the large variability between cells made confirmation of a statistically significant difference impossible. However, the distribution of miR-132 became less Gaussian compared to the control population, which suggests the transfection was successful.

Overall this chapter highlights the challenges that arise from the large variability that can occur in intercellular miR-132, which in turn make measurement of the absolute concentration problematic. Currently, without the ability to overcome these challenges, live cell imaging of miR-132 is not currently able to provide deep insights into neuroblastoma detection or progression.

The results contained in this chapter are currently awaiting publication.

5.5 References

1. Ambros, V. The functions of animal microRNAs. *Nature* **2004**, *431*, 350-355.

2. Lu, J.; Getz, G.; Miska, E.; Alvarez-Saavedra, E.; Lamb, J.; Peck, D.; Sweet-Cordero, A.; Ebet, B.; Mak, R.; Ferrando, A.; Downing, J.; Jacks, T.; Horvitz, H.; Golub, T. MicroRNA expression profiles classify human cancers. *Nature* **2005**, *435*, 834-838.

3. Munker, R.; Calin, G. A. MicroRNA profiling in cancer. *Clin. Sci.* **2011**, *121*, 141-158.

4. Kusenda, B.; Mraz, M.; Mayer, J.; Pospisilova, S. MicroRNA biogenesis, functionality and cancer relevance. *Biomedical Papers (Olomouc)* **2006**, *150*, 205-215.

5. Fu, S. W.; Chen, L.; Man, Y. miRNA Biomarkers in Breast Cancer Detection and Management. *J. Cancer* **2011**, *2*, 116-122.

6. Castaneda, C. A.; Teresa Agullo-Ortuno, M.; Fresno Vara, J. A.; Cortes-Funes, H.; Gomez, H. L.; Ciruelos, E. Implication of miRNA in the diagnosis and treatment of breast cancer. *Expert Rev. Anticancer Ther* **2011**, *11*, 1265-1275.

7. Anand, S.; Majeti, B. K.; Acevedo, L. M.; Murphy, E. A.; Mukthavaram, R.; Scheppke, L.; Huang, M.; Shields, D. J.; Lindquist, J. N.; Lapinski, P. E.; King, P. D.; Weis, S. M.; Cheresh, D. A. MicroRNA-132-mediated loss of p120RasGAP activates the endothelium to facilitate pathological angiogenesis. *Nat. Med.* **2010**, *16*, 909-U109.

8. Calin, G.; Liu, C.; Sevignani, C.; Ferracin, M.; Felli, N.; Dumitru, C.; Shimizu, M.; Cimmino, A.; Zupo, S.; Dono, M.; Dell'Aquila, M.; Alder, H.; Rassenti, L.; Kipps, T.; Bullrich, F.; Negrini, M.; Croce, C. MicroRNA profiling reveals distinct signatures in B cell chronic lymphocytic leukemias. *Proc. Natl. Acad. Sci. U. S. A.* **2004**, *101*, 11755-11760.

9. Liu, X.; Yu, H.; Cai, H.; Wang, Y. The expression and clinical significance of miR-132 in gastric cancer patients. *Diagn. Pathol.* **2014**, *9*, 57.

10. Park, J.; Henry, J. C.; Jiang, J.; Esau, C.; Gusev, Y.; Lerner, M. R.; Postier, R. G.; Brackett, D. J.; Schmittgen, T. D. miR-132 and miR-212 are increased in pancreatic cancer and target the retinoblastoma tumor suppressor. *Biochem. Biophys. Res. Commun.* **2011**, *406*, 518-523.

11. Meseguer, S.; Mudduluru, G.; Manuel Escamilla, J.; Allgayer, H.; Barettino, D. MicroRNAs-10a and-10b Contribute to Retinoic Acid-induced Differentiation of Neuroblastoma Cells and Target the Alternative Splicing Regulatory Factor SFRS1 (SF2/ASF). *J. Biol. Chem.* **2011**, *286*, 4150-4164.

12. Nudelman, A. S.; DiRocco, D. P.; Lambert, T. J.; Garelick, M. G.; Le, J.; Nathanson, N. M.; Storm, D. R. Neuronal Activity Rapidly Induces Transcription of the CREB-Regulated MicroRNA-132, In Vivo. *Hippocampus* **2010**, *20*, 492-498.

13. Wu, J.; Xie, X. Comparative sequence analysis reveals an intricate network among REST, CREB and miRNA in mediating neuronal gene expression. *Genome Biol.* **2006**, *7*, R85.

14. Filipowicz, W.; Bhattacharyya, S. N.; Sonenberg, N. Mechanisms of post-transcriptional regulation by microRNAs: are the answers in sight? *Nat. Rev. Genet.* **2008**, *9*, 102-114.

15. Pratt, A. J.; MacRae, I. J. The RNA-induced Silencing Complex: A Versatile Gene-silencing Machine. *J. Biol. Chem.* **2009**, *284*, 17897-17901.

16. Herlihy, B. In *Cells;* The Human Body in Health and Illness; Elsevier Health Sciences: **2014**; pp 36-37.

17. Drioli, E.; Giorno, L. In *Biological Membranes and Biomimetric Artificial Membranes;* Comprehensive Membrane Science and Engineering; Elsevier Science: **2010**; pp 1.

18. Lents, N. DNA II: The Structure of DNA. *http://www.visionlearning.com/en/library/Biology/2/DNA-II/160* (accessed 02/14, 2014).

19. Friedman, M. H. *Principles and Models of Biological Transport;* Springer Berlin Heidelberg: 2012; .

20. Chen, C.; Okayama, H. High-Efficiency Transformation of Mammalian-Cells by Plasmid Dna. *Mol. Cell. Biol.* **1987**, *7*, 2745-2752.

21. Chu, G.; Hayakawa, H.; Berg, P. Electroporation for the Efficient Transfection of Mammalian-Cells with Dna. *Nucleic Acids Res.* **1987**, *15*, 1311-1326.

22. Fahrenkrog, B.; Aebi, U. The nuclear pore complex: Nucleocytoplasmic transport and beyond. *Nat. Rev. Mol. Cell Biol.* **2003**, *4*, 757-766.

23. Cros, J.; Palese, P. Trafficking of viral genomic RNA into and out of the nucleus: influenza, Thogoto and Borna disease viruses. *Virus Res.* **2003**, *95*, 3-12.

24. Soreq, H. Novel roles of non-coding brain RNAs in health and disease. *Front. Molec. Neurosci.* **2014**, *7*.

25. Bier, M.; Hammer, S.; Canaday, D.; Lee, R. Kinetics of sealing for transient electropores in isolated mammalian skeletal muscle cells. *Bioelectromagnetics* **1999**, *20*, 194-201.

26. Idone, V.; Tam, C.; Andrews, N. W. Two-way traffic on the road to plasma membrane repair. *Trends Cell Biol.* **2008**, *18*, 552-559.

27. Idone, V.; Tam, C.; Goss, J. W.; Toomre, D.; Pypaert, M.; Andrews, N. W. Repair of injured plasma membrane by rapid Ca2+-dependent endocytosis. *J. Cell Biol.* **2008**, *180*, 905-914.

28. Pakhomov, A.; Miklavcic, D.; Markov, M. In *Advanced Electroporation Techniques in Biology and Medicine;* CRC Press: **2010**; pp 429.

29. Magill, S. T.; Cambronne, X. A.; Luikart, B. W.; Lioy, D. T.; Leighton, B. H.; Westbrook, G. L.; Mandel, G.; Goodman, R. H. microRNA-132 regulates dendritic growth and arborization of newborn neurons in the adult hippocampus. *Proc. Natl. Acad. Sci. U. S. A.* **2010**, *107*, 20382-20387.

30. White, A. K.; VanInsberghe, M.; Petriv, O. I.; Hamidi, M.; Sikorski, D.; Marra, M. A.; Piret, J.; Aparicio, S.; Hansen, C. L. High-throughput microfluidic single-cell RT-qPCR. *Proc. Natl. Acad. Sci. U. S. A.* **2011**, *108*, 13999-14004.

31. Morris, M.; Vidal, P.; Chaloin, L.; Heitz, F.; Divita, G. A new peptide vector for efficient delivery of oligonucleotides into mammalian cells. *Nucleic Acids Res.* **1997**, *25*, 2730-2736.

32. Milletti, F. Cell-penetrating peptides: classes, origin, and current landscape. *Drug Discov. Today* **2012**, *17*, 850-860.

33. Madani, F.; Lindberg, S.; Langel, U.; Futaki, S.; Graslund, A. Mechanisms of cellular uptake of cell-penetrating peptides. *Journal of biophysics (Hindawi Publishing Corporation : Online)* **2011**, *2011*, 414729.

34. Felgner, P.; Gadek, T.; Holm, M.; Roman, R.; Chan, H.; Wenz, M.; Northrop, J.; Ringold, G.; Danielsen, M. Lipofection - a Highly Efficient, Lipid-Mediated Dna-Transfection Procedure. *Proc. Natl. Acad. Sci. U. S. A.* **1987**, *84*, 7413-7417.

35. Felgner, J.; Kumar, R.; Sridhar, C.; Wheeler, C.; Tsai, Y.; Border, R.; Ramsey, P.; Martin, M.; Felgner, P. Enhanced Gene Delivery and Mechanism Studies with a Novel Series of Cationic Lipid Formulations. *J. Biol. Chem.* **1994**, *269*, 2550-2561.

36. Felgner, P.; Ringold, G. Cationic Liposome-Mediated Transfection. *Nature* **1989**, *337*, 387-388.

37. Wyllie, A. H.; Kerr, J. F.; Currie, A. R. Cell death: the significance of apoptosis. *Int. Rev. Cytol.* **1980**, *68*, 251-306.

38. Shapiro, S.; Wilk, M. An Analysis of Variance Test for Normality (Complete Samples). *Biometrika* **1965**, *52*, 591-&.

39. Mehmet, M.; Akin, P. Type I error rate and power of three normality tests. *Information Technology Journal* **2003**.

40. Keskin, S. Comparison of several univariate normality tests regarding type I error rate and power of the test in simulation based small samples. *Journal of Applied Science Research* **2006**, *2*, 296-300.

41. Razali, N. M.; Wah, Y. B. Power comparisons of shapiro-wilk, kolmogorov-smirnov, lilliefors and anderson-darling tests. *Journal of Statistical Modeling and Analytics* **2011**, *2*, 21-33.

CHAPTER 6

Detection of miR-132 by Displacement Assay

6.1 Introduction

The detection of short nucleic acids, specifically miRNAs, is important for the detection and diagnosis of a number in diseases, including cancer.[1-3] The early detection of cancer has been shown to improve survival rates for a number of cancers. [7-9] To achieve detection before the onset of clinical symptoms, a method of detection which is highly sensitive and suitable for wide scale screening is required.

Detection of miRNA in solution is challenging due to the short nature of the nucleic acid strand, typically 17-25 nucleotides or 5-9 nm in length.[1] Also, for physiological samples, the concentration of miRNA can be extremely low, often in the sub picomolar range.[2] The current state of the art, PCR, requires amplification of the initial quantity of miRNA to achieve measurable levels.[3-5]

According to survey findings from 'Testing Sites Holding a Certificate of Waiver under the Clinical Laboratory Improvement Amendments of 1988" (USA) point of care devices use "waived" testing which requires "simple tests with a low risk for an incorrect result".[6] While PCR allows for ultra-sensitive detection[7-9], the equipment and personnel required mean that this technology is not currently applicable to a point of care setting[10-12]. While other methods of detecting miRNA are currently possible, these suffer from poor sensitivity, in the case of optical devices, or high complexity, as shown in Chapter 1 for electrochemical detection. The objective of this research is to achieve the amplification free detection of ultra-low concentration of miR-132 through a novel displacement assay in which a single binding event can produce a measureable signal, i.e., sensitivity towards the single molecule level.

This technology is well suited for use in a flow based system, and is therefore suitable for a point of care setting. This can aid in wide scale screening of disease by improving the availability and reducing the time taken to achieve a measurement. Future work will focus on optimising the sensitivity of the assay, and integration into a flow chip, to allow for high speed, sensitive miRNA detection.

Figure 6.1 shows the scheme used in this assay, which utilises the strong recognition of nucleic acids for complementary strands.[13-15] In this prototype nucleic acid assay, a capture strand of DNA, complementary to miR-132, was bound to a surface. A carboxy functionalised probe strand of DNA, partially complementary (11 out of 22 bases) to this capture, was then attached to an amino functionalised 3µm radius microsphere

using 1-Ethyl-3-(3-dimethylaminopropyl)carbodiimide (EDC) coupling. These microspheres where then allowed to hybridise with the surface immobilised capture strands. When the fully complementary miRNA target was added, it should displace the probe strand, freeing the microsphere into the contacting liquid. Unlike the initial target miRNA, the displaced sphere can be visualised using conventional microscopy. The microsphere can also be labelled with a fluorescent dye, allowing it to be quantified using fluorescence.

The major benefit of this approach is that the detection surface can be prepared in advance as part of a disposable microfluidic chip. When a detection is performed, a small volume of blood or plasma can be added to the device, with no other reagents required. This system should be able to produce a result within minutes, allowing for rapid diagnosis and treatment. Since a single displacement even releases a large microsphere, this generates a large easily measurable signal, either using a simple fluorescence reader, or alternatively by the generation of an electrical current as the large magnetic microspheres moves through an inductive coil. This assay has the potential for single molecule detection of miRNA, as a single hybridisation event results in a measurable signal.

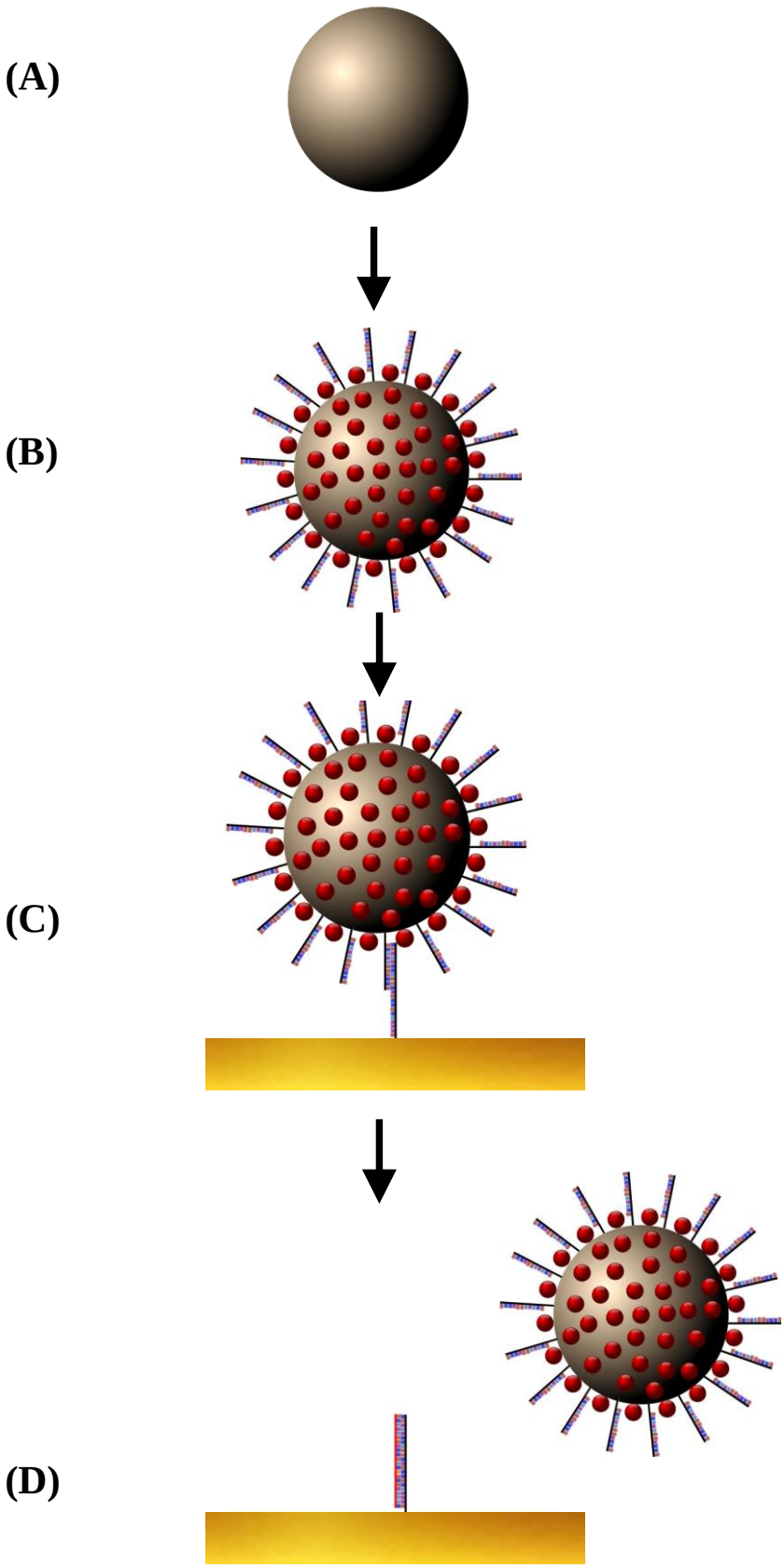

Figure 6.1: Scheme of displacement assay showing, (A) a 3µm microsphere,(B) EDC coupling of probe DNA and Cy5 Dye, (C) attachment of a microsphere to Au surface via thiolated capture strand, (D) displacement of microsphere upon addition of target miRNA.

6.2 Experimental

6.2.1 Materials

Cyanine5 amine dye was purchased from Lumiprobe at 95% purity. 3 µm ProMag 3 Series COOH microspheres were purchased from Polyscience. $[Ru(bpy)_2PIC\text{-}COOH]^{2+}$ was synthesised by Dr. Kellie Adamson and was fully characterised using NMR, HPLC, voltammetry and elemental analysis. DNA and RNA were purchased from Exiqon at ≥80 % purity. The following sequences were ordered for the detection of miR-132:

Capture: 5'–CGA-CCA-TGG-CTG-TAG-ACT-GTT-A–3'-SH

Probe: 5'–AGC-CAT-GGT-CG-3'-NH_2

miR-132 Target: 5'-UAA-CAG-UCU-ACA-GCC-AUG-GUC-G-3'

All other reagents were purchased from Sigma Aldrich. Gold coated silicon wafer, 99.999% Au, 100 nm thick, was used for images. For DNA hybridization, phosphate buffered saline (PBS) was prepared at a phosphate buffer concentration of 0.01 M and a sodium chloride concentration of 0.154 M using PBS tablets (Sigma Aldrich) in RNase free water. 1-Ethyl-3-(3-dimethylaminopropyl)carbodiimide (EDC) was purchased at ≥99.0 % purity.

6.2.2 Emission Spectroscopy

Emission spectra were obtained using a Jasco V-670. Emission and excitation slits were typically 2.5 nm. Solvents used were PBS unless otherwise stated.

6.2.3 Imaging

Imaging was performed using a Zeiss LSM 510 confocal microscope, which was used for particle visualisation, with a HeNe laser at 633 nm and with an LP650 filter at 10% for Cy5 labelled microspheres, and excitation with argon ion laser at 458 nm and with an LP615 filter at 4.1% for $[Ru(bpy)_2PIC\text{-}COOH]^{2+}$ dye. A 63x oil emersion objective lens (NA 1.4) was used, with a further 4x zoom obtained using the scanning software.

6.2.4 Electrochemical Set-Up

Measurements were performed using a CH Instruments Model 660. A three-electrode electrochemical cell was used for electrochemical measurements. The working electrode was a 100 nm thick Au coated silicon wafer (Sigma Aldrich), the reference electrode was silver/silver chloride (Ag/AgCl in 3 M KCl), and the counter electrode was a platinum wire. Solutions were deoxygenated before use with nitrogen. Experiments were carried out at room temperature (~20 °C). All glassware was cleaned in an acidic solution comprised of three parts H_2O, one part HNO_3.

6.2.5 DNA Immobilisation

Au wafer electrodes were immersed in a 10 µM solution of thiolated probe DNA in PBS buffer for 14 hours. Electrodes were then rinsed in deionised water to remove loosely attached oligos.

6.2.6 EDC Coupling

For EDC coupling a buffer was prepared with 0.01 M K_2HPO_4 and 0.15M NaCl and was pH adjusted with NaOH to pH 5.5. 10 µL (1.27×10^7) of the microspheres were washed twice with 100 µL of the coupling buffer and then re-suspended in 100 µL of coupling buffer. Cy5 dye and probe DNA was added at the required concentration. 100 µL of 5 mg ml^{-1} EDC in coupling buffer was then prepared, and 20 µL of the EDC solution was further added. All of the work with EDC was performed as quickly as possible, since EDC is highly reactive in aqueous environments. The solution was mixed by pipetting and subsequently incubated for 2 hours at room temperature.

Following the reaction, the reaction vessel was placed close to a magnet to coalesce the particles and the supernatant was removed. The particles were then washed 5 times with 200 µL of PBS, with magnetic separation of the particles. The functionalized microspheres where then resuspended in 100 µL of PBS.

6.3 Results and Discussion

6.3.1 Capture Deposition on Au

The objective to this work was the displacement of large particles to produce a significant measurable signal. The first element of this was the functionalization of a Au surface with the capture DNA. The capture strand was designed with a thiol bond which spontaneously forms a strong bond with Au.[16] To probe the binding of the thiolated DNA to the Au, a 100 nm thick Au coated silicon wafer was immersed in 1 µM capture solution for 14 hours. A voltammogram was recorded in 0.1 M H_2SO_4 before and after the deposition of the DNA. The results for this experiment are shown in Figure 6.2.

Before DNA deposition, a Au oxide reduction peak is visible at approximately +0.8 V. This peak gave a microscopic electrode area of 0.221 cm^2 using Equation 2.2. After deposition of DNA this active area was reduced to 0.095 cm^2, which represents a reduction of 57 % due to DNA adsorption. The shape of the voltammogram also changed, becoming sloped due to an increase in the resistance. This provides excellent evidence for the blocking of the surface by the thiolated DNA and suggests an appropriate coverage of the electrode surface, ie., the capture DNA strands are sufficiently far apart that they can hybridise with the target strands on the particle but are not so dense that the particle is essentially irreversibly bound due to the formation of many linakages.[17]

Since the capture DNA had been successfully bound to the Au surface, the next objective was to assess the ability of the probe strand to hybridise with the capture DNA.

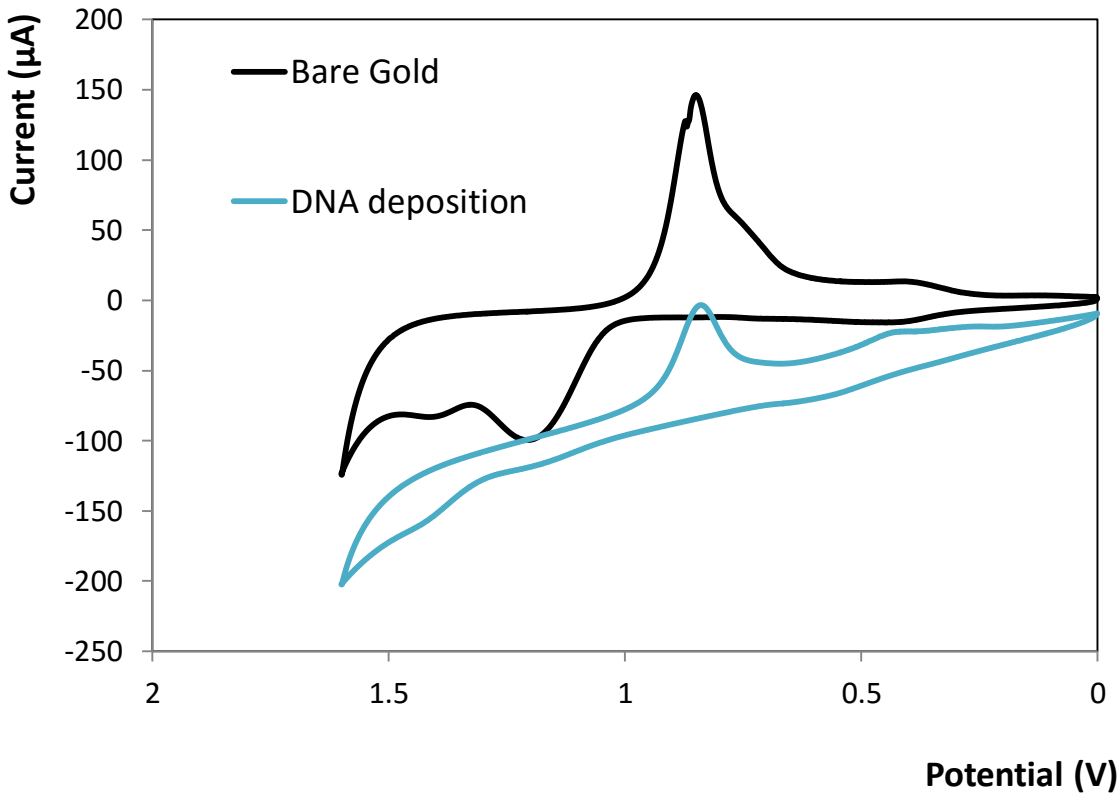

Figure 6.2: Cyclic voltammograms in 0.1 M H_2SO_4 of a Au wafer electrode, before and after the deposition of 1 µM capture DNA in PBS for 14 hours. The reference electrode was silver/silver chloride.

6.3.2 Capture / Probe Hybridization

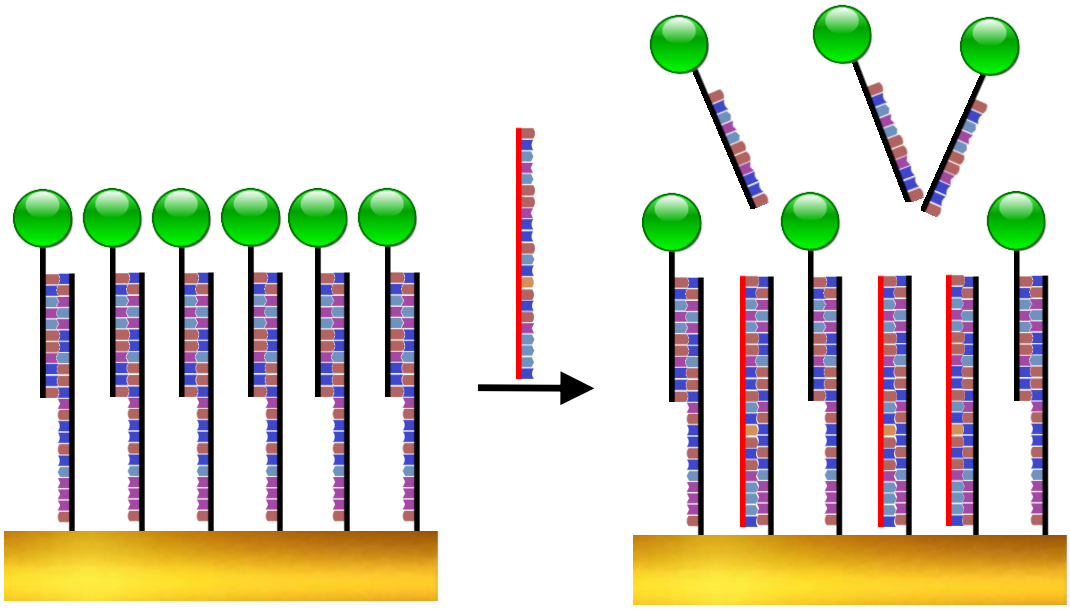

Figure 6.3: Scheme for the attachment of the capture DNA to Au, followed by hybridization of the [Ru(bpy)$_2$PIC-COOH]$^{2+}$ labelled probe strand (left). Displacement of probe after the addition of the miRNA target (right).

To visualise the hybridisation of the probe strand to the capture, an EDC coupling was performed between an amine functionalised DNA and a carboxy functionalised [Ru(bpy)$_2$PIC-COOH]$^{2+}$ dye. This dye was chosen as it emits at 610 nm and its lifetime depends on the local microenvironment. The coupling was performed with 5 µM DNA and 40 µM dye in coupling buffer with 5 mg EDC for 12 hours to ensure high labelling efficiency of the probe strand. A Au wafer, modified with capture DNA, was then immersed in the reaction mixture for 12 hours at room temperature. The Au wafer was rinsed 5 times with PBS to remove any non-specifically attached dye. The capture-probe-[Ru(bpy)$_2$PIC-COOH]$^{2+}$ wafer was then imaged under a confocal microscope to visualise the dye.

Figure 6.4 (A) shows the signal received after modification of the surface with capture DNA. No measurable fluorescent signal was detected. Figure 6.4(B) shows the Au surface after hybridisation of the [Ru(bpy)$_2$PIC-COOH]$^{2+}$ labelled probe DNA. A uniform signal was detected across the Au surface. To ensure that the signal was not due to backscatter from the Au, a small area was imaged intensively for 10 minutes. After scanning, the fluorescence intensity in this region significantly reduced; this is consistent with bleaching of the dye in this area. This experiment suggested that the probe strand had successfully hybridised to the capture modified Au surface.

The next objective was to determine if the dye labelled probe could be displaced with miR-132. The Au wafer was placed in a 1 µM solution of the target for 3 hours. It was then removed from the solution and rinsed with PBS. The Au wafer was reimaged by confocal microscopy, see Figure 6.4(C). The intensity before the RNA target was added was 496±8 A.U., which then dropped to 211±10 A.U.. This represents a reduction of 57 % in intensity and provides good evidence for the effective displacement of the $[Ru(bpy)_2PIC\text{-}COOH]^{2+}$ labelled probe by the target miRNA.

Based on this experiment, it was decided that the underlying displacement mechanism was working as expected, and so the next objective was the preparation and displacement of the microspheres with the intention that a small number, ideally one, binding event could be detected on the basis of displacing the luminescent microsphere.

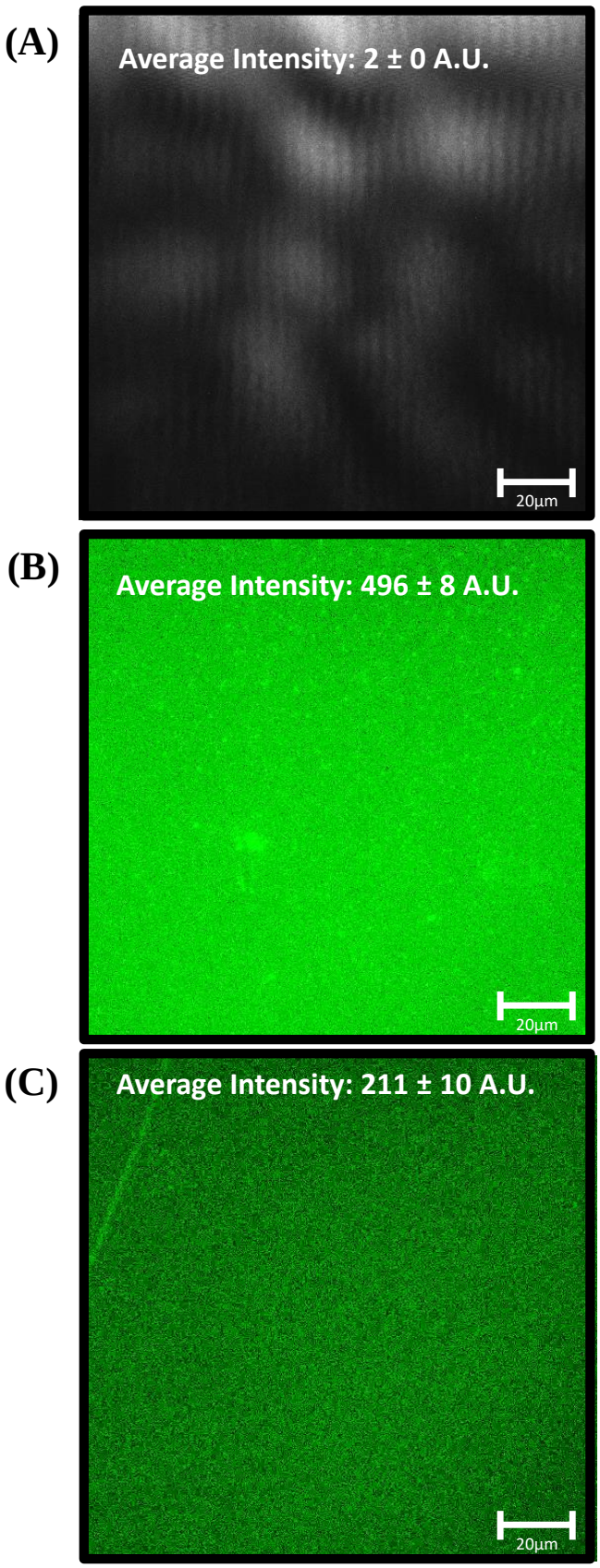

Figure 6.4: Confocal fluorescence microscopy of bare Au wafer with (A) capture DNA, (B) $[Ru(bpy)_2PIC\text{-}COOH]^{2+}$ labelled probe DNA, and (C) 1 µM target. Excitation with an argon ion laser at 458 nm and with a LP615 filter at 4.1 %.

6.3.3 Cy5 Amine

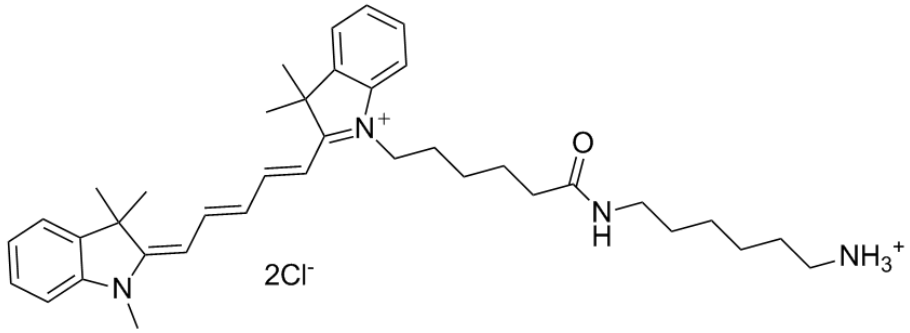

Figure 6.5: Structure of Cyanine 5 Amine.

In order to aid the visualisation of the microspheres, the decision was made to co-immobilise a dye along with the probe DNA strand. The photophysics of the Cyanine-5 amine (Cy5) dye were investigated to determine its suitability for use as part of the displacement assay. This dye had a number of attractive properties for integration into the displacement assay. The dye is water soluble, which is essential as the microspheres are not stable in most organic solvents.[18] It contains an amine group which allows for convenient coupling to the microsphere. Cy5 has a reasonable quantum yield[19] at 0.2 and acceptable photostability[20].

Figure 6.6 shows the absorption and emission spectra for 10 µM Cy5 in PBS. The maximum emission was found at 662 nm, which closely matches the literature value of 670 nm[21]. A broad absorption peak is seen from approximately 500 nm to 700 nm, with maximum absorbance at 640 nm, which is close to the 650 nm value previously reported.[22] These spectra show a very small stokes shift for Cy5, with significant overlap between the emission and absorption spectra. This suggests that self-quenching of the dye is likely to occur at high concentrations.

To further probe the photophysical properties of the dye, its lifetime in aqueous solution was examined.

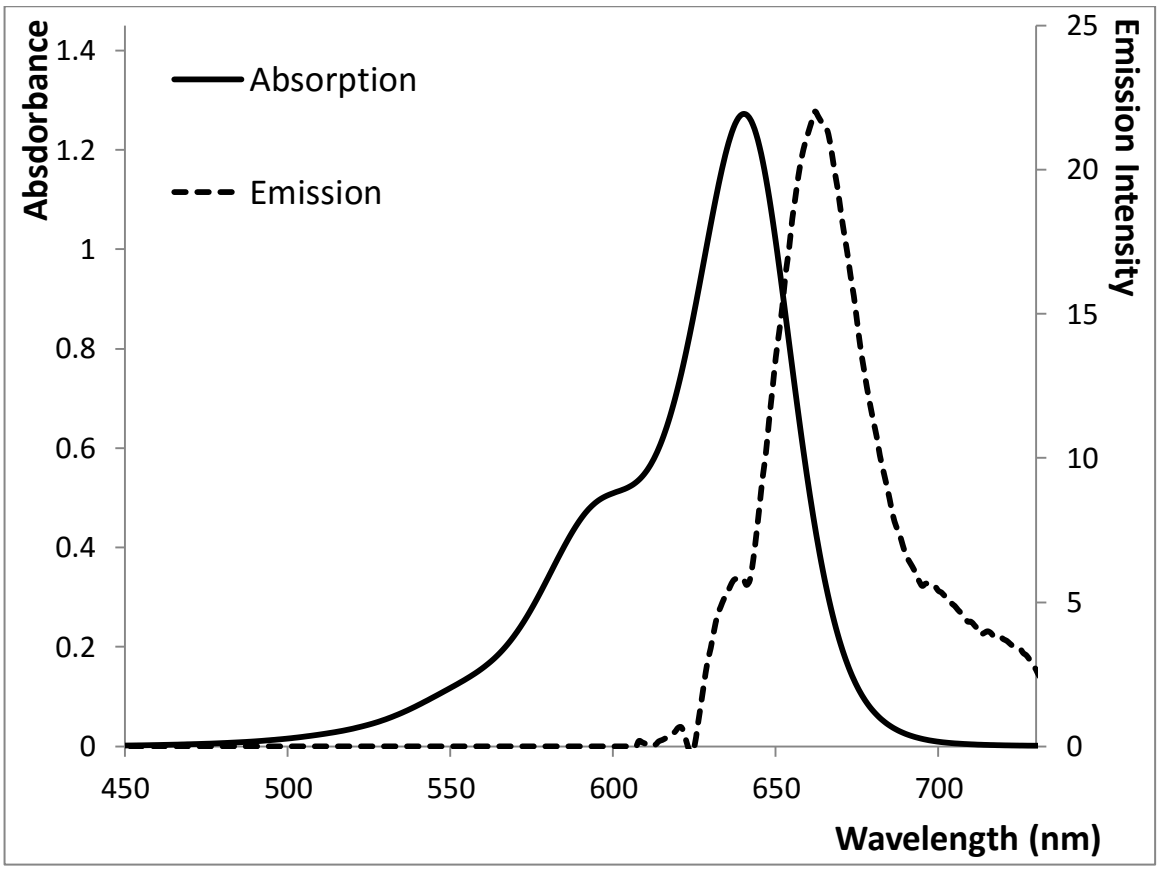

Figure 6.6: Absorbance and emission spectra of 10 µM Cy5 in PBS. Excitation at 600 nm with excitation and emission slits at 2.5.

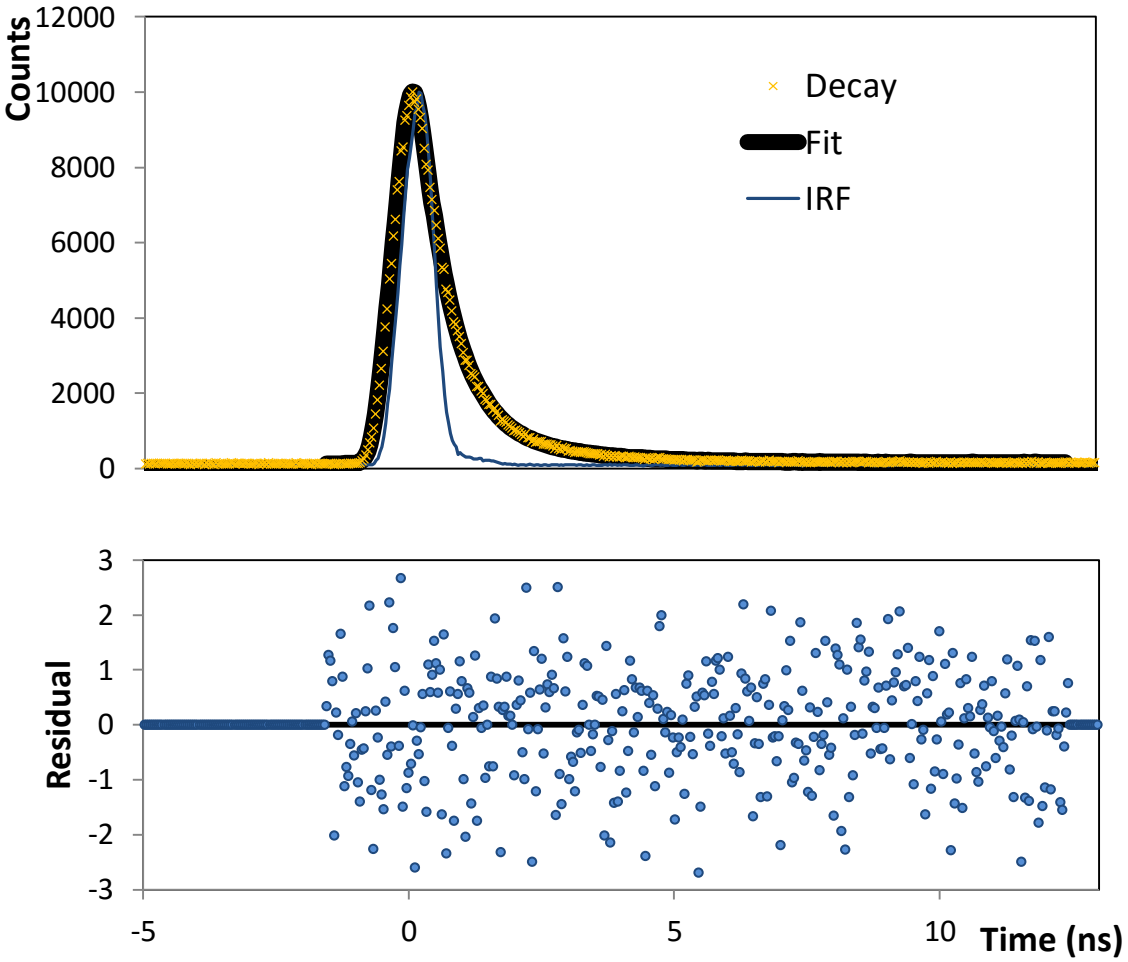

τ_1 (ns)		τ_2 (ns)		x^2
0.5±0.0	88%	1.6±0.0	12%	1.135

Figure 6.7: Time correlated single photon counting lifetime for 10 µM Cy5 in PBS with fit (top) and residual plot (bottom).

The photophysics of Cy5 has been shown to be highly oxygen dependent. [23-25]. For this experiment, working in deoxygenated solutions was not practical, so the lifetime was measured in a normal PBS solution. The lifetime of the dye was examined using time correlated single photon counting. Figure 6.7 shows the fit to the TCSPC data for the lifetime measurement. The decay could not be accurately fitted using a single exponential, so a bi-exponential model was used. The residual plot shows an even distribution over the analysed range which suggests a bi-exponential model is sufficient to describe this decay. A shorter lifetime at 0.5±0.0 ns accounted for 88 % of the signal, with a longer component at 1.6±0.0 ns contributing 12 % of the signal. The shorter lifetime is believed to be due to instrument noise, as previously observed in Section 3.3.5. The longer lifetime of 1.6±0.0 ns is similar to the literature values of 1.8 ns.[26,27]

A concentration curve for the Cy5 dye was prepared to examine the effect of concentration on the fluorescent intensity of the dye, based on the spectral overlap observed in Figure 6.6. The concentration was varied between 1 µM and 1000 µM. The results for this experiment are shown in Figure 6.8 and Figure 6.9. From 1 µM to 50 µM the emission intensity increased, reaching a maximum of 19±1 A.U. At higher concentrations, the intensity began to fall. At 100 µM the intensity was 14±1 A.U., decreasing to 4±0 A.U. at 500 µM. As the concentration further increased, the intensity approached 0, reaching 2±0 A.U. at 1 mM. The shape of the emission spectra also changed significantly over the concentration range. At 10 µM and below, the spectra contains only a single peak. As the concentration was increased, a second peak becomes visible at approximately 716 nm. The position of maximum intensity also changes, increasing linearity with the log of concentration as shown in Figure *6.10*. The photophysics of Cy5 have been analysed in a number of studies, with self-quenching indicated due to cis-trans isomerisation[28,29], reverse intersystem crossing[30,31], phosphorescence[32,33] and millisecond blinking[23,34,35].

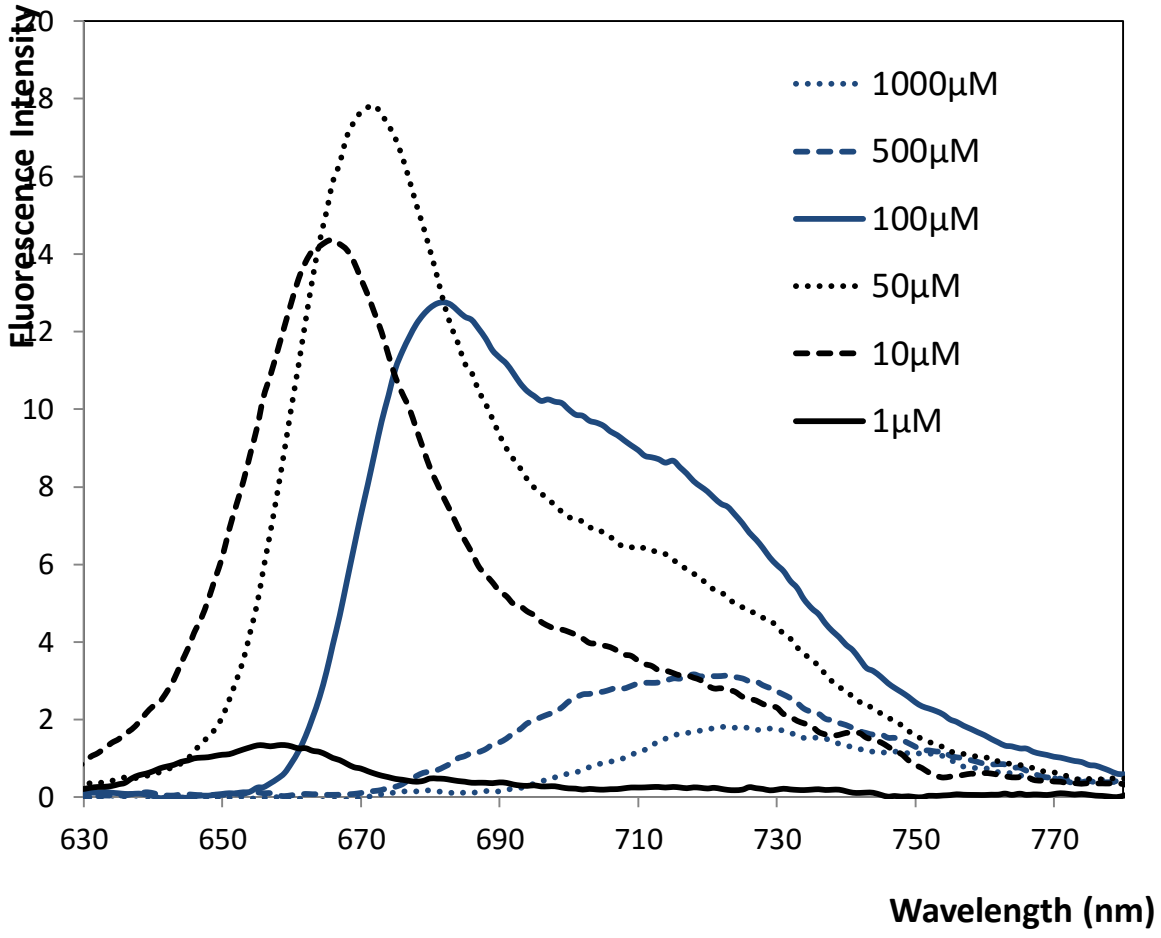

Figure 6.8: Emission spectra for a range of Cy5 concentrations from 10 µM to 1 mM in PBS. Excitation at 600 nm with excitation and emission slits at 2.5.

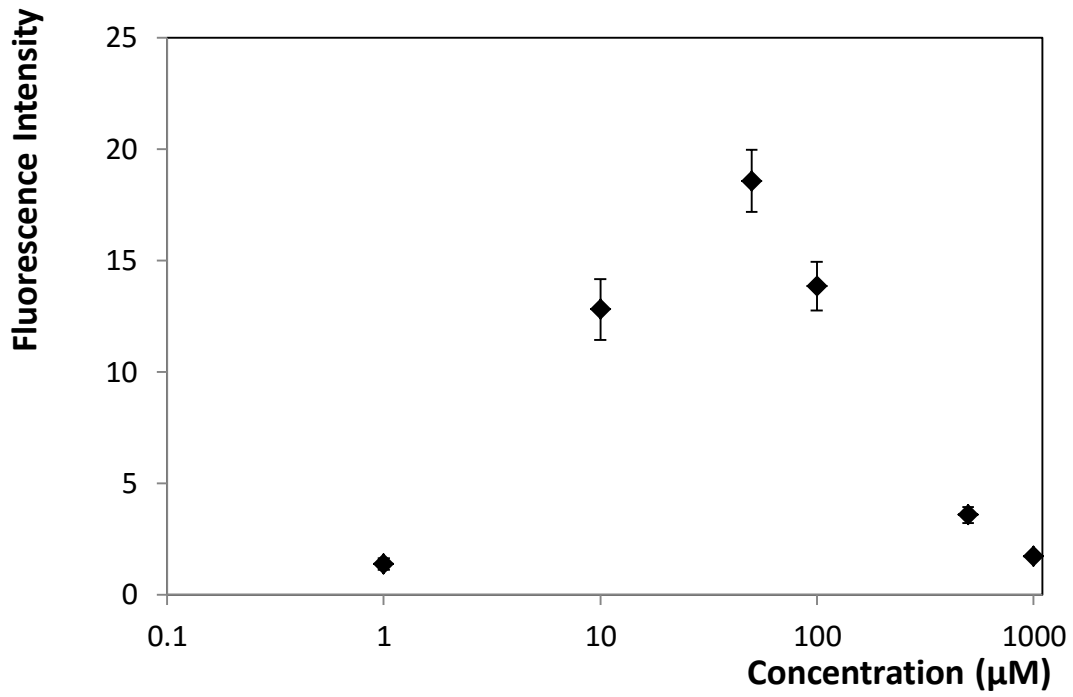

Figure 6.9*: Maximum emission intensity for a range of Cy5 concentrations from 10 µM to 1 mM in PBS. Excitation at 600 nm with excitation and emission slits at 2.5. Results for 3 repeats are shown. Where error bars are not visible, they are smaller than the icon.*

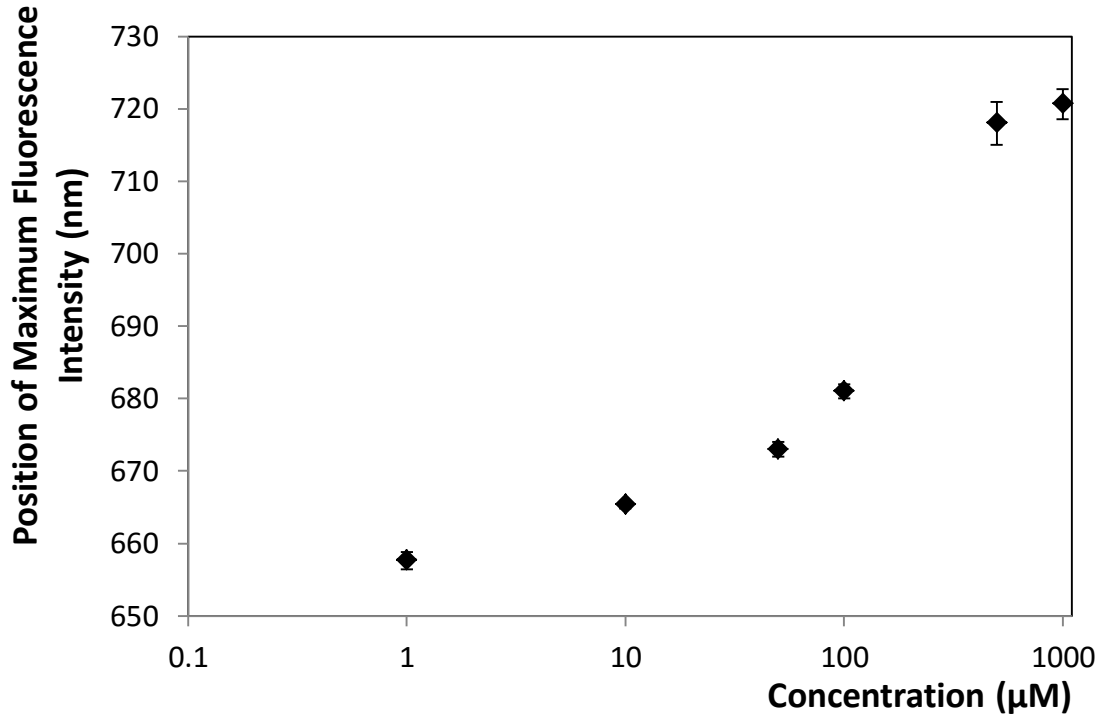

Figure 6.10*: Position of maximum emission intensity for a range of Cy5 concentrations from 10 µM to 1 mM in PBS. Excitation at 600 nm with excitation and emission slits at 2.5. Results for 3 repeats are shown. Where error bars are not visible, they are smaller than the icon.*

Based on the reduction in intensity observed at high dye concentration, the close overlap observed between the absorption and emission spectra, and previous reports of self-quenching at high concentration[36,37], the energy transfer between Cy5 molecules was calculated since this will help identify the optimum separation/loading of the dye on the microsphere surface.

Table 6.1: Calculated values for Förster energy transfer for self-quenching of Cy5.

Forster Distance (Å)	89.331
Rate of Electron Transfer (1/s)	2.342×10^{26}
Dexter Value (1/eV)	1.114
J value (cm^6)	1.370×10^{-11}

The distance between two molecules of Cy5 at which energy transfer is 50 % efficient (R_0) can be represented as:

$$R_0 = \frac{8.8 \times 10^{-25}\, K^2 \phi_D}{n^4} J$$

Equation 6.1: Critical Förster energy distance

Where K^2 = Orientation factor

ϕ_D = Fluorescence quantum yield

n = Refractive index

J = Spectral overlap integral

The orientation factor was assumed to be 2/3 for rapidly rotating randomly orientated donor and acceptor molecules.[38] The refractive index was 1.333 for water.[39] The quantum yield was 0.2, as previously reported.[40] The spectral overlap was calculated based on the spectra shown in Figure 6.6. Based on this calculation, the critical Förster energy distance was calculated as 89 Å. This is a short distance, so a high degree of self-quenching is expected for high concentrations of the dye. At a concentration of approximately 0.56 µM quenching is expected to be 50 % efficient.

The photophysics of the Cy5 had been characterised, so the next objective was coupling of the dye to the microspheres.

6.3.4 Microspheres with Cy5

The Cy5 dye was attached to the microspheres by EDC coupling. EDC allows for the efficient coupling of primary amines to carboxylic acid groups.[41-43] It is also water soluble, which is necessary for working with the microspheres due to poor stability in organic solvent.[44,45] The microspheres are uniformly modified with carboxy groups which act as the attachment site for the coupling reaction. Based on the manufacturer's specifications, each microsphere contains 4.44×10^9 carboxy groups. The coupling was performed with 1.27×10^7 microspheres, so the reaction mixture contained 5.64×10^{16} carboxy groups. This gives an effective concentration of 0.45 µM during the coupling. 500 µM Cy5 was added to ensure complete coverage of the microspheres.

The results of this experiment are shown in Figure 6.11. The brightness of the dye was sufficient to allow for visualisation of the microspheres. The cross section shows that the dye is localised to the outside of the microsphere as expected. To analyse the effect of bleaching on the brightness of the particles, a small area was scanned intensively for 5 minutes. After scanning, the brightness of the particles increased from 1603±42 A.U. to ≥4095 A.U. According to the manufacturer's specification, the area of occupation for a single carboxylic acid group on the surface is 0.7 $Å^2$. Assuming complete coverage of a microsphere with Cy5 and 0.7 Å separation between the microspheres, Forester energy transfer would be 100 % efficient. This significant increase in fluorescence intensity is constant with bleaching of the Cy5 dye, which lowers the local concentration, resulting in an increase in the observed intensity.

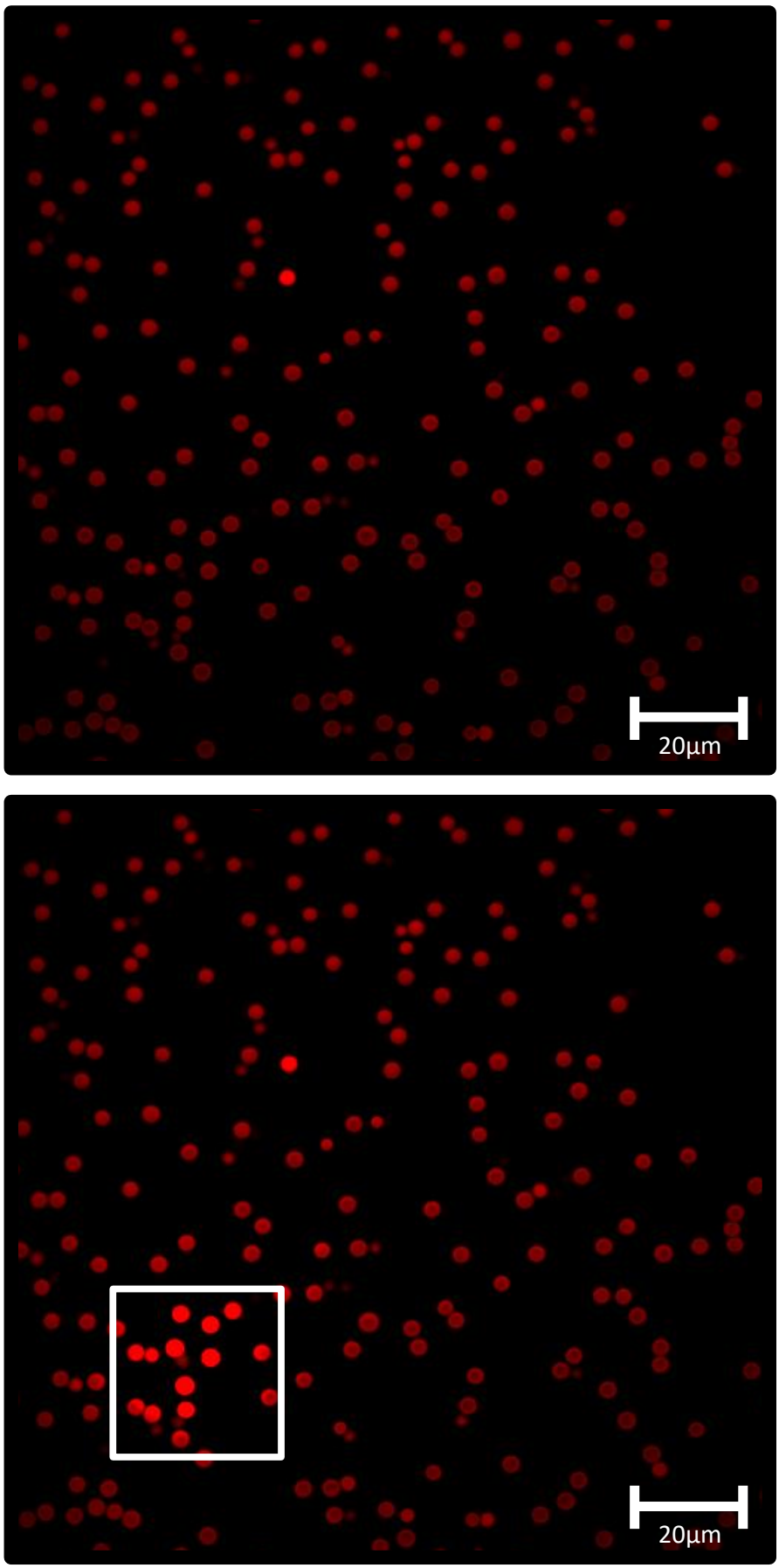

Figure 6.11: Confocal fluorescence microscopy of 1.27 x 10^7 3µm microspheres after EDC coupling of with 0.5 mM Cy5. Excitation at 633 nm with LP165 filter at 10 %.

6.3.5 Microspheres with Cy5 and Probe

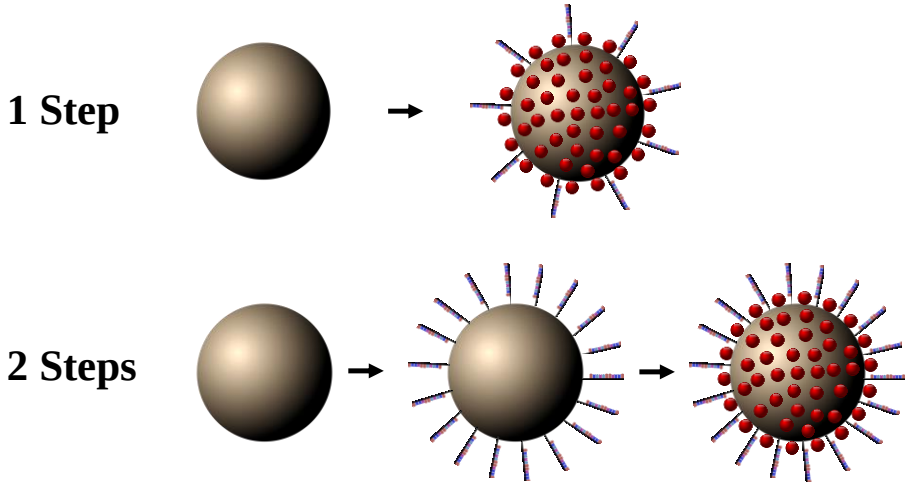

Figure 6.12: Scheme showing the two approaches for the modification of microspheres with Cy5 and probe DNA.

For the attachment of the probe strand to the microsphere two approaches were examined. The first approach was to simultaneously attach the probe strand and dye (1 Step). This coupling was performed with 1 mM Cy5 and 5 µM probe DNA. The objective of this experiment was to achieve a microsphere with a moderately low surface coverage of DNA so that it does not bind too strongly to the capture strand modified surface. The second approach was to first react the microspheres with probe DNA and then fill the vacant sites with Cy5 (2 Steps). This approach could give a much higher surface coverage of probe DNA, and a lower coverage of Cy5. In this experiment the concentration of carboxy groups was approximately 0.45 µM. 10 µM of probe DNA was coupled with the microspheres, which was expected to result in a high surface coverage of DNA. This was then followed with 1 mM Cy5.

The results for this experiment are shown in Figure 6.13. The intensity of the 1 Step reaction was 862±155 A.U., which is considerably higher than the 1558±455 A.U. observed for the particles modified in two discrete steps. This is consistent with a *higher* dye coverage for the 1 Step reaction resulting in a higher local dye concentration, leading to increased trivial quenching due to the small Stokes shift. The difference in intensity between the two reactions suggests that the probe DNA was successfully attached to the microspheres. The goal of this work was the displacement of the microsphere from a capture functionalised Au surface. Preferably, only a *single* probe strand would link the microsphere to the surface. For this reason the 1 Step

microspheres were considered to be the most appropriate, as the surface coverage of probe DNA should be considerably lower.

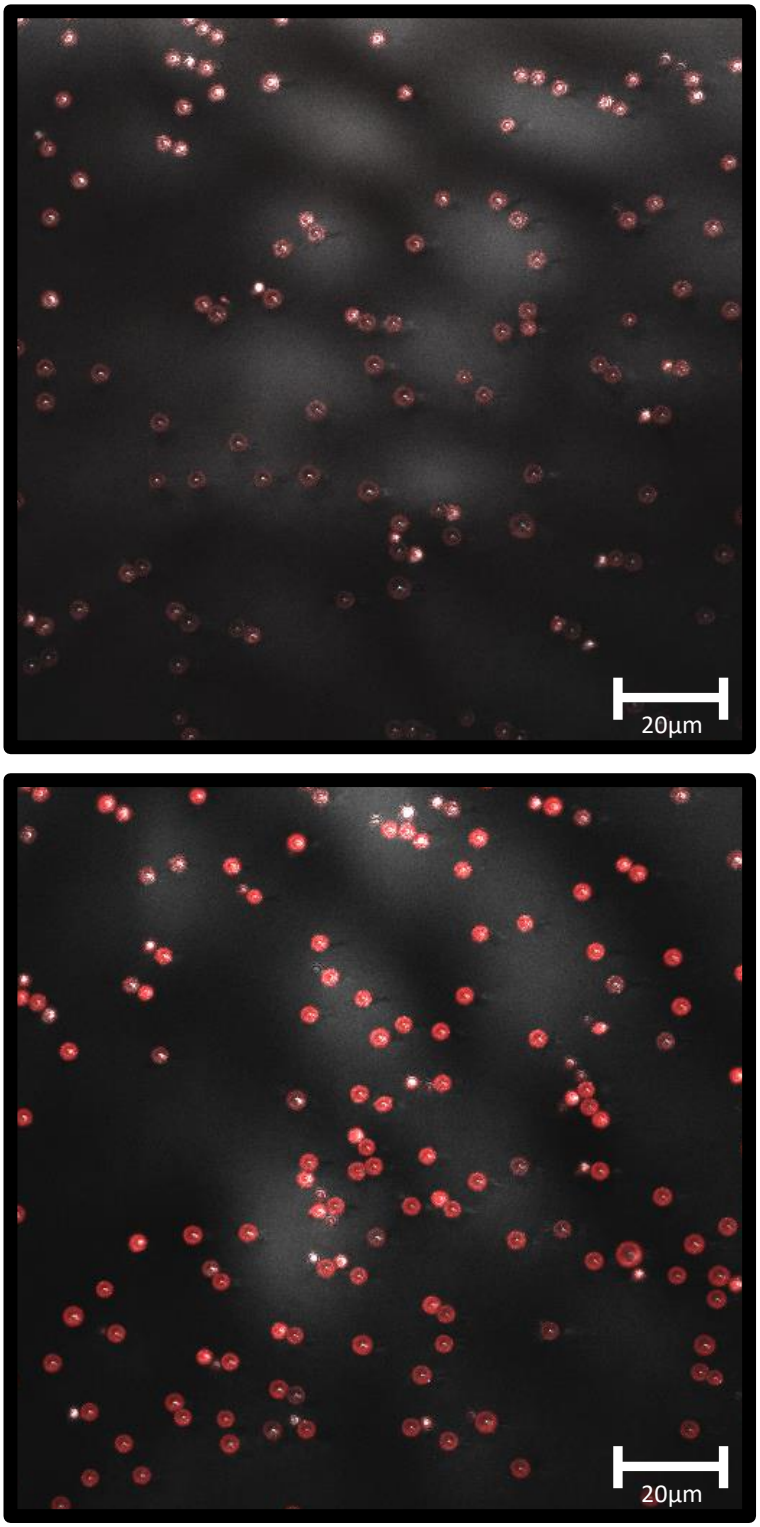

Figure 6.13: Confocal fluorescence microscopy of 1.27 x 10^7 3 µm microspheres after (A) EDC coupling of with 1 mM Cy5 and 5 µM probe, and (B) EDC coupling of 10 µM probe followed by EDC coupling with 1 mM Cy5. Excitation at 633 nm with LP165 filter at 10 %.

6.3.6 Attachment of Microspheres with Probe to Capture Modified Au

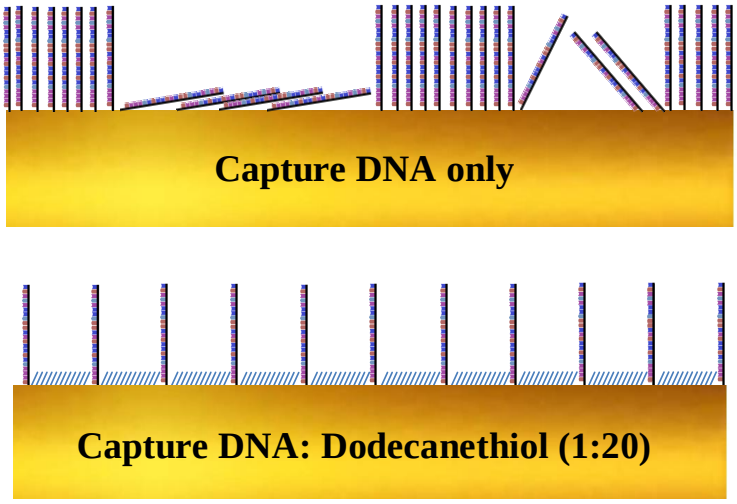

Figure 6.14: Scheme showing deposition of capture DNA onto Au (top), and co-deposition of capture DNA with dodecanethiol (bottom).

The next objective was the attachment of the microspheres to the Au surface via hybridisation of the probe DNA to the capture strand. As previously discussed, ideally the microsphere would be attached to the surface by a single probe/ capture hybridisation, so that a single miRNA binding event would result in displacement of the microsphere. The 1 Step microspheres were preferred, due to the lower surface coverage of probe strand, however as previously shown in Figure 6.4, the deposition of capture onto the Au surface would result in very high coverage of capture DNA. In order to examine the effect of surface coverage of capture DNA on the binding of the probe, 1 µM of capture was co-deposited with 10 µm of dodecanethiol. It was hoped that this would result in lower surface coverage of the capture strand, while simultaneously improving the orientation of the capture DNA on the surface to improve the availability of the capture to the probe.

Au wafer was modified with capture DNA. Microspheres where then deposited onto the surface, in solution, and allowed to hybridize for 14 hours. The surface was then rinsed with PBS to remove loosely bound microspheres. The microspheres were 3 µm in size, so were visible to the naked eye in bulk. During the washing phase of the experiment it was noted that the majority of the microspheres were liberated from the surface. The Au wafer was then imaged by confocal microscopy. The results of this experiment are

shown in Figure 6.15. The surface coverage was much lower than expected (given the long hybridisation time one would anticipate the spheres to be close packed), with some areas of the Au wafer showing no microspheres present.

Figure 6.16 shows the results for the Au wafer with capture and dodecanethiol co-deposited on the surface. As in the previous experiment, the majority of the microsphere appears to be removed during the washing phase of this experiment. The confocal images show very low surface coverage, similar to that seen for the previous experiment.

To test if the microspheres, which were visible on the surface, were attached via the probe capture hybridisation, or due to non-specific interactions, the Au wafer was immersed in 10 μM target miRNA for 3 hours. The Au wafer was then gently rinsed to remove any displaced microspheres and imaged again under confocal. No difference in the surface coverage was observed, which suggests that the microspheres were adhered by non-specific interactions or the probe could not access the capture strands underneath the bound microspheres.

Repeats of this experiment showed similar results, with no displacement of the microspheres upon the addition of miR-132 target. These results suggested that either the capture probe hybridisation was not occurring, or alternatively, that the strength of this interaction was not sufficient to hold the microsphere at the surface.

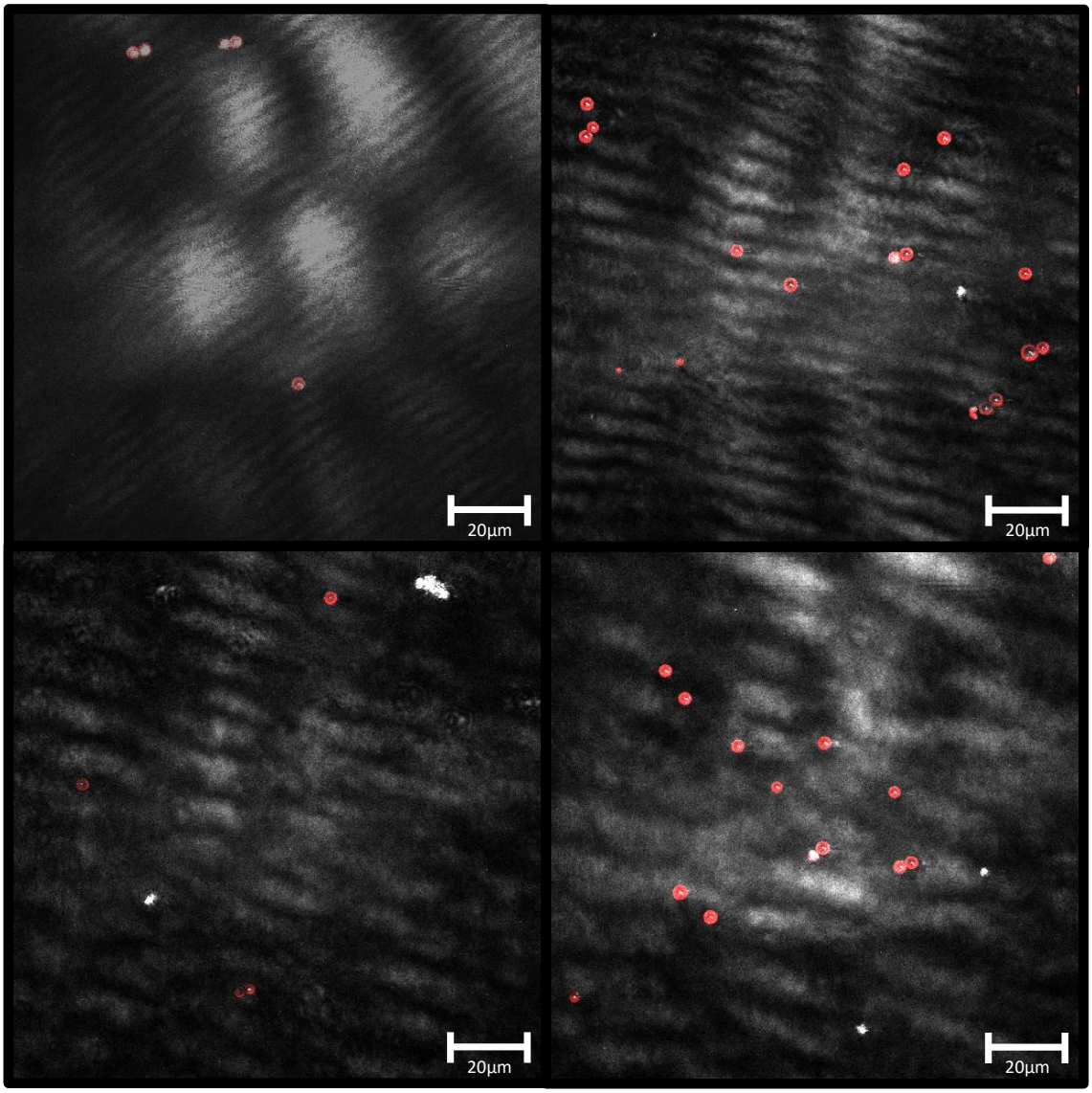

Figure 6.15: Confocal fluorescence microscopy of 1.27 x 10^7 3 µm microspheres after EDC coupling of 5 µM probe DNA with 1 mM Cy5 after 4 hours deposition on Au wafer functionalised with 1 µM capture for 14 hours. Excitation at 633 nm with LP165 filter at 10 %.

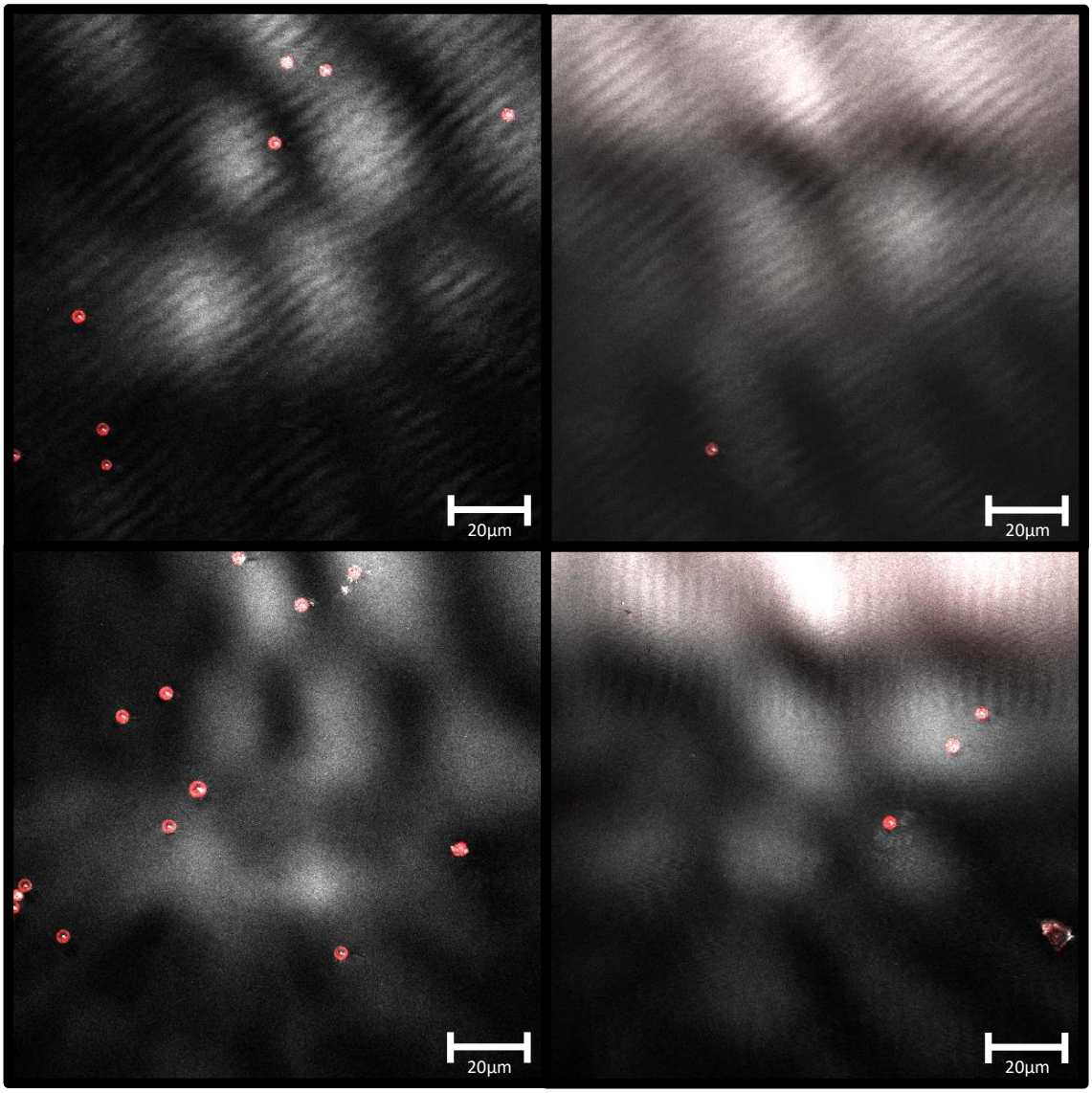

Figure 6.16: Confocal fluorescence microscopy of 1.27 x 10^7 3µm microspheres after EDC coupling of 5 µM probe DNA with 1 mM Cy5 after 4 hours deposition on Au wafer functionalised with 10 µM dodecanethiol and 1 µM capture for 14 hours. Excitation at 633 nm with LP165 filter at 10 %.

6.3.7 Potential Controlled Deposition

Previous experiments had demonstrated that the probe strand was capable of hybridising to the capture DNA, and that it had been successfully displaced by the addition of miR-132 target, which suggested that there was no issue with the quality of the nucleic acid used. One possible explanation for this is electrostatic repulsion of the negatively charged spheres (due to deprotonation of the carboxy groups) by the negatively charged DNA capture strands. Based on the manufacturer's specification, a single unmodified microsphere has a surface charge of 0.078 aC. This charge could be the cause of repulsion between the negatively charged capture DNA on the Au surface and the probe strand.

To investigate this issue, Au wafer was functionalised with capture DNA. A potential of +0.3 V was applied for 2 hours during the deposition of the probe and Cy5 functionalised microspheres. This potential is positive of the potential of zero charge for clean Au but is not expected to change the DNA capture layer structure. The objective was to attract the microspheres to the surface where they could then hybridise. The surface was then gently rinsed to remove non-specifically bound microspheres. Figure 6.18 shows the results for this experiment. A large number of microspheres were visible on the surface of the Au. While the microspheres were visible using the backscattered light, no fluorescent signal was visible. This result was unexpected, and was also very different to the confocal images previously seen.

The next objective was to test the microsphere's ability to be displaced by the target miRNA. To measure the displacement of microspheres, the system was set up as shown in Figure 6.17. The confocal system available uses an inverted microscope and an oil immersion lens. Images were collected by placing a thin glass cover slide over the lens, and placing the Au wafer with the Au side down onto the glass. When PBS was added between the glass and Au wafer, the Au wafer rose in height away from the lens. This placed the Au surface outside the maximum confocal distance of the system. The microspheres are heavier than water, and so they would sink to the glass surface if displaced from the Au. In this experiment, PBS was added and the surface of the glass was imaged after 15 minutes. As can be seen in Figure 6.18(B), very few particles were detected after this time. This suggested that the microspheres were well attached to the Au surface, either by capture / probe hybridisation or by non-specific interactions.

miR-132 target was then added to bring the concentration in the PBS to 10 µM. The glass surface was imaged again after another 15 minutes. A significant number of microspheres were present on the surface of the glass. This experiment indicates that these microspheres were successfully displaced from the surface of the Au.

Of interest in this experiment is the loss of fluorescence by the dyes when bound to the surface of the Au, which was reversed upon release onto the glass. This suggests that the loss of fluorescence was not as a direct result of the potential controlled deposition. One explanation for this is quenching of the dye excited state by the Au surface. This would provide further evidence for the successful attachment of the microspheres to the Au surface in this experiment. If this is the case, then this could potentially act has a highly sensitive method for the detection of analyte binding. If displacement of the microsphere causes “switching on” of the dye, then this would provide a large easily measurable signal, with very low background.

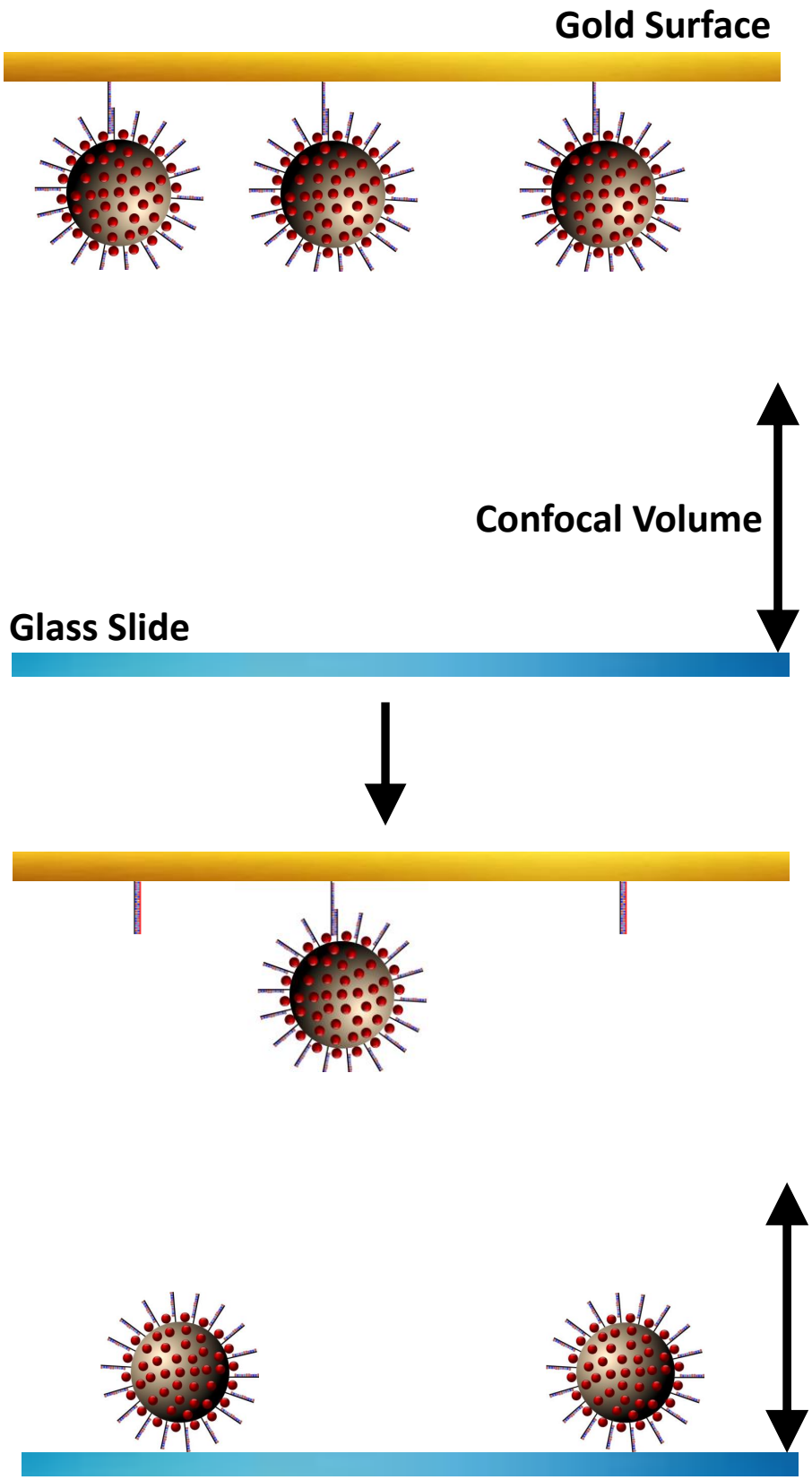

Figure 6.17: Scheme showing detection of microspheres using inverted confocal microscope, whereby displaced microspheres are released from the Au surface and fall onto the underlying glass, where they are detected.

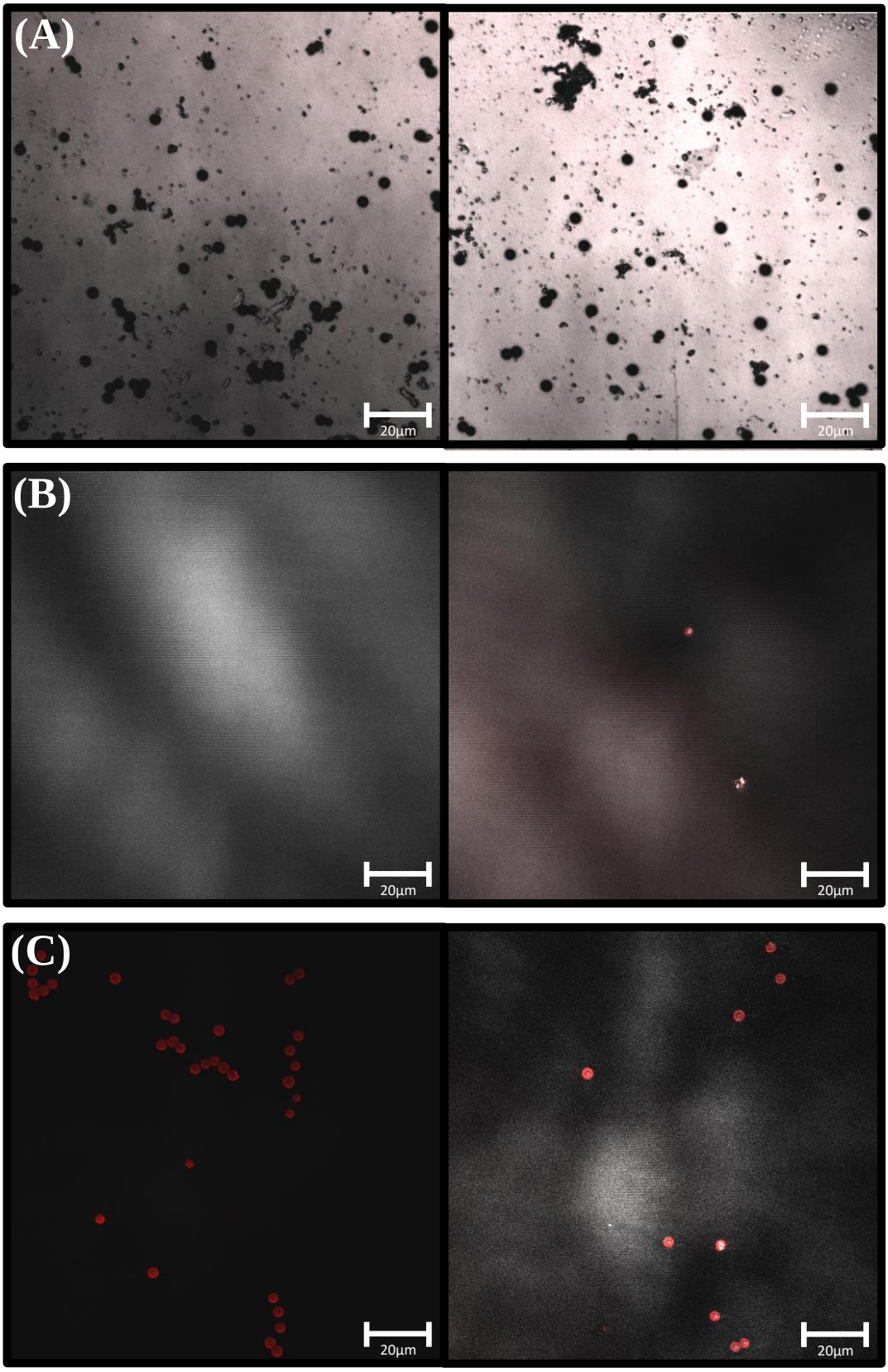

Figure 6.18: Confocal fluorescence microscopy of 1.27 x 10^7 1-Step microspheres after 4 hours deposition with applied potential of +0.3 V in PBS on Au wafer functionalised with 1 µM capture for 14 hours. Excitation at 633 nm with LP165 filter at 10%. (A) microspheres on Au wafer surface, (B) glass surface 15 minutes after addition PBS and (C) glass surface 15 minutes after the addition of 10 µM target miRNA.

This experiment appeared to be successful in the displacement of the microspheres by addition of target miRNA. The next objective was to determine the concentration dependence of the displacement of the microspheres. Unfortunately, repeats of this experiment produced highly inconsistent results. The primary issue was the capturing of the microspheres on the Au surface. In follow up experiments, this surface coverage varied from no microspheres present, to a similar surface coverage as that seen in Figure 6.18. The reasons for this inconsistency are not known and further investigations are justified.

6.4 Conclusions

The objective of this work was the detection of miR-132 by displacement assay. The displacement assay was shown to work using a Au surface modified with capture DNA, and probe functionalised with a $[Ru(bpy)_2PIC\text{-}COOH]^{2+}$ dye. When the miR-132 target was added, the intensity of the $[Ru(bpy)_2PIC\text{-}COOH]^{2+}$ dye was reduced, which suggests that the displacement had successfully taken place.

To generate a large analytical signal for the displacement of a single probe strand by the target, a 3µm microsphere was prepared with a probe strand and a dye, Cy5 to aid in the visualisation of the probe by fluorescent microscopy. The surface coverage of the probe on the surface could be controlled by the order in which the DNA and dye were attached, or by the relative concentration of the two.

Immobilisation of the microsphere onto capture functionalised Au was initially unsuccessful, with very low surface coverage and no displacement with the addition of miR-132. This was believed to be due to electrostatic repulsion between the negatively charged microsphere, and the negatively charged capture surface. To overcome this issue, a positive potential was applied to the surface. Microspheres appeared to adhere to the surface after this process, with the fluorescence of the dye not visible, possibly due to transfer of the excited state into the Au mediated by the DNA duplex.

However, repeats of this experiment gave highly inconsistent results, with very low surface coverage for some experiments, and no apparent displacement of the microspheres with the addition of target in others. A number of factors may explain this result. In this experiment the capture/ probe hybrid has an associated association and disassociation rate, as does the capture/ target hybrid. In order for the assay to perform as expected, the association of the microspheres must be sufficient to anchor the particle to the surface. The disassociation rate must be high enough to facilitate the preferential binding of the target, which allows the displacement to occur. The design of the DNA strands was optimised so that the association of the target with the capture strand would be considerably more energetically favourable than the capture/ probe hybrid, based on the number of matching bases.

Negative charging of the microspheres caused the dissociation of the capture/ probe hybrid to become more favoured, which while beneficial for displacement, caused issues for the immobilisation of the microspheres. This issue appears to have been

solved by the potential controlled deposition; however other approaches are also considered possible. The addition of charged moieties to the microsphere could be adjusted to make the net charge neutral or slightly positive. This should remove the need for an applied potential.

Another potential issue is the transport of the target past the microsphere. These large particles may slow the diffusion of the target miRNA to the surface. This means that the effective concentration at the surface is considerably lower than in solution. This factor could be mitigated by controlling the dispersion of capture DNA on the surface so that microspheres have greater separation or by tuning the capture strand length. This should be controllable by co-deposition with an alkane thiol monolayer as previously discussed. This would also improve the sensitivity of the assay, since capture DNA present on the surface, which is not bound to a microsphere, competes for miRNA target added, further lowering the effective concentration available to displace the microspheres.

For the microsphere to be successfully displaced, the association of the target/ capture needs to be high, as does the disassociation of the capture/ probe. The design of the DNA strands is sufficient to allow this to occur for a single linkage from the probe to the surface as illustrated by the successful displacement of the $[Ru(bpy)_2PIC\text{-}COOH]^{2+}$ probe. However, for the microspheres, the number of linkages to the surface is potentially much higher. A single microsphere could have multiple probe/ capture hybrids immobilising the particle to the surface. This means that even though disassociation of the probe/ capture hybrid is favourable, the high number of linkages makes displacement highly unlikely.

This issue could be resolved by reducing the surface coverage of capture, as discussed previously, and of the probe strand. For the probe strand this should be achievable by varying the concentration of the probe with respect to the Cy5 dye or another blocking group. Ideally, only a single capture and probe strand would then be available. This should allow for a single target binding event to cause the release of the microsphere.

Overall a number of issues remain with this assay, with further optimisation required to achieve the determination of ultra-low concentrations.

6.5 References

1. Hartl, D. L.; Ruvolo, M. In *Genetics;* Jones \& Bartlett Learning: **2011**; pp 32.

2. Wang, J.; Yi, X.; Tang, H.; Han, H.; Wu, M.; Zhou, F. Direct Quantification of MicroRNA at Low Picomolar Level in Sera of Glioma Patients Using a Competitive Hybridization Followed by Amplified Voltammetric Detection. *Anal. Chem.* **2012**, *84*, 6400-6406.

3. Bustin, S. Absolute quantification of mRNA using real-time reverse transcription polymerase chain reaction assays. *J. Mol. Endocrinol.* **2000**, *25*, 169-193.

4. Udvardi, M. K.; Czechowski, T.; Scheible, W. Eleven Auen rules of quantitative RT-PCR. *Plant Cell* **2008**, *20*, 1736-1737.

5. Schmittgen, T. D.; Lee, E. J.; Jiang, J.; Sarkar, A.; Yang, L.; Elton, T. S.; Chen, C. Real-time PCR quantification of precursor and mature microRNA. *Methods* **2008**, *44*, 31-38.

6. Howerton, D.; Anderson, N.; Bosse, D.; Granade, S.; Westbrook, G. Survey Findings from Testing Sites Holding a Certificate of Waiver Under the Clinical Laboratory Improvement Amendments of 1988 and Recommendations for Promoting Quality Testing. **2005**, *54(RR13);1-25*.

7. Shi, C.; Liu, Q.; Ma, C.; Zhong, W. Exponential Strand-Displacement Amplification for Detection of MicroRNAs. *Anal. Chem.* **2014**, *86*, 336-339.

8. Jia, H.; Li, Z.; Liu, C.; Cheng, Y. Ultrasensitive Detection of microRNAs by Exponential Isothermal Amplification. *Angew. Chem. -Int. Edit.* **2010**, *49*, 5498-5501.

9. Zhang, J.; Li, Z.; Wang, H.; Wang, Y.; Jia, H.; Yan, J. Ultrasensitive quantification of mature microRNAs by real-time PCR based on ligation of a ribonucleotide-modified DNA probe. *Chem. Commun.* **2011**, *47*, 9465-9467.

10. Yang, S.; Rothman, R. E. PCR-based diagnostics for infectious diseases: uses, limitations, and future applications in acute-care settings. *The Lancet Infectious Diseases* **2004**, *4*, 337-348.

11. Yager, P.; Domingo, G. J.; Gerdes, J. Point-of-care diagnostics for global health. *Annu. Rev. Biomed. Eng.* **2008**, *10*, 107-144.

12. Gubala, V.; Harris, L. F.; Ricco, A. J.; Tan, M. X.; Williams, D. E. Point of Care Diagnostics: Status and Future. *Anal. Chem.* **2012**, *84*, 487-515.

13. Yakovchuk, P.; Protozanova, E.; Frank-Kamenetskii, M. D. Base-stacking and base-pairing contributions into thermal stability of the DNA double helix. *Nucleic Acids Res.* **2006**, *34*, 564-574.

14. Drummond, T. G.; Hill, M. G.; Barton, J. K. Electrochemical DNA sensors. *Nat. Biotechnol.* **2003**, *21*, 1192-1199.

15. Wang, K.; Tang, Z.; Yang, C. J.; Kim, Y.; Fang, X.; Li, W.; Wu, Y.; Medley, C. D.; Cao, Z.; Li, J.; Colon, P.; Lin, H.; Tan, W. Molecular Engineering of DNA: Molecular Beacons. *Angew. Chem. -Int. Edit.* **2009**, *48*, 856-870.

16. Marie, R.; Jensenius, H.; Thaysen, J.; Christensen, C.; Boisen, A. Adsorption kinetics and mechanical properties of thiol-modified DNA-oligos on Au investigated by microcantilever sensors. *Ultramicroscopy* **2002**, *91*, 29-36.

17. Silva, M. M.; Cavalcanti, I. T.; Barroso, M. F.; Sales, M. G. F.; Dutra, R. F. Gold electrode modified by self-assembled monolayers of thiols to determine DNA sequences hybridization. *Journal of chemical sciences* **2010**, *122*, 911-917.

18. Mujumdar, R. B.; Ernst, L. A.; Mujumdar, S. R.; Lewis, C. J.; Waggoner, A. S. Cyanine dye labeling reagents: sulfoindocyanine succinimidyl esters. *Bioconjug. Chem.* **1993**, *4*, 105-111.

19. Malicka, J.; Gryczynski, I.; Fang, J.; Lakowicz, J. Fluorescence spectral properties of cyanine dye-labeled DNA oligomers on surfaces coated with silver particles. *Anal. Biochem.* **2003**, *317*, 136-146.

20. Altman, R. B.; Terry, D. S.; Zhou, Z.; Zheng, Q.; Geggier, P.; Kolster, R. A.; Zhao, Y.; Javitch, J. A.; Warren, J. D.; Blanchard, S. C. Cyanine fluorophore derivatives with enhanced photostability. *Nature Methods* **2012**, *9*, 68-U178.

21. Mujumdar, R. B.; Ernst, L. A.; Mujumdar, S. R.; Lewis, C. J.; Waggoner, A. S. Cyanine dye labeling reagents: sulfoindocyanine succinimidyl esters. *Bioconjug. Chem.* **1993**, *4*, 105-111.

22. YU, H.; Chao, J.; Patek, D.; Mujumdar, R.; Mujumdar, S.; Waggoner, A. Cyanine Dye Dutp Analogs for Enzymatic Labeling of Dna Probes. *Nucleic Acids Res.* **1994**, *22*, 3226-3232.

23. Rasnik, I.; McKinney, S. A.; Ha, T. Nonblinking and longlasting single-molecule fluorescence imaging. *Nature Methods* **2006**, *3*, 891-893.

24. Altman, R. B.; Terry, D. S.; Zhou, Z.; Zheng, Q.; Geggier, P.; Kolster, R. A.; Zhao, Y.; Javitch, J. A.; Warren, J. D.; Blanchard, S. C. Cyanine fluorophore derivatives with enhanced photostability. *Nat. Methods* **2012**, *9*, 68-U178.

25. Heilemann, M.; Margeat, E.; Kasper, R.; Sauer, M.; Tinnefeld, P. Carbocyanine dyes as efficient reversible single-molecule optical switch. *J. Am. Chem. Soc.* **2005**, *127*, 3801-3806.

26. Rigler, R.; Elson, E. S. In *Fluorescence Correlation Spectroscopy: Theory and Applications;* Springer Berlin Heidelberg: **2012**; pp 95.

27. Zhao, M.; Huang, R.; Peng, L. Quantitative multi-color FRET measurements by Fourier lifetime excitation-emission matrix spectroscopy. *Opt. Express* **2012**, *20*, 26806-26827.

28. Widengren, J.; Schwille, P. Characterization of photoinduced isomerization and back-isomerization of the cyanine dye Cy5 by fluorescence correlation spectroscopy. *J Phys Chem A* **2000**, *104*, 6416-6428.

29. Huang, Z.; Ji, D.; Wang, S.; Xia, A.; Koberling, F.; Patting, M.; Erdmann, R. Spectral identification of specific photophysics of Cy5 by means of ensemble and single molecule measurements. *J Phys Chem A* **2006**, *110*, 45-50.

30. Eggeling, C.; Widengren, J.; Brand, L.; Schaffer, J.; Felekyan, S.; Seidel, C. Analysis of photobleaching in single-molecule multicolor excitation and forster resonance energy transfer measurement. *J Phys Chem A* **2006**, *110*, 2979-2995.

31. Huang, Z.; Ji, D.; Xia, A. Fluorescence intensity and lifetime fluctuations of single Cy5 molecules immobilized on the glass surface. *Colloid Surf. A-Physicochem. Eng. Asp.* **2005**, *257-58*, 203-209.

32. Huang, Z.; Ji, D.; Xia, A.; Koberling, F.; Patting, M.; Erdmann, R. Direct observation of delayed fluorescence from a remarkable back-isomerization in Cy5. *J. Am. Chem. Soc.* **2005**, *127*, 8064-8066.

33. Zheng, Q.; Jockusch, S.; Zhou, Z.; Altman, R. B.; Warren, J. D.; Turro, N. J.; Blanchard, S. C. On the Mechanisms of Cyanine Fluorophore Photostabilization. *Journal of Physical Chemistry Letters* **2012**, *3*, 2200-2203.

34. Ha, T.; Tinnefeld, P. Photophysics of Fluorescent Probes for Single-Molecule Biophysics and Super-Resolution Imaging. *Annu. Rev. Phys. Chem.* **2012**, *63*, 595-617.

35. Aitken, C. E.; Marshall, R. A.; Puglisi, J. D. An oxygen scavenging system for improvement of dye stability in single-molecule fluorescence experiments. *Biophys. J.* **2008**, *94*, 1826-1835.

36. Demchenko, A. P. In *Advanced Fluorescence Reporters in Chemistry and Biology I: Fundamentals and Molecular Design;* Springer Berlin Heidelberg: **2010**; pp 68.

37. Wittwer, C.; Herrmann, M.; Moss, A.; Rasmussen, R. Continuous fluorescence monitoring of rapid cycle DNA amplification. *BioTechniques* **1997**, *22*, 130-&.

38. Neckers, D. C.; von B\unau, G.; Jenks, W. S. In *Photophysical Probes of DNA Sequence-Directed Structure and Dynamics;* Advances in Photochemistry; Wiley: **2009**; pp 174.

39. Rajadhyaksha, M.; Gonzalez, S.; Zavislan, J.; Anderson, R.; Webb, R. In vivo confocal scanning laser microscopy of human skin II: Advances in instrumentation and comparison with histology. *J. Invest. Dermatol.* **1999**, *113*, 293-303.

40. Mujumdar, R.; Ernst, L.; Mujumdar, S.; Lewis, C.; Waggoner, A. Cyanine Dye Labeling Reagents - Sulfoindocyanine Succinimidyl Esters. *Bioconjug. Chem.* **1993**, *4*, 105-111.

41. Sheehan, J.; Boshart, G.; Cruickshank, P. Convenient Synthesis of Water-Soluble Carbodiimides. *J. Org. Chem.* **1961**, *26*, 2525-&.

42. Montalbetti, C. A. G. N.; Falque, V. Amide bond formation and peptide coupling. *Tetrahedron* **2005**, *61*, 10827-10852.

43. Kurzer, F.; Douraghi.K. Advances in Chemistry of Carbodiimides. *Chem. Rev.* **1967**, *67*, 107-&.

44. Gilles, M.; Hudson, A.; Borders, C. Stability of Water-Soluble Carbodiimides in Aqueous-Solution. *Anal. Biochem.* **1990**, *184*, 244-248.

45. Sehgal, D.; Vijay, I. A Method for the High-Efficiency of Water-Soluble Carbodiimide-Mediated Amidation. *Anal. Biochem.* **1994**, *218*, 87-91.

CHAPTER 7

Conclusions and Future Work

7.1 Conclusions and Future Work

The ability to detect short strands of nucleic acids, including micro RNA (miRNA), has a range of implications for the detection of diseases such as cancer, and can inform the staging and treatment of these conditions as explored in Chapter 1. The current state of the art, polymerase chain reaction (PCR), is capable of detecting ultralow concentrations of nucleic acids, however the equipment, skilled personnel and time required for measurements limits this approach to centralised labs. miRNA have the potential to detect the presence of disease before the onset of visible symptoms, and this early detection can improve patient outcomes, especially in the case of cancer. In order to realise this potential, methods of miRNA detection which are fast, affordable, accurate and highly sensitive are required. To achieve wide scale screening, the device should ideally be available in a point of care setting.

Points of care devices are required to be simple, accurate and to have no reasonable expectation of failure. PCR is currently not able to achieve this standard, and so alternate methods of miRNA detection have been widely explored. Electrochemical detection of miRNA has the potential to fulfil these criteria. A single electrochemical event can generate a large, easily measurable signal. This allows the amplification free detection of miRNA. By integrating an electrochemical detection strategy into a microfluidic device, ultrasensitive point of care detection is possible.

The highly sensitive strategies developed here, electrocatalytic nanoparticles, molecular beacons (MB) and displaceable microspheres, for the detection of nucleic acids represents a powerful, versatile platform technology. The systems have been demonstrated for single targets but multiplexed detection of several nucleic acid targets should be possible by varying the size and metal composition of the regioselectively modified nanoparticles or the dye emission wavelength in the MB/labelled spheres.

With further development, the particle based assays should be suitable for point of care detection of nucleic acid disease biomarkers, potentially as part of a flow based system. Moreover, the regioselective platinum nanoparticles should be capable of the reduction of water which would allow the production of a reagent free device. Beyond electroanalytical applications, regioselective nanoparticles have significant potential for the creation of nanoscale structures. The dual functionality of these particles allows for the potential attachment of different probes, which facilitates the creation of 3D nanostructures. The use of conductive linkers would enable the production of size tuneable nanowires, see Figure 7.1, which have wide ranging applications.

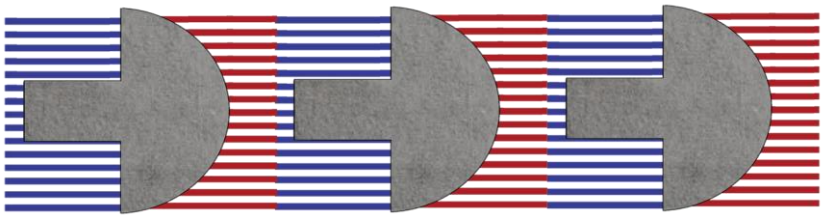

Figure 7.1: Potential size tuneable nanowires using PtNPs functionalised on either end with a conductive linker.

In this work, the expression of miR-132 in live neuroblastoma cells was examined. The high variability and nuclear localisation of miR-132 within individual cells provides a valuable insight into the role of miR-132 in neuroblastoma. While the high variability of the results reported may be impacted by the passage number of the cultured cells, analysis of primary tumour cells using this MB system may be able to provide information on the functional role of miR-132 in neuroblastoma at the single cell level.

The MB unexpectedly emitted even in the absence of the target which increases the limit of detection. The number of self-binding bases was adjusted in an effort to reduce this background but no significant improvement was achieved. Further optimisation of the number of bases in the stem region, and adjustment of the dye and quencher used

may allow for an improved limit of detection. Integration of quantum dots could also potentially aid in detection by improving the emission intensity and sharpen the emission profile which is useful for multiplexing. Quantum dots can have issues with toxicity and in efficient quenching, so integration into a MB may prove challenging. In this work, electroporation and lipid based transfection was used for the transport of the molecular bacon into the cell. Modification with cell penetrating peptides could allow for transport of the beacon into the cell without the use of additional reagents, which is desirable for use in a clinical setting. The attachment of a charged species to the MB may also improve the uptake of the MB.

A displacement assay for the detection of miR-132 was also reported. This assay has significant potential for point of care detection based on the large signal produced from the binding of a single particle. At present, issues remain with the density of capture and target DNA which allows for linkage of the beacon to the surface via multiple hybridisations. This significantly reduces the potential limit of detection. Further optimisation is required to overcome this issue.

Another issue was the negative charge of the microsphere, which caused repulsion between the capture and probe strands. While this is attractive for easy displacement of the particles, it also caused issues with the attachment of the microsphere to the surface. This could be overcome by the addition of positively charged groups, which could be modulated to achieve a neutral or slightly positive charge. In this work, binding of the microsphere to the gold surface caused quenching to the attached dye. This is highly attractive for the detection of miRNA, since this provides a large, easily measurable signal upon displacement. This has the potential for to provide a simple point of care detection strategy, whereby whole blood is added to a displacement array, and displacement of the microspheres causes switching on of a significant fluorescent

signal. This detection could also be mediated by a flow based system, or using magnetic separation.

This displacement assay should be capable of the release of any particle. This could allow for an assay using nanoparticles as the sensing elements, or a species which exhibits electrochemiluminescence (ECL). This could allow for simple multiplexing, where a different species is released in response to different miRNA target binding. This could allow for sensitive, selective detection of multiple miRNA on a single microfluidic chip.

Electrochimica Acta 128 (2014) 61–66

Contents lists available at ScienceDirect

Electrochimica Acta

journal homepage: www.elsevier.com/locate/electacta

Dual function metal nanoparticles: Electrocatalysis and DNA capture

Elaine Spain*, Eoin Brennan, Tia E. Keyes, Robert J. Forster*

School of Chemical Sciences, National Centre for Sensor Research, Dublin City University, Glasnevin, Dublin 9, Ireland

ARTICLE INFO

Article history:
Received 3 July 2013
Received in revised form
20 September 2013
Accepted 1 October 2013
Available online 18 October 2013

Keywords:
Electrocatalytic platinum nanoparticles
Self assembled monolayers
Sonication
DNA detection
Enzyme biosensor
Mastitis

ABSTRACT

Dual function platinum nanoparticles (PtNPs) incorporating two functions, i.e., DNA capture and electrocatalysis that are physically separated, are described. The physical separation of the two functions significantly enhances the sensitivity of DNA detection giving attomolar limits of detection. The regio-selective functionalisation has been achieved using defects within a dodecanethiol (C_{12}) monolayer deposited on a gold electrode. These defects–nucleation sites allow for the electrodeposition of electrocatalytic, mushroom shaped PtNPs. The monolayer allows one side of the nanoparticle to be functionalised with a 20-base oligonucleotide with a C3 spacer thiol (probe) that selectively captures a sequence specifically associated with the strain of *Staphylococcus aureus* associated with mastitis. Once functionalised with capture strand DNA, the particles are released by sonication which maintains the structural integrity of the DNA. Thus, the desorbed nanoparticles are capable of biorecognition on the top curved side and electrocatalytic reduction of hydrogen peroxide on the non-functionalised lower surface. A second gold disc electrode was modified with a 15-base oligonucleotide with a C3 spacer thiol (capture). The presence of a 41-base target oligonucleotide, *S. Aureus*, which hybridized with both capture and probe oligonucleotides, brings the PtNP close to the electrode surface facilitating the electrocatalytic reduction of hydrogen peroxide generating a significant current for each hybridisation event. This highly sensitive detection approach opens up the possibility of avoiding polymerase chain reaction (PCR) or nucleic acid sequence-based amplification (NASBA) based amplification of the target.

© 2013 Elsevier Ltd. All rights reserved.

1. Introduction

Platinum nanoparticles (PtNPs), have attractive properties for analytical applications including electrocatalysis which can dramatically enhance the sensitivity of detection [1], photophysical properties that can enhance energy harvesting [2–5], as well as energy storage and conversion [6–10].

We previously described the regio-selective functionalisation of metal nanoparticles that were functionalised on one side with DNA while the opposite side was electrocatalytically active [11,12]. Particles functionalized in a regio specific manner also allows for different linkers, e.g., assorted DNA sequences or antibodies and nucleic acids, to be co-immobilized in distinct areas giving superior control over the direction of assembly and facilitating multianalyte detection using a single nanoparticle. The regio-selective hemi-spherical PtNPs were obtained by depositing a thiolated self-assembled monolayer onto the gold electrode surface before electrodeposition. The top surface of these PtNPs was then functionalised with thiolated terminated probe strand DNA, and a short current pulse at a current density of approximately 100 mA cm^{-2} was applied to the nanoparticle modified electrode with the objective of melting the nanowire connecting the hemispherical nanoparticle to the electrode. These rather aggressive conditions were used to rapidly desorb the functionalised nanoparticles, which, once in solution would diffuse away from the electrode surface thus retaining their functionality of the bound nucleic acid without causing any damage to the bound DNA. However, the aggressive current step not only removed the PtNPs but also the templating alkane thiol monolayer, and results suggested that induced additional surface roughening of the gold disc electrode also took place [12].

Sonication is frequently used to break up aggregates during purification [13], mixing of two or more nanomaterials [14] and many other types of solution processing techniques [15–18]. It can also be used to remove nanospheres masks and release surfaced confined nanoparticles [19,20]. Therefore, sonication represents an attractive approach for the release of regio-selectively functionalised metal nanoparticles in a manner that causes minimal damage to the underlying electrode and perhaps allowing the monolayer template to be reused.

In this contribution, we describe a simple sonication-assisted desorption route for the production of highly dispersed and

* Corresponding authors. Tel.: +353 861273781.
E-mail address: elainespain@gmail.com (E. Spain).

0013-4686/$ – see front matter © 2013 Elsevier Ltd. All rights reserved.
http://dx.doi.org/10.1016/j.electacta.2013.10.025

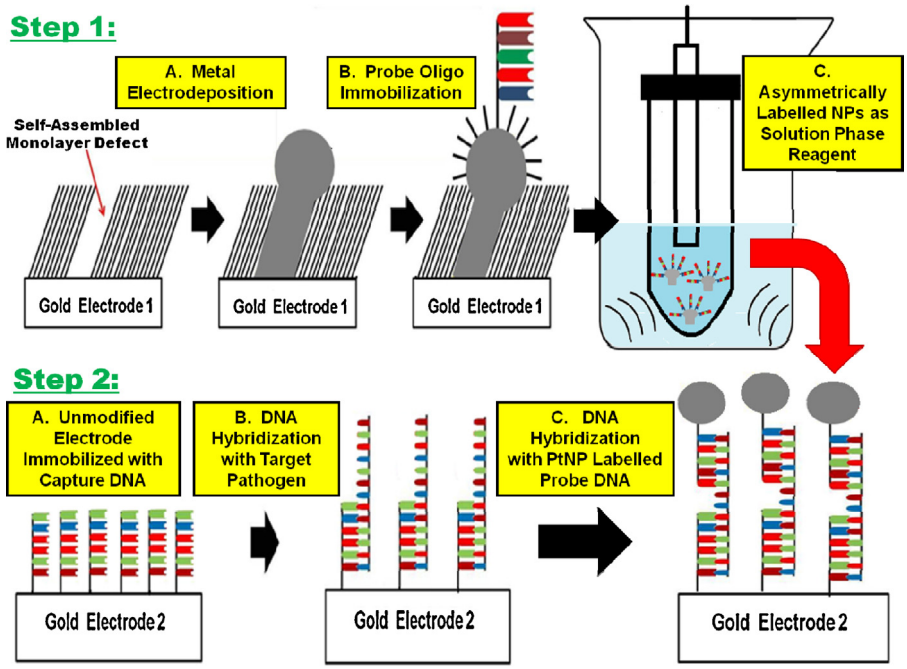

Scheme 1. Platinum nanoparticle formation and regio-selective DNA functionalization.

uniform PtNPs. Using this method, DNA functionalized PtNPs were easily isolated from the monolayer templated electrode and remained separated after sonication. As illustrated in Scheme 1, our approach is based on PtNPs that have been electrodeposited onto an electrode functionalised with a dodecanethiol monolayer in which defects template the nanoparticle electrodeposition. The top surface of these PtNPs is functionalized with thiol terminated probe strand DNA. Then the electrode is sonicated to break the nanowire connecting the hemispherical nanoparticle to the electrode causing disconnection of the DNA functionalized PtNPs. These DNA labelled electrocatalytic particles are then used in a hybridization assay to determine low concentrations of the target by measuring the faradaic current associated with reduction of peroxide in solution. The target is a DNA sequence from the specific bacteria that causes mastitis (mammary gland inflammation). This nucleic acid detection strategy represents a significant advance over current practice where mastitis is detected based purely on clinical signs e.g. udder swelling and irritation (i.e., tender to the touch), fever as well as reduced milk production.

2. Experimental

2.1. Materials

Dodecanethiol was obtained from Sigma–Aldrich. The buffer, denoted as 1 M NaCl-TE, contained 1.0 M NaCl, 10 mM Tris–HCl, and 1 mM ethylenediaminetetraacetic acid (adjusted to pH 7.0 by adding 1.0 M NaOH) and was used for DNA hybridization. Platinum nanoparticles (diameter 50–70 nm) that were used for uniform functionalization with a probe strand DNA were purchased from Eurogentec©^{TM} and their purity was >98%. The base sequences are as follows:

Capture: 5′-CGG-CAG-TGT-TTA-TCA-3′-SH

Target: 5′-TGA-TAA-ACA-CTG-CCG-TTT-GAA-GTC-TGT-TTA-GAA-GAA-ACT-TA-3′

Probe: SH-5′-TA-AGT-TTC-TTC-TAA-ACA-GAC- -3′

Base mismatch: 5′-TGC-TAA-ACA-CTG-CCG-TTT-GAA-GTC-TGT-TTA-AAA-GAA-ACT-TA-3′

3 Base mismatch: 5′-TGC-TAA-ACA-CTG-CCG-CTT-GAA-GTC-TGT-TTA-GAT-GAA-ATA-TA-3′

2.2. Instrumentation

A three-electrode electrochemical cell was used at a temperature of 22 ± 2 °C. The working electrode was a 2 mm radius planar gold disc. It was polished with a nylon cloth with 1 μm diamond polish and thoroughly rinsed with Milli-Q water and ethanol before sonication in Milli-Q water for 5 min. Voltammetry in acid was used to determine the surface roughness factor by scanning the electrode between +1.500 and −0.300 V. The counter electrode was a large area coiled platinum wire and a silver/silver chloride (Ag/AgCl in 3 M KCl) acted as reference. SEM images were taken using a Hitachi S3000N scanning electron microscope at an accelerating voltage of 5 kV. Dynamic Light Scattering (DLS) experiments were performed at 25 °C on a Nanosizer NanoZS (Malvern Instruments, Malvern, U.K.) using a detection angle of 173° and a 3 mW He-Ne laser was operating at a wavelength of 633 nm. The polydispersity indices were calculated from the cumulants analysis as defined in ISO13321 [21]. The intensity size distributions were obtained from analysis of the correlation functions using the Multiple Narrow Modes algorithm based upon a non-negative least-squares fit [22] using Dispersion Technology software (v. 5.3, Malvern Instruments; Worcestershire, U.K.). The values used for the viscosity of platinum in 0.01 M H_2SO_4 were 26.7 cPa s at 298 K.

2.3. Monolayer self assembly

The gold electrodes were cleaned by placing them in piranha solution (3:1 mixture of sulphuric acid and 30% hydrogen peroxide. **CAUTION:** This mixture reacts violently with organic material!) for 20 min, followed by thorough rinsing with ultra-pure water. The electrode was then scanned between +1.500 and −0.300 V in 0.01 M H_2SO_4 to measure the surface roughness of the gold electrode, and to ensure that the electrode is electrochemically clean. Afterwards, the gold disk electrode was washed with ethanol and

then placed in a 1 mM solution of dodecanethiol in ethanol and monolayer self-assembly allowed to proceed for 7 h. After the formation of the monolayer, the substrate was rinsed four to five times with ethanol and dried under a N_2 stream.

2.4. DNA probe immobilization and hybridization

2.4.1. Step 1: Fabrication of regio-selectively DNA functionalized platinum nanoparticles

Platinum nanoparticles were electrodeposited from 1 mM hydrogen hexachlorideplatinate(IV) hydrate (H_2PtCl_6) in 0.5 M H_2SO_4 using the defects within the self-assembled monolayer as templates. Subsequently, in Step 1B, the PtNPs were functionalized with probe oligo (5′ thiolate) by immersing the nanoparticle functionalized electrode in a 10 μM solution of the probe DNA strand dissolved in 1 M NaCl-TE Buffer for 2 h. The modified electrodes were then washed with deionized water for 15 s to remove loosely bound oligo and immersed in 0.01 M H_2SO_4. The oligo functionalized PtNPs were then removed via sonication for 1 h and re-dispersed in 0.01 M H_2SO_4.

2.4.2. Step 2A: Monolayer of capture strand DNA

A monolayer of capture strand DNA was prepared on a freshly polished and electrochemically cleaned gold disk electrode by immersing it in a 10 μM solution of the capture strand DNA dissolved in 1 M NaCl-TE Buffer. After 5 h, the electrode was rinsed with deionized water for 15 s to remove loosely bound oligo.

2.4.3. Step 2B: Hybridization of target oligo to the capture surface

Hybridization of the target at concentrations between 10 pM and 1 μM to the immobilized capture strand was performed at 37 °C in 1 M NaCl-TE Buffer for 90 min. Following hybridization, the modified electrode was rinsed thoroughly with buffer.

2.4.4. Step 2C: Probe hybridization

The nanoparticle labelled probe DNA was then hybridized to the complementary section of the target not used for binding to the capture strand for 2 h at 37 °C in 1 M NaCl-TE Buffer. Finally, before quantitation, it was thoroughly washed with deionized water.

2.5. Electrochemical detection of Staphylococcus Aureus ss-DNA target

Following assembly of the capture-target-nanoparticle labelled probe DNA sequence, the modified electrode was placed in an aqueous solution of 0.01 M H_2SO_4 and the current measured at −0.250 V after equilibration for 10 min. Then, sufficient hydrogen peroxide was added to give a final concentration of 200 μM, and the reduction current associated with peroxide reduction at the bound PtNPs was measured at −0.250 V after 10 min. The analytical response is taken as the difference in current, Δi, measured before and after peroxide addition.

3. Results and discussion

3.1. Cyclic voltammetry

Self assembled monolayers, SAMs, of alkane thiols on gold allow the interfacial properties to be tuned for particular applications. They adsorb rapidly to give films that initially have a high defect density which slowly anneal to give well-ordered films [23]. Here, defective monolayers are deliberately created by using a relatively short monolayer deposition time. Fig. 1(A) and (B) illustrate cyclic voltammograms for the 2 mm radius gold electrodes before and after deposition of the defective monolayer, respectively. The active surface area can be determined using voltammetry in 0.01 M

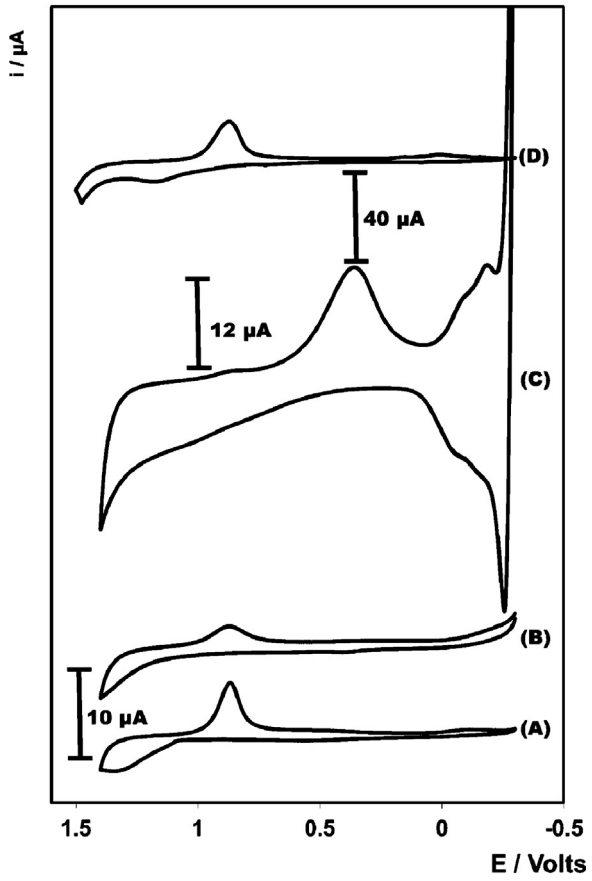

Fig. 1. Cyclic voltammograms of (A) 2 mm unmodified gold electrode, (B) after deposition of a defective C_{12} monolayer, (C) following electrodeposition of PtNPs into the monolayer defects (D) after the PtNPs have been desorbed via sonication. The scale bar for (A) and (B) are 10 μA while for (C) and (D) it is 40 μA. The supporting electrolyte is 0.1 M H_2SO_4. The counter electrode was a large area platinum wire, and the reference electrode was saturated Ag/AgCl (3 M KCl).

H_2SO_4 as the supporting electrolyte by creating and subsequently reducing a gold oxide monolayer on the unmodified fraction of the electrode. By comparing the charge passed before and after monolayer deposition, the area available for platinum nanoparticle, PtNP, electrodeposition can be determined. Monolayer deposition decreases the area under the gold oxide reduction peak current at approximately +0.87 V from 0.034 cm^2 for the unmodified electrode (roughness factor of 1.08) to 0.028 cm^2 following monolayer deposition. This result confirms that there are a substantial number of sites for metal deposition at the partially blocked surface. PtNPs were deposited into the defects within the monolayer from a 0.5 M sulphuric acid solution containing 1 mM hydrogen hexachlorideplatinate(IV) hydrate (H_2PtCl_6). Fig. 1(C) illustrates the cyclic voltammogram following nanoparticle deposition at an applied potential of −0.250 V for 180 s. After the electrochemically deposition of PtNPs, the area under the platinum oxide reduction peak [24,25] (between 0.05 and 0.3 V vs. Ag/AgCl) increased while the area associated with gold oxide formation and reduction decreased significantly. Significantly, the microscopic area following deposition of the PtNPs is 0.296 cm^2, i.e., nanoparticle deposition increases the area available for DNA deposition by a factor of approximately 11 when compared to dodecanethiol templated electrode, i.e., the radius of the electrodeposited PtNPs is significantly larger than that of the templating defects leading to mushroom shaped particles. Following binding of the probe oligo, the nanoparticle modified electrode was removed via sonication for 1 h at 90 sonics min with the objective of disconnecting the

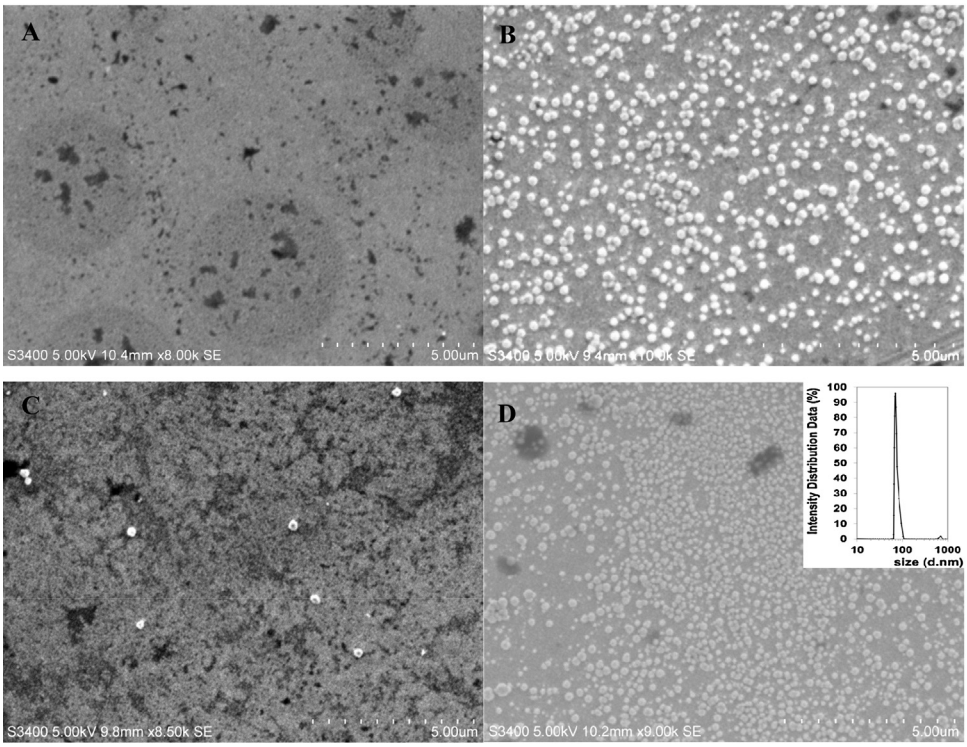

Fig. 2. SEM images of (A) a gold electrode following deposition of the templating monolayer following, (B) electrodeposition of PtNPs for 180 s, (C) after the PtNPs have been desorbed via sonication and (D) drop cast film of desorbed nanoparticles from suspension (inset: particle size distribution measured using DLS for desorbed PtNPs in suspension). The acceleration voltage is 5 kV.

nanowire linking the hemispherical nanoparticle to the electrode. This method successfully desorbed the nanoparticles. Fig. 1(D) shows that the peak heights associated with both platinum oxide reduction and hydrogen adsorption–desorption are dramatically lower after desorption of the PtNPs. Significantly, the area under the gold oxide peak, reduction peak centreed at approximately +0.8 V increases after nanoparticle desorption to 0.030 cm^2, which is indistinguishable from that found for the defective templating monolayer before deposition 0.028 cm^2. Significantly, in contrast to the previously reported current jump approach [11,12], sonication successfully removes the PtNPs with minimal alkane thiol monolayer desorption.

3.2. SEM

Fig. 2(A) shows an SEM image of the gold electrode following deposition of the defective alkane thiol template for 7 h and electrodeposition of the PtNPs (Fig. 2(B)) using a deposition time of 180 s. It is challenging to accurately determine the size distribution of the templating defects in the monolayer using SEM. However, it is clear that with an electrodeposition time of 180 s that the radius of the nanoparticles typically exceeds the size of the defects by at least 50%, i.e., the electrodeposited nanoparticles are mushroom shaped. The image reveals a relatively high surface coverage of nanoparticles with a radius of 70 ± 30 nm. This particle shape will result in approximately two thirds of the total nanoparticle surface (hemisphere) being modified by probe strand DNA with approximately one third (disk) being unmodified and available for electrocatalysis. Fig. 2(C) displays an SEM of a sonicated gold electrode; where, the electrodeposited PtNPs within a defective C_{12} monolayer have been removed. The SEM demonstrates that the sonication step successfully removes the majority of the PtNPs from the electrode surface. Fig. 2(D) shows an image for a gold substrate onto which a droplet of the suspended nanoparticles has been drop cast and allowed to dry. This image reveals that desorption does not change the average particle size significantly and a relatively high concentration of nanoparticles in the suspension can be achieved. In addition to the SEM characterization, the radius of the suspended nanoparticles was obtained by DLS, (inset Fig. 2(D)), as 70 ± 30 nm, which is consistent with the SEM data.

3.3. Binding of regio-selectively decorated nanoparticles

In order to successfully detect DNA, the desorbed nanoparticles must be both electrocatalytically active and be capable of binding the target DNA. As illustrated in Scheme 1, an electrode modified with DNA capture strands was first allowed to hybridize with the target strand, part of which is complementary to the capture strand. This electrode was then placed into the NP suspension for 90 min during which time the non-hybridized section of the target hybridizes with the oligo bound to the metal nanoparticle. Fig. 3(A) illustrates the voltammogram obtained for an electrode in 0.01 M H_2SO_4 after electrodeposition of the PtNPs and functionalisation with the probe strand DNA. Fig. 3(B) shows the response obtained for a pristine gold electrode modified with the capture strand DNA after both the target and the nanoparticle functionalized probe strand hybridization steps have occurred. Both of these figures show well defined peaks for Pt oxide formation in the 0.6 to 1.2 V range, reduction of Pt oxide at approximately +0.3 V, as well as peaks in the range of −0.05 V to −0.3 V associated hydrogen adsorption–desorption, respectively. These observations indicate successful binding of the nanoparticles suggesting that the DNA functionalized PtNPs can be removed into suspension using sonication. Control experiments in which the target is not added or where the nanoparticles are either not functionalized with DNA, or are functionalized with non-complementary DNA, do not exhibit

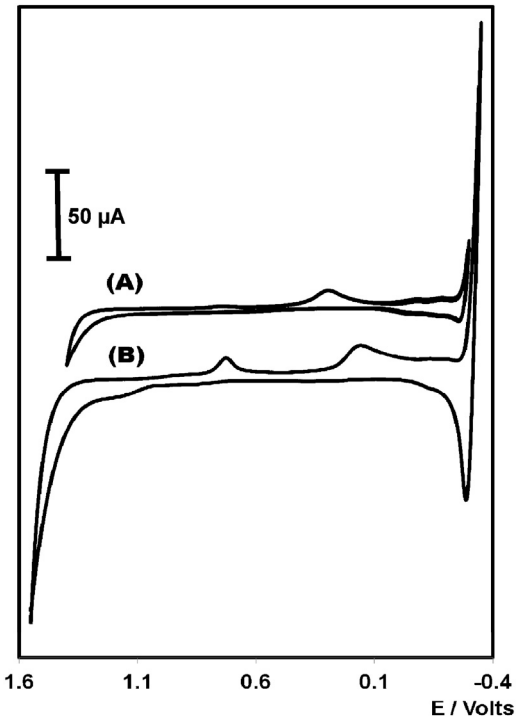

Fig. 3. (A) Cyclic voltammogram of a 2 mm radius gold disc electrode after electrodeposition of the PtNPs and functionalization with probe DNA (step 3 of Scheme 1), (B) cyclic voltammogram of a 2 mm radius gold disc electrode after modification with the capture strand DNA and hybridization with the target and the nanoparticle labelled probe sequence where the target strand concentration is 1 μM. The supporting electrolyte is 0.01 M H_2SO_4, and the scan rate is 100 mV s^{-1}.

features associated with platinum oxide or hydrogen adsorption, i.e., the extent of non-specific adsorption of the functionalised nanoparticles is very low.

3.4. Electrochemical detection of S. Aureus DNA

Platinum nanoparticles are well known to catalyze the reduction of hydrogen peroxide. The probe-modified PtNPs were hybridized with the modified electrode containing the DNA sequence complementary to the probe ssDNA to form a surface-bound duplex (dsDNA). The analytical performance of the DNA sensor using the regio-selectively modified nanoparticles was investigated and compared with that observed for nanoparticles that are uniformly functionalized with the probe DNA. The catalytic activity of the PtNPs bound through DNA hybridization (Step 2-C in scheme) was assessed by applying fixed potential of −0.2500 V to the working electrode and the difference in current, Δi, observed before and after the addition of 200 μM H_2O_2, measured. Fig. 4 shows the dependence of Δi on the log [DNA] for detection of pathogen DNA where the probe strand is either unlabelled or is labelled with regio-selectively modified PtNPs. In each case, an acceptably linear response is observed for concentrations of sequence-specific DNA from *S. Aureus* from 10 pM to 1 μM. The sensitivity of the 2 mm gold disc electrode (▲) following hybridisation of the DNA where the probe DNA strand is unlabelled is 0.0314 μA^{-1}, reflecting the poor electrocatalytic properties of the DNA modified gold electrode. These low currents in the absence of PtNP labels indicate that the background current associated with direct reduction of hydrogen peroxide at the underlying electrode is low. This result is significant as the magnitude of this background current will directly influence the limit of detection. In contrast, the sensitivity of the assay involving regio-selectively modified PtNPs labelled with probe strands (♦) is approximately 28 times larger, 8.8×10^{-2} μA^{-1}, than that

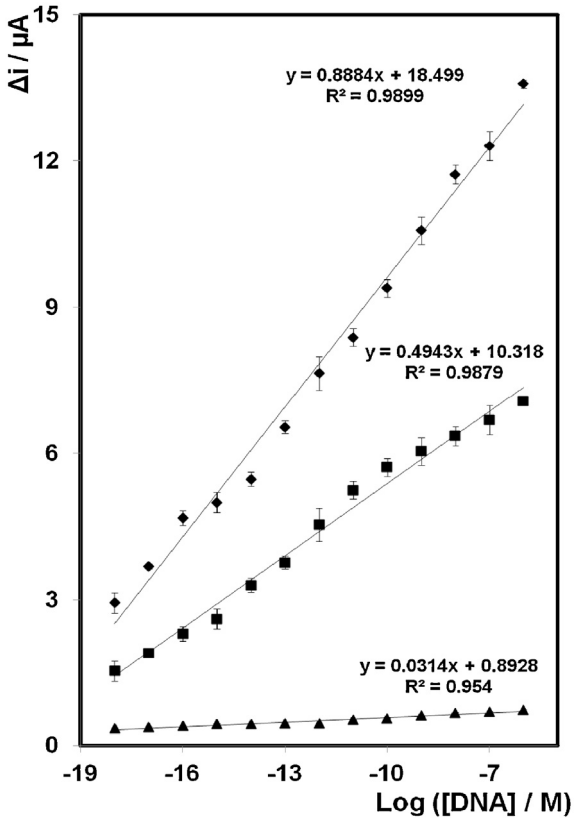

Fig. 4. Calibration plots for the electrochemical detection of *S. Aureus* mastitis DNA on a 2 mm diameter bare electrode following hybridization with probe DNA immobilize regio-selectively on PtNPs (♦) and where the probe is unlabelled (▲). A control experiment showing the response of the electrode with uniform PtNPs functionalized with a homogenous full DNA monolayer is also illustrated (■). In all cases, a final concentration of a 200 μM solution of H_2O_2 in aqueous 0.01 M H_2SO_4 was added. Δi represents the difference in current before and after addition of the H_2O_2 at an applied potential of −0.250 V following approximately 10 min equilibration time. Where error bars are not visible, they are smaller than, or comparable to, the size of the symbols.

found in the label free assay, indicating that a significant population of the nanoparticles are desorbed by the sonication–desorption technique. This result clearly indicates that physically separating the two functions of the nanoparticles, i.e., electrocatalysis and molecular recognition, leads to a significant improvement in assay performance. The dramatically higher sensitivity and wide linear dynamic range indicates that the desorbed nanoparticles retain both their electrocatalytic and DNA binding capabilities. Also, the high current density observed suggests that heterogeneous electron transfer from the PtNPs, through the DNA linker, to the underlying electrode is relatively facile.

Fig. 4 also highlights a control experiment (■); where, commercially bought PtNPs in suspension were homogenously labelled with probe DNA and then investigated for the catalytic activity for the H_2O_2 oxidation–reduction reaction. An acceptably linear response is observed for concentrations of sequence-specific DNA from *S. Aureus* from 10 pM to 1 μM. However, the sensitivity of the uniform PtNP electrode is 4.9×10^{-2} μA^{-1}, reflecting the poor electrocatalytic properties of the round PtNPs with a full DNA monolayer compared to the regio-selective decorated PtNPs. The current associated with direct reduction of hydrogen peroxide at the metal centre is low as for electrocatalysis to occur, electrons need to run through the DNA monolayer before it reaches the PtNP surface. These low currents indicate that the regio-selective decorated PtNPs provides a surface that is covered in DNA to give you

molecular recognition with another uncoated side to give a clean surface for catalysis.

The selectivity of the sensor was also investigated using a target DNA sequence that contained a single mismatch. Significantly, the differential current observed for this one base mismatch DNA sequence was a factor of four smaller than that found for the fully complementary sequence suggesting high discrimination ability. Moreover, *S. epidermis* which has 3 base mismatches, gives no measureable current response demonstrating the system is robust with respect to false positives. This result is particularly important as *S. epidermis* can often be mistaken for *S. Aureus* and its presence incorrectly associated with mastitis. It also further confirms that the bound DNA has not been denatured as the particles are desorbed off the electrode surface.

4. Conclusion

It was demonstrated that PtNPs could be regio-selectively functionalized (upper surface only) with DNA while the remainder of the particles surface is unmodified allowing efficient electrocatalysis to occur. An efficient strategy for desorbing regio-selective electrocatalytic PtNPs via sonication is presented. The key advantage of this simple sonication-assisted desorption route is the isolation of highly dispersed and uniform PtNPs nanoparticles without any damage to the bound DNA or underlying gold electrode. These desorbed particles can then quickly sample the solution and can selectively detect target strand DNA at attomolar concentrations by stirring rather than waiting for target strands to arrive at the electrode interface. This is particularly important for detection of sub-femtomolar DNA where diffusion is too slow to allow the surface coverage of the target to approach equilibrium on a meaningful timescale. The assay is characterized by a wide dynamic range, high sensitivity, a low detection limit and an excellent ability to discriminate against interferences.

Acknowledgment

This material is based upon works supported by the Science Foundation Ireland under Grant No. 10/IN.1/B3021.

References

[1] S.J. Kwon, A.J. Bard, DNA analysis by application of Pt nanoparticle electrochemical amplification with single label response, J. Am. Chem. Soc. 134 (2012) 10777–10779.
[2] S.J. Cho, J. Ouyang, Attachment of platinum nanoparticles to substrates by coating and polyol reduction of A platinum precursor RID F-6063-2011, J. Phys. Chem. C 115 (2011) 8519–8526.
[3] Y. Li, H. Yu, W. Song, G. Li, B. Yi, Z. Shao, A novel photoelectrochemical cell with self-organized TiO2 nanotubes as photoanodes for hydrogen generation, Int. J. Hydrogen Energ. 36 (2011) 14374–14380.
[4] S. Oh, W. Nam, H. Joo, S. Sarp, J. Cho, C. Lee, et al., Photoelectrochemical hydrogen production with concentrated natural seawater produced by membrane process, Sol. Energy 85 (2011) 2256–2263.
[5] K. Wang, J. Yang, L. Feng, Y. Zhang, L. Liang, W. Xing, et al., Photoelectrochemical biofuel cell using porphyrin-sensitized nanocrystalline titanium dioxide mesoporous film as photoanode, Biosens. Bioelectron. 32 (2012) 177–182.
[6] J. Suntivich, H.A. Gasteiger, N. Yabuuchi, H. Nakanishi, J.B. Goodenough, Y. Shao-Horn, Design principles for oxygen-reduction activity on perovskite oxide catalysts for fuel cells and metal-air batteries, Nat. Chem. 3 (2011) 546–550.
[7] X. Zhang, W. Lu, J. Da, H. Wang, D. Zhao, P.A. Webley, Porous platinum nanowire arrays for direct ethanol fuel cell applications, Chem. Commun. (2009) 195–197.
[8] B. Braunchweig, D., Hibbitts, M., Neurock, A., Wieckowski, Electrocatalysis A direct alcohol fuel cell and surface science perspective, Catalysis Today.
[9] M. Watanabe, D.A. Tryk, M. Wakisaka, H. Yano, H. Uchida, Overview of recent developments in oxygen reduction electrocatalysis, Electrochim. Acta 84 (2012) 187–201.
[10] A. Kloke, F. von Stetten, R. Zengerle, S. Kerzenmacher, Strategies for the fabrication of porous platinum electrodes, Adv. Mater. 23 (2011) 4976–5008.
[11] E. Spain, B. Miner, T.E. Keyes, R.J. Forster, Regio selective functionalisation of gold nanoparticles with DNA, Chem. Commun. 48 (2012) 838–840.
[12] E. Spain, E. Brennan, H. McArdle, T.E. Keyes, R.J. Forster, High sensitivity DNA detection based on regioselectively decorated electrocatalytic nanoparticles, Anal. Chem. 84 (2012) 6471–6476.
[13] G.P. Sanganwar, R.B. Gupta, Nano-mixing of dipyridamole drug and excipient nanoparticles by sonication in liquid CO2, Powder Technol. 196 (2009) 36–49.
[14] K. Niesz, D.E. Morse, Sonication-accelerated catalytic synthesis of oxide nanoparticles, Nano Today 5 (2010) 99–105.
[15] Y. Kim, J. Kang, S. Lim, J. Song, Facile synthesis of monodispersed PdO nanoparticles within mesoporous silica with sonication, B. Kor. Chem. Soc. 26 (2005) 1129–1131.
[16] G.Q. Zhang, H.P. Wu, M.Y. Ge, Q.K. Jiang, L.Y. Chen, J.M. Yao, Ultrasonic-assisted preparation of monodisperse iron oxide nanoparticles, Mater. Lett. 61 (2007) 2204–2207.
[17] X. Ma, Y. Shen, G. Wu, Q. Wu, B. Pei, M. Cao, et al., Sonication-assisted sequential chemical bath deposition of CdS nanoparticles into TiO2 nanotube arrays for application in solar cells, J. Alloy. Compd. 538 (2012) 61–65.
[18] F. Basarir, T. Yoon, Sonication-assisted layer-by-layer deposition of gold nanoparticles for highly conductive gold patterns, Ultrason. Sonochem. 19 (2012) 621–626.
[19] A.V. Whitney, J.W. Elam, S.L. Zou, A.V. Zinovev, P.C. Stair, G.C. Schatz, et al., Localized surface plasmon resonance nanosensor: A high-resolution distance-dependence study using atomic layer deposition, J. Phys. Chem. B 109 (2005).
[20] A. Haes, J. Zhao, S. Zou, C. Own, L. Marks, G. Schatz, et al., Solution-phase, triangular Ag nanotriangles fabricated by nanosphere lithography, J. Phys. Chem. B 109 (2005) 11158–11162.
[21] International Organization for Standardization (ISO), Methods for Determination of Particle Size Distribution Part 8: Photon Correlation Spectroscopy, in: International Standard ISO13321, 1996.
[22] C.L. Lawson, R.J. Hanson, Solving least squares problems, Soc. Ind. Appl. Math. (1995).
[23] L. Srisombat, A.C. Jamison, T.R. Lee, Stability A key issue for self-assembled monolayers on gold as thin-film coatings and nanoparticle protectants, Coll. Surface A: Physicochem. Eng. Aspects 390 (2011) 1–19.
[24] P. Bartlett, J. Marwan, The effect of surface species on the rate of H sorption into nanostructured Pd RID C-4606-2008, Phys. Chem. Chem. Phys. 6 (2004) 2895–2898.
[25] B. El Roustom, G. Sine, G. Foti, C. Comninellis, A novel method for the preparation of bi-metallic (Pt-Au) nanoparticles on boron doped diamond (BDD) substrate: application to the oxygen reduction reaction, J. Appl. Electrochem. 37 (2007) 1227–1236.